Toward a single molecule study of asymmetric experiment

Assa Sittner

THÉSE DE DOCTORAT DE L'UNIVERSITE PIERRE ET MARIE CURIE

Specialité

Biophysique

École doctorale de physique de la région Parisienne

Preséntée par

M. Assa Sittner Pour obtenir le grade de

DOCTEUR DE L'UNIVERSITÉ PIERRE ET MARIE CURIE

Sujet de la thése :

Vers une étude de la division asymétrique des cellules à l'échelle de la molécule unique

Soutenue le 08.01.2010 devant le jury composé de :

Directeur de thése :	*Dr. Maxime Dahan*
Rapporteurs :	*Dr. Laurent Cognet*
	Pr. Thomas Schmidt
Examinateurs :	*Dr. Yohanns Bellaïche*
	Pr. Denis Cote

Contents

Introduction

Le but de ce projet est de développer de nouveaux outils pour explorer des processus d'organisation intracellulaire dynamique dans les cellules vivantes, avec une sensibilité sans précédent. Ce travail se concentre sur deux aspects principaux : le développement d'outils pour l'étude en molécule unique de la division cellulaire asymétrique, et la mise au point de sondes monovalentes qui permettent le suivi d'une protéine individuelle utilisant un nanocristal semiconducteur (ou quantum dot, QD).

Suivi de molécules individuelles avec des nanocristaux semiconducteurs

Nous employons des méthodes de molécule unique, qui nous permettent de suivre le mouvement de chaque molécule séparément. En observant des processus à l'échelle de la molécule individuelle, il est possible d'obtenir des informations sur des processus biologiques qui sont inaccessibles par des mesures sur toute la population. Ainsi, les mesures à l'echelle de la molécule unique peuvent apporter des renseignements sur l'hétérogénéité de l'échantillon [1] et l'existence d' événements aléatoires non-sychronysés dans l'échantillon [2], qui sont habituellement cachés par les effets de moyennage. Ceci est obtenu, en utilisant des fluorophores nouveaux, appelés nanocristaux semiconducteurs ou quantum dots (QDs), qui permettent de détecter et suivre une seule molécule unique en milieu vivant. Les QDs sont des nanoparticules ayant un diamètre de quelques nanomètres et des propriétés physiques uniques. Ils surpassent les protéines fluorescentes [3, 4] et les colorants organiques [5] dans plusieurs aspects de photophysique. Leur coefficient d'extinction exceptionnellement élevé, plus de 10 fois celui des meilleurs colorants organiques, conduit à une émission de fluorescence intense. Cette propriété permet la détection et l'imagerie des QDs avec un rapport signal sur bruit élevé, même en utilisant des configurations standard de microscopie de fluorescence. Le rapport signal sur bruit élevé permet aussi la localisation des QDs avec une précision de quelques nanomètres, bien en deçà de la limite de diffraction ($\sim 250nm$). Un autre avantage important des QDs est leur photo-stabilité remarquable. Leur capacité de résister une exposition constante à la lumière d'excitation pour de longues périodes de temps (minutes ou quelques heures), sans être photodétruit, est de loin supérieure à celle des protéines fluorescentes ou des colorants organiques (0,1 à 10 secondes). Cette propriété permet l'observation des processus cellulaires dans une échelle de temps physiologique. Une expérience typique de suivi d'un QD unique (Single Quantum Dot Tracking, SQDT) est réalisée en prenant des séquences d'images de QDs mobiles à à la membrane ou à l'intérieur des cellules. Les trajectoires de ces QDs sont analysées en ajustant leurs déplacement quadratique moyen (MSD) pour extraire des paramètres de transport tels que le coefficient de diffusion.

Même si les QDs inertes (également dénommés « QDs libres ») peuvent être utilisés pour observer une variété de phénomènes cellulaires, comme les changements en micro-rhéologie [6] dans l'espace et le temps, et la compartimentation cellulaire [7], ces applications ne profitent pas pleinement des propriétés des QDs. En conjuguant les QDs à des molécules d'intérêt, nous pouvons précisément sonder le comportement dynamique de ces molécules dans la cellule. Ceci

peut être réalisé, en utilisant des méthodes de conjugaison basées sur l'affinité (utilisant des paires telles que des anticorps et de leurs épitopes, ou le système avidine-biotine [8]), ou une liaison non spécifique covalente basées sur la réticulation [9].

Les QDs sont d'abord fonctionnalisés *in-vitro*, soit directement avec la molécule d'intérêt (dans la plupart des cas, une protéine), soit avec une molécule de « ciblage », c'est à dire une molécule réactive qui peut se lier spécifiquement une protéine endogène d'intérêt. Dans le premier cas, si la conjugaison est fait correctement, le comportement intracellulaire des QDs devrait refléter le comportement de la protéine d'intérêt. Dans le dernier cas, le comportement intracellulaire du QD dépend aussi de la capacité de la QD pour trouver sa cible, la protéine d'intérêt, et à s'y attacher. Ceci nous amène à une autre question importante dans le domaine du SQDT : le problème de valence [10]. Lorsque les QDs sont conjugués à une protéine d'interêt, ou une molécule de ciblage, le résultat est un mélange de stoechiométries différentes des complexes QD :protéine (ou QD :molécule de ciblage), en raison de la stochasticité de réactions de conjugaison chimiques. L'utilisation d'un tel mélange des QDs pour le suivi pourrait donner des résultats difficiles ou impossibles à interpréter, car un QD donné peut se fixer à un nombre inconnu de molécules d'intérêt, et même pire, chaque molécule liée au QD peut avoir des propriétés de transports totalement différentes. Afin de faire face à ce problème, nous avons développé : (i) une stratégie de ciblage, fondée sur un fragment de chaîne variable d'anticorps (ScFv) [11], une version minimal et monovalente de l'anticorps couramment utilisé, (ii) une methode de couplage qui permet de contrôler le valence des complexes QD-protéines.

La polarité cellulaire et la division cellulaire asymétrique

La division cellulaire asymétrique (DCA) est définie comme une division cellulaire dans laquelle une cellule mère donne naissance à deux cellules filles avec des destins différents (ce qui se manifeste à travers par exemple la taille, le contenu ou le profil d'expression). Au cours de la division, le contenu de la cellule mère est inégalement séparé entre les cellules filles. Afin d'atteindre cet objectif, la distribution de certaines molécules doit maintenir une asymétrie stable et robuste pendant toute la division. La génération d'une répartition asymétrique de certains éléments de la composition ou la structure de la cellule est appelée la polarisation [12]. Ces éléments sont appelés déterminants cellulaires. Une question importante est de comprendre les processus de transport qui génèrent cette polarité et assurent la localisation dynamique des déterminants cellulaires.

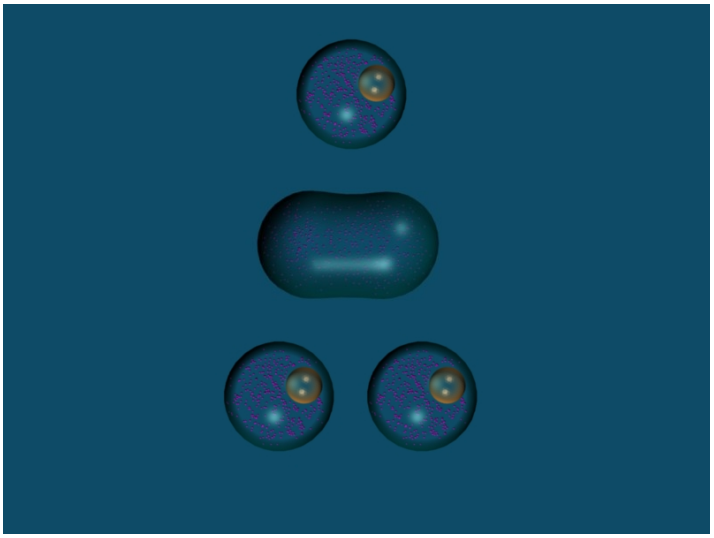

(a) La division cellulaire symétrique.

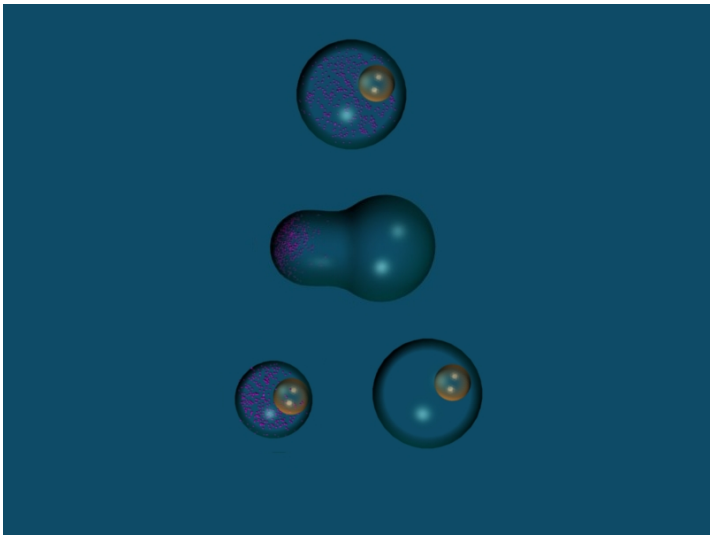

(b) *La division cellulaire asymétrique, dans la taille et le contenu.*

FIG. 1 – *La division cellulaire symétrique et la division cellulaire asymétrique. Les petites sphères violets représentent un composant de la cellule qui devient asymétriquement distribue au cours de l'ACD.*

La DCA peut être trouvée dans des organismes de tous les niveaux, des bactéries (comme la bactérie bien étudié *Caulobacter crescentus* [13]) aux cellules souches humaines [14]. D'un point de vue de physique, la division cellulaire asymétrique est intéressante dans le contexte de l'auto-organization. Une des définitions de l'auto-organisation [15] stipule qu'elle est un processus dans lequel un motif au niveau macroscopique émerge uniquement à partir de nombreuses interactions entre des composants de niveau inférieur du système. En outre, les interactions qui donnent naissance à la structure macroscopique sont dictées par des « règles » microscopiques, fondées uniquement sur des informations locales. A la lumière de cette définition, les méthodes de molécules uniques sont très prometteuses pour élucider les phénomènes d'auto-organisation, en raison de leur sensibilité et leur grand contenu d'information, en évitant les effets de moyennage sur l'échantillon. En outre, le processus de DCA, dans lequel la cellule travaille contre l'entropie de mélange afin de « trier » son contenu interne, n'a jamais été étudié en détail, de façon quantitative. L'étude de la DCA est également pertinente pour la recherche sur le cancer, car il a été constaté que la suppression de certains déterminants cellulaires augmente la prolifération des cellules et que certaines de ces protéines agissent comme des suppresseurs de tumeurs.

Notre étude se concentre sur la division cellulaire asymétrique dans les cellules souches neurales de *Drosophila melanogaster*, appelés neuroblastes. Au cours de la division asymétrique des neuroblasts, avant la séparation de la cellule-mère en deux cellules-filles, certaines molécules dans le cytoplasme se redistribuent de façon asymétrique (polarisée). L'axe de polarisation dans ces cellules est appelé l'axe apico-basal, qui est l'un des axes morphologiques du corps de la drosophile.

Au cours de la division, quelques éléments au sein du contenu de la cellule-mère sont triés : soit à la partie basale, soit à la partie apicale. Nous avons choisi d'étudier trois de ces molécules : PON [16], Miranda [17] and Pins [18]. Les deux premières se localisent dans la partie basale de la cellule, tandis que la dernière, Pins, se localise dans la partie apicale de la cellule.

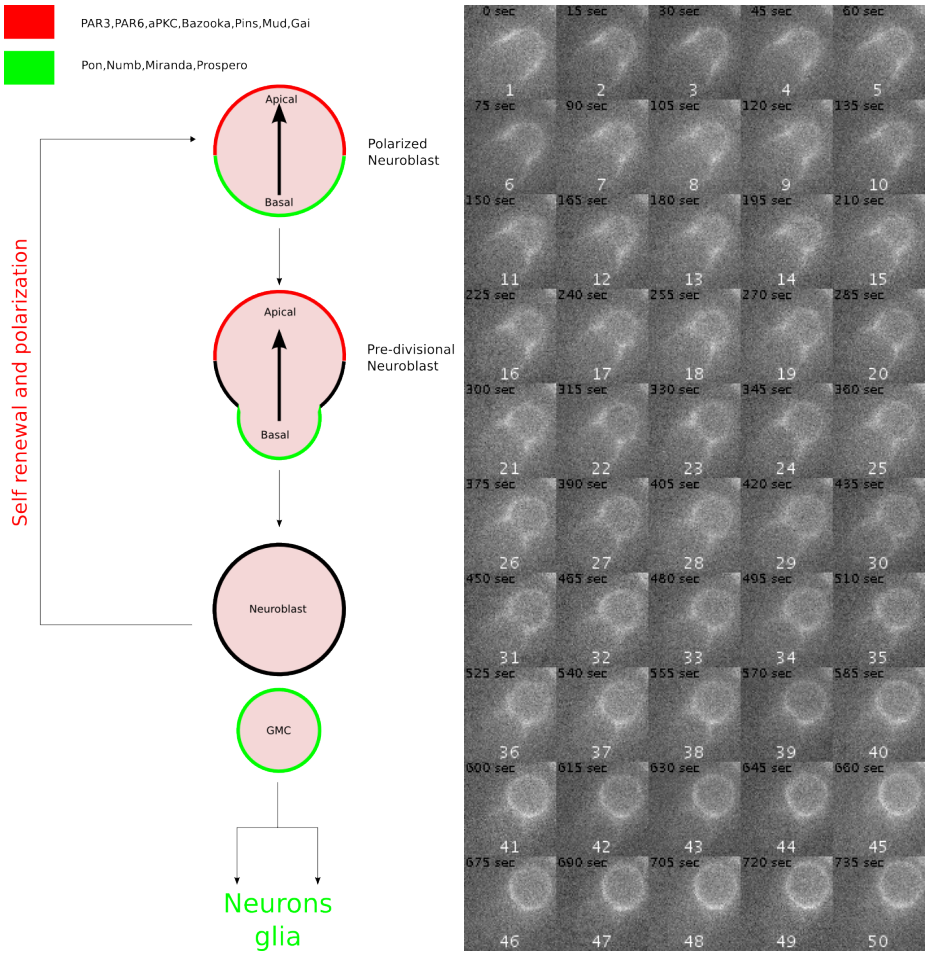

(a) *Un schéma de la division cellulaire asymétrique dans les neuroblastes de la drosophile. Un neuroblaste se polarise (génère une asymétrie importante dans la distribution de sa contenu) et ensuite, se divise selon l'axe de polarisation en deux cellules filles différentes. Une des cellules filles est une cellule mère ganglion (GMC), qui est un précurseur du système nerveux central de la mouche. L'autre cellule est encore un neuroblaste qui peut alors répéter le processus de nombreuses fois (ce phénomène, appellé l'auto-renouvellement ou "self renewal", est caractéristique aux cellules souches.). Différentes protéines dans le cytoplasme sont triées entre la partie apicale et la partie basale se la cellule et, plus tard, entre les deux cellules filles (neuroblaste et GMC, respectivement).*

(b) *Une division asymétrique dans les neuroblastes exprimantes PON-GFP , vu par l'imagerie en fluorescence. Au début (image 1), un croissant fluorescent est vu, qui est la proteine PON-GFP polarisée (dans la partie basale de la cellule). Tant que la division se poursuit, le sillon de division apparaît sur la frontière du croissant PON-GFP. Le sillon de division se rétrécit, jusqu'à ce qu'il ferme définitivement, en donnant lieu à la cellule mère Ganglion (GMC), qui contient PON-GFP.*

FIG. 2 – *La division asymétrique cellulaire chez des neuroblastes de Drosophila melanogaster*

Résultats

Internalisation de sondes dans les cellules

Sachant que l'internalisation des QDs est l'une des limites techniques les plus importantes pour le SQDT, [19], la première étape du projet était de comprendre et de décrire le mouvement de QDs non-conjugués à l'intérieur des cellules. Par conséquent, nous avons optimisé l'internalisation des QDs dans des cellules vivantes, et caractétérisé le mouvement de QDs inertes dans le cytoplasme. Nous avons également comparé les les deux méthodes les plus courantes pour l'internalisation de QDs : la micro-injection [20] et l'influx pinocytique [21] en analysant la diffusion de QDs individuels. Puis, nous avons étudié la diffusion des QDs non-conjugués dans diverses lignées de cellules. Nous avons trouvé des différences significatives dans les coefficients de diffusion intracellulaires entre les cellules d'insectes et des cellules des mammifères (voir **Figure 11.12**). Nous avons également constaté que les QDs les plus lents sont concentrés autour de noyaux de cellules.

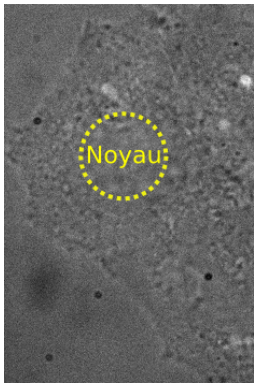

(a) *Une image d'une cellule HeLa en lumière blanche.*

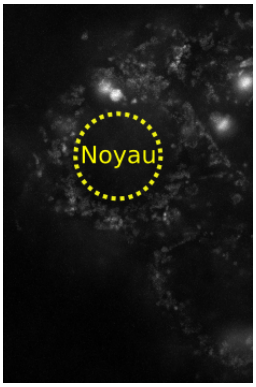

(b) Une projection d'intensité maximale d'un film pris dans le canal QD excitant les QDs lecte le signal fluorescent. Les QDs diffuse à l'intérieur de la cellule, mais sont exclus du noyau.

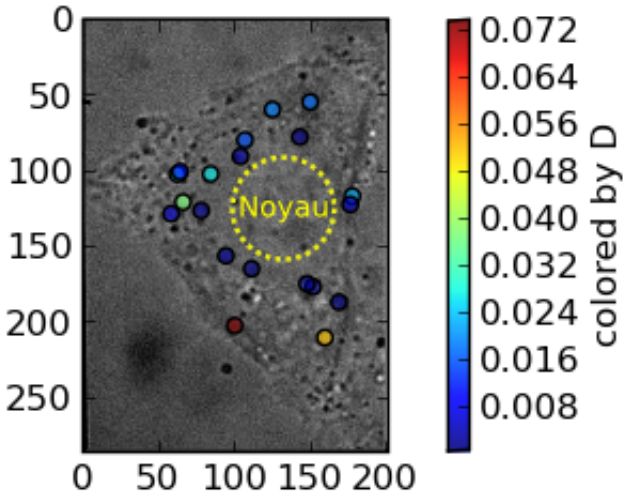

(c) *Un exemple de la dépendance du coefficient de diffusion sur la localisation dans le cytoplasme de la cellule : les coefficients de diffusion plus faible sont concentrées autour du noyau. Les points représentent le coefficient de diffusion d'une trajectoire et sont situés dans le centre de la trajectoire. Les couleurs sont selon la valeur du coefficient de diffusion en micron carré par seconde, du bleu au brun.*

FIG. 3 – *Un exemple de la diffusion QD intérieur d'une cellule.*

Préparation de protéines et conjugaison à des QDs

Après avoir caractérisé l'internalisation et la diffusion des QDs, nous avons produit plusieurs protéines recombinantes, afin de les conjuguer aux QDs et d'internaliser les complexes. Nous avons réussi à produire les protéines Pins et Miranda, un fragment de chaîne variable d'anticorp (ScFv) anti-GFP et d'autres protéines nécessaires pour le projet. Ces protéines ont également été modifiées pour permettre la conjugaison avec QDs, et les complexes QD-protéines ont été validés et caractérisés. Nous avons également développé une nouvelle méthode pour la conjugaison QDs-protéines sur matrice solide, pour éliminer les QDs libres (qui ne sont pas liés à une protéine) de l'echantillon et pour contrler le valence des complexes QD-protéines. Cette méthode utilise des contraintes spatiales de manière à "forcer" la monovalence des QDs. En outre, nous avons développé et démontré une méthode pour la caractérisation de complexes de protéines, basé sur l'électro-transfert sur membranes.

Ciblage et suivi intracellulaire

Après des études de l'internalisation et la diffusion de QDs et la production de nos protéines d'intérêt, nous avons procédé au ciblage des protéines dans les cellules vivantes. Nous avons d'abord réalisé des expériences de ciblage intracellulaire avec une protéine cible qui est concentrée dans des domaines ponctuels (tel que le centrosome), afin de clairement démontrer la co-localisation des QDs et de la cible, et de valider ainsi la méthode. Ensuite, nous avons ciblé la protéine PON-GFP exprimée de façon endogène, en utilisant des QDs conjugués à un anticorps antiGFP. L'étape suivante a consisté à conjuguer les protéines Pins et Miranda à des QDs *in vitro* et de quantifier l'efficacité de leur localisation dans les neuroblastes. En termes de localisation, nous avons obtenu des résultats positifs pour toutes les protéines (Pins, PON and Miranda) (voir **Figure 5**). Toutefois, en raison de l'épaisseur des cellules neuroblastes, nous n'avons pu encore obtenir des trajectoires de longueurs suffisantes, qui permettraient une analyse plus approfondie des propriétés de transport de ces protéines.

(a) *Un neuroblaste exprimant PON-GFP, en division, après internalisation QDs conjugués à anti-GFP : canal GFP.*

(b) *Un neuroblaste exprimante PON-GFP, en division, après internalisation QDs conjugués à anti-GFP : une projection de l'intensité maximale du film pris dans le canal QD.*

(c) *une superposition de l'image prise dans le canal GFP (en vert) et la projection de l'intensité maximale du canal QD (en rouge).*

FIG. 4 – *Un exemple d'une co-localisation de l'anti-GFP QDs et PON GFP.*

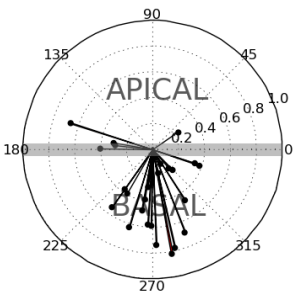

(a) *Barycentres des* ***QDs*** *activés contre* ***PON-GFP*** *(avec un anticorps). Chaque point représente une moyenne sur une cellule entière.*

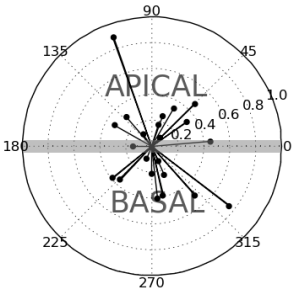

(b) *Temoin-****barycentres des QDs conjugué à des anti-corps inertes****. Chaque point représente une moyenne sur une cellule entière.*

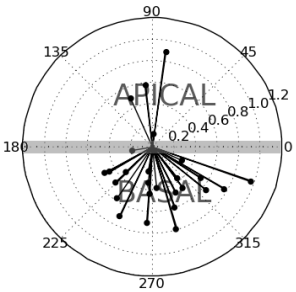

(c) ***Barycentres des QDs conjugués à la protéine Miranda****. Chaque point représente une moyenne sur une cellule entière.*

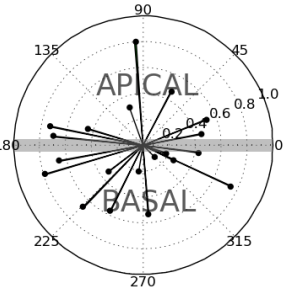

(d) *Temoin - barycentres des QDs inertes. Les experiences ont ete realisées dans les même conditions que les expériences avec Miranda ou broches, mais avec des QDs inertes (QD-SAV + biotin). Chaque point représente une moyenne sur une cellule entière.*

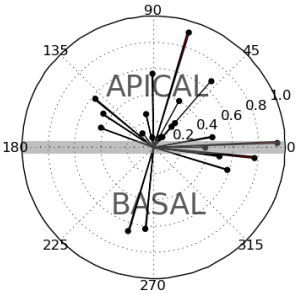

(e) *Barycentres des QDs conjugués á Pins. Chaque point représente une moyennesur une cellule entière.*

FIG. 5 – *Des résultats obtenus pour le ciblage des protéines localisés de façon asymétrique (polarisées) dans les cellules neuroblaste en division. PON et Miranda sont localisés dans la partie basale de la cellule en division, alors que Pins est localisée dans la partie apicale. Comme on peut le voir sur ces graphiques, la localisation des QDs reflète la localisation des protéines à lesquelles ils sont conjugués.*

Des sondes monovalentes

Nous avons démontré, pour la première fois, la réalisation de véritables sondes monovalentes pour le suivi des protéines membranaires, basées sur l'utilisation de fragments ScFv. D'abord, nous avons mesuré la cinétique de liaison de la ScFv à sa protéine cible, GFP, en utilisant la spectroscopie TIRF sur une surface fonctionnalisée avec le scFv [22]. Ensuite, nous avons conjugué le ScFv à des QDs et caractérisé le resultat en matiére de valence QD :protéines. Ces résultats nous ont permis de réaliser des expériences de suivi d'un récepteur membranaire (PDGF-R [23]) fusionnés à une protéine fluorescente extracellulaire. Nous avons comparé les coefficients de diffusion des QDs monoScFv et des QDs poly-ScFv. Il est interéssant de noter qu'on a trouvé aucune différence significative entre les deux cas (voir **Figure 15.1**).

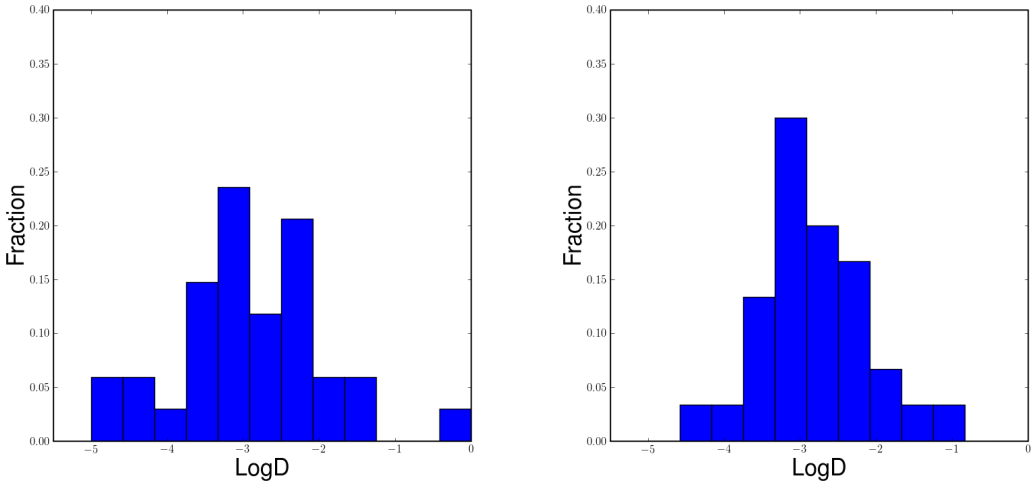

(a) *Un histogramme montrant la distribution des coefficients de diffusion pour les QDs monoScFv.*

(b) *Un histogramme montrant la distribution des coefficients de diffusion pour les QDs poly- ScFv.*

FIG. 6 – *De façon surprenante, une comparaison entre les distributions de diffusion coefficients (sur une échelle logarithmique naturelle), ne montre aucune différence significative entre les QDs ScFv monovalentes et polyvalentes.*

Discussion

Ce travail a montré la faisabilité de l'étude de la division cellulaire asymétrique à l'échelle de la molécule unique. Les méthodes ont été conçues et développées pour la conjugaison et la caractérisation des complexes QD-protéines. Le méthode de conjugaison sur support solide que nous avons développée est susceptible de devenir une méthode de choix pour produire des QDs monovalent, en raison de sa simplicité et son rendement élevé, comparativement à la méthode existante, basée sur l'électrophorèse sur gel [10].

Outils pour l'étude de la division cellulaire asymétrique

Nous avons réussi à cibler les protéines localisées de manière asymétrique dans des neuroblastes en division. Cela ouvre la voie à des études intracellulaires de ce phénomène, en utilisant des QDs individuels Ce travail a également mis en évidence la limite principale de ce système expérimental : la nature tridimensionnelle des mouvements. En raison de l'épaisseur de la neuroblate, les QDs sortent du plan focal très souvent. En conséquence, l'obtention des trajectoires suffisamment longues pour le calcul des paramètres de transport, devient très difficile. Afin de faire face à ce problème, nous recommandons d'utiliser un laser de puissance plus elevée pour l'excitation de QDs. Cela nous permettra à reduire le temps d'exposition et donc, d'acquérir les données de façon plus rapide (un temps d'acquisition de quelques millisecondes) et d'obtenir plus de points dans un temps d'observation donné d'un QD. Il est aussi envisageable de mettre en place des techniques de suivi 3D, récemment mises au point [24].

Toutefois, certaines informations peuvent encore être extraites des données que nous avons obtenues, en analysant la répartition spatiale de "courts-déplacements" dans les films obtenus. Les déplacements des QDs entre deux images consécutives sont regroupés et analysés en fonction de leur emplacement par rapport à une carte polaire normalisée d'un neuroblaste polarisé. Une telle analyse n'a pas besoin des trajectoires longues mais peut, quand même, révèler des différences dans la mobilité des protéines entre les différents domaines de la cellule. Cette analyse est actuellement en cours.

Sondes monovalentes Nous avons réussi à produire des sondes monovalentes pour le suivi des proteines membranaires extracellulaires. Ces sondes sont basées sur un fragment de chaîne variable d'anticorp (ScFv). Ces sondes doivent avoir des nombreuses applications dans le suivi des diverses protéines membranaires, mais doivent être améliorées afin de répondre aux exigences rigoureuses du suivi intracellulaire.

Part I

Introduction

The purpose of the project

The goal of this project is to develop novel tools to explore dynamic organizational processes in living cells, with unprecedented detail and sensitivity. In particular, we are interested in the process of asymmetric cell division (ACD), during which a mother cell divides asymmetrically into two different daughter cells. This process is a key mechanism in the generation of cellular diversity in organisms of all levels. During the course of ACD, prior to the separation of the mother cell into daughter cells, it needs to generate an asymmetric spatial distribution for some of its content. This symmetry-breaking process is called **polarization** *i.e.* the generation of a polarized structure. One of the ways to study polarization is to characterize the intracellular transport mechanisms that generate it.

As a means to observe intracellular transport in detail, we employ single-molecule methods, which allow us to separately follow (or track) the movement of single molecules. By observing one event at a time, we can obtain much more information about the process, compared to simultaneous measurements of the entire population [2, 1]. We are using novel and powerful fluorophores, quantum dots (QDs), which allow for single molecule detection and tracking. On the technical level, we developed methods to cope with technical difficulties associated with intracellular, single-molecule, tracking experiments. These include the delivery of such fluorophores into living cells and the targeting of specific molecules inside it, as well as control over the stoichiometry of QD-protein complexes. The project combines different disciplines, such as single molecule imaging, molecular biology, and primary cell culture, thereby covering almost all aspects of an *in-vivo* single-molecule experiment.

In this manuscript we will first provide an introduction to single quantum dots tracking, as well as to the biological problem - asymmetric cell division. The introduction will also give an overview of the technical challenges involved in single molecule experiments in general and more specifically, in the study of asymmetric cell division. Then, in the methods section, we will explain how these technical challenges can be addressed by giving a detailed description of the experimental procedures, as well as the concepts behind them. We will then present the results, and finish with a discussion and future perspectives.

Chapter 1

Single quantum dot tracking

1.1 An overview of imaging methods in cellular biology

1.1.1 Historical perspective

The interest in living organisms and systematic studies of animals exist since ancient times [25]. Therefore it is interesting to note that the smallest, basic, unit of life-the cell[1], is still far from understood. The primary reason is that cell biology, being a highly experimental domain, is mainly restrained by technical limitations. Consequently, the progress in the field has been strongly correlated with the development of new techniques. The biological cell was first discovered in 1665 (about 60 years after the development of the first microscopes) by Robert Hooke [26, 27], who improved the microscope models available at the time to allow the observation of a dead plant tissue. A few years later, De Leeuwenhoek observed live cells using his own state-of-the-art elaborate devices [28] that already reached magnification on the order of 300X, and a resolution in the range of one micron. The developments slowed down in the following years, due to the rise of the compound microscopes that were, at first, less powerful than De Leeuwenhoek's instrument.

In 1833, Brown described the cell nucleus in cells from orchids. In 1838 and 1839, respectively, Schleiden and Schwann [29, 30, 31] published two separate works in which they stated, based on experimental observations, that the cell is the basic unit of structure, physiology and organization in living organisms and that it plays a dual role: a building block in a multicellular organism, and a distinct entity. During the second half of the nineteenth century, with the advance of imaging techniques, more and more cellular components and features were observed such as mitochondria [32] and the Golgi apparatus [33, 34], as well as functions such as division, growth and endocytosis.

1.1.2 Modern imaging techniques

One of the catalysts for the development of cell biology in the 20th century was the development of powerful imaging techniques. The development of electron microscopy (EM) [35, 36] in the 1930s led to the first electron micrograph of an intact cell in 1945 [37, 38]. The high resolution EM images provided a wealth of information, but were limited to fixed or frozen samples. Optical microscopy has also improved, with the development of differential interference contrast (DIC) in the 1950s [39]. This method could detect different features and textures within the cell, based on differences in refractive index. However, live cell imaging remained limited in terms of resolution and specificity.

[1] Viruses are considered as replicators rather than life forms.

Fluorescence imaging

Even though it was described as early as 1852 by Stokes, fluorescence was only applied to biological samples in the 1930s [40]. The first assays involved the staining of tissues and bacteria, and demonstrated the power of fluorescence as a specific contrasting method. The early applications of fluorescence microscopy were descriptive and qualitative, but as the understanding of the physical nature of fluorescence improved, these methods have become more quantitative.

Over the years, many applications of fluorescence imaging have been developed, from specific staining techniques in fixed cells, to live cell imaging. Several novel methods have been introduced, in order to cope with the challenges posed by the latter.

The basic experimental setups for fluorescence imaging are epifluorescent microscopes. These microscopes typically use the microscope's objective to excite a fluorophore within the sample with UV light, and collect the photons emitted from it. One of the main limitations of this method is the resolution in the dimension perpendicular to the focal plane. These systems suffer from a significant background noise, due to fluorescent emission from fluorophores that are outside the focal plane.

In order to cope with this problem, confocal imaging systems were developed, based on the design of the confocal microscope developed in the 1950s [41, 42]. The basic confocal designs use point illumination for fluorescent excitation and an optically conjugated pinhole, in order to collect fluorescent light only from a thin slice within the sample. This way, the sample can be explored along the direction perpendicular to the focal plane and out-of-focus background can be minimized. In addition, their sectioning ability can also be used to reconstruct 3D images of fluorescently labeled structures within the cell. Due to the point illumination, these systems relied on scanning the sample in order to obtain the desired image. The speed limitation, imposed by the scanning, prompted the development of a new and more advanced generation of confocal systems, called spinning-disc confocal [43], that had better speed and sensitivity. However, scanning and spinning-disc confocal systems remain significantly expensive, relative to conventional fluorescent imaging methods.

A simpler method that was developed in order to reduce out-of-focus noise and improve the signal-to-noise ratio in general, was total-internal-reflection-fluorescence (TIRF) imaging [44]. This method, originally developed in the early 1980s, uses the electromagnetic field generated when a laser beam reaches the total reflection angle with the surface of the glass slide holding the sample. This field can be seen as a wave that propagates in a direction perpendicular to the sample plane, vanishing quickly within about $100nm$ of depth inside the sample. The fact that TIRF does not penetrate deep into the sample is both its advantage and limitation: it minimizes out-of-focus noise, but it is limited for the study of cellular elements such as membrane proteins, which are very close to the sample surface.

The advances in fluorescence applications for live cells were not limited for imaging *per se*, but also led to the development of quantitative methods, for probing the inner works of the cell. Two of the most popular quantitative fluorescence techniques that were applied to live cells, were FCS and FPR [45], which were developed in the late 1970s. FCS, or fluorescence correlation spectroscopy [46], uses a small, laser-illuminated, diffraction-limited sample volume to measure the fluorescence intensity of fluorophores that go in and out of this volume. The intensity is then fitted with a normalized intensity autocorrelation function in order to extract transport parameters, such as the diffusion coefficient. FPR or fluorescence photobleaching recovery (later to become FRAP [47] - fluorescence recovery after photobleaching) consists of a brief exposure to a high power laser in a diffraction-limited volume within the sample, which irreversibly bleaches the contained fluorophores. An analysis of the fluorescence recovery (due to fluorophores coming from outside of the bleached spot) can reveal information about the modes of transport of the given fluorophore population, as well as kinetic parameters of binding and interaction inside the cell.

In the early days, these methods used organic dyes as fluorescent probes, which required

an extra labeling step before observing the biological sample. This limited their applicability, as it was difficult, for example, to reach intracellular domains [48]. The discovery of the green fluorescent protein (GFP) [49] and the consequent developments in the field of fluorescent proteins (FPs) were a major leap forward in the development of live-cell fluorescence imaging and especially intracellular imaging, which was finally acknowledged by a recently awarded Nobel prize [50]. Using a combination of fluorescence imaging and basic genetic engineering, it was possible to probe new domains inside the cell that were before inaccessible, by programming the cell to express the protein of interest fused to a fluorescent protein. The consequent boost in the development of quantitative fluorescence-based methods to explore live-cell dynamics such as FRAP and FCS was very significant [51]. Using these methods, it was possible to probe live cells, and to describe average transport properties in specific cellular compartments. The methods described thus far could be used to spatially explore the cell's interior and study intracellular domains.

Single molecule techniques

In the 1990s, technical developments from different fields converged into the new field of biological, single molecule spectroscopy [52]. Various methods were developed that provided new information regarding the heterogeneity in biological samples in *in-vitro* biological/biomimetic systems. These methods provided a range of possibilities for studying individual molecules, from spectroscopic studies, such as single-molecule FRET [53] to single-particle-tracking (SPT) [54] and even manipulation of single molecules [55, 56].

Gradually, these techniques began to be implemented *in-vivo*, starting from experiments on membrane dynamics [57, 58] that provided a new insight into membrane organization and signal transduction. However, the next level of complexity, single molecule studies of intracellular dynamics [59, 60] still poses many challenges and not many such works have been reported.

From the pure point of view of live cell imaging, the main advantages of single molecule methods are their sensitivity, which enables the detection of a single probe, and their high resolution, which allows for the localization of the probes with sub-diffraction accuracy. From a broader scientific perspective, these methods also have a higher information content, which allows to reveal the sample's internal heterogeneity. One of the most popular single-molecule methods is single molecule tracking, which relies on the ability to accurately localize a single probe within the microscope's field of view, and follow its movement. The probe can be either fluorescent (organic dye, fluorescent protein or quantum dot) or not (typically a gold nanoparticle or latex bead) and is attached to the molecule of interest. When applied to living cells, the probe can be attached to extracellular (membrane) or intracellular targets (see **Figure 1.1**).

Being at the technical cutting-edge of biophysical research, single molecule experiments can be very demanding but even so, they are used more and more due to their added value compared to ensemble methods.

Single-molecule vs. ensemble techniques The difference between single molecule and ensemble techniques is mainly a difference of scientific logic: *deductive* vs. *reductive*. The former (analogous to the ensemble approach) uses information of a general level to conclude about the individual case, whereas the latter (analogous to the single-molecule approach) uses information obtained from individual cases to draw a generalized conclusion. Ensemble methods probe the behavior of the entire sample at once and thereby observe a behavior that is averaged over a large number of molecules. Consequently, they have advantages such as high statistical significance and noise reduction.

However, averaging also causes a significant loss of information. Averaging over a sample loses the heterogeneity information arising from the different behaviors of molecules in the ensemble at the time of the measurement. This way, the existence of different sub-populations within the sample may not be detected. Another important aspect of single molecule behavior

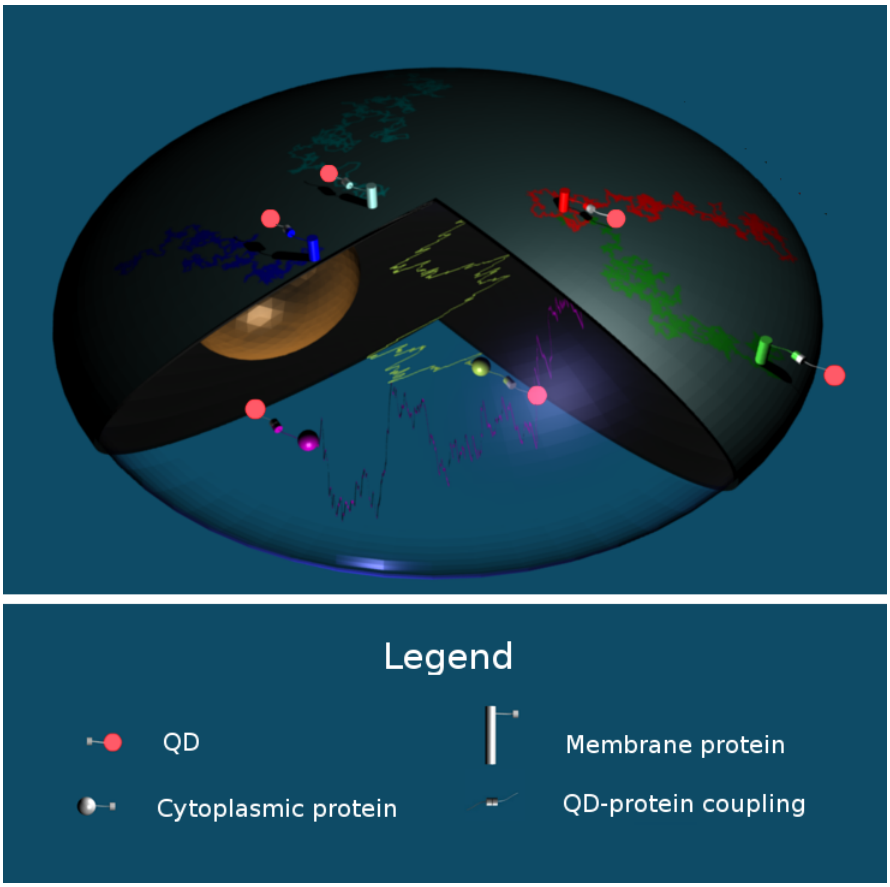

Figure 1.1: *A typical single molecule tracking experiment in living cells. Coupling of the protein (or other macromolecule) of interest to a QD allows the analysis of single trajectories. Proteins labeled with QDs diffuse on the cell membrane, or in the cytoplasm, and their positions (detected using the QD signal) are recorded as movies, which finally result in trajectories.*

that is lost, is the heterogeneity in the behavior of a given single molecule over time. Such heterogeneity arises from events that a single molecule undergoes during the timecourse of the observation (an example could be a reversible structural transition, or a chemical reaction). When observing an ensemble of independent molecules, such events are not synchronized or time-correlated, between individual molecules. As a result, at any given moment, the fraction of molecules in the ensemble, undergoing these events of interest is almost constant.

Thus, when one observes the average behavior of the ensemble, the information about the distribution of such events is lost only due to incoherence within the sample [2] (had these events been synchronized throughout the sample, they would have been detected using ensemble methods). It should be noted that some ensemble methods, such as crystallography, are based on sample coherence[2] [61] and perform the averaging over a highly correlated sub-population within the sample, thereby reducing the information loss.

Heterogeneity is one of the keystones of biological systems and can be found in different contexts: from heterogeneity in protein folding [62] to genetic heterogeneity as an evolutionary tool to acquire new molecular properties [63]. As such, the importance of heterogeneity on the molecular level cannot be overlooked. Single molecule experiments also offer unmatched sensitivity, which allows for the detection of processes involving a very small number of molecules

[2]Due to its periodic structure, the crystal acts as a powerful amplifier for points in reciprocal space (reflection planes) that are "in-phase" (spatially coherent) with each other [61].

(*e.g.* the ability of a single NGF molecule to induce endocytosis [64]) or probing the behavior of proteins that, for some reason, cannot be overexpressed, or exist in small numbers in the cell.

Example In order to illustrate the advantages of SPT in the detection of heterogeneous behavior, let us consider an example. A population of fluorescently-labeled molecular motors, detectable as single molecules, is being tracked inside a living cell. The motors alternate, with a certain probability, between Brownian motion ("freely diffusing" inside the cell) and directed motion (moving along a filament with a given average processivity), which is arbitrarily chosen to be the positive x-axis direction.

By observing individual trajectories (see **Figure 1.2**), one can detect these two states and extract the kinetic parameters (diffusion coefficient, processivity, speed....). An ensemble analysis, however, loses this information due to averaging. Given the stochasticity of this process (the phases of directed motion start at random, and last for a variable time) trajectories are not correlated, and an average picture over many trajectories masks the transitions between the different phases (see **Figure 1.3**). By plotting a residence time histogram (every bin represents the time that the motor spends in a corresponding interval of the x-axis) one can detect significant changes in the motor mobility. Since the binding and unbinding of the motor to the filament are random processes, these changes in mobility will occur at different times in each trajectory.

By looking at many histograms of individual trajectories, one can also obtain information such as the average processivity, from the distances between peaks and the peak sizes. On the other hand, when performing a similar analysis for the whole ensemble, the residence time histogram will appear more and more "smoothened" as the sample size grows bigger, due to the lack of coherence, or synchronicity, within the sample. This example shows a simultaneous measurement of 256 trajectories. By looking at the residence time histogram, it is already hard to determine whether there are different phases of movement. This example shows how a complex behavior, which is "averaged out" using ensemble methods, can be detected by SPT, using a relatively simple analysis.

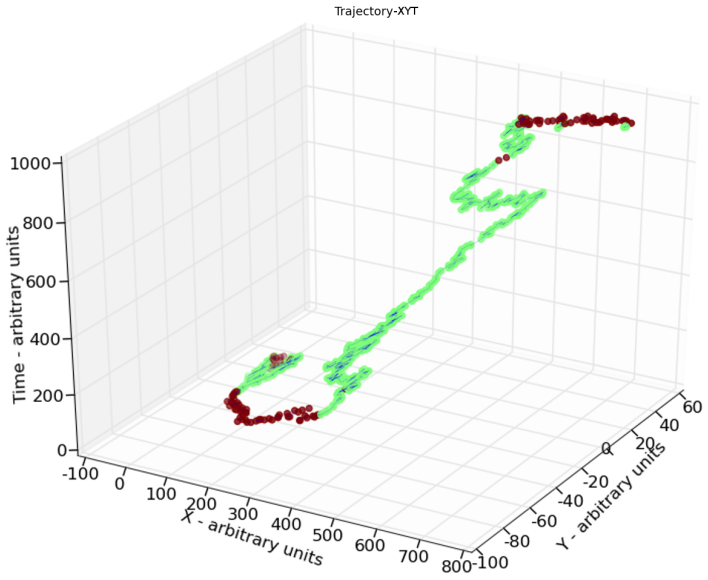

(a) *A trajectory of a single motor protein, alternating between the directed motion (in brown) and free diffusion (in green), in XYT space.*

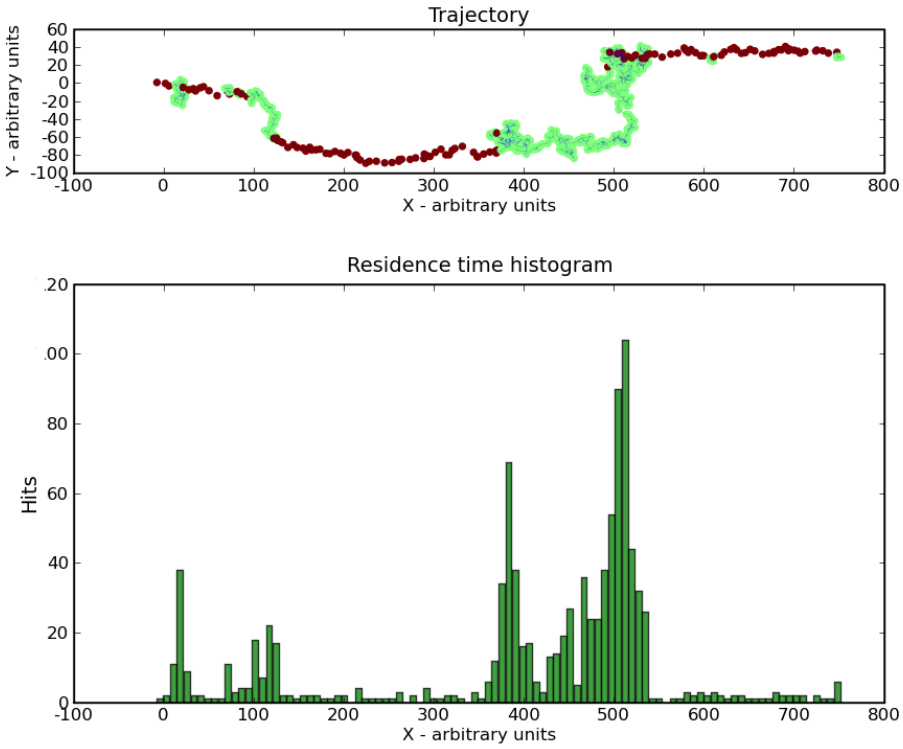

(b) *Top, a single motor trajectory in the XY plane. Bottom, a residence time histogram.*

Figure 1.2: *An example for the heterogeneity information obtained by SPT: a motor protein alternates between the bound state (directed motion-in brown) and the unbound state (free diffusion-in green). This behavior can be detected in single molecule trajectories, using a simple analysis. By appropriately projecting the 2D trajectory on a 1D axis and examining the residence time histograms along this axis, we can detect local changes in mobility.* ***Figure 1.2(a)*** *shows the trajectory in XYT space.* ***Figure 1.2(b)*** *shows the 2D trajectory and the corresponding residence time histogram.*

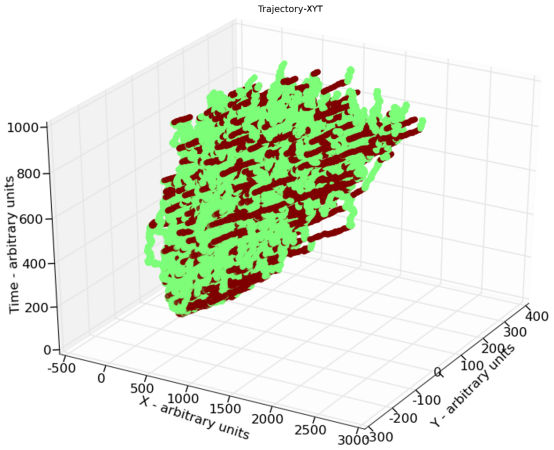

(a) *A superposition of 256 two-phase motor trajectories in XYT space. Notice how the two phases (shown in brown and green) are completely unsynchronized.*

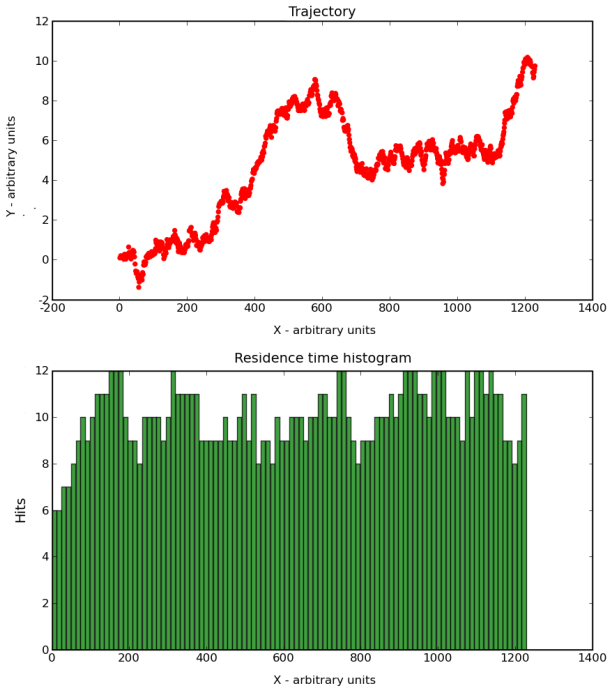

(b) *Top, an "effective trajectory" generated by averaging over the entire sample. Bottom, a residence time histogram.*

Figure 1.3: *Heterogeneity information is lost as a result of averaging over large populations. Averaging is demonstrated for a sample of 256 motor proteins, which alternate between directed and Brownian motion in an uncorrelated fashion. During the course of the experiment (under equilibrium conditions), the fraction of proteins in a given phase (directed or Brownian motion) does not change significantly, and therefore, the residence time histogram becomes more homogeneous as the sample size increases. The resulting behavior can be considered as an "effective trajectory" that describes an "average motor" moving in a directed motion with some effective diffusive component. Sub-figure 1.3(a) shows the trajectory in XYT space (notice the lack of coherence in the sample). Sub-figure 1.3(b) shows the "effective" 2D trajectory and the corresponding residence time histogram. Directed motion is indicated in brown and free diffusion is indicated in green.*

1.2 Using quantum dots (QDs) as a single molecule probe

In the field of fluorescence microscopy there exist three main families of probes [3] fluorescent proteins, organic dyes and QDs. For our single-molecule assays, we have chosen to use quantum dots (QDs) as a fluorescent probe. What follows is a comparison between the common fluorescent probes.

1.2.1 Fluorescent proteins (FPs)

This is a group of proteins that contain a natural fluorophore. They include a large variety of emission colors covering all the visible spectrum [3, 4]. Different FPs have been adapted and optimized in order to be used in almost all types of fluorescence experiments, from FRET [65, 66], through confocal microscopy and FRAP [67], to single molecule tracking [68]. Recently, photoactivable FPs have been developed, which can be switched between ON and OFF states, as well as between colors, and are mainly used in super-resolution imaging [69, 70]. The main advantage of FPs over other probes is that by using genetic engineering, they can be fused to a protein of interest and can be endogenously expressed by the cell, saving the need for internalization. Therefore, they are usually the preferred fluorophore in studies of intracellular domains, such as the cytoplasm, the nucleus [71] and even the nucleolus [72]. FPs are also more likely to be bio-compatible and less likely to be toxic. The main limitation of FPs compared to QDs is their low photostability, which does not allow prolonged exposure to UV excitation.

1.2.2 Organic dyes

This group includes fluorescent dyes produced by organic synthesis [5]. These are molecular fluorophores with a low molecular weight (up to a few kD). They are much smaller than fluorescent proteins, **let alone QDs** (see **Figure 1.5**), which may be advantageous in some cases. The optical properties of organic dyes depend on the electronic transition(s) involved and can be fine-tuned by elaborate design strategies if the structure-property relationship is known, for the given class of dye [73]. These dyes are categorized into families such as fluoresceins, Alexa, BODIPY, Rhodamines [74] and cyanine dyes [75]. Organic dyes are sometimes advantageous as they allow *in-vitro* protein labeling, saving the need for genetic engineering on one hand, and saving the more complicated handling of QDs on the other hand.

1.2.3 Semiconductor quantum dots

QDs are a relatively novel substance [73, 76, 77]. As a single molecule probe, they belong to a family of "large" probes such as latex beads, which are used in differential interference contrast (DIC) microscopy experiments, and fluorescence imaging (when coated with organic dyes) and gold nanoparticles, which are used in DIC, as well as in recently developed photothermal imaging techniques. [78, 79, 80].

Photophysical properties QDs are inorganic, semiconductor nanocrystals, with a diameter of a few nanometers and unique photophysical properties. Due to their characteristic dimension, which is below the Bohr exciton radius [81], their energy levels are quantized, and size-correlated. This way, small QDs emit at short wavelengths and larger QDs at longer wavelengths. The most popular QDs are composed of a CdSe crystal core with a ZnS shell (a core-shell particle), but other materials have also been reported [82, 83].

QDs outperform FPs and organic dyes in key photophysical aspects: their exceptionally high extinction coefficient, more than 10 times that of the best organic dyes, results in very high brightness. This property allows the detection and imaging of QDs with a high signal-to-noise ratio (SNR), even using standard fluorescence microscopy configurations. The high SNR also

allows accurate localization of QDs within a few nanometers, well below the diffraction limit ($\sim$ 250nm).

Another important advantage of QDs is their remarkable photostability: their ability to withstand constant excitation for long periods of time (minutes to hours) without being bleached is far superior to that of FPs or organic dyes (0.1 to 10 seconds). This property allows the observation of cellular processes on a physiological timescale. An observation of QDs under constant excitation over long periods of time also reveals their fluorescence intermittency (otherwise referred to as "blinking"). QDs stochastically alternate between the "bright" and "dark" states. This property can be used as a means to prove that a given fluorescent spot is indeed an individual QD [84]. However, it also complicates the processing in single molecule tracking data, as it creates discontinuities in the resulting trajectories. Another prominent feature of QDs are the characteristic shapes of the absorption and emission spectra. QDs have very broad excitation spectra, which extend deep into the UV range, and a narrow size-dependent emission peak, compared to FPs and organic dyes, in which the excitation and emission peaks show considerable overlapping [49, 85, 73]. This allows the simultaneous excitation of different colored QDs with minimal cross-talk between the different imaging channels.

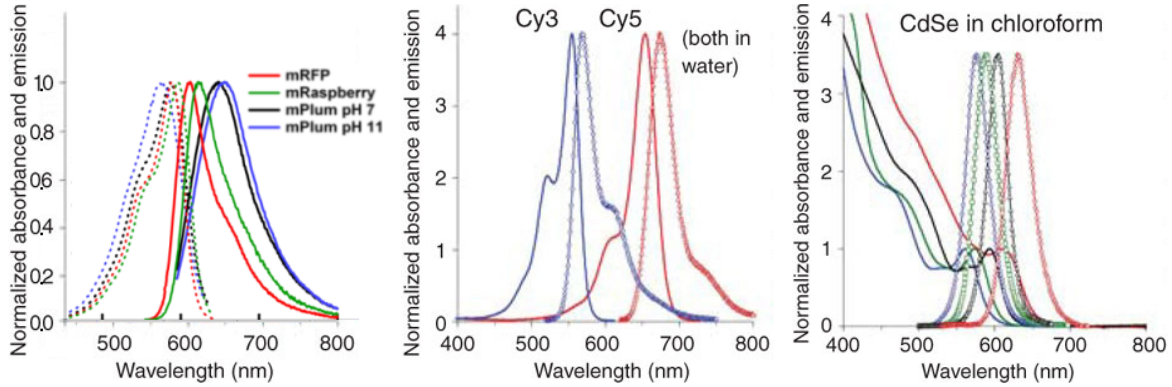

(a) *Excitation and emission selected fluorescent proteins.*

(b) *Excitation and emission curves for the commonly used Cy3 and Cy5 organic dyes*

(c) *Excitation and emission curves for CdSe quantum dots*

Figure 1.4: *A comparison of the Stokes shift between fluorescent proteins, organic dyes and QDs, taken from [73, 85]*

Bio-compatibility and size While the size and composition of the core-shell particle determine its photophysical properties, its colloidal properties are determined by the coating of the particle. In most cases, QDs are synthesized in non-polar solvents and therefore, in order to use them in aqueous, biological media, they need to be solubilized. Solubilization is performed by replacing the hydrophobic surface ligands, which were used during synthesis, with amphiphilic ligands that can mediate the interaction with water. Many solubilization schemes have been reported [73], using peptides [86], small molecules [87], polymer shells and polysaccharides. Certain coating schemes (*e.g.* using polyethylene glycol, PEG) do not only render the QDs more soluble, but also reduce their non-specific interactions with the biological medium. The result of solubilization is, in the ideal case, a highly soluble and biologically inert QD.

In addition to the solubility and passivation of QDs, particle size is also an issue. Apart from the size distribution of the core-shell particles, different solubilization schemes and subsequent conjugation with biological molecules significantly increase the diameter of QD particles. While the diameters of commercial QDs range from 20nm (solubilized, non conjugated) to about 40nm (conjugated to streptavidin or secondary antibodies), different solubilization schemes may yield smaller particles. Encapsulation of QDs in PEGylated micelles [7, 88, 89] resulted in slightly

more compact particles (a hydrodynamic diameter of 15-20nm). A surface coating based on coordinated monothiols produced particles with an average diameter of 11nm [90]. Two more prominent solubilization schemes are the use of DHLA-PEG [91, 92], and the use of two-domain engineered peptides [93, 94]. The former used linear PEG molecules functionalized with the di-thiol group DHLA (dihydrolipoic acid) and obtained particles with a diameter of 10-14nm. The latter used peptides containing a polycysteine "adhesive" domain that coordinates with the QD inorganic shell, and a hydrophilic domain that interacts with the aqueous environment. The amino acid sequence of the hydrophilic domain can be engineered to encode specific functions, or include PEG for better passivation. The bio-compatibility of these particles was demonstrated in numerous extracellular SPT works.

In many cases, though, smaller particle size may come at the expense of particle inertness. In the quest for smaller QDs, the surface coating of the QDs is replaced with smaller and smaller molecules (*e.g.* shorter and shorter polymer chains). Since the coverage of the QD surface is probably not perfect, leaving some of its hydrophobic shell exposed, small molecules may be less efficient in blocking hydrophobic interactions with the QDs environment.

Conjugation to reactive molecules, targeting and valence

Inert QDs can be used to monitor a variety of cellular characteristics such as changes in micro-rheology [6] in space and time and cell compartmentalization [7]. However, these applications certainly do not fully take advantage of the QD properties: in order to target specific molecules or domains in the cell, an additional layer of surface functionalization is needed. The QDs need to be conjugated to some biologically significant, reactive molecule that encodes the target specificity. This can be achieved using affinity-based methods (using affinity pairs such as antibodies and their epitopes, or the avidin-biotin system [8]), or using non-specific covalent binding methods based on crosslinking [9].

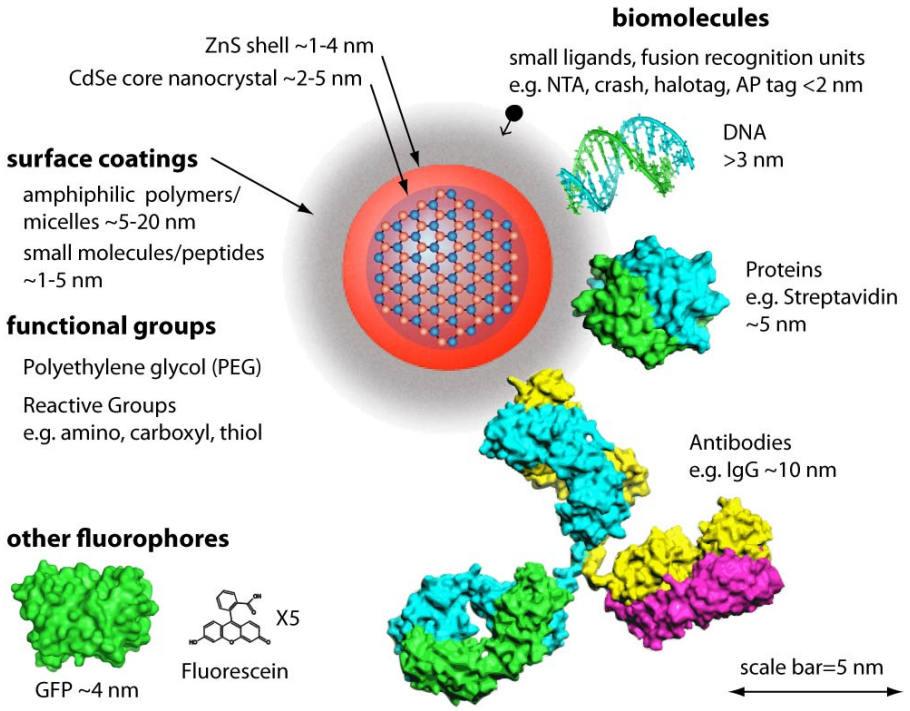

Figure 1.5: *A size comparison of a QD and biological molecules.*

Exogenous/extracellular targeting vs. Endogenous/intracellular targeting In the preparation of intracellular tracking experiments, QD and protein coupling can be performed either *in-vitro* or *in-vivo*. *In-vitro* coupling is simply coupling of the protein of interest and the QD in solution. The sample can then be purified if desired, and internalized into the cell, in order to observe its behavior. This approach offers more control over the coupling. On the other hand, the protein used for the coupling has to be expressed outside of the biological system (and therefore called **exogenous protein**), in a laboratory expression system such as *E. Coli*, yeast or baculovirus, and then purified, which usually complicates the work (many proteins are insoluble, prone to degradation or simply inactive, when expressed not in their original host).

The alternative approach is *in-vivo* coupling or targeting. In this case, QDs functionalized with some reactive molecule (streptavidin, antibody etc.) with a specific affinity towards the **endogenous protein** of interest are internalized into the cell, where the binding takes place. When using intracellular targeting, there is a much higher probability that the molecule we intend to target is functional, since it is being endogenously expressed. This approach has a few limitations though: first, the targeting molecule (a specifically reactive molecule, such as an antibody) needs to have a very high affinity (at least nanomolar), fast binding kinetics, and specificity towards the target. These properties are very important, since once the QDs are inside the cell, there is no way to tell which QD is bound to the molecule of interest and which is not (either dissociated or has never bound to the target). Second, it offers less flexibility in case one would like to modify the molecule of interest and observe different behaviors (in this case the organism needs to me mutated and such mutations are more complicated and possibly lethal).

Coupling methods As mentioned above, when performing single quantum dot tracking (SQDT) experiments over long observation times, high QD-target affinity is required (sub-nanomolar), in order for the complexes to remain stable throughout the experiment. Maybe the most popular high-affinity pair is the biotin-avidin (or streptavidin), which is one of the strongest non-covalent interactions in nature [8]: streptavidin coated QDs (QD-SAV) are used in order to bind to biotinylated macromolecules. Biotinylation can be performed either chemically, using chemically activated biotin (*e.g.* with NHS or maleimide) or enzymatically, using an enzyme that recognizes a specific signal peptide sequence, fused to the protein of interest (AviTag [95]). The reverse strategy has also been reported, where the streptavidin was fused to a protein of interest and the QD was biotinylated [96]. Another popular strategy is the use of antibodies against the protein of interest, or against a peptide sequence or protein that is fused to such as c-myc [97] or HA [98]. Alternative, emerging techniques include QDs that are reactive against polyhistidine tags [10, 99, 88] and enzyme-mediated covalent binding [100, 101]. Combinations of orthogonal targeting techniques have also been employed in cases of single and multi-color QD imaging [88].

Valence Ideally, in order for SQDT experiments to be more meaningful, the valence (number of molecules bound to a QD) of the QD-target complex should be 1 (1 protein bound to 1 QD). The "targeting molecules", such as streptavidin or antibodies are, in most cases, attached to the QD using chemical crosslinking to the QD's solubilizing layer. However, due to the stochastic nature of the crosslinking reaction, the result is always a mixture of QDs with different protein/QD ratios (or stoichiometries). The relatively large surface area of QDs and the nature of these chemical reactions (the surface of the solubilizing layer contains many possibly reactive groups) may result in QDs bearing many such molecules and therefore multiply-reactive against the target (biotin, epitope,...). Tracking such QDs could result in non-physiological and uninterpretable data (see **Figure 1.7**).

The commonly used strategy for obtaining monovalent QDs is to separate between QDs of different valences. This is done, typically, by using electrophoresis to resolve QDs with discrete

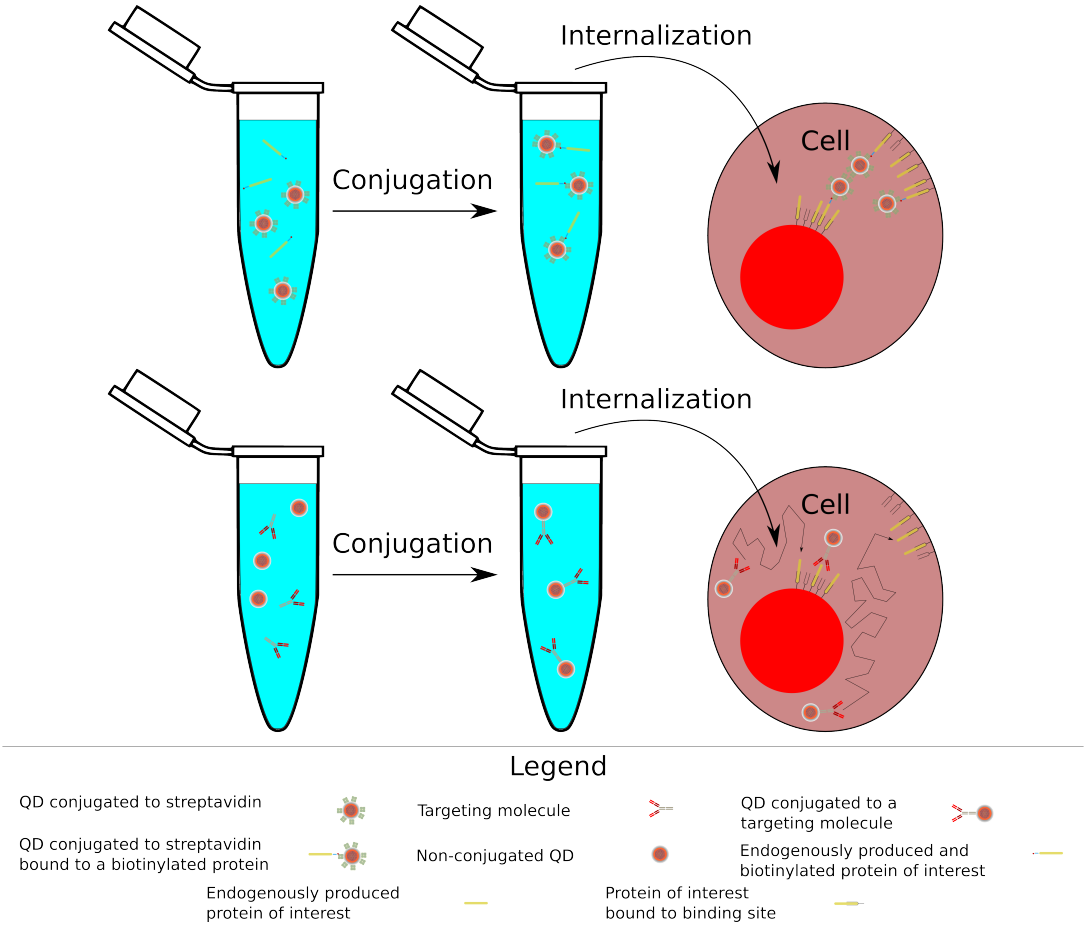

Figure 1.6: *Exogenous and Endogenous labeling.* ***Top:*** *In exogenous labeling, the QDs are conjugated in-vitro, directly to the protein of interest, which was produced outside of the cell, and then internalized into the cell.* ***Bottom:*** *In endogenous labeling-the QDs are conjugated to a targeting molecule (here drawn as an antibody), and then internalized into the cell. In this case, the QDs have to find the protein of interest and bind it tightly, in order to allow the observation of this protein's behavior.*

numbers of reactive molecules (0,1,2,3,....), based on differences in mobility [10]. When the desired resolution is achieved, the band corresponding to monovalent QDs is recovered from the gel. This method has two major drawbacks: first, it relies on significant differences in mobility between the different valences, which do not always exist (they depend on the QD, the conjugated protein and its effect on the overall mobility). Second, the efficiency of recovery from the gel is limited.

It must be remembered that having a single reactive molecule per QD is not always enough. Monovalence with respect to the targeting molecule (such as an antibody or streptavidin) does not always confer monovalence with respect to the target (a protein of biological interest, which is to be tracked). Standard reactive molecules are inherently polyvalent: streptavidin is tetravalent and IgGs are divalent. Therefore, improved variants have been developed: monovalent streptavidin [10, 102, 15] and single-chain variable fragments [11](ScFv), which are a monovalent and smaller alternative for IgGs.

Even though less important, in some cases the target itself is not monovalent: in cases of non-specific chemical biotinylation, the protein may bind more than one QD. This could also result in problems such as differences in diffusion coefficients and aggregation due to crosslinking (one polyvalent protein of interest can act as a bridge between several QDs that bind it).

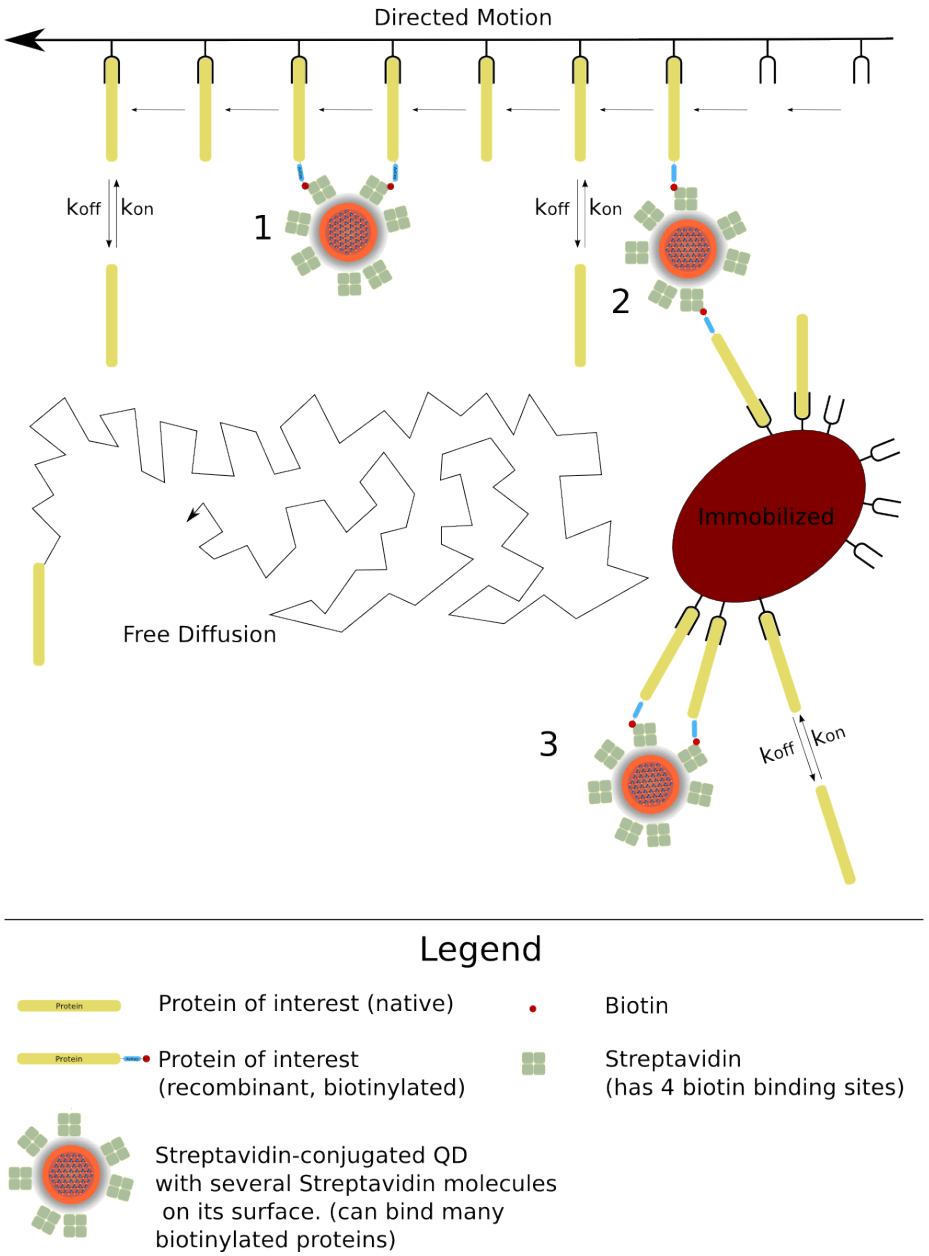

Figure 1.7: *A scheme demonstrating some experimental problems that can be caused by polyvalent QDs. Let us consider a heterogeneous environment, in which a given protein can have several different behaviors: directed motion, free diffusion and no movement (immobilization). If a QD is bound to several proteins (for example via multiple streptavidin molecules), their behavior will not necessarily be indicative of the native protein behavior. In example 1, the QD is bound to two proteins undergoing directed motion. Such a QD would probably move along its "tracks" with a non-physiological, high processivity. In example 2, a QD is bound to a source of directed motion, such as a motor moving along a filament, as well as to an immobilized binding site. In such a case, if the immobilized binding sites are very abundant, the directed motion could pass undetected or at least underestimated. Example 3 shows a QD bound to two immobilized binding sites. In cases where the binding to these sites is reversible on the timescale of the experiment, (e.g. diffusion binding mechanisms in cells) the effective binding can be unrealistically strong, due to the avidity of the divalent QD towards these binding sites. Obviously, the possibilities for such undesirable behavior are many, especially when the valence of QDs is higher than two and, in most cases, unknown.*

Specific requirements of intracellular tracking assays Intracellular tracking of quantum dot labeled proteins is a challenging task, which has additional requirements to those imposed by extracellular membrane tracking due to the specific technical challenges involved. Unlike the case of extracellular membrane tracking, where non-functional quantum dots can be washed away, in the intracellular case they remain inside the cell and cannot be removed, or distinguished from the functional ones. Therefore, such QDs can seriously compromise the quality of the data, in addition to what was mentioned before about polyvalent QDs. Quantum dots that are bound to an unknown number of target molecules should exhibit a complex and possibly uninterpretable behavior.

What is needed, therefore, in an ideal case, is a sample of QDs that contains 100% of monovalent QDs with respect to the protein of interest, in the case of exogenous targeting, and 100% of monovalent QDs with respect to the monovalent targeting molecule (ScFv, monovalent streptavidin) in the case of endogenous targeting. In the context of affinity, it should be stressed out that in extracellular membrane tracking assays, the affinity of the probe towards the molecule of interest is less crucial: the dissociated probes can simply be washed away and the ones remaining on the cell membrane can be assumed to be specifically bound to the molecule of interest. A low affinity, of course, may result in a shorter effective observation time (since the QD-target complex will naturally have a shorter lifetime), but if the medium volume is very large and rebinding is negligible, moderate binding affinities can be compensated by loading more probes. On the other hand, as mentioned before for in intracellular tracking assays, the dissociated probes (that are no longer attached to the molecule of interest) will still be tracked and could yield problematic results. This also demonstrates why exogenous labeling should be the method of choice for intracellular work - it is the only way we can be sure (provided that the complex lifetime is long enough) that the probe is attached to the molecule of interest.

1.3 Quantum dot internalization into live cells

Quantum dots hold a lot of potential for intracellular tracking. Their high photostability and quantum yield, as well as size-tunable narrow emission bands, allow us to study cellular organization and compartmentalization with unprecedented detail. One of the main limitations for the development of intracellular tracking experiments is QD internalization. Except for cases in which the process studied is in itself an internalization process (such as endocytosis, viral infection or receptor internalization), quantum dots have to be actively internalized into the cells. The seemingly fragile cell membrane acts as a surprisingly robust barrier when it comes to internalization of foreign particles. Interesting as it may be from a fundamental point of view, it is a major challenge when considering an intracellular tracking experiment (even though it is not unique for QDs). Internalization of QDs has been extensively covered in the review of Delahanty and Mattoussi [103]and therefore, only a brief summary will be given here.

1.3.1 An overview of internalization methods

As was mentioned before, the field of single molecule tracking and especially single quantum dot tracking is developing rapidly. However, while the number of publications on extracellular tracking (mostly membrane proteins) is exploding, the progress in the field of QD intracellular tracking has been much slower. What follows is a summary of QD internalization methods used to date. Quantum dot internalization methods can be divided into several categories:

Non-specific uptake This category includes internalization methods that rely on the cell's natural tendency for receptor-independent endocytosis, in conjunction with QD surface chemistry. By conjugating QDs to positively charged molecules, endocytosis of QDs can be significantly improved. The charge can come from either small molecules [104] or charged peptides

[105, 106]. In most cases these internalization methods result in quantum dots being trapped in vesicles within the cell and therefore cannot be used for cytoplasmic targeting.

Recognition-mediated delivery These are methods based on specific recognition between the chemically functionalized surface of the quantum dot, and a molecule on the cell membrane, which is actively internalized: this pair could be receptor-ligand [107, 108, 109, 110, 64, 111]or antibody-epitope [112, 113]. In most cases, the internalization method is also the process being studied.

Lipid/polymer-mediated delivery and endolysosomal escape These methods involve the use of lipid shells similar or identical to the ones used in RNA or DNA transfection. Lipid-embedded quantum dots are membrane-soluble and therefore, to some extent, membrane permeable. Duan *et al.* conjugated reduced toxicity derivatives of PEI (known to burst out of endosomes) to QDs to make them membrane-permeable [114]. Qi and co-workers used a similar concept with amphipol-coated QDs, in order to internalize siRNA into cells [115]. In a recently published work, Jablonski *et al.* show a non-specific, endocytosis-independent cytoplasmic delivery of QDs using a combination of pyrenebutyrate and poly-arginine [116]. Kim *et al.* embedded quantum dots into large biodegradable polymeric nanoparticles that enable endosomal escape of the quantum dots, upon acidification of their environment [99].

Forced delivery methods This category includes methods that induce some non-physiological conditions upon the cell and are more likely to internalize monodisperse freely-diffusing quantum dots. Therefore, these are usually the methods of choice for intracellular tracking and especially targeting experiments.

Micro- and nanoinjection Pressure-driven injection of QDs into cells has been reported in several cases. It involves using very fine needles in order to pierce through the cell membrane and introduce quantum dots into the cytoplasm [7, 117], or even directly into the nucleus [118]. This method is less common, due to the high cost of the system, and its low yield (one cell at a time). More recently, nanoinjection has also been reported, using nanotubes [119] or more recently, nanofabricated surfaces [120].

Electroporation QD delivery using electroporation has also been reported [121, 122], even though with limited success, due to QD aggregation [123].

Pinocytic influx This is a simple method, in which osmotic shock is used in order to burst hypertonic pinosomes [21] and thereby release QDs into the cytoplasm. This method was already used in single quantum-dot tracking experiments [59, 124]. This is method of choice for this project and will be discussed in detail in the **Methods** part.

1.3.2 Additional technical issues regarding QD internalization

Metabolism and the effect on the cell

It is of utmost importance though, to characterize the diffusion of internalized non-targeted QDs, before considering the use of a given method, since some internalization processes (especially the second group) could be implicated or at least have some dependence on cellular metabolism. It should be noted, that there are some evidence that QDs conjugated to endocytosed molecules, do not always follow the same pathway as the native molecule. For instance, transferrin and ricin show abnormal cellular metabolism when conjugated to QDs [125].

Diffusion and targeting

It is also important to test that the biological molecule conjugated to the QD (protein of interest/antibody/nucleic acid....) retains its functionality given the internalization method used. Some internalization pathways may be harmful for proteins, due to harsh conditions in endosomes and lysosomes [126]. Needless to mention, that tracking of cytoplasmic targets also requires that the quantum dots, once internalized, freely diffuse inside the cytoplasm in search of their target rather than be sequestered inside vesicles and endosomal domains.

1.4 The analysis of Mean Square Displacement (MSD)

1.4.1 Theoretical background

The foundations for this type of analysis were laid down by Einstein in his theory of Brownian motion. He found that the mean square displacement (MSD) of an ideal Brownian particle is proportional to time.

$$< (\vec{r}(t+\tau) - \vec{r}(t))^2 >= 2 * dim * D * \tau \tag{1.1}$$

where r is the position vector (in the right dimensionality), τ is the travel time, and dim is the dimensionality of the problem. The mean squared displacement is defined as:

$$\rho(\tau) = \int\int P(\vec{r}')(\vec{r} - \vec{r}')^2 P(\vec{r}|\vec{r}', \tau) d\vec{r} d\vec{r}' \tag{1.2}$$

for Brownian motion:

$$P(\vec{r}|\vec{r}', \tau) = \frac{1}{4\pi D\tau} \exp \frac{-(\vec{r} - \vec{r}')^2}{4D\tau} \tag{1.3}$$

for directed motion (Brownian + drift at velocity v)

$$P(\vec{r}|\vec{r}', \tau) = \frac{1}{4\pi D\tau} \exp \frac{-(\vec{r} - \vec{r}' - \vec{v}\tau)^2}{4D\tau} \tag{1.4}$$

where $P(\vec{r})$ is the steady state probability distribution of particle positions and $P(\vec{r}|\vec{r}',\tau)$ is the probability that a particle will be at $\vec{r}$ at a time t, given that at a time $t - \tau$ it was at $\vec{r}'$. This should be averaged over the entire ensemble, but since the process is stationary, it can calculated over an individual trajectory [127] as:

$$\rho(\tau) = \int |\vec{r}(t+\tau) - \vec{r}(t)|^2 \tag{1.5}$$

But since an experimental trajectory is a collection of discrete coordinates, we should use:

$$\rho(\tau) =< [\vec{r}(t+\tau) - \vec{r}(t)]^2 > \tag{1.6}$$

In 2D:

$$\rho_x(n * \Delta T) = \frac{\sum_{i=0}^{N-n} (x_{i+n} - x_i)^2}{N - n} \tag{1.7}$$

$$\rho_y(n * \Delta T) = \frac{\sum_{i=0}^{N-n} (y_{i+n} - y_i)^2}{N - n} \tag{1.8}$$

In total:

$$\rho_{2D}(n * \Delta T) = \rho_x(n * \Delta T) + \rho_y(n * \Delta T) = \frac{\sum_{i=0}^{N-n} (x_{i+n} - x_i)^2 + (y_{i+n} - y_i)^2}{N - n} \tag{1.9}$$

where N is the number of time points, and $\tau = n * \Delta T$ is a given time interval (when $n = 1$, it is the time between movie frames).

Chapter 2

Polarity and asymmetric cell division

2.1 Background and definitions

Interestingly, from a physics point of view, life belongs to a group of phenomena in which open or continuous systems can decrease their internal entropy at the expense of substances, or free energy, taken in from the environment (and subsequently rejected in a degraded form) [128]. In more simple words, living systems belong to a class of **self organizing systems**. Another definition for self organization [15] states, that it is a process in which a pattern at the global level emerges solely from numerous interactions among lower level components of the system. Furthermore, the interactions that give rise to the global pattern are dictated by "microscopic" rules, based only on local information. The living cell consists of a hierarchical structure, comprising many layers of organization: from intramolecular, through inter-molecular, to organelles and compartments. The organization is controlled and orchestrated in space and time: cell functions that are highly based on spatial rearrangement, such as cell division, are also controlled by a clock - the cell cycle [129]. Cells also re-organize as a response to external stimuli *e.g.*, the redistribution of membrane receptors as a response to a substrate concentration gradient [58] or spindle rearrangement as a response to mechanical stimulus [130]. One of the most striking examples of cellular organization is the process of polarization, *i.e.* the formation of cell polarity. Cell polarity is defined as an asymmetry of either cell shape or the distribution of cellular content (organelles, proteins, nucleic acids....) [12].

Polarity is implicated in many cellular processes: from chemotaxis [131, 132], directed growth [133, 134, 135] and cell division [136], up to tissue and organ morphogenesis [137, 138]. Asymmetric cell division [139](ACD), is one of the most remarkable examples for polarity. During ACD, polarity is essential, in order to obtain an unequal segregation of cell content between daughter cells. In this chapter, we will give an overview of ACD in different systems, in order to demonstrate the universality of this process. We will then give a more detailed description of ACD in our system of interest, *Drosophila melanogaster* neuroblasts and finally, mention some of the relevant questions in the field.

ACD is one of the mechanisms used by cells in order to generate cell diversity (it may have additional roles in cell maintenance [140]). It is defined as a cell division in which one mother cell gives rise to two daughter cells with distinct fates (manifested by size, content and expression profile [139], see **Figure 2.1**). During the division, the content of the mother cell is unevenly segregated between the daughter cells. In order to achieve that, the concentration profile of certain molecules has to maintain a stable and robust polarized distribution throughout the division. Some of these molecules (mostly proteins), determine the fate of the daughter cell into which they are eventually segregated. These molecules, which have to be correctly and reproducibly sorted into their designated daughter cell, are called cell fate determinants (CFDs), and act directly or indirectly on the cell's expression profile, activating its unique developmental program.

ACD can be found in organisms in all levels, from bacteria, such as the well studied bacterium *Caulobacter crescentus*, to human stem cells. The study of asymmetric cell division is also relevant for cancer research, since it was found that deletion of certain cell fate determinants leads to over-proliferation of the cells and that some of these proteins act as tumor suppressors, as well as the fact that asymmetric cell division was also found in tumors [141].

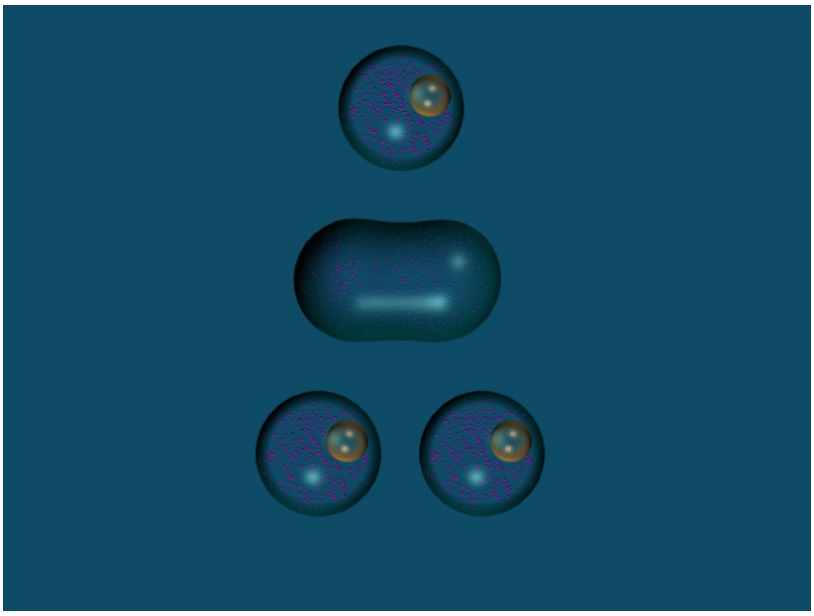

(a) *Symmetric cell division*

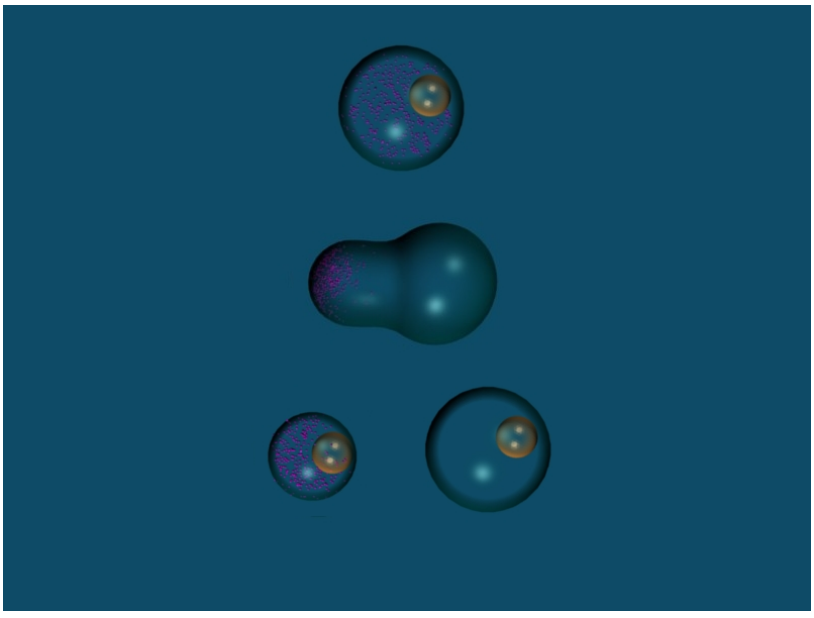

(b) *Asymmetric cell division, in size and content*

Figure 2.1: *Symmetric vs. asymmetric cell division. The small purple spheres represent a component of the cell that gets asymmetrically distributed in the course of ACD.*

2.1.1 The two types of ACD

ACD can be categorized as **extrinsically** or **intrinsically** controlled division [142](see **Figure 2.2**). In the case of an extrinsically controlled division, the polarity signal comes from the surrounding niche (the tissue micro-environment). In this type of division, the cell orientates its spindle perpendicularly to the niche, in order to maintain self-renewal (a process in which one daughter cell regains the faculties of the mother cell, *i.e.*, a cell of type A divides, giving rise to a cell of type A and a cell of type B.). This way, only one daughter cell stays in contact with the niche, which determines its type, and the other acquires a different fate. Such cells, when isolated, cannot reproduce the polarity required for asymmetric cell division.

In the case of an intrinsically controlled division, the polarity signal does not depend on a cellular niche. At interphase, the cell sets up a polarity axis and uses it to guide the asymmetric localization of cell fate determinants. The polarity information is then used to orient the mitotic spindle according to the distribution of the cell fate determinants in order to ensure that these molecules are partitioned correctly into their designated daughter cell.

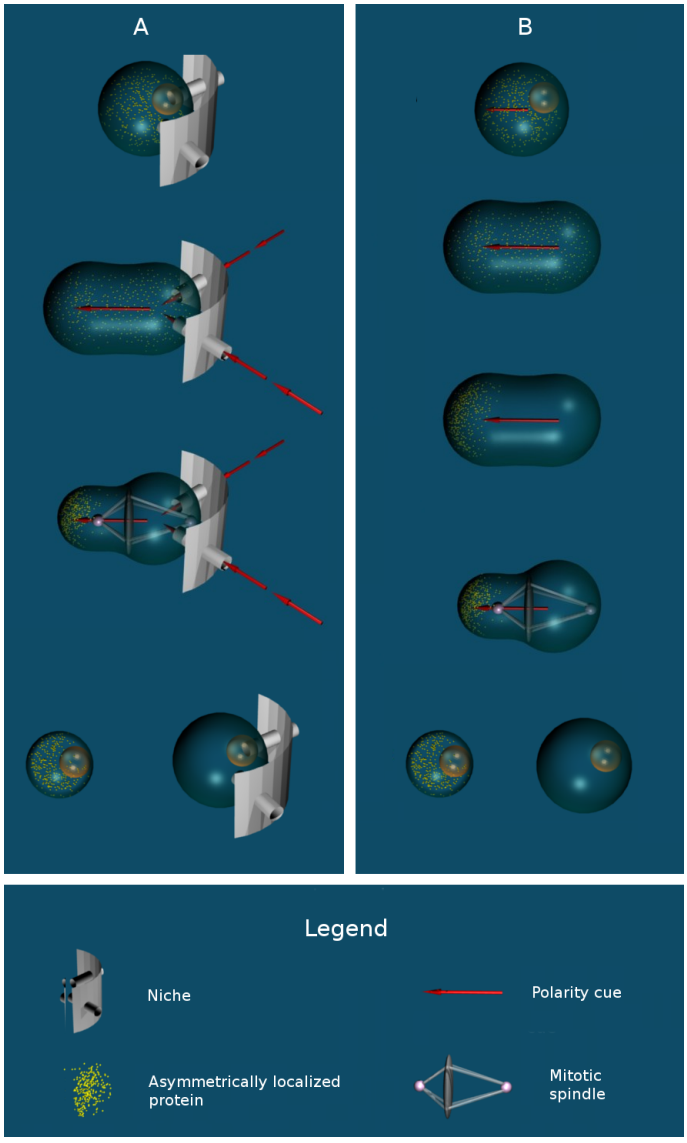

Figure 2.2: *Extrinsically controlled (A) vs. intrinsically controlled (B) asymmetric cell division: the polarity axis (and polarity cue) is shown as a red arrow, and a cell fate determinant (protein or mRNA) is shown in magenta.*

2.2 Examples for asymmetric cell division

2.2.1 *Caulobacter crescentus*

This extensively studied bacterium [143] can be found in two forms: the swarmer cell, which is a motile, chemotactic cell, propelled by a flagellum and the stalked cell, which is non-motile and attached to the surface using an adherent protrusion called "stalk". Only the stalked cells divide, asymmetrically, giving rise to one stalked cell and one swarmer cell, which can later change into a stalked cell (see **Figure 2.3**). The division, in which one stalk cell gives rise to a swarmer cell and a stalk cell is an example of self renewal and can be used as a model to study this phenomenon, which is an important characteristic of stem cells. A large body of data, which has been accumulated thus far about *Caulobacter crescentus*, outlines a sophisticated system that tightly controls protein localization and synchronizes it with the cell cycle [13].

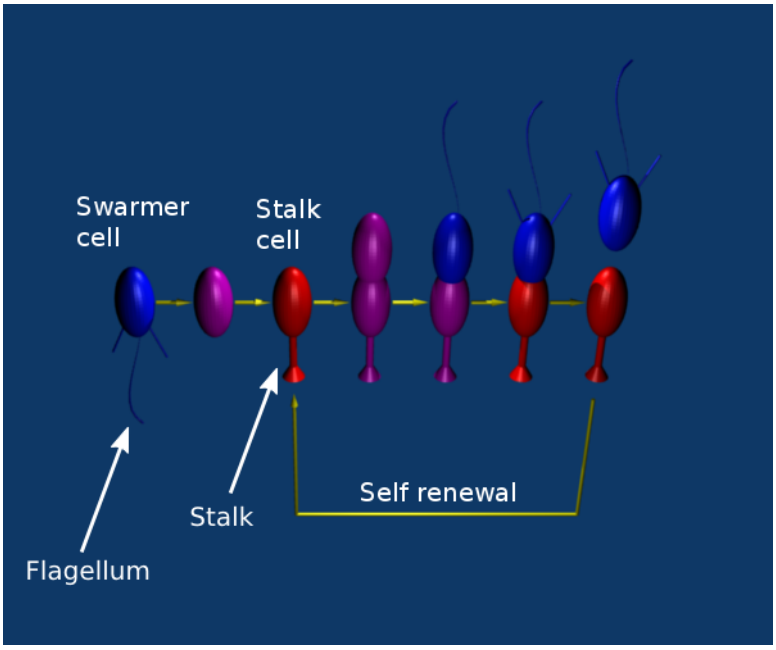

Figure 2.3: *A schematic of the Caulobacter crescentus cell cycle*

2.2.2 *Saccharomyces cerevisiae*

The budding yeast is known to divide asymmetrically [133], by budding a small daughter cell. However, the cell division of the budding yeast is asymmetric not only in size, but also in content. Even though in budding yeast both daughter cells eventually have the same fate, there are many evidence for asymmetric segregation of cell content such as proteins, nucleic acids, and even organelles [144, 145]. There are two types of differential inheritance in budding yeast:

Differential inheritance of cell fate determinants

Similarly to higher organisms, different daughter cells inherit different factors that determine their developmental programs (fate) [145] such as the ASH1 mRNA, which determines a yeast cell's mating type switching ability [146].

Differential inheritance of cellular material

The cellular material of the budding yeast mother cell is carefully sorted: the bud is made out of entirely new membrane, and damaged proteins stay in the mother cell (this phenomenon is related to aging and can also be found in many bacteria.). Nuclear ribosomal DNA circles, related to aging are also restricted from the daughter cell by a mechanism involving anchoring to nuclear pores and a septum-associated diffusion barrier (see **Figure 2.4**). A very interesting exception is the repeated inheritance of old spindle pole body (the yeast equivalent of a centrosome) by the budding cell, thus rendering the spindle pole "immortal".

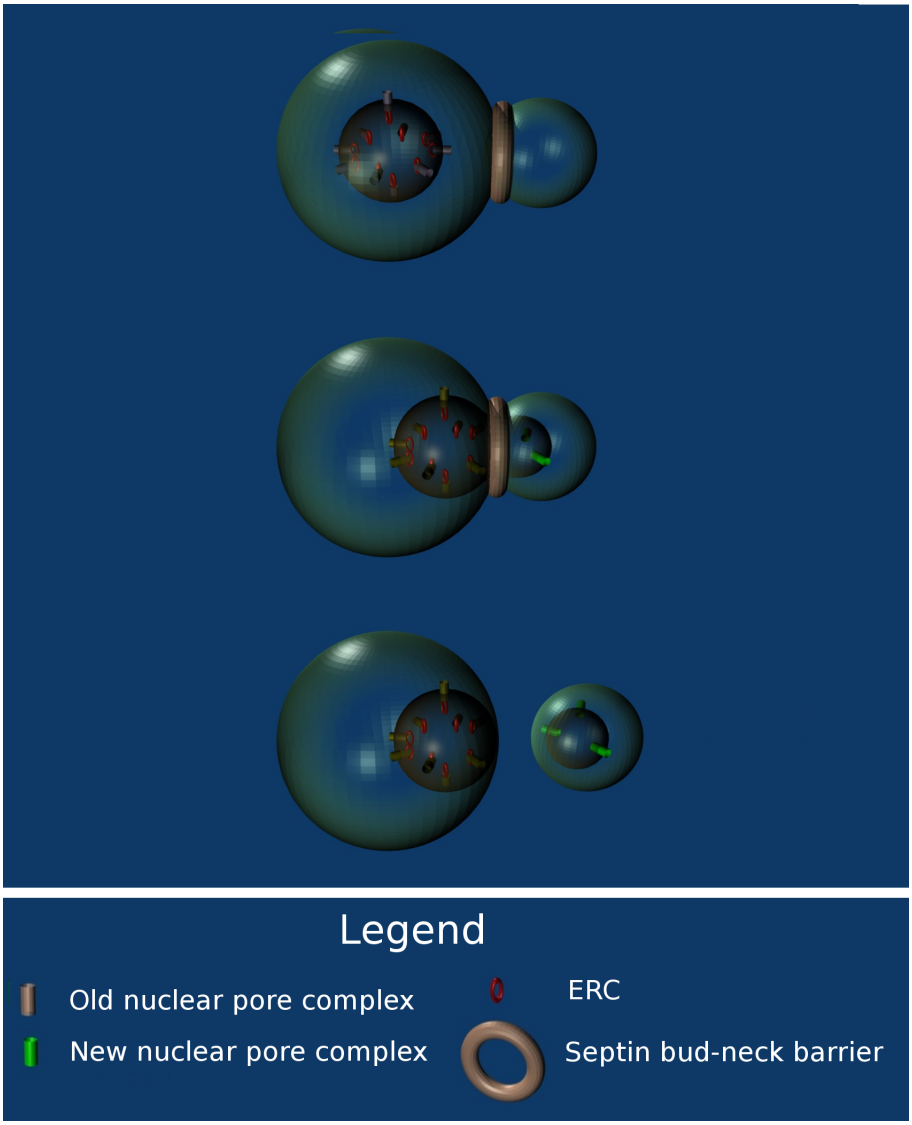

Figure 2.4: *A schematic of the Saccharomyces cerevisiae cell division, showing how during cell division, maternal nuclear pores are not allowed to pass into the budding cell. This way ERCs (Extrachromosomal rDNA circles), which are associated with nuclear pores, are prevented from being propagated into the next generation.*

.

2.2.3 *Caenorhabditis elegans*

The development of *Caenorhabditis elegans* heavily relies on asymmetric cell divisions. In fact, it was found that out of the 949 non-gonadal cell divisions during the development of this organism, 807 are asymmetric [139]. In this organism, polarization starts already with the sperm entry into the oocyte. The position of the sperm entry defines the posterior end of the zygote (also known as the p0 cell) which then divides according to the anterior-posterior axis (see **Figure 2.5(b)**). This division results in a large, anterior cell called the AB cell, and a small cell, called P1.

Except for the size difference, the cells also have different fates: the AB cell will form mainly ectoderm, while the P1 cell will develop into germline, endo- and mesoderm. More than 25 years ago, a landmark mutation study in *Caenorhabditis elegans* discovered six proteins called Par-1 to Par-6 (for Partition defective [147]). These proteins, except for Par-2, which is probably unique to *Caenorhabditis elegans*, were found to be highly conserved, and implicated in all aspects of polarity, in various organisms from yeast to human.

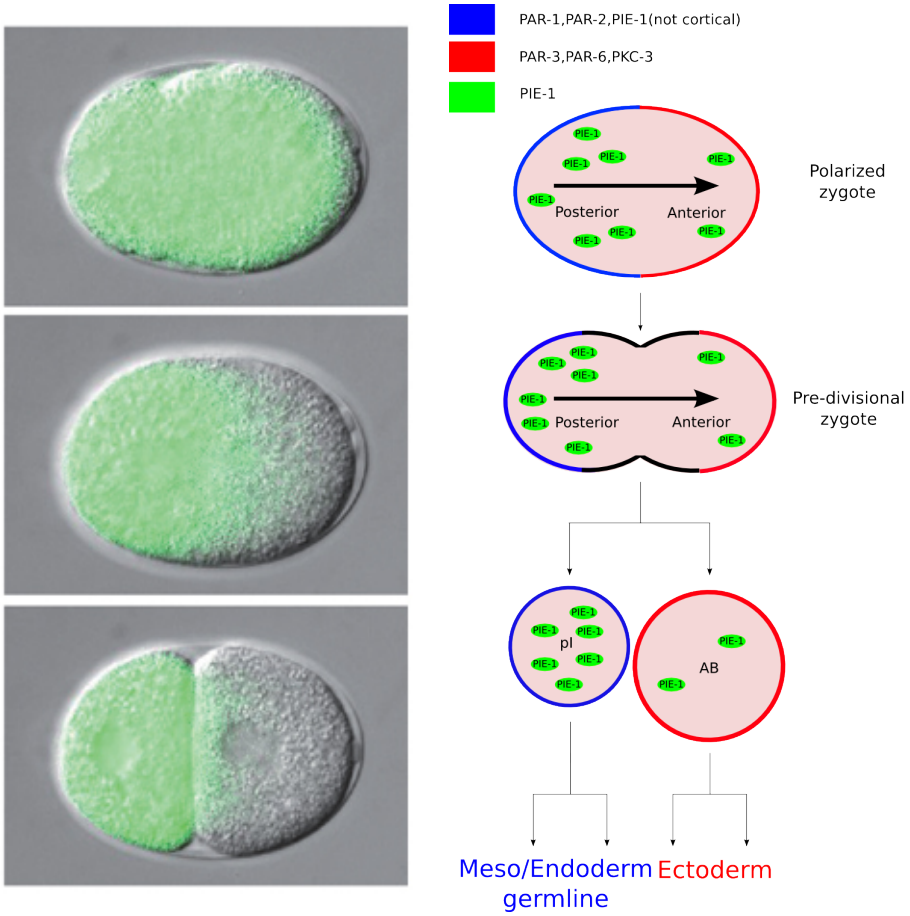

(a) *Asymmetric localization of the protein PIE-1 during the asymmetric cell division of Caenorhabditis elegans zygote. taken from* [148].

(b) *A schematic of asymmetric cell division in the Caenorhabditis elegans zygote.*

Figure 2.5: *Asymmetric cell division in Caenorhabditis elegans.*

2.2.4 *Drosophila melanogaster*

Maybe the most prominent examples for ACD in *Drosophila* occur in the fly's nervous system. ACD in flies has been mostly studied either in neuroblast cells or in the sensory organ precursor (SOP) lineage. From a developmental point of view, the most important difference between these two model systems is that in contrast to neuroblasts, SOP cells do not divide in a stem-cell like fashion (no self renewal) and therefore cannot be used as stem-cell models.

pI cells

These cells follow a stereotyped cell lineage, which results in a complete, bristle sensory organ, composed of four distinct cells. It is generated through a series of asymmetric divisions [149, 150] starting from the pI cell, which is located at the pupal notum. This cell divides in a direction **parallel** to the plane of the epithelial cells, along the fly's antero-posterior axis (see **Figure 2.6**), into a small anterior pIIb cell and a large posterior pIIa cell [151]. Both of these cells then undergo asymmetric cell divisions, and in the next generation, one of pIIb's "asymmetric" siblings undergoes an additional asymmetric cell division. This finally yields five different cells, which, following an apoptosis of one of them, become a sensory organ.

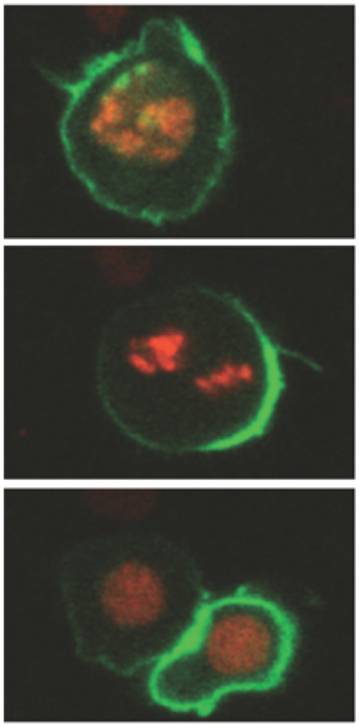

(a) *The course of the first asymmetric cell division in Drosophila melanogaster SOP cells expressing the asymmetrically localized protein PON, fused to GFP (right) as seen by fluorescence microscopy (taken from [136])*

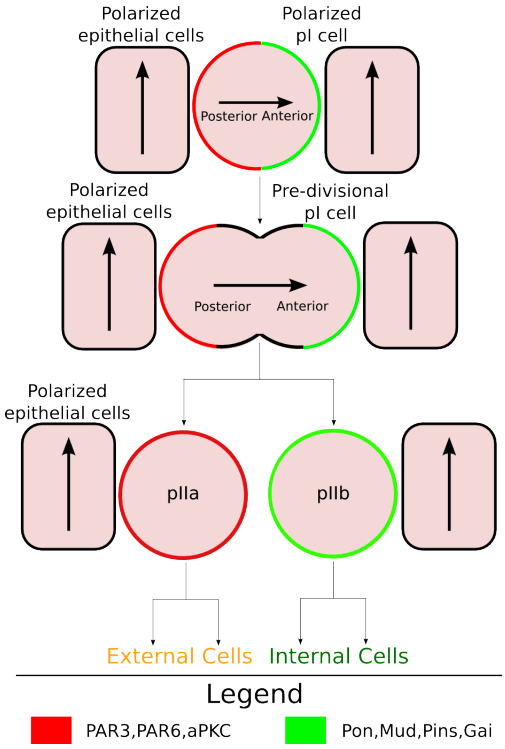

(b) *A schematic of asymmetric cell division in Drosophila melanogaster SOP (sensory organ precursor)*

Figure 2.6: *Asymmetric cell division in Drosophila melanogaster SOP cells.*

Neuroblasts

Neuroblasts are precursors of the fly's central nervous system. These cells divide in a stem cell-like fashion, **perpendicular** to the plane of the epithelial cell layer from which they delaminate. These cells divide asymmetrically, giving rise to a new neuroblast and a ganglion mother cell (GMC). This system is the subject of this work and will later be discussed in more detail.

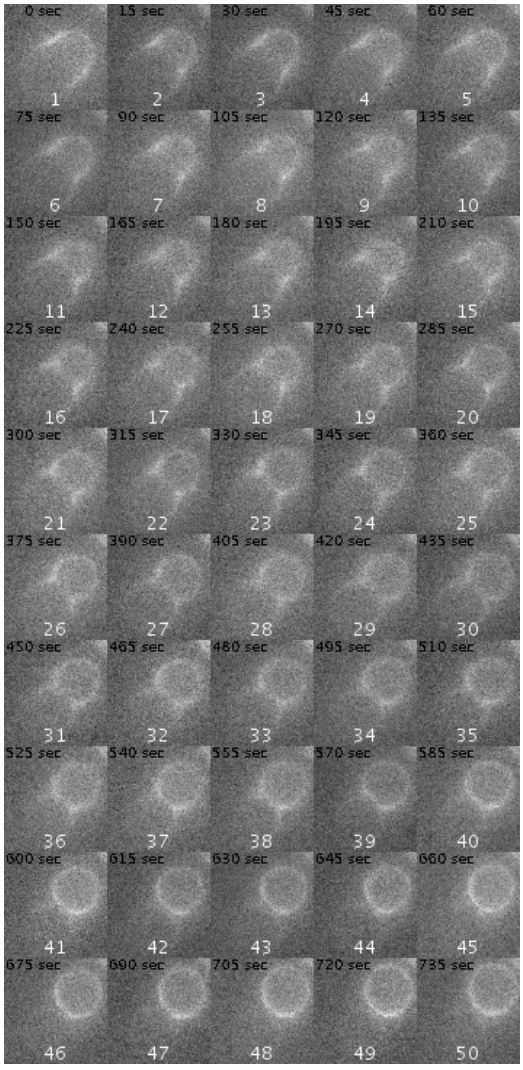

(a) *An asymmetric division in PON-GFP Drosophila neuroblasts, as seen by fluorescence imaging. In the beginning (frame 1), a fluorescent crescent is seen, which is the polarized PON-GFP (in the basal part of the cell). As the division proceeds, the cleavage furrow appears on the border of the PON crescent. The cleavage furrow narrows down, until it finally closes, giving rise to the ganglion mother cell (GMC), which contains PON.*

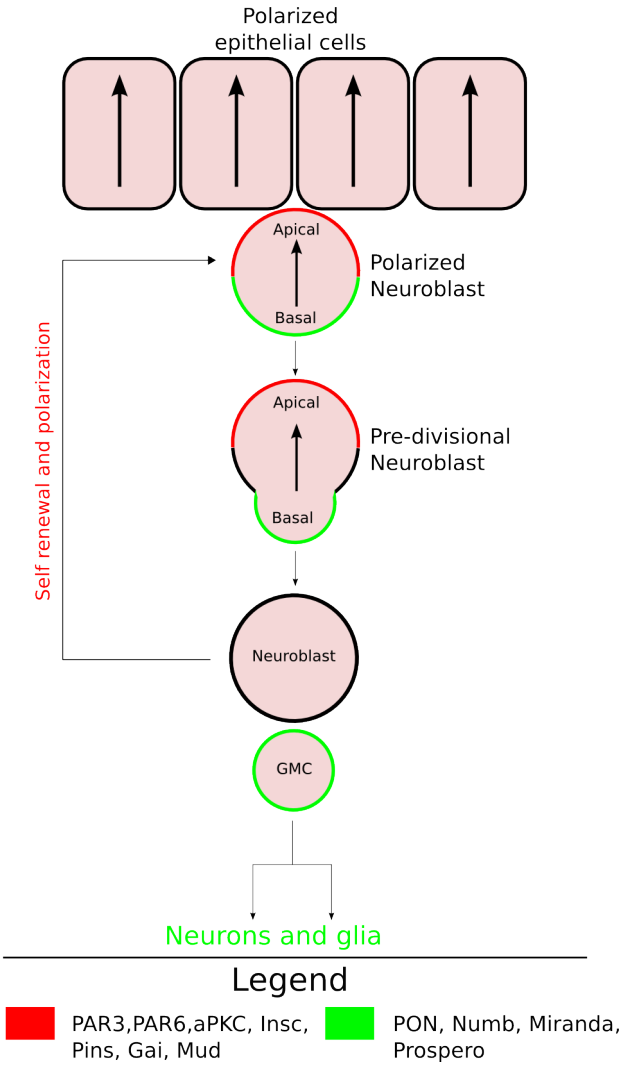

(b) *A schematic of asymmetric cell division in Drosophila neuroblasts*

Figure 2.7: *Asymmetric cell division in Drosophila melanogaster neuroblasts*

2.2.5 Mammalian

There are numerous examples for asymmetric cell division in mammals, such as mouse neurogenesis and muscle stem cells [142], but maybe the most striking example is asymmetric cell division of T lymphocytes [152]: it was found that following a prolonged interaction between a naive T cell and an antigen-presenting cell, the T cell can divide asymmetrically to produce a differentiated cell (effector cell), committed to react to the acute immunogenic stimulus, and a memory cell, which preserves the useful clone through a memory lineage and can later produce effector cells if need be.

ACD and cancer Many of the proteins involved in asymmetric cell division are actually tumor-suppressors. Mutants of such proteins show over-proliferation, and malignancy in allografts [153] (transplants between two different organisms of the same species). Different explanations for over-proliferation have been suggested, such as reversal of cell fate due to ectopic cell fate determinants and symmetric proliferation due to spindle misalignment.

Even though cancer and tumorigenesis are usually associated with defects in asymmetric division that lead to over-proliferation, recently, there has been an increasing interest in asymmetric cell division in the context of tumor growth. There are more and more evidence that tumors contain a small number of "cancer stem cells" that divide asymmetrically, giving rise to a heterogeneous tumor [141].

2.3 Asymmetric cell division of *Drosophila melanogaster*

The experimental system chosen for the project is the *Drosophila melanogaster* larval neuroblast. The reason we chose this system is the large body of data that has been accumulated about ACD in neuroblasts, and the relative simplicity of culturing and genetic manipulation of flies.

Neuroblasts are precursors of the fruit fly's central nervous system. They undergo multiple rounds of stem-cell like asymmetric cell division. Every such division gives rise to one neuroblast (self-renewal) and one ganglion mother cell (GMC), which is smaller and subsequently divides only once, into two differentiating neurons (see **Figure 2.7**). There are two types

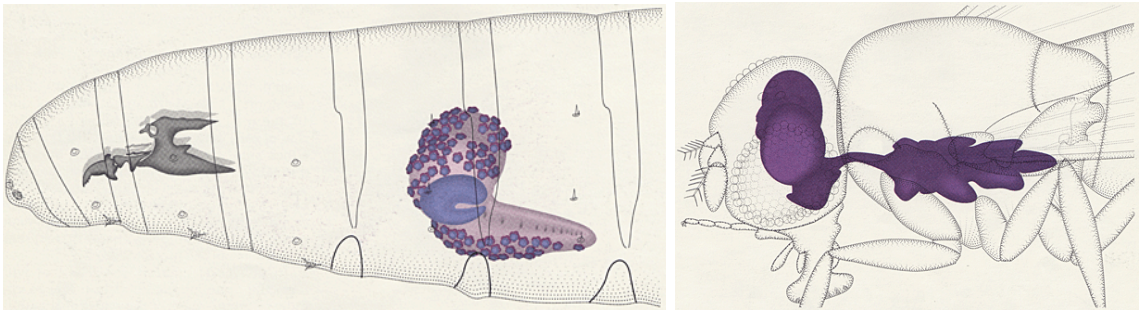

(a) *The central nervous system in the third instar larva, dorso-lateral aspect, oriented anterior-left.*

(b) *The central nervous system in the adult fly, dorso-lateral aspect, oriented anterior left.*

Figure 2.8: *Central nervous system (indicated in purple): larva vs. adult* [154]

of neuroblasts: embryonic and larval. Embryonic neuroblasts are precursors of the relatively simple larval nervous system. They delaminate from the neuroectoderm and then go through multiple asymmetric cell divisions along the apical-basal axis. These neuroblasts have limited self-renewal capability (as they become smaller and smaller with each division) and therefore are a less attractive model for stem cell division. Larval neuroblasts, which are the ones used in this project, can divide hundreds of times, re-growing to their original size after every division.

These neuroblasts differ in size and developmental timing, according to their location in the brain. The study of asymmetric cell division in general, and in particular in flies, concentrates on two main aspects:

- Asymmetric localization of cell fate determinants.
- Spindle positioning.

2.3.1 Asymmetric localization of cell fate determinants - a detailed description

The different fates of the neuroblast daughter cells are conferred by cell fate determinants that are unequally segregated between the daughter cells. These molecules (proteins or mRNA) act upon the expression profile of a specific daughter cell, in order to generate the desired cell type. In fact, since neuroblasts undergo self renewal, the cell fate determinants need only to act on the expression profile of the ganglion mother cell (GMC). Maybe the most important cell fate determinant is Prospero (Pros), a transcription factor that is segregated into the GMC and later enters its nucleus, where it activates its developmental program. The division of a Pros mutant neuroblast gives rise to a "defective" GMC that fails to express GMC markers. Two other important cell fate determinants were identified: Numb and Brat (Brain tumor). Numb is a phosphotyrosine binding protein that acts as a repressor of the Notch signaling pathway [155], and was found to determine cell fate in SOP cells, and also in embryonic neuroblasts (although more limited). Brat is also segregated into the GMC to interact with many proteins implicated in asymmetric cell division. The molecular mechanism leading to localization is partly known:

The highest layer of the localization mechanism, includes two apically localized protein complexes The first complex is the PAR complex: Par-3 (Bazooka), Par-6 and aPKC. Par-6 is a small protein that binds Cdc42 (through its CRIB domain) and aPKC (through its N-term PB1 domain). Par-3 (Bazooka or Baz) contains three PDZ domains that can transiently bind aPKC. The second complex is composed of Gαi, Pins and Mud [156], which is linked to the PAR complex through the protein Inscuteable.

A lower layer of the localization mechanism consists of two adaptor proteins: PON and Miranda. Cell fate determinants are carried into the GMC by the adaptor proteins Miranda, which carries the protein Prospero, and PON, which carries Numb (therefrom its name, partner of numb). To date, it is not clear how is the localization signal passed between the layers, i.e. how these apical complexes "transmit" the polarity to Miranda and PON. One model suggests that an intermediate protein called Lgl (Lethal Giant Larvae), upon phosphorylation in the apical cortex, becomes localized in the basal part of the cell, where it recruits proteins to the cortex [142]. It should be noted though, that there is a "backup" mechanism for the localization of basal cell fate determinants. This pathway was discovered when Inscuteable mutants that initially lost the basal localization, partially or completely regained it by telophase. This phenomenon was termed "telophase rescue" [157, 158].

We hereby summarize what is known about the localization of these two adaptor proteins:

Miranda is a multiple-adaptor protein with a complex localization pattern During interphase, Miranda is localized to the apical cortex whereas at the onset of mitosis, it starts moving to the basal cortex, passing through the cytoplasm [159, 160]. The localization of Miranda requires both myosin II and myosin VI, which act successively: after forming a transient apical crescent, Miranda becomes uniformly distributed in the cytoplasm and cortex in a myosin II dependant fashion (probably by exclusion from the apical cortex by myosin II, which gets locally activated, directly or indirectly, by Lgl). Throughout prophase and metaphase, Miranda

slowly starts to form a basal crescent in a myosin VI dependant fashion. A recent work challenges this model [161], and offers a different one, in which Miranda is directly phosphorylated by aPKC (which is possibly regulated by Lgl), leading to its dissociation from the cortex. The role of myosin II, though, remains unclear. Either way, the mode of transport and localization of Miranda is not completely understood.

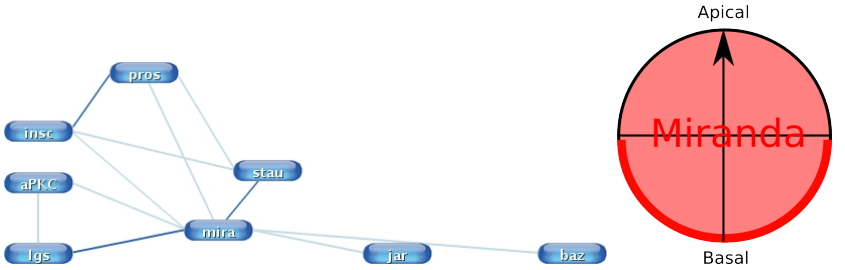

(a) *A summary of the Miranda's interactions*

(b) *The distribution of Miranda at late metaphase.*

Figure 2.9: *Some of the known interactions for Miranda [162] (**Figure 2.9(a)**), and the expected localization pattern for Miranda during late metaphase (**Figure 2.9(b)**) . As can be seen, Miranda interacts with both apical and basal proteins.*

The localization mechanism of PON The current model for the localization of PON is very similar to the first model for Miranda: aPKC phosphorylates Lgl in the apical part of the cell. The phosphorylated Lgl is inactive and therefore cannot positively regulate the recruitment of PON and Numb in this cellular domain [163]. It was also found that the localization of PON depends on its phosphorylation by the kinase Polo [164]. Dynamic localization of PON in pI cells also was studied using FRAP analysis, which found that PON is recruited to the basal cortex directly from the cytoplasm with a very high exchange rate, rather than by cortical diffusion. During interphase, PON is distributed all over the cell, in the cytoplasm and on the cortex. At the onset of prophase, PON starts to show transient accumulation in different sites on the cortex. On late prophase, the PON crescent starts to nucleate and becomes more and more pronounced as the cell moves into metaphase. The spindle aligns itself with respect to the PON crescent in a way that PON and Numb are segregated exclusively into one daughter cell. It should be noted though that PON is not essential for Numb localization: in PON mutants, Numb was still localized asymmetrically but at a later stage of division, even though this results in defective self-renewal [164]. It was found that the domain responsible for PON localization is its fourth domain, the C-terminal domain [165].

Numb was the first discovered in SOP cells, where it inhibits the Notch signaling pathway by binding to alpha-adaptin, an endocytotic protein, possibly involved in the intracellular trafficking of Notch intermediates. In the larval brain, numb mutants over-proliferate and generate a tumor-like phenotype [166]. Numb mutants divide into two cells of unequal size, both with the expression pattern and proliferation characteristic of neuroblasts. Neuroblast asymmetric cell division has been observed in isolated neuroblasts and therefore is considered to be driven by an intrinsic mechanism. During the division, several proteins get localized to the apical cortex of the neuroblast. Some of these proteins have been shown to affect spindle orientation.

2.3.2 Spindle positioning in *Drosophila melanogaster*

The polarization of cell fate determinants serves no purpose if the spindle is not orientated in a way that ensures that these proteins end up exclusively in the GMC (see **Figure 2.11**). One of the proteins that were found to be implicated in spindle orientation is Pins (Partner of

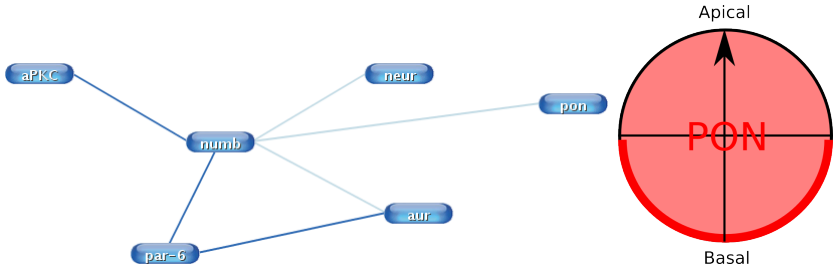

(a) *A summary of interactions for Numb and PON.* (b) *The distribution of PON at prophase.*

Figure 2.10: *Some of the known interactions for PON and Numb [162] (**Figure 2.10(a)**) and the expected localization of PON during mitosis (**Figure 2.10(b)**).*

Inscuteable). On one hand, it was found that larvae of Pins mutant flies suffer from a reduction of the number of Neuroblasts [167]. On the other hand, live imaging experiments [168] show that in Pins mutants, the neuroblasts divide symmetrically, and that malignant tumors can develop from Pins mutant tissue, transplanted in other flies (allograft tissue) [169]. Two spindle localization pathways are thought to co-exist [170] (both involving the protein Pins): the Pins-Gαi-Mud pathway and the Pins-Dlg-Khc73 pathway.

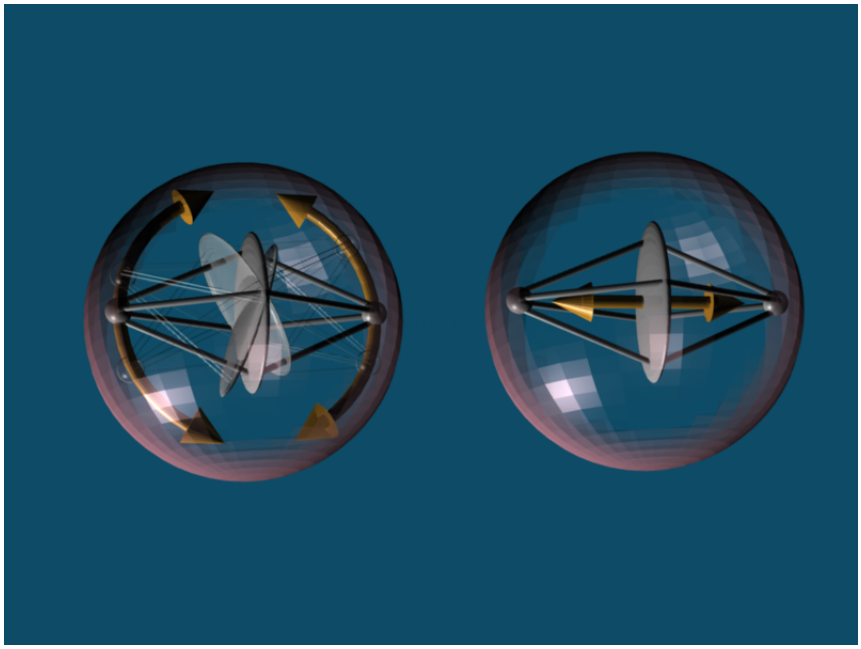

Figure 2.11: *The main degrees of freedom in spindle positioning: rotation of the spindle axis (left site), and translation of the division plane along the spindle axis (right side) [162]. In the context of ACD, rotation is important in order to align the spindle axis with the polarity, and thereby achieve strict segregation of cell fate determinants. Translation is important in order to control daughter cell sizes.*

The Pins-Gαi-Mud pathway

In this pathway, these three proteins form a complex, which is linked to the PAR complex through Inscuteable. In a recent study, it was found that Gαi and Mud cooperatively compete with Pins Intramolecular interactions, to form this complex [171], in which the Pins-Gαi in-

teraction mediates the apical localization of Pins, whereas the Pins-Mud interaction mediates spindle positioning. This way, the PAR complex, which is also involved in the formation of the basal crescent (and using some feedback loop also receives information about the orientation of the crescent) synchronizes it with spindle alignment. This is achieved through a putative interaction of Mud with the dynein-dynactin complex that can exert a pulling force, restraining one centrosome to the apical cortex and thereby aligning the spindle with the apico-basal axis. On the other hand, it must be noted that the dynein-dynactin complex has never been detected in the apical cortex of neuroblasts.

The Pins-Dlg (the tumor suppressor Discs large, involved in telophase rescue) and Khc73

Based on mutation analysis and immunopreciptation, it was proposed that a parallel pathway exists, in which the plus-end directed khc-73 (the plus-directed kinesin motor heavy chain 73) interacts with a cortical protein called Dlg, leads to the localization of the Pins-Gαi complex (based on the requisition of Dlg for the formation of Pins-Gαi complexes [172]), which in turn orients the spindle [173]. The problem with this model is that it does not explain why khc-73 associates with Dlg only on one spindle pole.

Since these two suggested pathways share many key player (Dlg, Pins,Gαi,Mud) and also partly rescue each other, it is not perfectly clear whether they are not, in fact, a single pathway rather than two distinct ones.

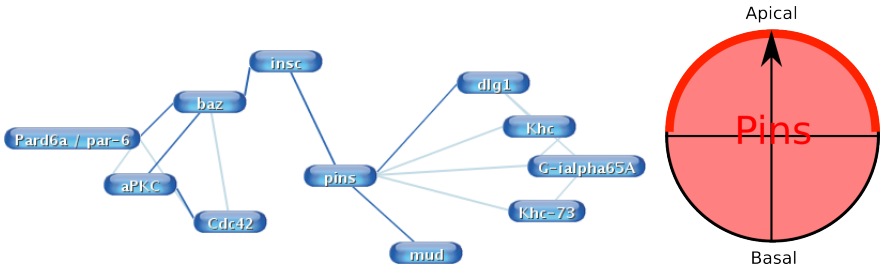

(a) *A summary of some of the important interaction for Pins, all limited to apical proteins [162].*

(b) *A summary of some of the important interaction for Pins, all limited to apical proteins [162].*

Figure 2.12: *A summary of Pins' interactions (**Figure 2.12(a)**), and the expected localization pattern for Pins (**Figure 2.12(b)**), in dividing neuroblasts.*

2.3.3 Neuroblasts as a model for cancer research

Neuroblasts have another advantage as a model for studying cancer: it was previously suggested that niche-dependant stem cells are much more limited in their ability to cause tumors, since the finite capacity of the niche can only support a limited number of cells [14].

2.3.4 Conserved features and principles in asymmetric cell division

Overall, some principles of asymmetric cell division seem to be conserved and appear in all systems: asymmetric cell division seems to go through four steps (see **Figure 2.2**):

1. Before division, the polarity axis is determined, relatively to the cell body. This is a symmetry breaking event, even though in some cases the polarity axis is inherited by the cells (as in the case of neuroblasts delaminating from the neuroectoderm)

2. Cell fate determinants are distributed in a polarized fashion according to this axis.
3. The mitotic spindle aligns with the polarity axis, as a means to ensure that corresponding cell fate determinants are inherited by one cell only.
4. As the division comes to an end, the cell fate determinants determine the distinct cell fate for each cell.

2.3.5 Questions arising from the observation of asymmetric cell division

How is polarity initiated and amplified?

This is a problem of a more general context of polarity, and is relevant to all other instances of polarity. Studies on yeast polarization, have tried to explain this in terms of a positive feedback loop, governed by Cdc42, and initiated by a stochastic event [174, 175] or more formally using the Turing reaction-diffusion model [176, 177]. After polarity is initiated, it gets amplified by some biochemical circuit. This process, which can be observed in many systems, relies on the recruitment of the proteins implicated in cell division [178].

How is polarity maintained?

As mentioned before, polarity has to be robustly maintained, throughout asymmetric cell division, in order to make sure that cell fate determinants reach their designated daughter cell. If this fails, the consequences could be grave: over-proliferation or cell death. Therefore, there should be a mechanism that minimizes the leakage of CFDs into the "wrong" daughter cell. From a thermodynamic point of view, this process should require a lot of resources from the cell, in order to decrease the mixing entropy of many diffusing molecules. Different mechanisms have been found for maintaining polarity: from diffusion barriers [179] to active transport and diffusion-capture, and reaction-diffusion [180] (see **Figure 2.13** for examples). An understanding of the network of interactions involved, could shed light on this phenomena and answer the question which is the most efficient mechanism for the task, and why.

How is polarity coordinated with spindle positioning?

This question is specific to asymmetric cell division. The molecules involved in translating the polarity information into spindle positioning are known, as well as some of the network of interactions between them. However, we still do not know the physical nature of this system, which receives the chemical information from the gradient of cell fate determinants and translates it into mechanical constraints that orient the spindle accordingly, thus making sure that during cytokinesis the cell content is correctly partitioned. This aspect has been studied extensively [170], but mostly using genetic tools, rather than by quantitative methods, which may lead to conflicting results, as mentioned before for the ACD proteins.

2.3.6 Advantages of SQDT in the context of polarization

Single molecule tracking could be very instrumental in coping with questions such as the ones mentioned above. In cases of mechanisms based on reaction-diffusion, we would expect to have, in analogy to the polarized distribution of a given protein, a polarized distribution of diffusion coefficient values [1][181]. The high spatial resolution could serve us well in producing such a map inside the cell. For example: Daniels *et al.* [180] studied the asymmetric localization of the cell fate determinant PIE-1 in *C. elegans*. They proposed a model of "binary counter-diffusion", which is based on some conversion reaction that PIE-1 undergoes on the surface of

[1] In his seminal paper, Turing gave a very simple condition for a two-component (activator/inhibitor) system [177]. The basic requirement is a difference in diffusion coefficient between the two components [181].

small intracellular granules, leading to a change in diffusion rate. The authors' main difficulty was in explaining how exactly this conversion-reaction happens. Since the size of these granules (P-granules) is on the scale of the diffraction limit, it was not possible to investigate the phenomenon using FRAP (the method used in the article). Another advantage of SQDT in such cases is the ability to study polarization over time, since cell division is on the timescale of minutes, which requires a highly photostable probe.

Our experimental strategy for coping with these questions By tracking single copies of proteins that are asymmetrically distributed or implicated in spindle alignment and analyzing their movement, we will obtain information about the localization mechanism of these proteins.

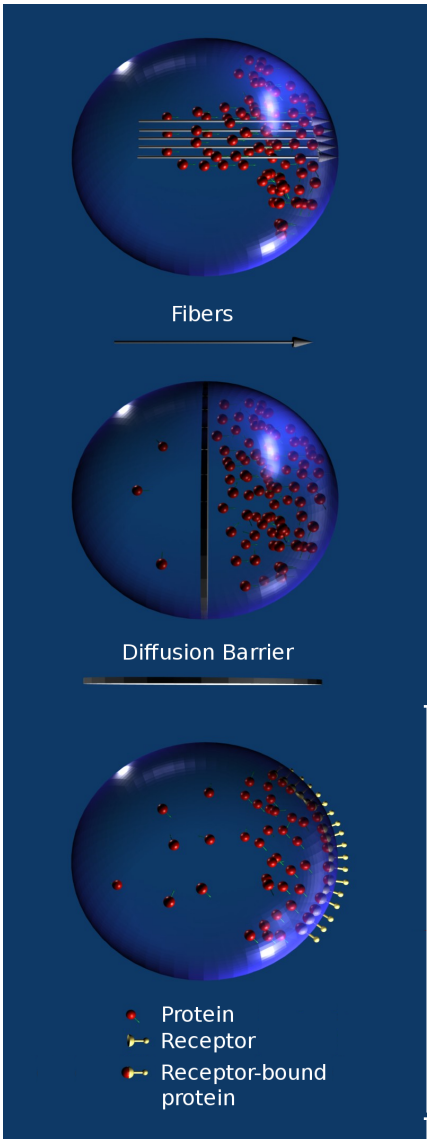

Figure 2.13: *A cartoon, showing possible mechanisms for asymmetric localization/polarization of proteins: Top:* ***directed transport*** *- for example, by nucleating actin filaments to create directed "tracks" that actively transport the protein. Center:* ***using a diffusion barrier*** *that "sorts" the cell content and thereby creates an asymmetry in protein concentration. Bottom: by using an* ***asymmetrically localized intracellular membrane receptors****, the cell can concentrate the protein in an asymmetrical cortical domain.*

Part II

Methods

Chapter 3

Experimental layout - asymmetric cell division

The experiment is composed of a few steps:

1. Preparation of the cell culture: as mentioned before, we are studying larval neuroblasts, which are primary cells taken from the larval brain. Therefore, the first step is to prepare a primary culture from larval brains. This is done by dissecting mature larvae with the desired phenotype (in our case PON-GFP). The brains are dissociated and plated on a poly-lysine coated glass cover-slip.
2. Preparation of QD-protein complex: the proteins of interest that were prepared beforehand, need to be coupled to QDs. For endogenous labeling, we conjugated the QDs to an antibody against GFP (to target PON-GFP). For exogenous labeling, we directly conjugated QD-SAV with either Pins-biotin or Miranda-biotin.
3. Internalization of the QD-protein complexes into the cells, using pinocytic influx.
4. Observation and data collection: the cover-slip is inserted into an observation chamber, which is mounted onto the microscope. The sample is then illuminated with UV light using an optimized filter set (according to the fluorophore: QD or GFP) and image sequences are collected.
5. Data analysis: the resulting trajectories are analyzed, in order to obtain parameters that can characterize the movement of the proteins.

A set of three proteins that are implicated in asymmetric cell division were chosen for this project:

- PON (Partner of Numb)
- Pins (Partner of Inscuteable, also called rapsynoid)
- Miranda

These proteins were cloned, expressed (with different levels of success) and purified in different expression systems, in order to be able to conjugate them to quantum dots and introduce them into live cells.

Chapter 3

Chapter 4

Experimental setup

The imaging experiments were performed on an inverted OLYMPUS IX-71 microscope, equipped with a Roper QuantEM 512SC EMCCD camera and a fast shutter (uniblitz), controlled by Metamorph software. Illumination was performed using a UVICO UV (Rapp opto-electronic) lamp.

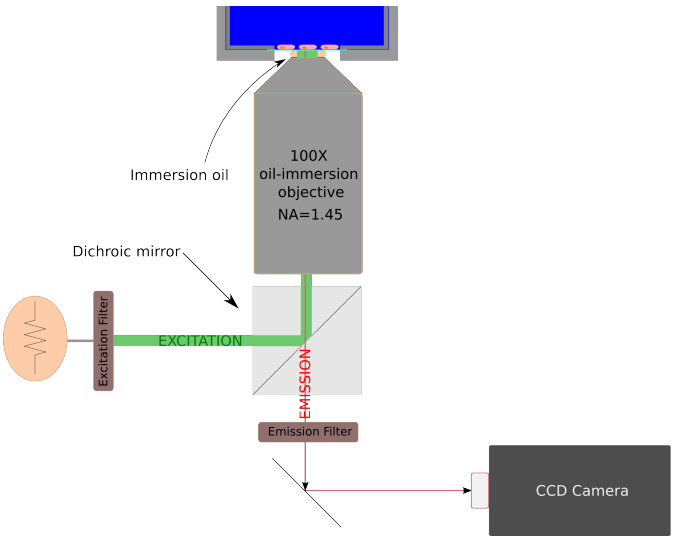

(a) *A schematic of the experimental setup used in the experiment*

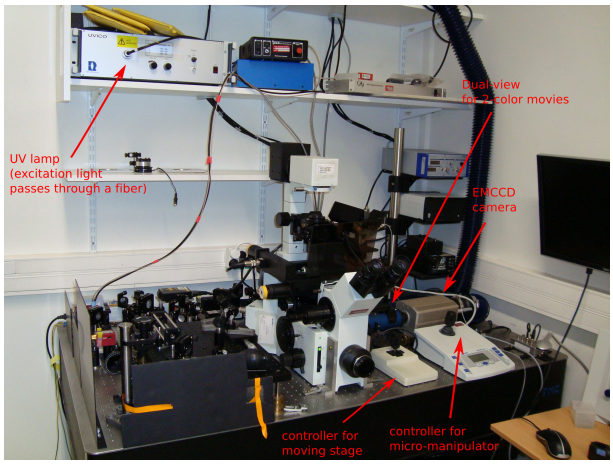

(b) *A photo of the experimental setup*

Figure 4.1: *The experimental setup.*

Chapter 4

Chapter 5

Fly work

5.1 *Drosophila melanogaster* as a model system in biology

What follows is a brief overview of the *Drosophila melanogaster* model system. The life cycle of *Drosophila melanogaster* is relatively simple [182, 183]:

1. Eggs are layed
2. Eggs develop into larvae
3. Larvae develop into pupae
4. Pupae develop into adult flies

Since this project depends on the production of larvae (we use mature larvae, or "third instar larvae"), the generation time of *Drosophila* is important. The generation time of *Drosophila* can be controlled by the temperature: at 25^{o}C, it is 10 days (see **Figure 5.1**), at room temperature (21^{o}C -22^{o}C), its is 12-13 days and at 18^{o}C it is about 19 days.

5.1.1 Husbandry

Female flies can mate with more than one male, and store the sperm from multiple matings. Therefore, when performing genetic crosses, it is advisable to select virgin females (this is done visually using specific features of virgin females). Otherwise, the results will not be explicable in terms of Mendelian genetics.

5.1.2 Basic genetics and notation

Drosophila have 5 chromosomes, which are written as: (X/Y);2;3;4 (where X/Y is the sex chromosome). Genotypes are listed only when a mutation is present and are italicized. The notation n/m, means that for a given chromosome, the fly genotype contains one allele with genotype n and one allele with genotype m. The notation n/+, means that for a given chromosome, the genotype is one allele of genotype n and one wild type genotype. Recessive mutations are written in lower case and dominant mutations are capitalized[96].

Male flies do not perform genetic recombination: This phenomenon can be exploited by different crossing schemes to ensure that the gene of interest is not lost by recombination during meiosis.

5.1.3 Genetic tools in Drosophila

The two main genetic tools used in this project are the UAS-GAL4 system [184] and balancers [185]. The former allows to over-express a certain protein of interest (such as PON-GFP in our

case) in a specific subpopulation of cells, by correlating this over-expression to the expression pattern of a different, possibly independent, protein. The latter are artificially manipulated chromosomes that prevent homologous recombination with their native counterparts (due to multiple inversions), and contain recessive lethal (lethal when homozygote) mutations, which prevent the loss of their native chromosome counterpart by inheritance. Thus, balancers serve to maintain the genetic information in recombinant flies over many generations.

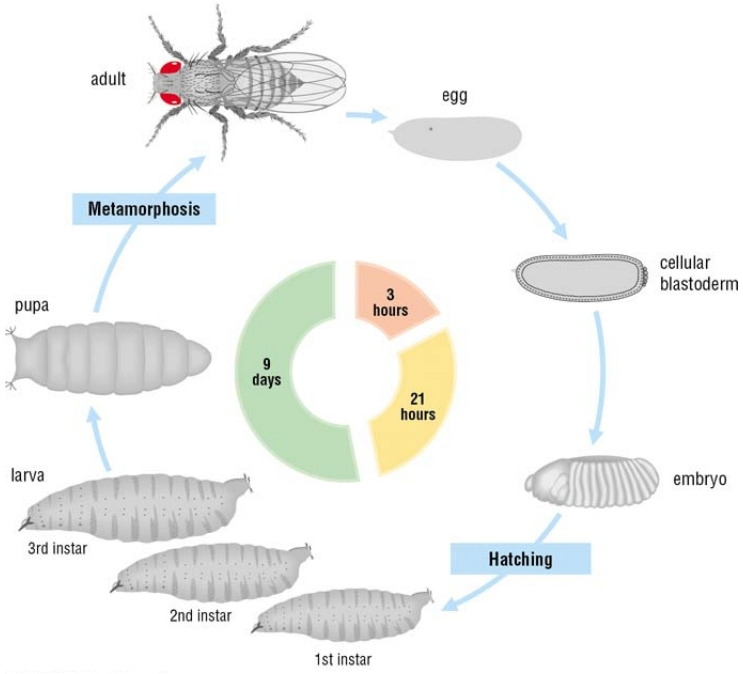

Figure 5.1: *Life cycle of Drosophila melanogaster (taken from [186]).*

5.2 Genetic crosses

Generating a stable stock of PON-GFP flies driven by Inscuteable-Gal4 (Insc-Gal4) In order to image larval neuroblasts that express PON-GFP (PON-GFP will be used both as a target and as an orientational marker in dividing neuroblasts), we needed a stable fly strain that overexpresses PON-GFP, driven by Inscuteable-Gal4 (PON-GFP is expressed wherever the gene Inscuteable is expressed). We started from a fly strain expressing PON-GFP driven by the Neuralized-Gal4 (PON-GFP is expressed wherever the gene Neuralized is expressed), and used genetic recombination and crosses, in order to obtain homozygote ;Inscuteable-Gal4;PON-GFP; flies.

We hereby describe the crossing steps used to obtain homozygote ;Inscuteable-Gal4;PON-GFP; flies. After most crossing steps, the progeny of interest was chosen using phenotypic markers. These markers are used to report the genotype of the fly: chromosome balancers, for example, usually have visual phenotypes that allow one to tell whether the balancer was inherited by a given fly and select only the flies that carry the balancer. The visual phenotypic markers used here were: w-white eyes (eye color can be superseded by colors coming from other genes, such as PON-GFP); *Tb*-tiny bristles (larvae are identified being very short); *Sb*-short bristles (the hairs on the back of the fly); *Cyo*-curly wings; *If*-inflated.

1. *w;;Neuralized-Gal4,UASPON::GFP/TM6,Tb;* flies were crossed with *w* (white-eyed) flies.

2. From the progeny, virgin females were collected for recombination (in order to get rid of the Neuralized driver), which is now possible since the third chromosome is not balanced. These females were *w;;Neuralized-Gal4,UASPON::GFP/+;* and were later crossed with *w* flies.

3. From the progeny, *w;;UASPON::GFP/+;* virgin females (where the third chromosome is unbalanced) were selected based on their orange eyes, and crossed with *w;;TM3,Sb/TM6,Tb;* males. In order to balance the third chromosome, which has lost the *Neuralized-Gal4* gene, as we wanted, by recombination.

4. From the resulting progeny, we chose *w;;UASPON::GFP/TM6,Tb;* flies and let them mate among themselves (for amplification), to obtain homozygote *w;;UASPON::GFP;* that were selected by the lack of *Tb* phenotype).

5. Then, virgin female *w;;UASPON::GFP;* flies were crossed with *w;Insc-Gal4;;* males. The resulting flies were *w;InscGal4/+;UASPON::GFP/+;* (the second and third chromosome are not balanced). Therefore, we took males from the progeny (since males cannot perform recombination) and crossed them with female virgin *w;If/Cyo;MKRS,Sb/TM6,Tb;*. From this step on, the presence of *InscGal4* and *UASPON::GFP* was verified by UV excitation, which revealed a strong green signal at the larval salivary glands.

6. The resulting progeny, *w;InscGal4/Cyo;UASPON::GFP/TM6,Tb;* was crossed again with *w;If/Cyo;MKRS,Sb/TM6,Tb;*.

7. Then, *w;InscGal4/Cyo;UASPON::GFP/TM6,Tb;* flies were left to mate among themselves, producing the homozygote *w;InscGal4;UASPON::GFP;*, which was identified visually by the lack of *Sb*,*Tb*,*If* and *Cyo*, and by the green fluorescence in the salivary glands.

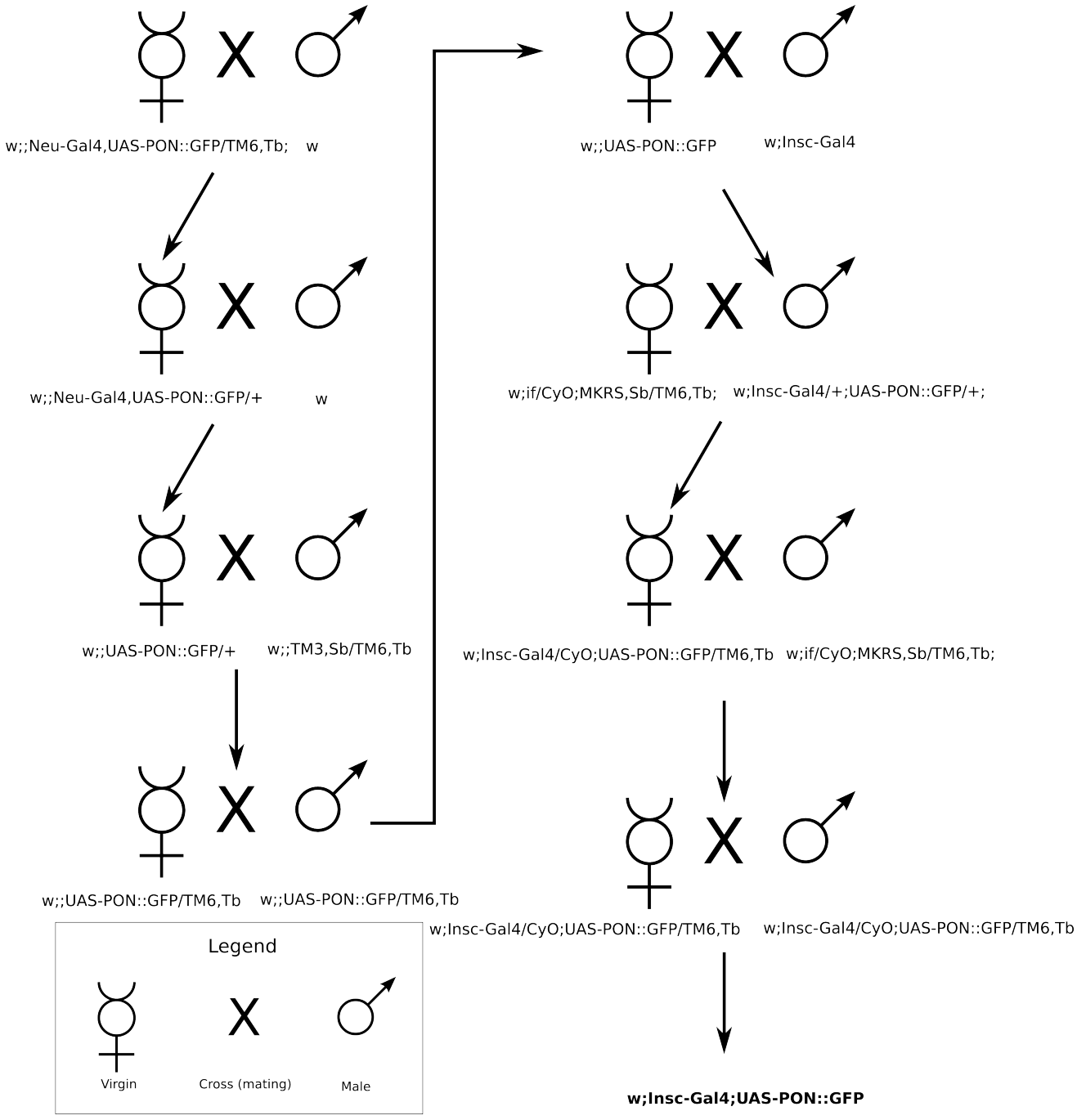

Figure 5.2: *An outline of the genetic crosses we used, in order to produce the homozygote ;InscGal4;UAS-PONGFP flies used throughout the project.*

5.3 Larvae dissection and neuroblast culture

As mentioned before, in this project we used larval neuroblasts from *Drosophila*. In order to observe the neuroblasts, we collected third-instar larvae from the Insc-Gal4, UAS-PONGFP homozygote clone. After rinsing the larvae in water, we transferred them into a dissection buffer (see **Appendix**) and used sharp tweezers to open the larva body and collect the brain. The brains were then incubated with collagenase, in order to digest the connective tissue, rinsed and dissociated by pipetting. Then, the dissociated brains were plated on polylysine-coated coverslips (20 brains per coverslip) and incubated at 23^{o}C, for two hours to attach. Then, the medium is changed to FEED (see **Appendix**) and the cells were returned into the incubator, ready for further imaging and manipulation.

Chapter 6

Protein expression and purification

This chapter describes the cloning, expression and purification procedures for the proteins used in this project. The cloning section also includes the results of tests performed in order to validate the DNA constructs. The results of protein expression are described in the "**Results**" part.

6.1 Cloning and design

Proteins produced in this project Several proteins were produced, in order to be used in this project:

1. For the study of asymmetric cell division:
   (a) PON
   (b) Pins
   (c) Miranda
2. For the targeting of membrane receptors using monovalent QDs: Anti-GFP single chain variable fragment.
3. In addition, some proteins were produced in order to be used in different tests:
   (a) Monobiotinylated GFP: this protein was used to test *in-vivo* and *in-vitro* biotinylation, binding to QD-SAV, and solid-support coupling as well as to serve as a target for the binding of anti-GFP single chain antibody in binding measurements.
   (b) BirA: this protein was used for *in-vitro* biotinylation.
   (c) Nucleoplasmin: this protein was used as a control for internalization and targeting in cells.

The opposite-ends two-tag design The design of the ACD protein constructs (PON, Pins and Miranda) is based on a two-tag concept: the expressed protein includes two tags: one for purification (*e.g.* HisTag, MBP....), which allows binding and elution from a purification resin, and the other for conjugation (biotin), which should have a very high affinity towards the QD. We then decided to place the tags on opposite sides of the protein, in order to make sure that once the biotinylated protein is purified using the purification tag, only the full length construct will bind to the QD (see **Figure 6.1**).

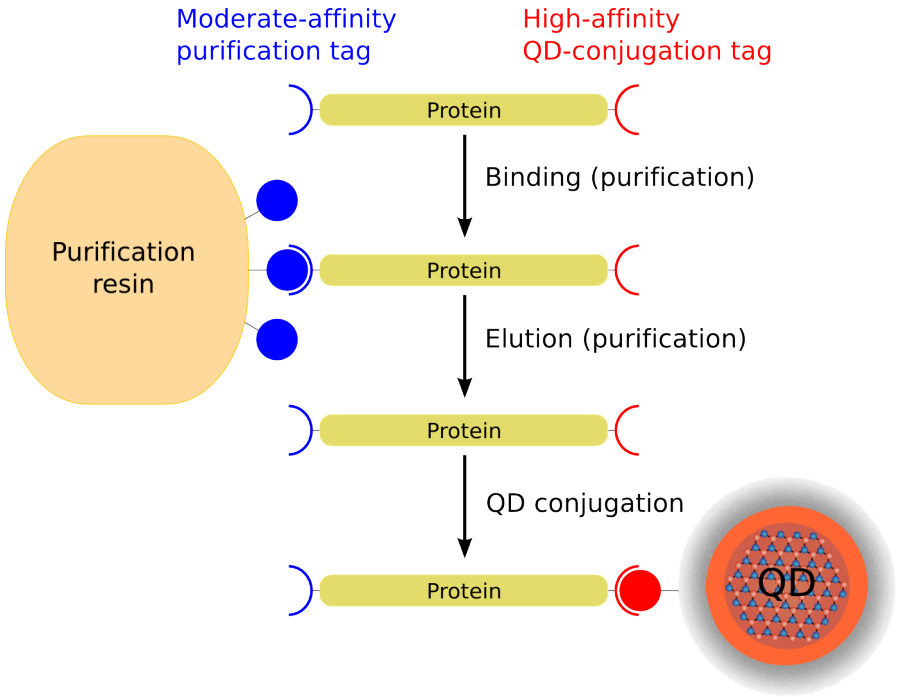

Figure 6.1: *A schematic of the two-tag design.*

Expression systems Two expression systems were used: the *baculovirus*/SF9 and the *E. coli*. The former is technically more complicated, but is usually the method of choice for large and possibly insoluble eukaryotic proteins. The baculovirus system chosen for this project was the BAC-TO-BAC system (Invitrogen). In this system, the gene of interest is cloned into a commercial vector and transformed into a special strain of *E. coli* (DH10Bac), where the vector performs a transposition into a viral DNA (bacmid). The bacmid is then transfected into insect cells (SF9) in order to obtain a virus. The virus then undergoes a few cycles of amplification and finally, when the concentration is high enough, used for large-scale infection of the cells that yields high amounts of protein.

For *E. coli* we used standard protocols for expression, except in the case of periplasmic expression, in which we optimized the existing protocols. Periplasmic expression is usually considered as a better choice for weakly soluble proteins and/or proteins that do not fold well in *E. coli* under standard expression conditions (such as ScFvs). The expressed protein is typically targeted into the periplasm of this Gram-negative bacterium, using a signal peptide. Once in the periplasm, the different REDOX potential and possibly native chaperones usually allow for a better folding of the protein to take place.

6.1.1 PON

Baculovirus constructs

These constructs were derived from a pFastBac HTc vector, into which a GFPuv (pFastBac HTc-GFPuv) fusion protein was inserted at the StuI site: from this vector two different vectors were generated:

1. pFastBac HTc-AviTag-GFPuv in this construct, the AviTag (biotinylation tag) is upstream to the GFP. In order to generate this construct, we first prepared the N-terminal

AviTag fragment by annealing the two synthetic strands, AviTagN1 and AviTagN2. The resulting N-terminal AviTag fragment had a 5' EcoRI site and 3' SfoI site. Then, the vector was generated by digesting pFastBac HTc-GFPuv with the EcoRI and SfoI, extracting from an agarose gel and ligating with the N-terminal AviTag fragment (see **Figure A.1**).

2. pFastBac HTc-GFP-AviTag: In this construct, the AviTag (biotinylation tag) is downstream to the GFP. In order to generate this construct, we first prepared the C-terminal AviTag fragment by annealing the two synthetic strands, AviTagC1 and AviTagC2. The resulting C-terminal AviTag fragment had a 5' XbaI site and a 3' HindIII site. Then, the vector was generated by digesting with XbaI and HindIII, extracting from an agarose gel and then ligating with the C-terminal AviTag fragment (see **Figure A.1**).

The concentrations of the resulting constructs were estimated using Lambda HindIII calibration. Then they were amplified using mini-preps and sequentially digested by XbaI and NotI. The resulting double-digested DNA was purified by gel extraction and ligated with a short DNA adaptor, in order to introduce the rare restriction site SfiI. The adaptor was prepared by annealing two synthetic DNA strands in a final concentration of $50ng/\mu l$. The product of the ligation reaction was transformed into *E. coli* DH5α as a prior step to cloning the PON sequences. A colony PCR was then performed using the primers PH and SV40 (Invitrogen), in order to find the positive clones. One colony (*i.e.* one clone) was chosen for each construct (pFastBac HTc-AviTag-GFPuv and pFastBac HTc-GFPuv-AviTag) and used to start a DNA maxiprep. The concentrations of the DNA were $0.69\mu g/\mu l$ for pFastBac HTc-AviTag-GFPuv and $0.925\mu g/\mu l$ for pFastBac HTc-GFPuv-AviTag. The constructs were verified by PCR using combinations of the primers PH and SV40, and forward and reverse primers for the AviTag (see **Figure 6.2**). This DNA was then double digested by NotI and SfiI and purified on an agarose gel (see **FigureA.1**).

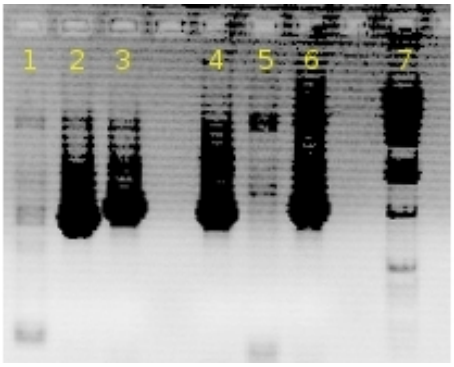

Figure 6.2: *A PCR test for the intermediate constructs pFastBac HTc-AviTag-GFPuv and pFastBac HTc-GFP-AviTag. This gel is a qualitative test, to verify that the inserts were cloned correctly, and that the two clones (N-terminal AviTag and C-terminal AviTag) that were done at the same time, did not cross contaminate.* ***Templates****: in lanes 1-3, template is pFastBac HTc-AviTag-GFPuv; in lanes 4-6, template is pFastBac HTc-GFP-AviTag.* ***Primer pairs****: in lane 1, primers are PH+Cterminal AviTag-reverse; in lane 2, primers SV40+Nterminal AviTag-forward; in lane 3, primers PH+SV40; in lane 4, primers PH+Cterminal AviTag-reverse; in lane 5, primers SV40+Nterminal AviTag-forward; in lane 6, primers SV40+PH; lane 7 was loaded with 1KB ladder. Lanes 1 and 4 are negative controls for cross-contamination. We can see that the expected band for the inserts (500bp) was obtained.*

preparation of inserts PON inserts were obtained using high fidelity (HiFi)-PCR on a PBHA2 plasmid (a derivative of pMAC5-8) into which the PON cDNA has been cloned (see

Figure 6.3). By using different primers inside the PON gene we obtained the following DNA inserts:

1. PON123-FUS: the first three domains of the PON protein, to be fused to a C-terminal AviTag.
2. PON123-STOP: the first three domains of the PON protein terminated by a stop codon, to be fused to an N-terminal AviTag.
3. FullPON-FUS: the full PON protein, to be fused to a C-terminal AviTag.
4. FullPON-STOP: the full PON protein terminated by a stop codon, to be fused to an N-terminal AviTag.
5. PON4-FUS: the fourth domain of the PON protein, to be fused to a C-terminal AviTag.
6. PON4-STOP: the fourth domain of the PON protein, terminated by a stop codon, to be fused to an N-terminal AviTag.

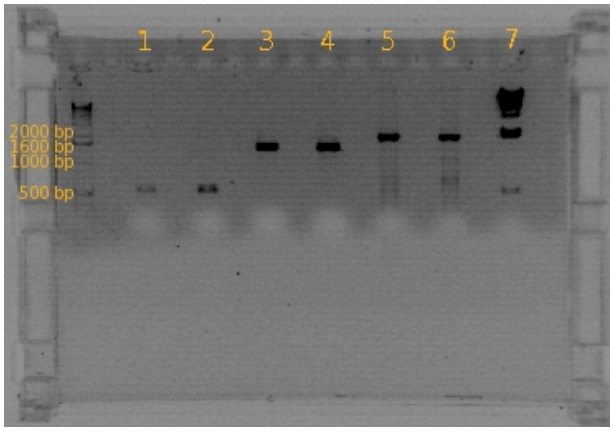

Figure 6.3: *High fidelity (HiFi), double digested (NotI and SfiI) PON inserts: 1, PON4-STOP fragment; 2, PON4-FUS fragment; 3, PON123-STOP fragment; 4, PON123-FUS fragment; 5, FullPON-STOP; 6, FullPON-FUS; 7, Lambda HindIII ladder. The migration agrees with the expected sizes for these fragments.*

These fragments were then purified using agarose gel electrophoresis and cloned into a dephosphorylated, pGEM vector digested with SmaI (produces blunt ends), in order to store the fragments. This vector allows the selection of pGEM containing the PCR fragment using blue-white selection. Then, the pGEM vectors containing the inserts were amplified and digested with NotI and SfiI, and the double digested inserts were purified on an agarose gel.

Final ligation The vectors pFastBac HTc-AviTag-GFPuv and HTc-GFPuv-AviTag were digested with NotI and SfiI, dephosphorylated and ligated with the following inserts: pFastBac HTc-AviTag-GFPuv was ligated with PON4-STOP and pFastBac HTc-GFPuv-AviTag was ligated with PON4-FUS, PON123-FUS and FullPON-FUS.

Verification of the DNA constructs

The resulting DNA constructs were validated by sequencing, using the primers PH and SV40(Invitrogen). The sequences found perfectly matched the predicted sequences.

Preparation of bacmids

The validated plasmid vectors were transformed into E. coli DH10Bac for transposition into bacmids. The bacteria were spread on multi-antibiotic selection plates (BAC-TO-BAC, Invitrogen) to select for positive transposition events. Finally, three positive colonies were used for a bacmid prep, which yielded the bacmid DNA. For the Full PON, three clones were obtained. The bacmids were verified using a low density agarose gel and a PCR using the primers M13 reverse (Invitrogen) and PON Nter (for a list of primers, see **Appendix**).

Bacterial construct

We also cloned PON into an MBP fusion vector pMal-C2 parallel-III using a simple cassette cloning. This vector is based on the commercial pMal-C2, into which the complete MCS of pFastBac HTc was cloned. In this case, we digested pMalC2-parallel-III and pFastBac HTc-GFPuv-PON4-AviTag with EcoRI and HindIII. Both digestions were loaded on an agarose gel in order to separate the vector (the large fragment from the pMal digestion) and the insert, containing PON4 (the small fragment from the pFastBac digestion). The insert and vector were ligated, and positive clones were found by means of colony PCR.

6.1.2 Pins

For Pins we prepared two constructs: a baculovirus construct and a bacterial construct.

Baculovirus construct The Pins gene was extracted from a pEYFP-Pins transfection plasmid containing the full Pins cDNA, in a HiFi-PCR reaction using the primers for the N-terminus and C-terminus of Pins. The resulting HiFi PCR fragment was run on an agarose gel, extracted, digested with XbaI and purified again on an agarose gel. Then, we digested a pFastBac HTc-GFPuv-PON4-AviTag construct with XbaI, and the blunt cutter SfoI(EheI) and separated the double-digested vector on an agarose gel. Finally, the vector and insert were ligated. The resulting plasmid was then used to transform *E. coli* DH10BAC (Invitrogen), to yield the bacmid that was used for the transfection of SF9 cells (from which the initial viral stock was obtained). The bacmid clones were tested using PCR (see **Figure 6.5**) and an agarose gel migration assay.

Preparation of the insert For the baculovirus construct, the insert was produced using a HiFi PCR with the N-terminal and C-terminal primers for Pins, resulting in a 2000 bp fragment. The fragment was purified on a gel, ligated, and ligated with a double-digested, dephosphorylated vector. The ligation product was transformed into *E. coli* $DH5\alpha$ and tested by colony PCR. The positive clones were amplified, sequenced and found to be correct.

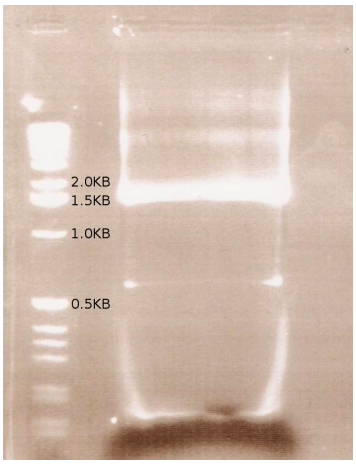

(a) *An agarose gel, showing the results of the HiFi PCR for the Pins gene insert. This fragment was produced using high fidelity PCR using primers that were designed by us (see* ***Appendix****), in order to be cloned into the pFastBac vector. The expected size for the PCR product is ∼1600bp. As can be seen from the gel, the fragment was successfully produced.*

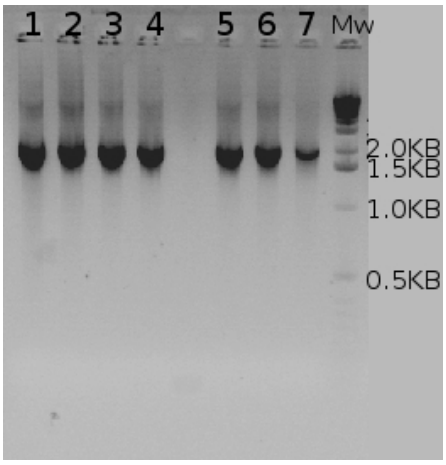

(b) *A PCR test for the cloning product: pFastBac HTc-Pins-AviTag. After cloning the insert we verified that indeed, it was incorporated into the host pFastBac plasmid. This was done using a standard PCR reaction, whose products were loaded on an agarose gel for analysis. The results show a band that has the expected size of the Pins insert, ∼1600bp.*

Figure 6.4: *Tests for the cloning of Pins into the baculovirus vector pFastBac.*

Preparation of bacmids

The validated plasmid vectors were transformed into *E. coli* DH10Bac for transposition into bacmids. The bacteria were spread on multi-antibiotic BAC TO BAC plates. Finally, three positive colonies were amplified and used for a bacmid prep, which yielded the bacmid DNA. They bacmids were verified using a low density agarose gel and a PCR using primer M13 reverse (Invitrogen) and Pins Nter.

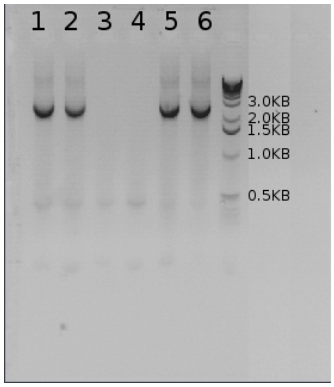

Figure 6.5: *A PCR test for the Pins bacmids for three selected clones (numbered 1,6 and 9).*

Bacterial construct This construct was based on a pET32b vector. The vector was digested with NcoI and HindIII, gel-purified and dephosphorylated. Then, it was ligated with a Pins DNA fragment and extracted from the baculovirus vector using NcoI and HindIII.

6.1.3 Miranda

Baculovirus constructs

Simple construct The insert was prepared by HiFi PCR, using the primers for the N-terminus and C-terminus of the full Miranda gene (for a list of the primers, see **Appendix**). The result was a DNA fragment of $\sim 2000bp$ with a C-terminal XbaI site. The insert was loaded on an agarose gel, extracted and subsequently digested with XbaI. The backbone vector used, was the C-terminal AviTag PON4 pFastBac construct, digested with SfoI and XbaI that was purified by agarose gel electrophoresis and then dephosphorylated.

Dual expression construct This is a dual-expression vector containing Miranda and the *E. coli* enzyme BirA (biotin ligase). This construct was prepared at a later stage, in order to circumvent the need for *in-vitro* biotinylation. The backbone vector was a pFastBac Dual vector, which contains two promoters: P_{PH} and P_{p10}. BirA was taken from an existing expression vector (pCDF-Duet) by first digesting with HindIII, then performing a klenow fill-in and subsequently digesting with NcoI. The resulting BirA fragment was purified by gel electrophoresis and ligated into the pFastBac Dual backbone that was digested with NcoI and PvuII and dephosphorylated. The resulting plasmid was amplified and then digested with RsrII and HindIII (in the P_{PH} MCS), gel-purified and ligated with a Miranda fragment that was digested out of the pFastBac HTc construct using RsrII and HindIII. The BirA construct was verified on an agarose gel. The Miranda insert was cloned using a cassette cloning (with no need for HiFi PCR) and therefore, since the chances of failure are usually very low, was verified only later, when it was already in the bacmid.

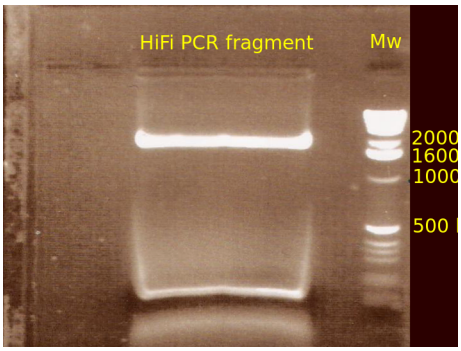

(a) *The HiFi Miranda insert: we have produced the insert for the Miranda construct, by performing a high-fidelity (HiFi) PCR on the Miranda cDNA. The result, which had the expected size for the Miranda gene ($\sim 2000bp$), was then loaded on an agarose gel and purified from primers and proteins. This figure shows the gel, before the band was cut for purification. The molecular weight marker is on the right.*

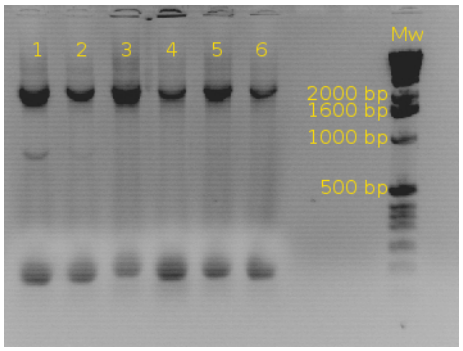

(b) *A PCR test for the cloning product: after cloning the pFastBac MirandaAviTag, we verified it by performing a PCR using the N-terminal and C-terminal primers for Miranda, on selected clones. The result was loaded on an agarose gel (lanes 1-6) together with a molecular weight marker (Mw). The bands in the gel correspond to the size of the Miranda gene, $\sim 2000bp$.*

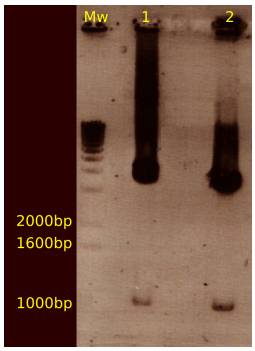

(c) *A HiFi PCR for the Tag-less BirA fragment, which was later purified from the gel and cloned into the pFastBacDual vector together with Miranda, in order to produce biotinylated Miranda. The gel shows two clones. The 1000bp fragments are the HiFi BirA genes.*

Figure 6.6: *Important PCR tests during the cloning of Miranda baculovirus constructs.*

Preparation of bacmids

Following a bacmid prep for three clones, they were checked on a low density agarose gel, and in a PCR reaction. The validated plasmid vectors were transformed into *E. coli* DH10Bac for

transposition into a bacmid. The bacteria were spread on multi-antibiotic BAC TO BAC plates (Invitrogen). Finally, three positive clones were used for a bacmid prep, which yielded the bacmid DNA. They were verified using a low density agarose gel and a PCR using the primers M13 reverse and PON Nter.

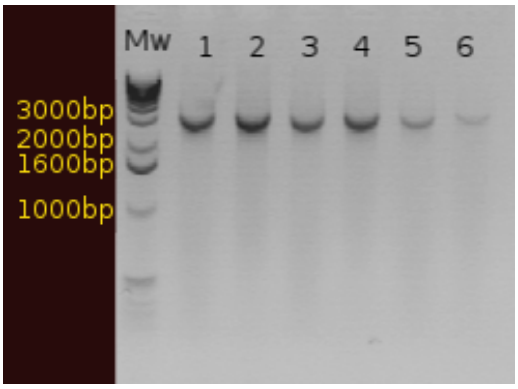

(a) *A PCR test for the bacmid clones. The PCR for the simple Miranda bacmid was performed using the primers M13F and P10 (For a scheme, see* ***Figure D.2*** *in the* ***Appendix****) that together with the Miranda gene and surrounding parts, should give 3200bp, which is about what we have here.*

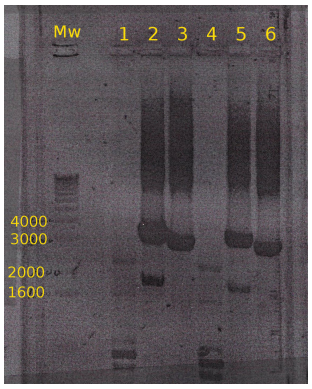

(b) *A PCR test on the Miranda dual-expression bacmid. We have chosen two clones, and performed three different PCR tests on each one of them, by using three combinations of primers, assuring that both BirA and Miranda are in the bacmid, and that the result is not an artifact from the plasmid. The results were positive: lanes 1,4 give the BirA+Gentamicin gene in the bacmid=2500bp (weak, but can be seek); lanes 2,5 give Mira+BirA+inter-promoter region=3600bp; lanes 3,6 give pH promoter+Miranda gene+M13 reverse region=3200bp.))*

Figure 6.7: *PCR tests for the Miranda bacmids: after performing a transposition of the Miranda gene from the pFastBac into the bacmid (using the BAC TO BAC system from Invitrogen), the bacmids were verified. The simple expression bacmid was verified using a simple PCR test, while the dual expression bacmid was verified using a PCR with several combinations of primers, in order to test for Miranda and BirA.*

6.1.4 Anti-GFP single chain variable fragment

Anti-GFP ScFv cDNA was obtained from F. Perez in the form of a pHENII phagemid. The construct was double-digested with NcoI and NotI (consensus sites in most single chain constructs) and cloned into pET26b that was digested correspondingly. The vector pET26b contains a sequence encoding for the PelB signal peptide, fused upstream to the MCS. This signal peptide targets the expressed protein to the periplasm of gram-negative bacteria such as *E. coli*, where it is cleaved from the protein by a native peptidase. Thus, the expressed protein has the PelB peptide in the N-terminus and a HisTag at the C-terminus.

6.1.5 GFP

The GFP-AviTag fragment from the intermediate vector pFastBac HTc GFP AviTag (in the early steps) was sub-cloned into pET29 HTb (a pET 29 vector into which the full MCS of pFastBac HTb has been cloned). pFastBac HTc GFP AviTag and pET 29 HTb were digested with NcoI and HindIII and loaded on an agarose gel. In pFastBac HTc GFP AviTag, the NcoI site overlaps with the first ATG and therefore is reading-frame-independent, and HindIII is located after the stop codon, which follows the AviTag (properties that make cloning much easier).

6.2 Protein expression

6.2.1 Baculovirus/SF9 expression and purification

Transfection

For each one of the baculovirus constructs, three clones were selected and transfected into SF9 cells, using cellfectin (Invitrogen) according to the manufacturer's instructions. After the transfection, the cells were observed, to see that the bacmids budded out as viruses and caused a widespread infection of the cell population.

Virus amplification cycles

72 hr post-transfection, infection was verified by examining the cells under the microscope. The cells looked infected (abnormally large and granulated). In the case of PON-GFP, we also observed the cell pellet under UV excitation, where the green fluorescence from the GFP was detected, indicating that the infection was successful and resulted in a small-scale production. After centrifugation, we collected ~ 3 ml of the supernatant for the first infection cycle. In the first infection cycle, 250 μl of virus were added to 4 ml of cells at a density of $0.5-1*10^6 cells/ml$. Then, two more cycle of amplification using an low ratio of infectious virus particles to cells (also called multiplicity of infection or MOI) were performed, in increasing volumes. The viral stock from the last cycle was used as the final infection stock (P3 stock). This stock was used to infect $2-5*10^9$ cells with an estimated MOI of 10. 72 hrs later, cells were harvested and tested for expression, whereas the supernatant was stored at 4°C.

6.2.2 *E. coli* expression and purification

Cytoplasmic expression

The construct carrying the gene of interest was transformed into BL21-Rosetta bacteria (Novagen). The bacteria were grown overnight at 37^oC in LB supplemented with antibiotics as described in **Table 6.1**. The culture was then diluted to an OD of 0.1 in LB supplemented with the same antibiotics and biotin. The bacteria were then grown at 37^oC and induced at an OD of 0.7 with 1mM IPTG. After induction, the culture was transferred to 30 ^{o}C for 3 hours.

Bacterial lysis Bacterial cells were typically lysed in a buffer containing: 1% Triton X-100(sigma), 1x complete EDTA-free protease inhibitor cocktail (Roche), 10mM $MgCl_2$ (Sigma), $100g/ml$ DnaseI (Sigma), $0.5mg/ml$ Lysozyme 0.5mg/ml (Sigma), complete to 1x PBS (or TBS), supplemented with 1mM PMSF or Benzamidine (Sigma).

Periplasmic expression

Growth and induction We used an optimized protocol for the expression of single chain fragments. The construct, pET 26b (Novagen) carrying anti-GFP, was transformed into BL21-

	Proteins	Vectors	Supplements
1	GST-BirA	pGEX	Ampicillin Chloramphenicol
2	HisTag-GFP-AviTag BirA	pET29HTb(Novagen) pCDF(Novagen)	Kanamycin Streptomycin Chloramphenicol biotin
3	MBP-GFP-PON-AviTag BirA	pMal-C2(NEB) pCDF(Novagen)	Ampicillin Streptomycin Chloramphenicol biotin
4	HisTag-TRXb-Pins-AviTag BirA	pET32b(Novagen) pCDF(Novagen)	Ampicillin Streptomycin Chloramphenicol biotin

Table 6.1: *The conditions used for the expression of different proteins. Supplement concentrations:* $100\mu g/ml$ *Ampicillin,* $34\mu g/ml$ *Chloramphenicol,* $50\mu g/ml$ *Kanamycin,*$50\mu g/ml$ *Streptomycin,* $50\mu M$ *biotin.*

Rosetta (Novagen). The bacteria were grown overnight at 37^oC in LB supplemented with kanamycin and chloramphenicol. The culture was then diluted to an OD of 0.1 into the following medium: 2XYT, 85mM NaCl, 50mM K_2HPO_4, 5mM $MgSO_4$, 0.5% Glucose and the antibiotics. The bacteria were then grown at 30^oC and induced at an OD of 0.7 with 0.5mM IPTG. After induction, the culture was transferred to 18^oC for 24 hours for expression and *in-vivo* biotinylation.

Periplasmic extraction The bacteria were pelleted at by centrifugating at 2000g for 15', at 4^oC, resuspended with PBS and pelleted again. The washed pellet was then resuspended in the following ice-cold hypertonic buffer: 25% Sucrose, 2mM EDTA, in 50mM Tris-HCL at a pH=7.4. The suspension was then put on a rotator for 30' at 4^oC. Then, the suspension was pelleted at 2000g for 15' and resuspended in ice-cold water supplemented with 1mM Gadolinium Chloride (in order to block the plasma membrane). The resulting suspension was placed on ice for 30' and briefly vortexed every 5'. The periplasmic proteins were collected from the supernatant by centrifugating at 2000g for 15' at 4^oC. The supernatant was supplemented with 1xEDTA-free protease inhibitor (Roche) in 1xPBS+250mM NaCl prior to affinity purification.

Affinity purification

In this project we have used several types of affinity purification systems: GST/glutathione for BirA, MBP/amylose and HisTag/nickel-NTA. In short, the buffered protein solution was incubated with the washed resin for 1-2 hours, washed extensively and eluted according to the conditions in **Table 6.2**.

Purification tag	Resin	Wash Buffer	Elution
HisTag	NiNTA agarose	PBS 0.25M NaCl 20mM Imidazole	Protease OR PBS+ 250mM Imidazole
MBP (MalE)	Amylose	20mM Tris-HCl, 200mM NaCl, 1mM EDTA,	Protease OR 20mM Wash Buffer+ 10mM maltose
GST	Glutathione- Sepharose	PBS	Protease OR 50mM Tris, pH 8.0+ 10mM reduced Glutathione

Table 6.2: *Purification conditions for different affinity tags. Protease elution is performed for protein constructs that contain specific recognition sites for proteases such as Thrombin or TEV.*

6.3 Biotinylation

In this project we biotinylated proteins using the BirA system [187, 188, 189]. It is based on the specific recognition of the peptide sequence GLNDIFEAQKIEWHE, called AviTag or AP-TAG, by the BirA enzyme (biotin ligase). The enzyme ligates a biotin molecule to a lysine residue within the sequence. This way, we can obtain monobiotinylated proteins. This method of biotinylation has many advantages over the alternative method of non-specific chemical biotinylation, since it should have less negative effects on protein functionality. Moreover, these biotinylated proteins are homogeneous and monovalent, which is very important (polyvalent biotinylation may cause QD aggregation by forming "protein bridges" between streptavidin QDs).

6.3.1 *In vitro* Biotinylation

By expressing and purifying BirA, we obtained a concentrated, high-grade enzyme. For the reaction, we used $5\mu g$ of enzyme per 10nmol of substrate (at $40\mu M$), for 1 hour at 30^0C. The final reaction buffer composition is: 50mM bicine buffer pH 8.3, 10 mM ATP, 10 mM MgOAc, $50\mu M$d-biotin.

6.3.2 *in vivo* Biotinylation

E. coli

In this work, *in vivo* biotinylation in *E. coli* was achieved by co-transforming the bacteria with pCDF-Duet-BirA that encodes for a tag-less BirA (induced with IPTG) and a resistance to streptomycin, together with the expression vector for the AviTag protein. Even though BirA is a native *E. coli* protein, we chose to over-express it, in order to increase the yield of biotinylation. Before inducing the expression, the medium was supplemented with $50\mu M$ of biotin.

Baculovirus/SF9

Biotinylation in baculovirus-infected SF9 cells was achieved by cloning both BirA (Tag-less) and the protein of interest (Miranda or Numb) into a dual expression vector (see **Figure A.3(b)**, in the **Appendix**), which eventually become a dual expression virus. This is important, since BirA is not expressed in normal SF9 cells. Before the infection, the medium was supplemented with $50\mu M$ of biotin.

6.3.3 Tests for biotinylation

Biotinylation was tested in two assays: using western blots, using mouse anti-biotin and HRP-anti-mouse and retardation assays, in which the biotinylated protein was incubated with streptavidin (typically 30' on ice) and loaded on a polyacrylamide gel (PAGE). The migration was compared to a control (without streptavidin). Finally, our method of choice was the migration assay, due to its simplicity and specificity. In this method, the binding of streptavidin is detected as a "shift" in migration, corresponding to the size of streptavidin, which is added to the protein size as a result of the binding.

Chapter 7

Single chain binding measurements

A quantitative characterization of ScFv binding was performed on a TIRFS/Rif[1] setup, in collaboration with the group of J. Pielher. The ScFv molecules were immobilized on a silica chip functionalized with nickel-loaded PEG2000-Tris-NTA [190]. The flow cell was rinsed, and GFPuv (from which the HisTag was cleaved) was injected into the system. In order to detect GFP using TIRFS, the sample was excited with a 488nm Argon laser, and emission was collected using a 532nm interference filter. The reflected light for the Rif (Reflectance interferometry) detection was collected at 800nm, thus minimizing any leak between the channels. During the experiment, the TIRFS and Rif signals were recorded at a frequency of 1Hz. The resulting data were analyzed using Biaevaluation (Biacore) and Origin (Microcal). A detailed description of the experimental system is given in [22].

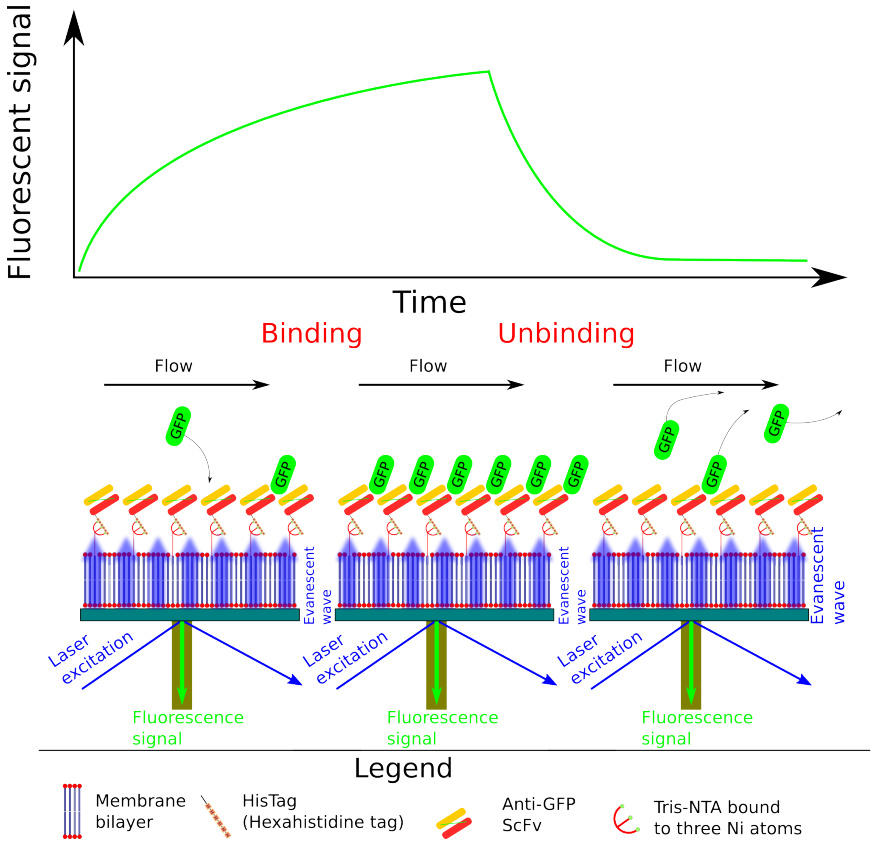

Figure 7.1: *Binding measurements for anti-GFP ScFv on a TIRFS system.*

[1]TIRFS-Total internal reflection fluorescence spectroscopy, Rif-Reflectance interference.

Chapter 7

Chapter 8

QD coupling and characterization

In single molecule experiments, the coupling and characterization of QD-protein complexes are very important. In this chapter we present the methods used for coupling (except for the trivial incubation of QD-SAV with biotinylated proteins) and characterization of such complexes. We also present two methods for coupling and characterization developed during this project and are included in this work as a proof-of-principle.

8.1 Coupling of QDs to proteins

8.1.1 Coupling of rabbit anti-GFP antibodies to commercial anti-rabbit QDs

These were the probes used for intracellular GFP targeting experiments done in this project. We mixed $1\mu l$ of anti-rabbit IgG QDs (QD-IgG) at $1\mu M$ with 0.5 $1\mu l$ of anti-GFP at $1mg/ml$, and $7.5\mu l$ of PBS. We incubated the mixture for 30' with agitation. Then, we added BSA or casein to 1% and continued to agitate for 15 min. These QDs are polyvalent: the nominal ratio of anti-GFP/QD is between 5/1 and 6/1 and therefore, the resulting QDs should have more than one IgG conjugated to them. This method has been used before, for tracking membrane receptors [191].

8.1.2 Coupling of NH_2-PEG QDs to proteins using the crosslinker BS_3

This method was used for the coupling of ScFv to NH_2-PEG QDs (Invitrogen). BS_3 (Bis[sulfosuccinimidyl] suberate) is a homobifunctional crosslinker, composed of two NHS-ester groups joined together by a short alkane chain (see **Figure 8.1**). The NHS esters are readily attacked by nucleophilic amine groups that replace the NHS, which is a good leaving group.

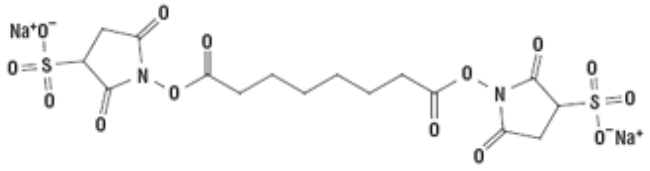

Figure 8.1: *The skeletal formula of BS_3 (Bis[sulfosuccinimidyl] suberate)*

8.2 Gel electrophoresis

Gel electrophoresis, and especially agarose gel electrophoresis [192], has been used to characterize nanoparticles. This method has been adapted from molecular biology and biochemistry, where it is used to characterize proteins and nucleic acids [193]. The basic models describe the mobility of a particle, in a gel, under an electric field, as a balance between charge and size [194, 195, 196, 197, 198] (more elaborate models include attractive/repulsive interactions with the gel medium [199]). Except for the QD::ScFv gels (10 mM borate at pH=8.0, 1% agarose), all gels were performed using 0.5xTBE and 0.5% agarose. The typical running voltage was 120-150V. As can be seen in **Figure 8.2**, the overall mobility of the QD-protein complex is determined by an overall balance between size and charge, depending on the specific QD and protein. When attempting to resolve QD-protein complexes of different protein/QD on a gel, what is important is the significance of the effect of the protein on the migration of the complex. This effect can be significant when there is a large difference in migration between the protein and the QD: for example, when the QDs are very "fast", but the protein is large and with a charge that balances out that of the QD, each protein molecule added will significantly reduce the migration of the QD-protein complex. In such a case, we would expect to see well-resolved, discrete bands on the gel, corresponding to QDs with different numbers of proteins on the surface, which migrate at different speeds. By analysing the gel, we can assign each band to a different protein/QD ratio (knowing the migration of free QDs from a control, and the fact that the more proteins are bound, the slower the migration).

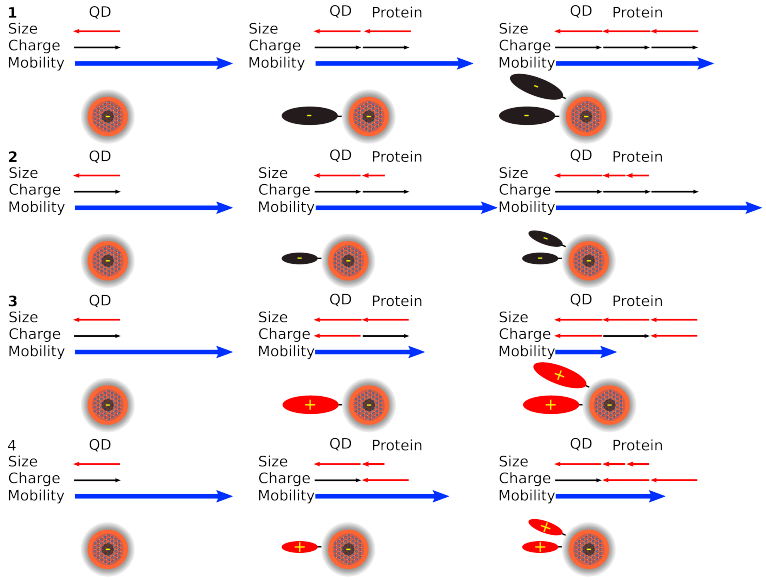

(a)

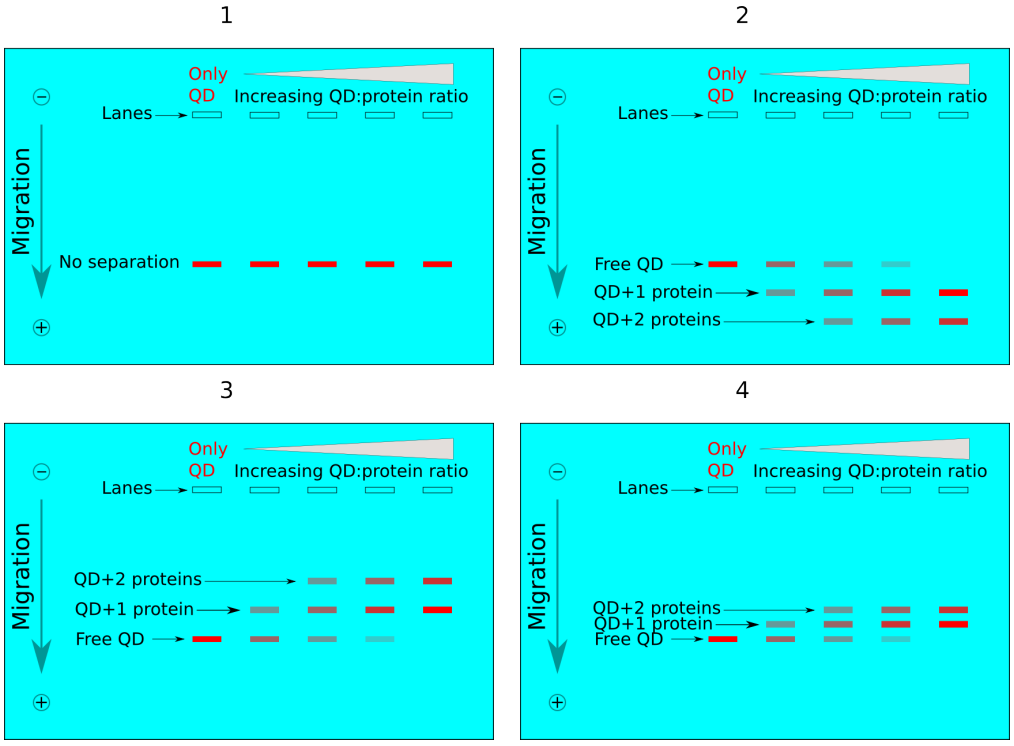

(b)

Figure 8.2: *Gel electrophoresis, for the separation of QDs with different valences.* ***Figure 8.2(a)*** *shows the effect of a QD-protein complex's overall mobility on the resolution of an agarose gel, using a few extreme examples. The contributions to mobility are represented by arrows: a red arrow for retardation and a black arrow for acceleration. The overall mobility of the complex is represented by a blue arrow. In this case, the non-conjugated QD is negative and therefore migrates from - to +, opposite to the electric field lines.* ***1****, When the effect of charge and size more or less cancel out. Such a protein has no significant effect on QD mobility.* ***2****: When the negative charge of the protein is slightly more significant than its retardation due to its size. Such a protein will increase the overall mobility of the complex.* ***3****: A large positive protein. Such a protein will have a strong retardation due to size and charge.* ***4****: A protein with a positive charge effect that is slightly more significant than its retardation due to size.* ***Figure 8.2(b)*** *shows the gel resolution for the cases described above.*

8.3 Electro-transfer(western blotting)

Description of the method

In many cases, there is a need to characterize QD-protein complexes. As mentioned before, one of the methods is gel electrophoresis, which allows an indirect estimation of the protein/QD ratio using electrophoretic mobility. Direct estimation of the protein/QD ratio, for a given band in a gel, or for an average sample containing QD-complexes with different QD-protein ratios is difficult: methods based on absorbance are not practical, since the molar extinction coefficient of QDs is at least two orders of magnitude higher than that of proteins, which makes protein quantification difficult, when the number of QDs and proteins is comparable. Moreover, in many cases the QDs contain proteins even before the conjugation (such as the streptavidin in the case of QD-SAV, or the surface bound peptides in the case of peptide-coated QDs), for which the protein/QD ratio is also fluctuating and adds an additional difficulty. This method works around this problem by using fluorescence to quantify the QDs, and chemiluminescence to quantify the proteins. The two measurements are completely independent: the QDs we use emit at 655nm when excited, while the chemiluminescence emits at 425nm without any excitation.

Conjugation reactions between QDs and proteins always result in a mixture of QD-protein complexes of different stoichiometric ratios, and free proteins. The electrotransfer method also uses the ability of the agarose gel to resolve the QDs from the free proteins, and allow a measurement of QD-protein complexes without the background of free proteins. When possible, the QD-protein complex mixtures can also be resolved into discrete bands on an agarose gel, allowing separate measurements for each band.

Electrotransfer has been traditionally used for the characterization of proteins [200] (usually after SDS-PAGE). We have developed an analogous method for the characterization of QD-protein complexes based on electro-transfer. The method allows one to use a "multiplexed" analysis combining fluorescence and chemiluminescence, in order to characterize and possibly quantify the results of the coupling. After running an agarose gel, the samples are transferred in a direction perpendicular to the gel migration into a membrane, which is then treated with primary and secondary, HRP-conjugated antibodies (see **Figure 8.4(a)**). The result is then revealed using an HRP substrate that allows a luminescent detection (no photo-excitation required) and thus allows to detect and quantify the protein and the QD using different and independent methods.

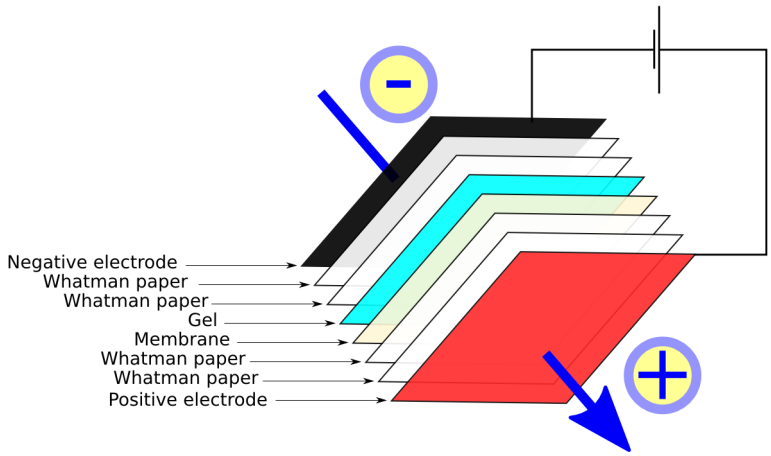

(a) *A scheme of the electrotransfer apparatus. The electric field drives the negatively charged QDs from the gel onto the membrane.*

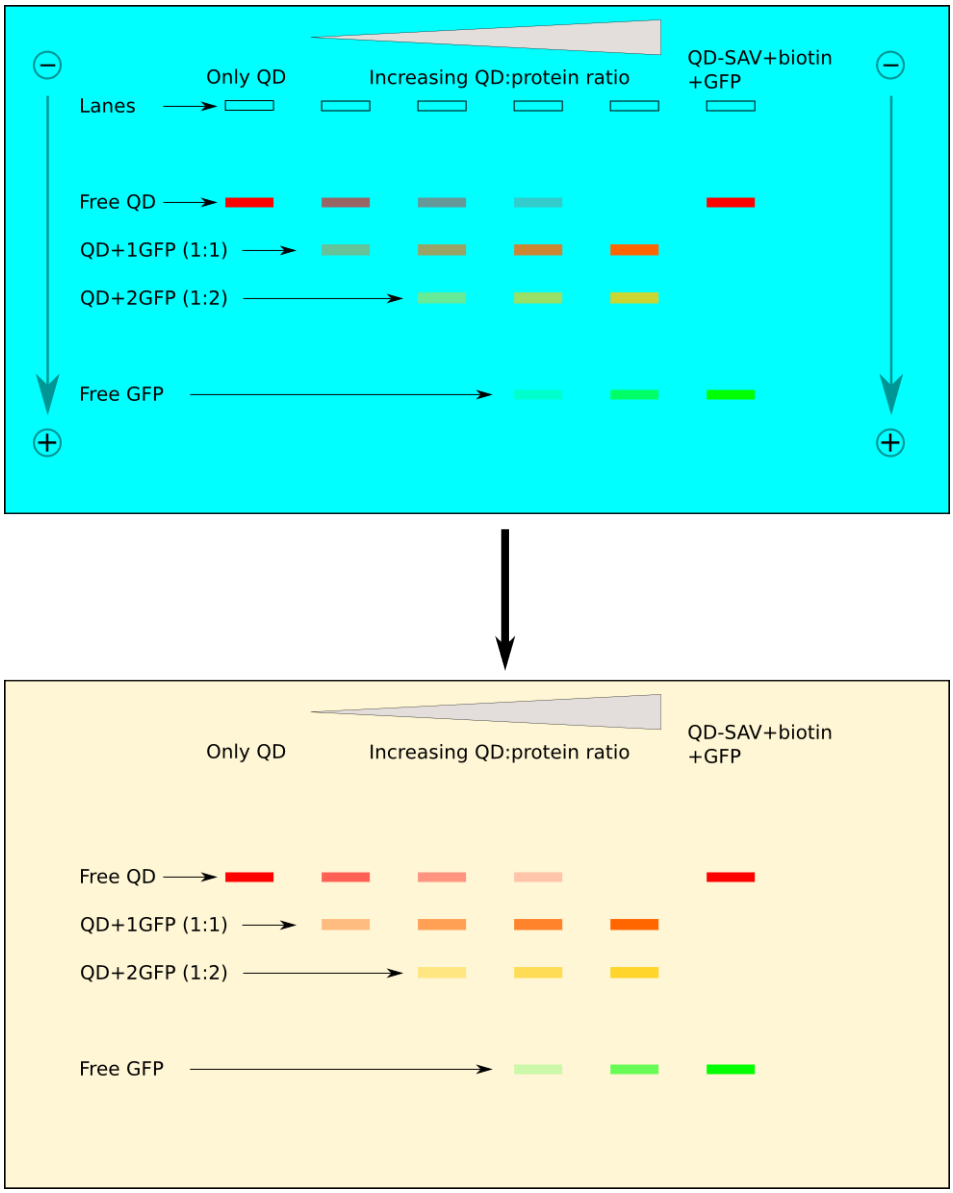

(b) *The result of electro-transfer from a gel to a membrane. QD are shown in red, and GFP in green. This scheme describes a scenario in which the conjugated protein (GFP in this case)* ***increases*** *the QD mobility. It also describes ideal separation into bands.*

Figure 8.3: *A scheme of the electrotransfer method for QDs*

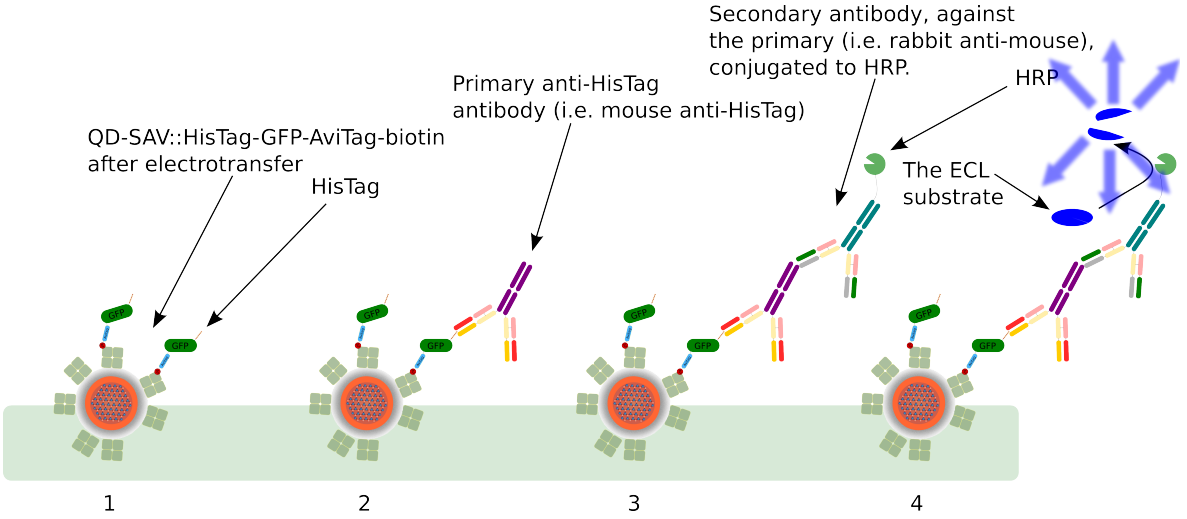

(a) *After the QDs are transferred onto the nitrocellulose membrane, they are incubated with a specific primary antibody against the protein, followed by a secondary antibody conjugated to the enzyme HRP, and targeted against the primary one. Then, Using the substrate ECL, HRP can produce a chemiluminescent reaction. For proteins, this is called a "western blot".)*

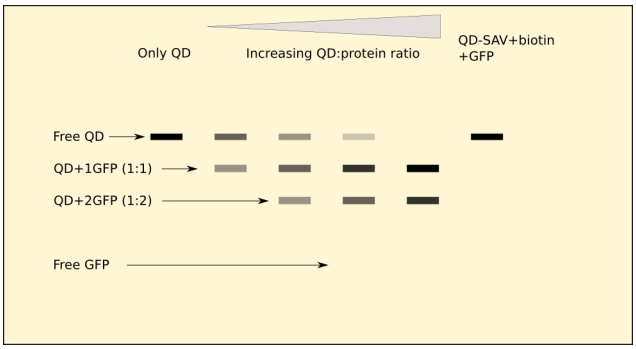

(b) *An observation of the membrane using QD fluorescence (green excitation/red emission).*

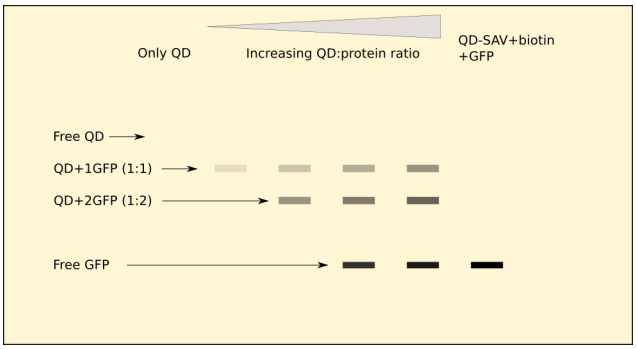

(c) *An observation of the membrane, using HRP-based chemiluminescence. In the case of GFP, looking at the membrane in the GFP channel (blue excitation/green emission) would yield a similar result.*

Figure 8.4: *A scheme, showing the information that can be extracted from electrotransfer of QDs. By separating the quantification methods of QDs and proteins, it should be possible to estimate the protein/QD ratio for each gel band separately, and also to titrate the QDs with protein, in order to determine the effective number of binding sites.*

Preparation and usage

As a first step when preparing the agarose gel, in order to obtain reproducibility, the distance between the bottom of the wells and the bottom of the gel, which determined the distance the QDs need to migrate vertically in order to reach the membrane, has to be adjusted. This is done by placing two 1-mm thick microscope glass slides (Menzel-glaser) at the bottom of the gel support and adjusting the level of the comb (CBS) until it touches the slides. The thickness of the gel determines the distance between the electrodes of the transfer apparatus "sandwich" (see **Figure 8.3(a)**) and therefore has to be controlled too. Therefore, we used 50 ml of agarose gel in mini-agarose gel apparatus (CBS scientific). The sample is loaded into a 0.5xTBE, 0.5% agarose gel, and allowed to migrate. During that time, the membrane and papers of the "transfer" sandwich are soaked with 0.5X TBE. Then, the transfer is performed at 4^0C for one hour at 14V using a pre-cooled apparatus. After the transfer is completed (this is validated by opening the "sandwich" and shining UV on the membrane), the membrane is passivated with 5% BSA in PBS+0.5% Tween (PBT) for one hour, washed three times for 5' with PBT and incubated with the primary antibody (Mouse anti-HisTag, in our case) at the dilution recommended by the provider (can be 1:1000-1:10000) for one hour. Then, the membrane is washed again (three times for 5' with PBT) and incubated with the secondary antibody (HRP-anti-mouse, in our case) for one hour and then washed again (three times for 5' with PBT, and then 5' with PBS). After being washed, the membrane is incubated with ECL substrate (Pins) for 1', wrapped in saran film and either observed in an electronic imager (LAS-3000, Fujifilm) or using hyperfilm (Amersham).

8.4 Coupling on a solid support

As mentioned before, "free" QDs are a menace to SQDT experiments and need to be removed from the sample. In order to cope with this problem, a simple system was developed, based on performing the coupling by anchoring the QDs to a surface. In short, this is done by using an affinity resin (NiNTA agarose, in our case), that first binds the protein using the purification tag (HisTag), and an incubation with QDs that bind the coupling tag (biotin).

On a small scale, we used $25\mu l$ of NiNTA resin (His-select, Sigma) per assay, in an eppendorf tube. We first washed the resin ($50\mu l$ of 50% slurry per assay) extensively in PBS. Then, we added excess HisTag-GFP-AviTag-biotin (1ul of $55\mu M$) for one hour of incubation on a shaker at 4^0C. Then, the resin was washed extensively in PBS using 5 cycles of of 2' centrifugation at 2500g, removal of supernatant and addition of cold PBS, in order to remove unbound GFP. Even though in the case of HisTag-GFP-AviTag-biotin, the binding is very efficient, this washing step is very important, since free biotinylated GFP can compete with resin-bound GFP on the QD-SAV binding, and seriously reduce QD binding. Then, $1\mu l$ of $1\mu M$QD-SAV (Invitrogen) are added to the resin, for a 2-hour incubation on a shaker at 4^oC. Then, the resin is washed as before (in order to remove free QDs) and incubated with 1ml of $5\mu M$ biotin, in order to saturate all available streptavidin sites. Lastly, the QD-GFP complexes are eluted with 300mM Imidazole+$1\mu M$ biotin at a pH of 7.4. The protocol could be adapted to other purification systems, such as GST or MBP, by using the corresponding resin and elution conditions, as described in 6.2.

This is a robust coupling method that is indifferent to reduced biotinylation efficiencies and partial protein degradation, as it is based on the two-tag design. Protein fragments that only contain the purification tag (such as HisTag or GST) will bind to the resin but not to the QDs, and fragments that only contain the coupling tag (biotin), will not bind to the resin and will be washed away. The steps of the protocol are described in **Figure 8.5**.

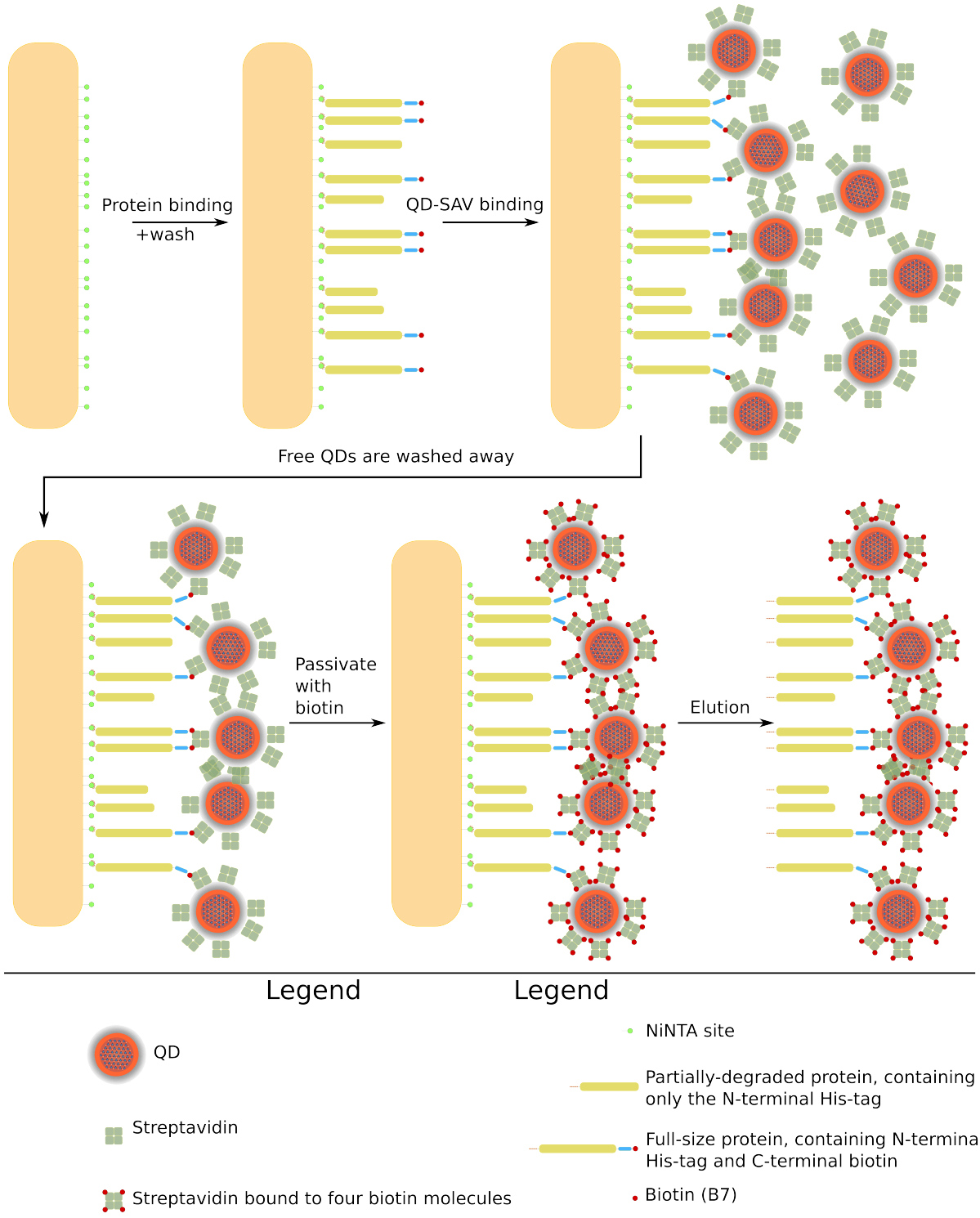

Figure 8.5: *A scheme showing a solid-support coupling of QDs to a protein, in the case of a protein with N-terminal HisTag and C-terminal Avitag-biotin.*

Chapter 9

QD internalization

9.1 Micro-injection

QDs were injected into HeLa and neuroblast cells, using an eppendorf femtojet pressure unit and an automated InjectMan NI2 micromanipulator. The injection was done using a constant flow (P_c=20hPa) at a low pressure. Normal injection was performed using commercial femtotips (eppendorf). The tips were passivated beforehand with 3% BSA. Neuroblast SLAM injection was performed as described in [201].

9.2 Pinocytic influx

This method is based on the protocol published in [21] and originally used for proteins. The cells are incubated in a hypertonic buffer (the cell medium complemented with 0.5M sucrose and 10% PEG 1000) that contains the molecules we would like to internalize. As a results, the cells start to lose volume (due to the osmotic pressure difference) and their membranes close to form pinosomes, which can be regarded as a way to internalize the solute in order to reduce the osmotic pressure difference, or a way to get rid of excess membrane. The pinosomes, which contain the hypertonic medium stay in the cytoplasm and do not fuse with lysosomes, possibly thanks to the PEG and sucrose in the medium [21]. Then, the cells are quickly transferred into a hypotonic environment (the normal medium, diluted with water). Under these conditions, the cells allow a lot of water to enter the cytoplasm in order to regulate the difference in osmotic pressure. This reduces the osmotic pressure in the cytoplasm, causing the pinosome to burst and release their content inside the cell.

We used a commercial product by Invitrogen to perform these experiments. In order to improve the efficiency of pinosome bursting, we increased the osmotic shock, by using a slightly more diluted hypotonic medium (43% water instead of 40%). For mammalian cells, we used the protocol supplied by the manufacturer: 10' incubation in the hypertonic medium, followed by a 2' incubation in the hypotonic medium. In the case of neuroblasts, the uptake was reduced. Therefore, we increased the incubation time to 15 min.

The main concern with this method is when pinosomes do not burst, and the QDs remain trapped inside them. These QDs, obviously, cannot interact with the cytoplasmic environment. In the course of this project, we performed several tests that confirm that the in the conditions we use, the QDs are indeed liberated from the pinosomes and are free to explore the cytoplasm, in search of their targets. One test was simultaneous two-color movies: we internalized a mixture of 655nm ("red") and 605nm ("orange") QDs into S2R+ cells, using pinocytic influx and recorded both fluorescence channels simultaneously in order to show that the movement is independent (see **Results**). This test takes advantage of the narrow emission bands and broad excitation spectra of QDs, which easily allow two-color imaging with almost no crosstalk between the fluorescence channels (both types of QDs were excited using green light at 525nm).

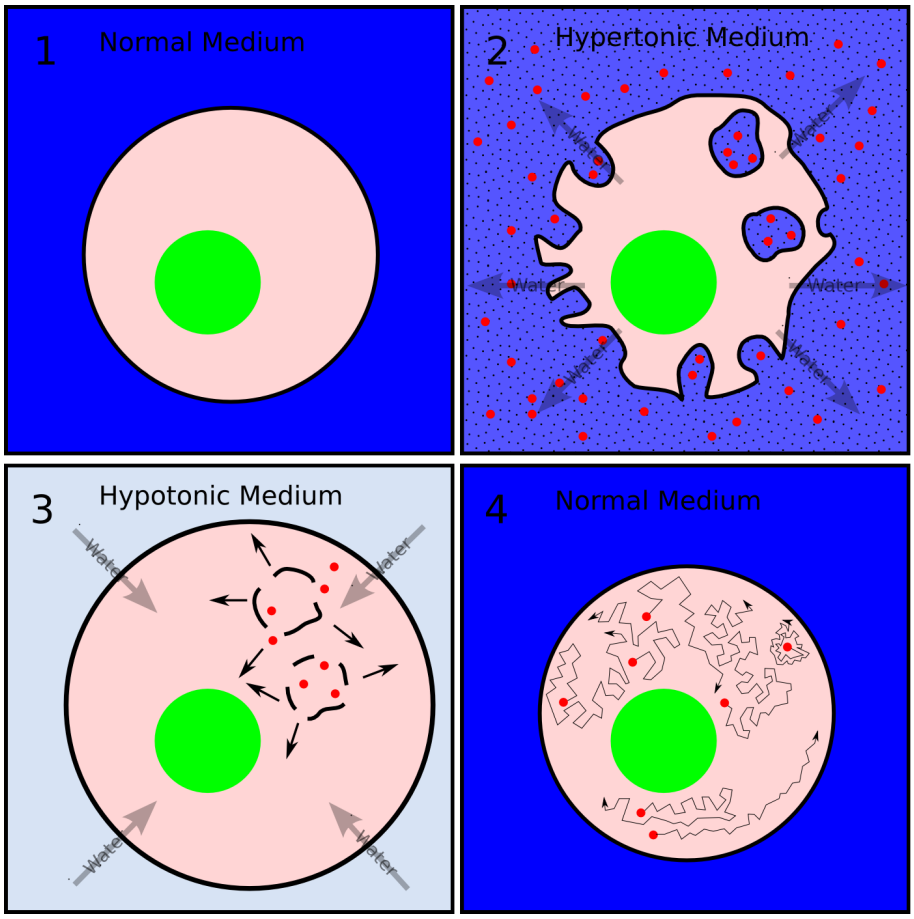

Figure 9.1: *QD internalization based on the pinocytic influx method:* ***1.****, the cell is cultured in normal medium;* ***2.****, The cell is incubated in a hypertonic medium containing the QDs. These conditions induce pinocytosis, and pinosomes containing the QD in a hypertonic medium, enter the cell;* ***3.****, Then, the cell is transferred to a hypotonic medium, causing an osmotic shock, which induces the bursting of the pinosomes and releases the QDs into the cytoplasm;* ***4.****, The cell is then transferred back to its normal medium to recuperate before observation.*

Another test we performed was simply a targeting test: probes that can bind to their target are, obviously, free to diffuse in the cytoplasm and react with their target molecule. This was first done using the protein nucleoplasmin [202], a nuclear chaperone, that participates in chromosome remodeling [203, 204]. This protein has a nuclear localization sequence, which targets it into the nucleus [205]. If such a protein, once internalized, can reach the nucleus, not only that it was liberated from the pinosomes, but also, it means that at least for some proteins, the conditions inside the pinosomes do not significantly affect the functionality.

Chapter 10

Analysis of movies

10.1 Trajectory analysis

Briefly, the acquired movies are passed through an analysis pipeline:

1. Detection of spots and reconnection, gives reconnected trajectories.
2. The trajectories are analyzed using an MSD analysis program we implemented in the Python [206, 207] programming language.

10.1.1 Detection and reconnection of trajectories

This is performed using the MTT software, developed by Sergé *et al.* [208], implemented on MATLAB (Mathworks). It consists of several steps:

Detection and reconnection of trajectories using the MTT algorithm

Preliminary peak detection Integrated intensities of individual fluorophores result in a PSF (point spread function), generated by the imaging system. The PSF is modeled as a 2D Gaussian, and the intensity at pixel i,j can be written as:

$$X_{i,j} = IG_{i,j}(i_0, j_0, r_0) + m + N_{i,j}(\sigma^2) \tag{10.1}$$

where I is the intensity of the particle, G is a bi-dimensional Gaussian modeling the PSF centered at (i_0, j_0) with a radius r_0, m is the mean background intensity and N models the background noise at (i_0, j_0) as Gaussian noise with a standard deviation of σ. The integrated particle intensity I is a random variable (due to particle-particle variability, blinking, bleaching, and noise from various sources). The peak detection is performed as a hypothesis test: in the case of H_1, the particle is present at $X_{i,j}$ and in the case of H_0 there is no particle ($X_{i,j} = m+N_{i,j}(\sigma^2)$). The peak search is performed using a sliding 2D pixel window (should depend on the imaging system's pixel size). This binary step only provides a "yes or no" answer to the question of whether there is a peak at a given coordinate i,j.

Estimation After a peak is detected, it is fit with a multi-parametric 2D Gaussian function combined with filtering (to remove outliers), which gives the sub pixel localization of the centroid a corrected intensity and the spread of the signal.

Deflation

In cases of high particle density in the sample, peaks of low intensity may be masked by neighbouring, partially-overlapping strong peaks. In order to resolve such peaks, the software

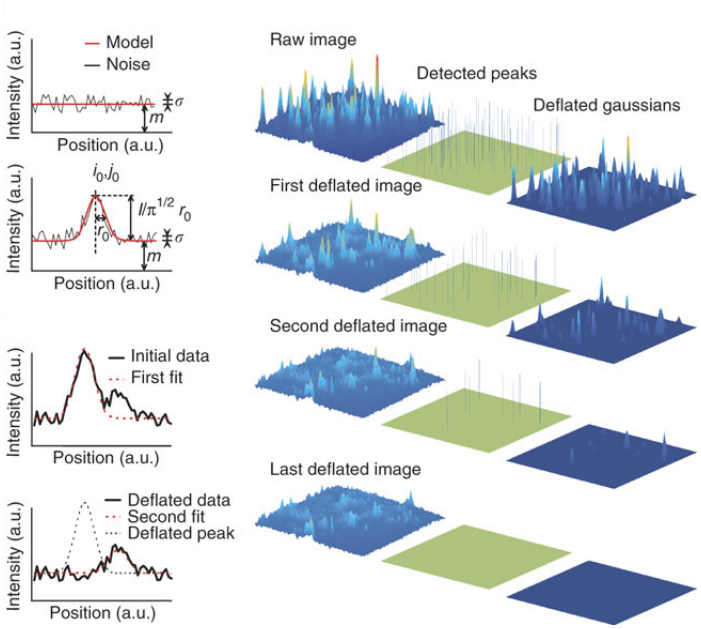

Chapter 10

Figure 10.1: *Detection, estimation and deflation in the MTT algorithm: the graphs on the left demonstrate the deflation. From top to bottom: Noise, an estimated peak, two overlapping peaks and deflation. The surfaces on the right show detection cycles, using a hypotheses test.*

generates a new image, with the initially detected peaks removed (see equation 10.2).

$$X_{out} = X_{in} - \sum_{P=1}^{P_{frame}} I_P G_{i,j}(i_P, j_P, r_P) \tag{10.2}$$

This is called a "deflated" image of the previously detected peaks, where P is the particle (or peak) index. We then go back to the preliminary detection step and iterate in a loop, in order to detect more and more peaks, until all peaks are detected.

Trajectory reconnection The detected peaks now have to be associated with trajectories (either existing ones or new). For a given trajectory, a reconnection domain is defined in the current frame, based on a 2D Gaussian probability law derived, from a maximum diffusion coefficient D_{max} defined by the user. By restricting this domain to a disc of radius r_{cutoff}, we define the statistical significance of this reconnection step (*e.g.* $r_{cutoff} = 3\sigma$ for 99%). In the case of blinking, where the last frame in the trajectory to be reconnected is a "dark" particle, which was not detected within the disk, a larger disk is defined (corresponding to the diffusion with D_{max} over two or more time intervals). In cases where the reconnection domains of several trajectories overlap, the software statistically decides how to reconnect the trajectories to the particles in the new image: all possible combinations within the reconnection domains are compared by examining their reconnection probabilities. In cases where there are more trajectories than particles in a given frame k ($T_k > P_k$), the software also has to decide which trajectory blinked, and in cases where $T_k < P_k$, it has to decide which of the detected particle starts a new trajectory (see **Figure 10.2**). Reconnection probabilities are a products of several terms, based on individual particle descriptors (local diffusion, intensity law, blinking probability), typically calculated from the last 5 frames. This allows us to "identify" the particles (with a given statistical significance) and associate a set of particles and a set of trajectories, with the best overall probability.

Post reconnection detection The detection of peaks also benefits from the existing trajectory information: "orphaned peaks" - peaks that were initially detected but not attributed to any trajectory, are re-tested with a more stringent test, in order to remove false positives that would result in artifactual trajectories, which could later overlap and interfere with real ones, or even just increase computational time.

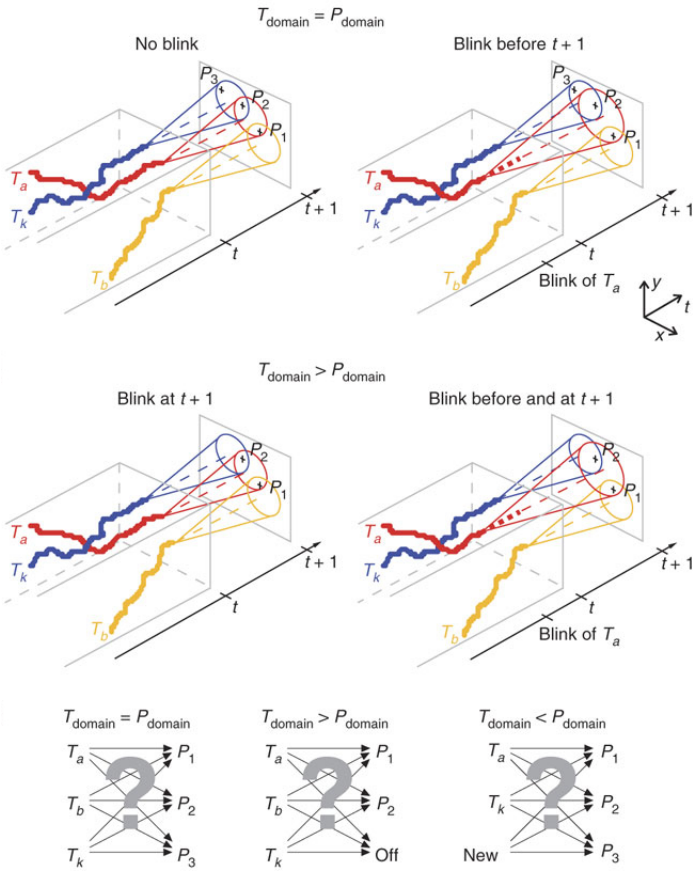

Figure 10.2: *Reconnection in the MTT algorithm for various scenarios, where T_k is the number of active trajectories and P_k is the number of detected particles in the new frame.*

An alternative method, for cases of weak signal to noise

Some of the movies, suffered from a reduced signal to noise ratio due to various factors such as increased cell autofluorescence and relatively dim QDs (such as EO6D-coated QDs). In these cases, we tracked individual QDs using an alternative method, which was found to work better.

1. The movies were treated with the Laplacian of Gaussian filter (LoG), also implemented in ImageJ, to facilitate spot detection. This is a fast algorithm that combines edge detection (Laplacian) and noise removal (Gaussian) in a single kernel.

2. We used the ImageJ plugin SpotTracker2D, to track individual QDs.

Both steps are described in the literature [209]. This main limitation of this algorithm, though, is that it is limited to tracking one particle at a time, which could be very time consuming.

The localization accuracy of QDs The resolution of an optical system is determined by the diffusion limit. It dictates the resolution of an optical system (the distance between two objects below which they can no longer be resolved, and appear as a single density). The diffraction limit is usually estimated as $\approx \lambda/2*NA$, where NA is the numerical aperture, which is typically 1.3-1.4, and λ is the emission wavelength, which in our case is 605nm or 655nm. Therefore, in our case, the diffraction limit is ∼225nm. However, a fluorescent object can be localized with an accuracy of one-order of magnitude better and even more, provided that enough photon are emitted from it. As described before, the particles are localized by fitting the fluorescent spots with a 2D-Gaussian function. The centroid of the Gaussian can be determined with subpixel accuracy [210], with an uncertainty that comes from shot noise (a Poissonian noise arising from the randomness of photon emission) and background noise, which arises from photons that did not originate in the particle. For 1D, we have:

$$\langle(\Delta X)^2\rangle = \frac{s^2 + a^2/12}{N} + \frac{8\pi s^4 b^2}{a^2 N^2} \tag{10.3}$$

The first fraction in this expression is the localization uncertainty arising from shot-noise, while the second one is the uncertainty arising from background noise. In the expression above, N is the number of photons collected, s is the standard deviation of the system's point spread function (PSF), $a^2/12$ is an error arising from pixelation (due to the "binning" of the spot into bins of finite size) and b is a constant background noise in the observed region. In cases that are dominated by shot noise (when N is large), such as the case of QDs, the uncertainty in the localization for one dimension can be reduced to:

$$\langle(\Delta X)^2\rangle \approx \frac{s^2}{N} \tag{10.4}$$

which reflects the trade-off between pixel size, integration time and localization accuracy.

Practical trajectory analysis

With a list of numbers, representing the coordinates, at hand, we need to describe the regime for the movement of the particle by calculating the MSD and fitting it with a model for Brownian motion (or any other type of motion), in order to obtain the relevant parameters, such as the diffusion coefficient. Therefore, we have implemented an automated analysis of the trajectories in the PYTHON [211, 206, 207] programming language. Since we would like to analyze every trajectory separately, we need to average the square displacement for a given correlation time τ over a single trajectory. In such a case, two main problems arise: first, such an average introduces a bias by averaging over dependent instances (the correlation times overlap) and second, the statistical error becomes very large for long correlation times, since there are less and less "pairs" to average over. Another, more practical problem arises when the reconnected trajectory has some "missing points" (either due to the blinking phenomenon of quantum dots, or simply because the QD went out of focus). These missing points should be excluded from the sum calculation by using the expression:

$$\rho_{2D}(n*\Delta T) = \rho_x(n*\Delta T) + \rho_y(n*\Delta T) = \frac{\sum_{i=0}^{N-n} (x_{i+n} - x_i)^2 + (y_{i+n} - y_i)^2}{N - n - d} \tag{10.5}$$

1.4 where d is the number of pairs that have at least one "dark" point (undetected, or "dark" QD that are not included in the calculation of MSD) . The result is an array of MSD vs. t (or $\rho(\tau)$), which is fitted to the desired model (given for 2D with the errors as calculated in [127]) (see **Figure 10.4**).

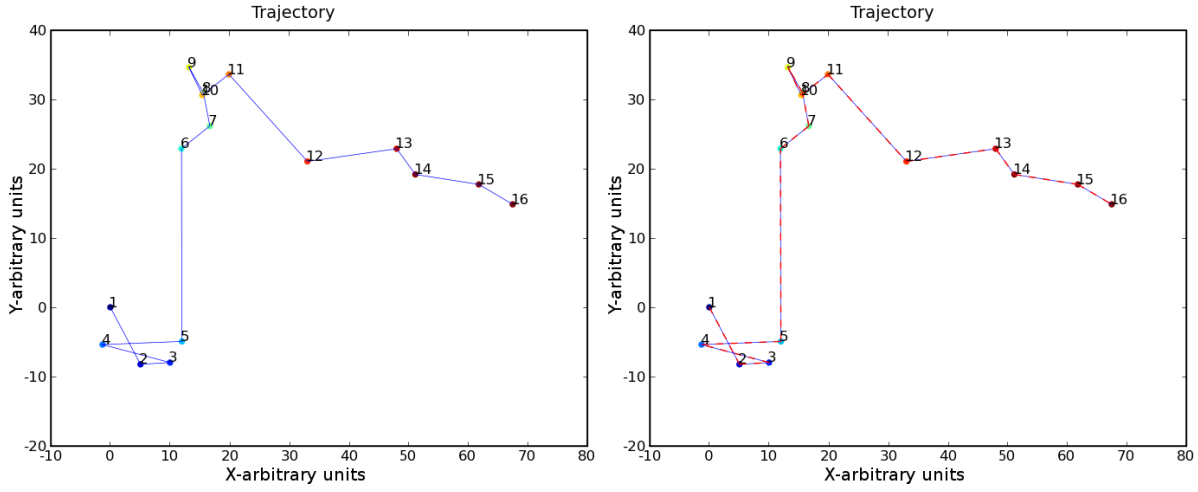

(a) *The trajectory*

(b) $\tau = 1 * \Delta t$

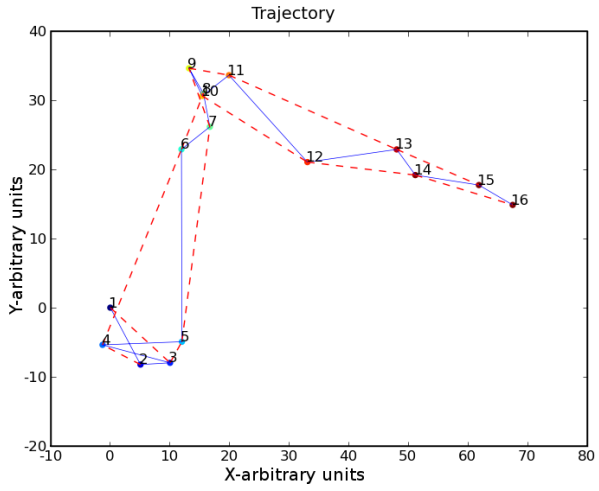

(c) $\tau = 2 * \Delta t$

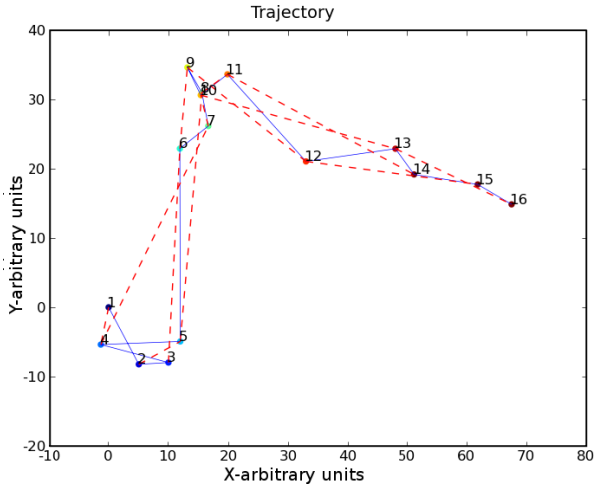

(d) $\tau = 3 * \Delta t$

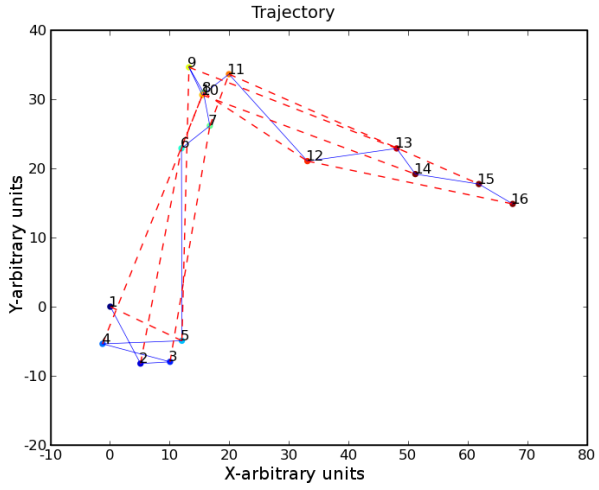

(e) $\tau = 4 * \Delta t$

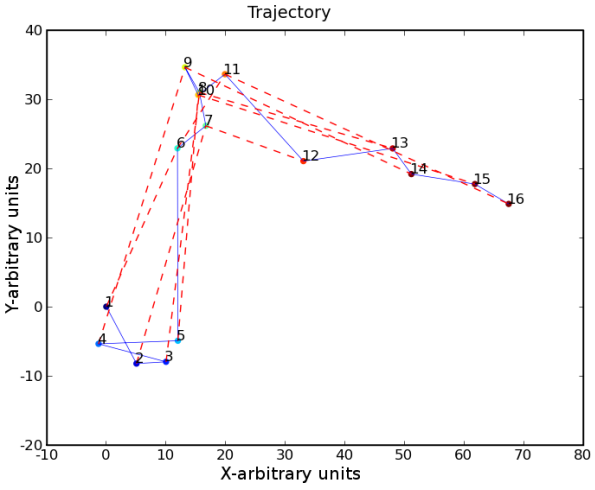

(f) $\tau = 5 * \Delta t$

Figure 10.3: *An example for MSD sampling for a 16-point 2D trajectory. The points in the XY plane are numbered and colored according to the order in the trajectory. For the calculation of the MSD, pairs that are used to calculate the squared displacement for a given time interval are connected by a broken red line.*

10.2 Transport regimes

Even though this project concentrates on free diffusion, we will also give a short description of several other transport regimes:

Brownian motion

This type of motion is pure diffusion. It should be expected for a particle diffusing in a medium without boundaries and without interactions, which is of course an idealized scenario. We can consider the particle as moving in a medium without boundaries if the observation time is smaller than the characteristic time representing the boundaries: $T_{obs} < L^2/D$ (where L is the characteristic dimension of the boundaries and D is the diffusion coefficient). For example, with $D \sim 0.2\mu m^2/sec$ and $L \sim 10\mu$, T_{obs} is almost 10 min, much longer than the observation time used in our experiments. By simply combining equations 1.2 and 1.3 and integrating, we obtain $\rho(\tau) = 4D\tau$. In this case the estimation error for the nth point in the MSD is $4Dn\Delta T\sqrt{\frac{2n^2+1}{3n(N-n+1)}}$, where ΔT is the time interval used in the calculation (typically the time between movie frames).

Directed motion

A motion that combines transport with a velocity v and some diffusion component [212], which is described by D. This model can describe, for example, molecular motors moving inside the cell [213, 105]. By simply combining equations 1.2 and 1.4 and integrating, we obtain $\rho(\tau) = 4D\tau + v^2\tau^2$. In this case, the MSD error for the diffusion coefficient D is the same as for Brownian motion. Since the velocity is calculated from the curvature of the MSD plot, its error is less straightforward an can be estimated as $< 2[\frac{D^2}{n(N-n)(\Delta T)^2}]^{\frac{1}{4}}$.

Confined Brownian motion

In this case, the particle undergoes Brownian diffusion in an area of characteristic dimension L with reflecting boundaries, giving $\rho(\tau) = \frac{L^2}{3}(1 - \exp(-\frac{12D\tau}{L^2}))$. This model can be used to describe the motion of certain membrane proteins, in domains that are defined by the cytoskeleton. The error for the nth point in the MSD is in this case $\frac{L^6}{30ND_{micro}n\Delta T}$.

Anomalous diffusion

In this case $\rho(\tau) = 4D\tau^\alpha$ with $\alpha < 1$, and can also be considered as a motion with a time-dependant diffusion coefficient. As described in [214], this type of motion results from a hierarchy of traps in different energy levels, where the number of traps for a given level is higher, the shorter the escape time (higher energy). When the distribution of traps is finite, we can observe a transition time, in which the anomalous diffusion, characterized by a power law, undergoes a transition into Brownian motion with a lower constant D. In biological systems, this type of motion can arise from non-specific binding [214] and molecular crowding [215]. The MSD error is calculated using the same expression as for the Brownian motion, but with the a time-dependent D.

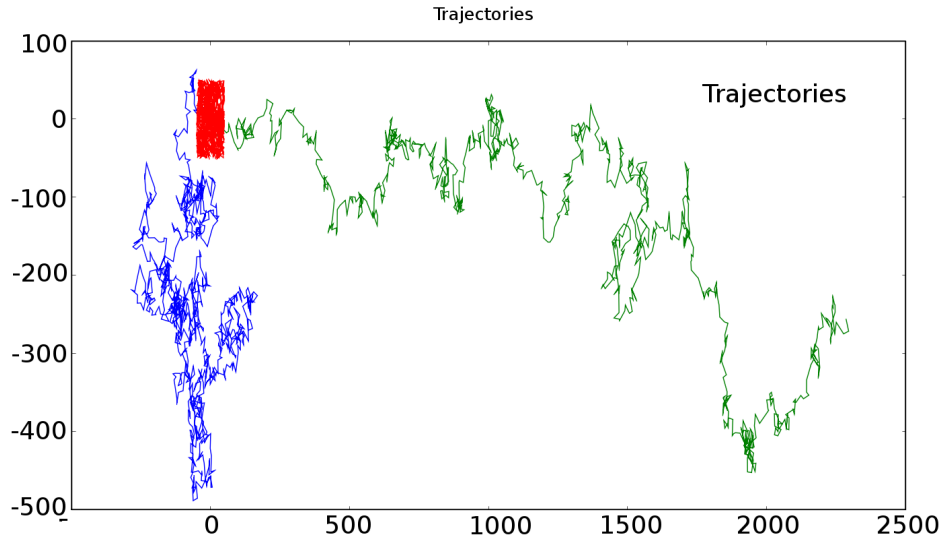

(a) *Trajectories*

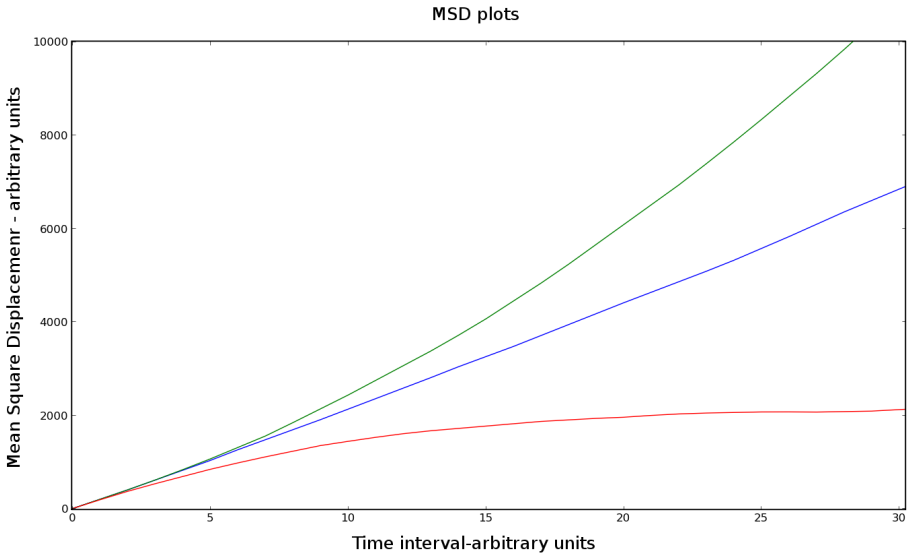

(b) *MSD plots*

Figure 10.4: *Examples for trajectories and their corresponding MSD plots: in blue - Brownian motion, in green - Brownian + drift (directed motion) and in red, confined Brownian motion in a rectangular region.*

Fitting experimental data

For every given trajectory, the MSD curve should be fitted with one of the models described above. Given the behavior of the MSD error, which grows very quickly with the correlation time τ, we do not want to use points with a very high τ. Even within the points that are used for the calculation, there is a difference in the level of confidence, due to the increasing error. Therefore, the fitting is performed by a weighted least-squares fitting, using the reciprocal of the error as weights. In addition, we never use the first point ($\tau = 0$) for fitting, since we never force the fitted curve to pass through the origin. The reason is, that when calculating the MSD, we always have some finite localization error ε, which is averaged in the calculation (given here for 1D):

$$\rho_x(n * \Delta T)_{Experimental} = \frac{\sum_{i=0}^{N-n} ((x_{i+n} + \varepsilon_{i+n}) - (x_i + \varepsilon_i))^2}{N - n} = \rho_x(n * \Delta T)_{Theoretical} + Err(n) \tag{10.6}$$

where the positive Err, which can be considered constant at small τ, is an intercept that depends on the localization error.

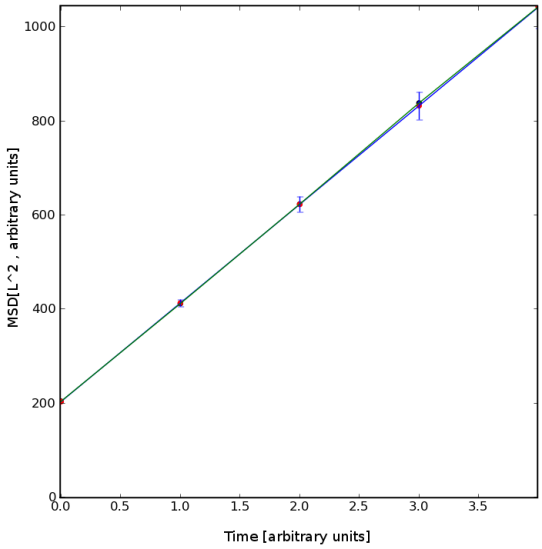

Figure 10.5: *Usually, the first four points of the MSD plot are the ones being fit, excluding t=0 [216].*

10.3 Colocalization analysis

10.3.1 Colocalization of dye-labeled anti-GFP ScFv and CFP

The quantification of colocalization between the dye-labeled ScFv and the CFP-labeled receptors was done using ImageJ's JACoP plugin [217]. The colocalization is shown using a two-channel cytofluorogram: a 2D scatter-plot of the intensity in channel 1 vs. the intensity in channel 2 (see example in **Figure 10.7(a)**). A colocalized signal should give a cytofluorogram with a positive correlation (*i.e.* for a given pixel, the intensity is either high in both channels or low in both channels). The correlation is usually described using the Pearson coefficient of the points in the cytofluorogram. Another type of analysis is the intensity correlation analysis (ICA), which is represented as a scatter-plot of the product of the deviations from the mean of the two channels vs. the intensity in a given channel. Points that are located in the first quadrant ("north-east") arise from significant colocalization events (see Fig. 15.7(e)). This analysis allows one to look only at the significant part of the colocalization, above the noisy background.

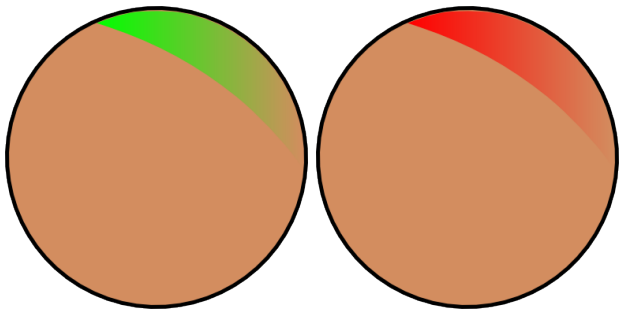

(a) *An example for a simple two-color colocalization.*

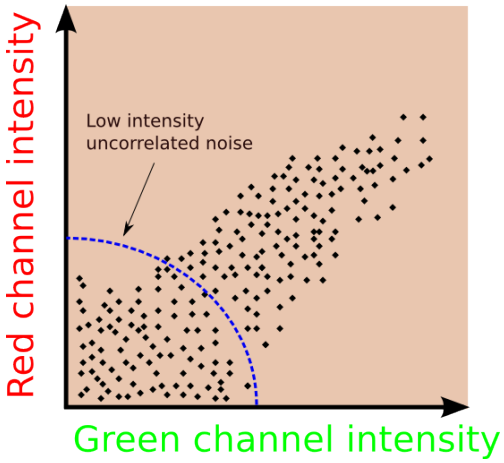

(b) *An example for a cytofluorogram*

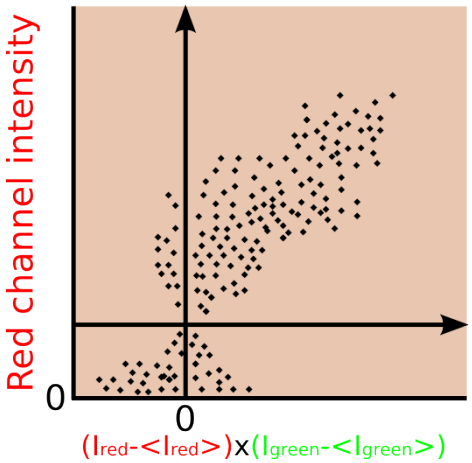

(c) *An example for an intensity correlation analysis (ICA)*

Figure 10.6: *Examples for colocalization analysis methods.*

10.3.2 Colocalization of GFP-labeled PON and sparse QDs

In the case of sparse QDs, standard colocalization methods are not adequate. These methods quantify the specificity of colocalization using the Pearson coefficient of the correlation between the two-color intensities (the QD channel and the target-protein channel). If the Pearson coefficient is very high (close to unity), the correlation is considered strong and the two color intensities are considered to be colocalized. But when we have a small number of high intensity, colocalized pixels and a large number of low intensity random pixels, this method cannot detect the colocalization, due to the effect of the random pixels on the Pearson coefficient.

This is the case of GFP colocalization with QDs, where a few pixels in the QD channel are colocalized with a **small fraction** of the high intensity pixels of the GFP channel. This results in a lot of noise, due to the majority of high intensity GFP pixels that are not colocalized with anything in the QD channel (see **Figure 10.7(b)**). In such a case, it is of course, impossible to fit the cytofluorogram with a straight line, not to mention obtaining a high Pearson coefficient, which is derived from this line, even when the QDs are colocalized with their target.

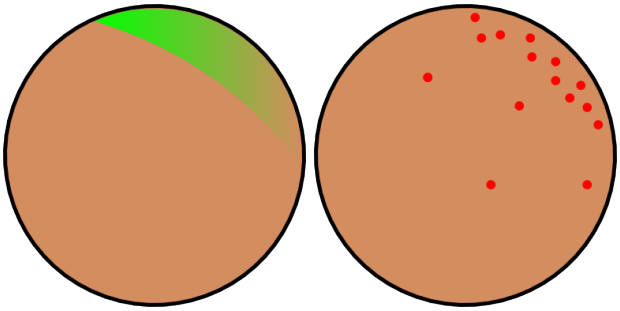

(a) *An example for a colocalization of QDs (right) with GFP (left).*

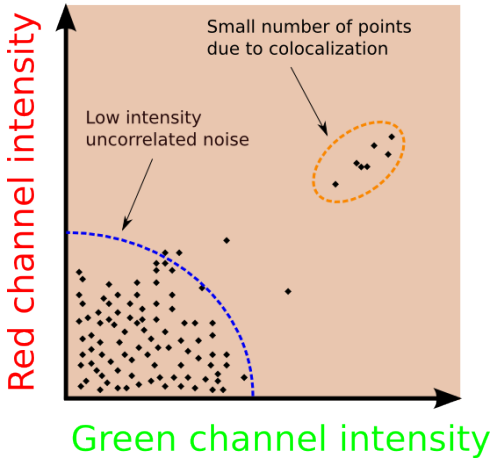

(b) *When QDs are sparse, the colocalization is masked by the noise*

Therefore, we used a semi-quantitative,"scoring" method: the GFP images were thresholded to 90% (all pixels with intensities higher than 90% of the maximum intensity were assigned the value 255, and all the rest were assigned the value 0). Then, for each movie, all the trajectories produced by the MTT algorithm were examined one by one vs. the thresholded image (see **Figure 10.7**). Then, a score is calculated in the following way:

$$\text{Score} = \frac{\frac{n_{QDsinside}}{n_{QDstotal}}}{\frac{n_{pixelsGFP}}{n_{pixelstotalcell}}} \tag{10.7}$$

Where $n_{QDsinside}$ is the total number of detected QD spots inside the thresholded area (a

detection of a QD in a single frame is counted as one.), $n_{QDstotal}$ is the total number of detected QDs, $n_{pixelsGFP}$ the number of pixels with an intensity above the threshold and $n_{pixelstotalcell}$ is the total number of pixels in the area that corresponds to the cell in the GFP image.

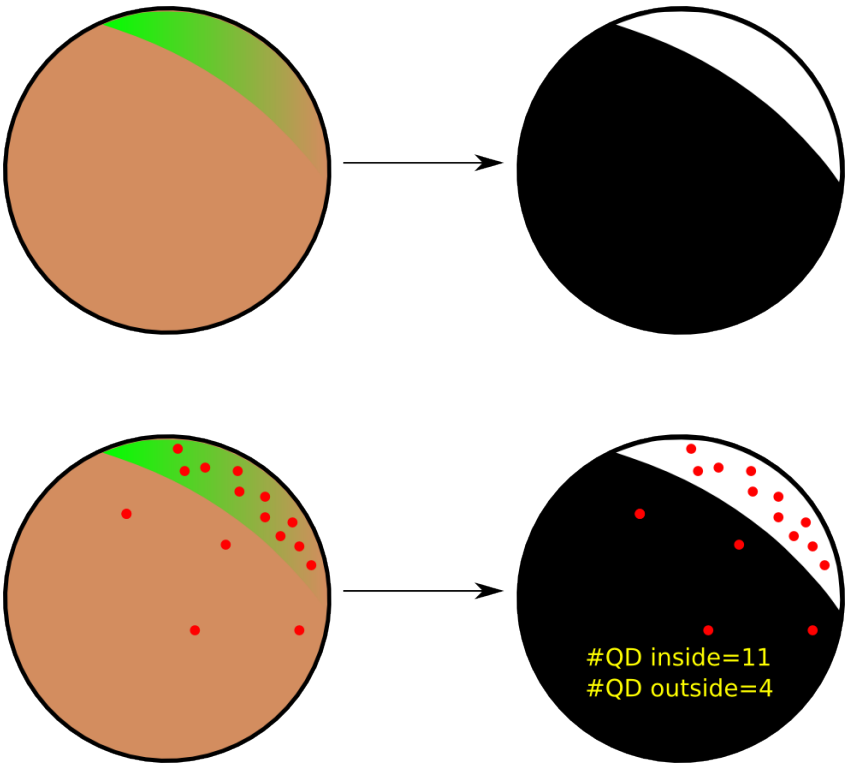

Figure 10.7: *An alternative scoring method, based on counting detected spots inside and outside the area of interest*

Part III

Results

Chapter 11

Introducing probes into the cells

Given that internalization is a critical step in intracellular QD assays [19], we first needed to test and characterize the QD internalization procedures. In order to do so, we have performed diffusion measurements for QDs in different cell lines. The two most efficient methods - micro-injection and pinocytic influx were also compared. We started our tests with HeLa cells, which are considered adherent and robust, and later proceeded to neuroblasts.

11.1 Micro-injection

Microinjection has been considered as an internalization method for neuroblasts, due to its proven efficiency in the internalization of small dyes and proteins into live cells. Another advantage of microinjection is that it allows to directly image and manipulate a given cell, and to observe the effect of internalization in real time, under the microscope (in most internalization methods, the internalization and observation are separated.). Some cell types are considered harder to inject than others, based on parameters such as adherence, rigidity and ability to recuperate from injection.

11.1.1 Tests

Injection of FITC-dextran into HeLa cells

As a reference test for the method, HeLa cells were micro-injected with 70kD FITC (fluorescein isothiocyanate)-dextran. Then, the cells were fixed with paraformaldehyde and observed. The cells seemed to remain intact and were found to have a strong signal in the FITC channel

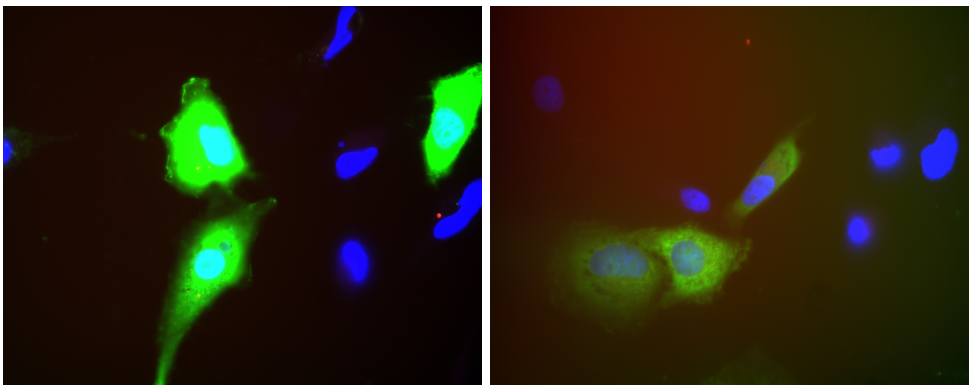

Figure 11.1: *Images of HeLa cells injected with FITC dextran (green) fixed and treated with DAPI (nuclei in blue). The efficiency of the internalization can be seen by the homogeneous distribution of the FITC around the nucleus.*

Injection of QDs into HeLa cells

We injected HeLa cells with commercial 655nm NH_2-PEG-QDs (Invitrogen). The QDs appeared to diffuse inside the cell (see **Figures 13.5(a)**, 13.5(b)). The QDs were tracked and the trajectories were analyzed.

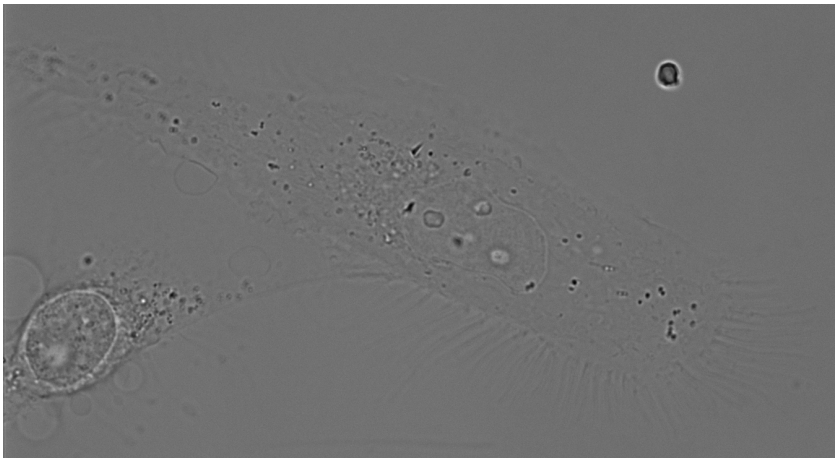

(a) *A transmission-light image of a HeLa cell.*

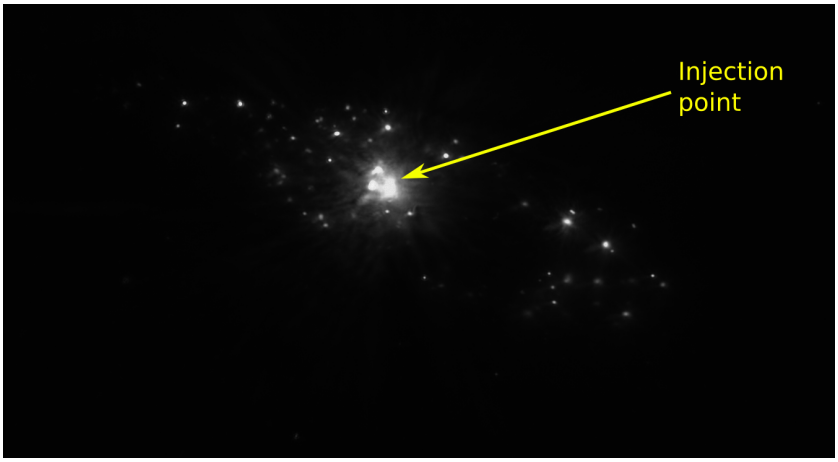

(b) *A single exposure of a HeLa cell, injected with 655nm NH_2-PEG-QDs (Invitrogen).*

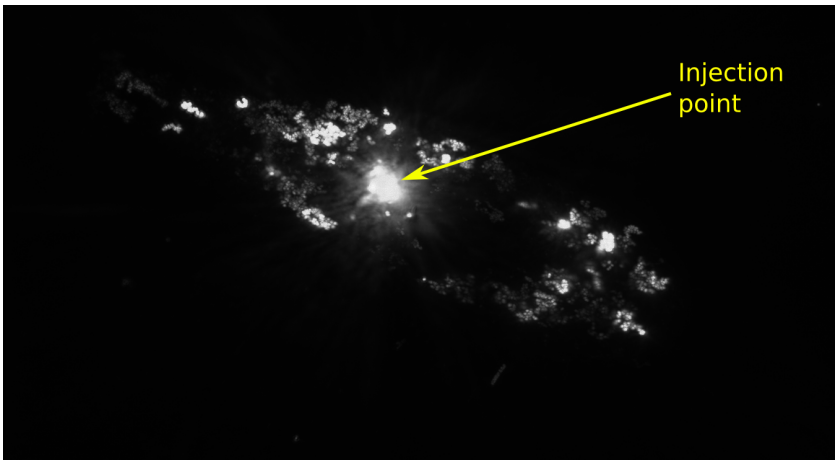

(c) *A maximum intensity projection of a movie taken in the QD channel, following Micro-injection. Notice the absence of QDs in the nucleus and the high concentration of immobile QDs in the injection point.*

Trajectory analysis We have tracked the non-conjugated QDs' movement inside the living HeLa cells, following microinjection. Then, we performed an MSD calculation for these trajectories and extracted the diffusion coefficients. These diffusion coefficients were used to compile a histogram of LogD (The natural logarithm of the diffusion coefficient). The analysis reveals at least two regimes for the movement of free QDs inside HeLa cells: a fast and slow regime. For the former, the LogD histogram (see **Figure 11.10**) can be fitted with a Gaussian, with a maximum at -3.22 ± 0.050. This corresponds to a characteristic diffusion coefficient of $4 \times 10^{-2} \mu m^2/sec$, with standard errors $+0.21 \times 10^{-2} \mu m^2/sec$ and $-0.19 \times 10^{-2} \mu m^2/sec$. The latter corresponds to a slow/confined regime (probably a mixture of several subpopulations, including static QDs and slowly diffusing QDs) and can not be fitted with a single distribution, but is roughly centered at -4.6, which corresponds to a diffusion coefficient of $1.00 \times 10^{-2} \mu m^2/sec$.

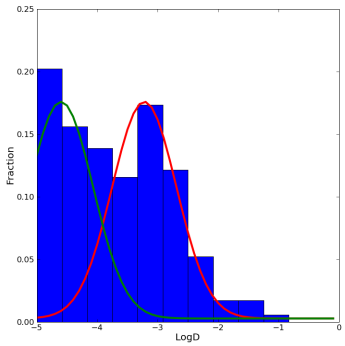

Figure 11.2: *A histogram of the fraction of trajectories as a function of LogD (the natural logarithm of the diffusion coefficient), from 60 trajectories. The characteristic diffusion coefficient is indicated by the red Gaussian curve and the immobile QD range is indicated by the green Gaussian (both serve as "guides" for the eye).*

Injection into *Drosophila* neuroblasts

The next step was the micro-injection of neuroblasts. We found that neuroblasts were hard to penetrate using the microinjector tip: they were very slippery, and weakly adherent. Microinjection succeeded only in rare cases, which usually ended by the death of the cell, due to the force that had to be repeatedly applied onto the cell.

Some limited success has been achieved using SLAM injection [201] (by our group member Fabien Pinaud), which uses a lipid-coated tip that fuses with the membrane and allows a more "gentle" injection. However, since this method was laborious and time consuming (the tip has to be changed after a small number of injections).

We therefore decided that microinjection should not be the method of choice in this project.

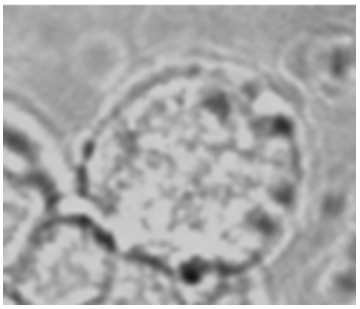

(a) *A transmission-light image of an interphase neuroblast cell, post SLAM injection.*

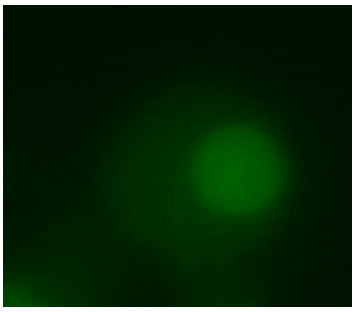

(b) *An interphase neuroblast cell, as seen in the GFP channel, post SLAM injection.*

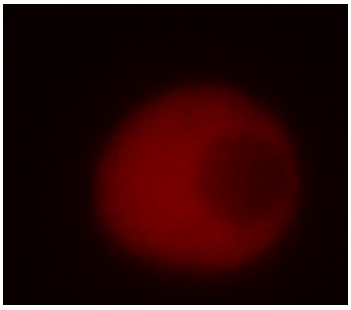

(c) *An interphase neuroblast cell, as seen in the Texas red channel, post SLAM injection.*

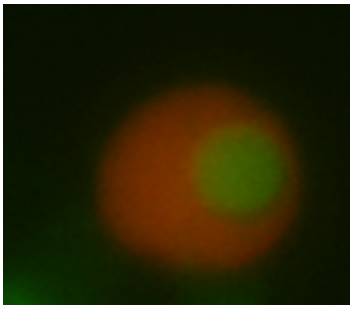

(d) *An overlay of the GFP and Texas red channels, post SLAM injection.*

Figure 11.3: *An example of a SLAM injection of Texas red into living neuroblasts (courtesy of Fabien Pinaud).*

11.2 Influx (osmotic shock)

11.2.1 Tests

As explained earlier, the main concern with the pinocytic influx method is an insufficient osmotic shock effect that does not burst the pinosomes. Quantum dots trapped in these pinosomes are unable interact with the intracellular environment, let alone target the protein of interest. Such QDs will appear either as an unusually strong fluorescent spot (should be detected by its "non-blinking" behavior), since the size of pinosomes is close to the diffraction limit, or as fluorescent spots undergoing fast confined movement in a case where the pinosome only increased its size as a response to a moderate osmotic shock.

Two-color movies

In order to address the problem of intact pinosomes we performed internalization experiments with a mixture of red (655nm emission) and orange (605nm emission) QDs. S2R+ cells were treated with pinocytic influx to internalize the mixture, and subsequently mounted on the microscope for imaging. The imaging was performed using a dual-view system [218] with 605/655 filters to measure separately and simultaneously the two emission wavelengths. Upon observation, the movement of 655 and 605 QDs looked completely uncorrelated. In some rare cases pinosomes were detected, in which both colors were observed in immobile fluorescent spots.

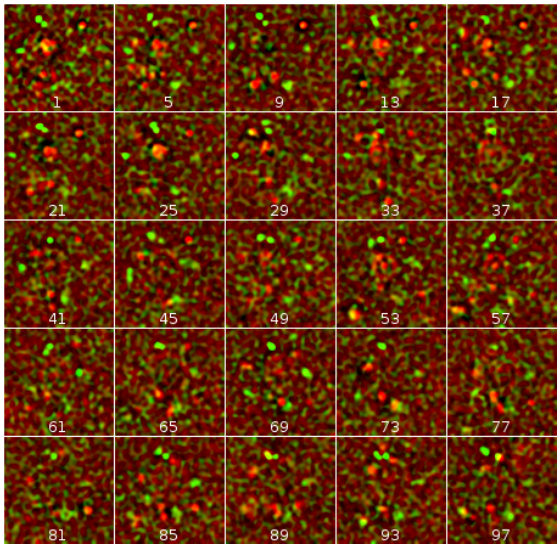

(a) *S2 cells were loaded with a mixture of 655nm and 605nm QDs using the pinocytic influx method, to show that they are not trapped in pinosomes. Had the pinosomes remained intact and not burst, we would see a strong colocalization between the two color QDs as the pinosomes should have contained both color QDs. This figure is a montage of two channels: 605nm in green and 655nm in red. As we can see, there is no significant colocalization between the two color quantum dots, which further supports the claim that in the conditions we use, the pinosomes indeed burst. The independent movement of the 655 and 605 QDs can be seen: the red and green spots do not colocalize in most frames, and even when they do in a given frame, it is only coincidental, as they can be seen to separate again.*

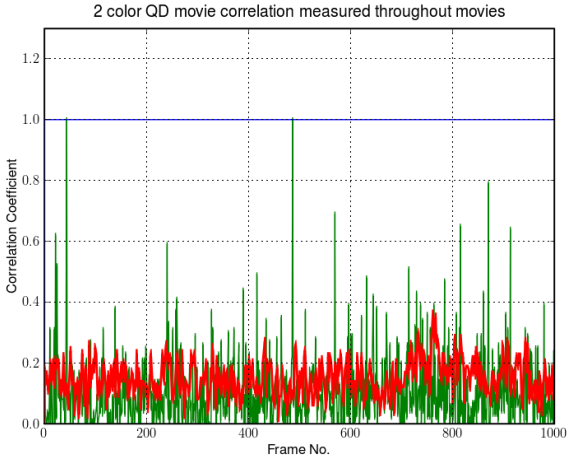

(b) *Intensity correlation coefficient in a two-color movie after pinocytic influx of nm and 605nm QDs. The blue curve is the positive control (the correlation between the 655nm channel and itself, equal to 1). The green curve is a negative control (the correlation between the 655nm channel and a randomly-shuffled copy of itself. The red curve shows the correlation between the 655nm channel and the 605nm channel. The results show that the correlation between the 605nm and 655nm QDs resembles that of a random sample.*

Figure 11.4: *Analysis of QD internalization using two-color QDs.*

11.2.2 Introduction of QDs into HeLa, 3T3 and S2 cells

After validating the method, we proceeded to study the difference in diffusion between different cell lines. We have chosen two mammalian cell lines and one insect cell line (S2R+, derived from *Drosophila*). These cells were used to study internalization and intracellular diffusion, before continuing further to targeting experiments.

HeLa cells

We used HeLa cells in order to test the pinocytic influx method. QDs appeared to diffuse inside the cell, excluded from the nucleus (see **Figure 11.5**).

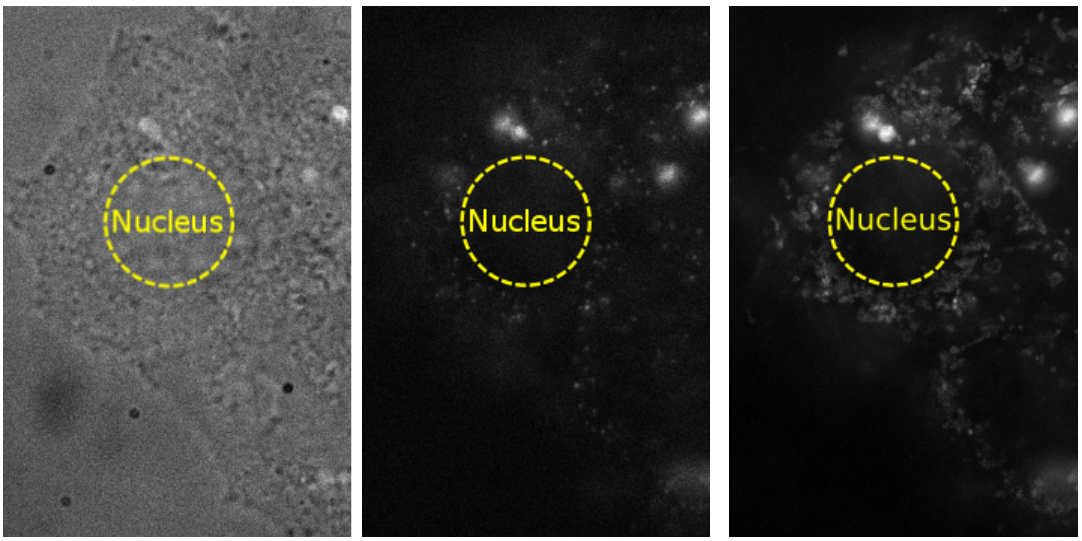

(a) *A transmission-light image of a HeLa cell.*

(b) *A single frame from a movie taken in the QD channel, following internalization.*

(c) *A maximum intensity projection of a movie taken in the QD channel, following internalization. The nucleus can be seen as a dark spot, as the QDs are excluded from it.*

Figure 11.5: *The internalization of QDs into HeLa cells.*

Trajectory analysis We tracked non-conjugated QDs moving inside the living HeLa cells. Then, we performed an MSD calculation for these trajectories and extracted the diffusion coefficients. These diffusion coefficients were used to compile a histogram of LogD (the **natural logarithm** of the diffusion coefficient, see **Figure 11.6**). This analysis reveals at least two regimes for the movement of free QDs inside HeLa cells: a fast regime, with a maximum -3.06 $\pm$ 0.107, which corresponds to a characteristic diffusion coefficient of $4.69 \times 10^{-2} \mu m^2/sec$ with standard errors $+0.53 \times 10^{-2} \mu m^2/sec$ and $-0.48 \times 10^{-2} \mu m^2/sec$, and a slow/confined regimes (probably a mixture of several subpopulations, including static QDs and slowly diffusing QDs) that could not be fitted with a single distribution, but is also centered at roughly -4.6-(-4.5), which corresponds to a diffusion coefficient of $1.00 \times 10^{-2} \mu m^2/sec$ (similarly to the case of the injected HeLa cells).

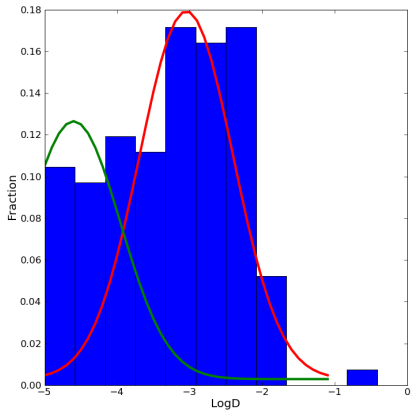

Figure 11.6: *A histogram of the Fraction of trajectories vs. LogD (The natural logarithm of the diffusion coefficient) for HeLa cells, post-internalization by the pinocytic influx method. The Gaussians serves as guides for the peak of the mobile QDs (in red), and for the immobile QDs region (green).*

S2 cells

Here we used a variant of the S2 cell line, called S2R+ [219], that is more adherent and therefore easier to work with (similarly to HeLa cells, these cells can be grown on a glass cover-slip, and do not require poly-lysine coating).

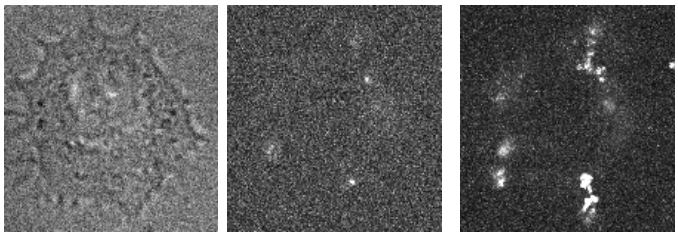

(a) *A transmission-light image of an S2R+ cell.*

(b) *A single frame from a movie taken in the QD channel, following internalization.*

(c) *A maximum intensity projection of a movie taken in the QD channel, following internalization.*

Figure 11.7: *The internalization of QDs into S2R+ cells*

Trajectory analysis We tracked non-conjugated QDs moving inside the living $S2R^+$ cells. We then performed an MSD calculation for these trajectories and extracted the diffusion coefficients. Then, these diffusion coefficients were used to compile a histogram of LogD (The natural logarithm of the diffusion coefficient, see **Figure 11.10**), based on 71 trajectories. Similarly to HeLa cells, the high peak can be fitted by a Gaussian. In this case, the peak was centered at -1.22 ± 0.07, which corresponds to a characteristic diffusion coefficient of $3.0 \times 10^{-1} \mu m^2/sec$ with standard errors $+0.17 \times 10^{-1} \mu m^2/sec$ and $-0.25 \times 10^{-1} \mu m^2/sec$. The rest of the data, corresponding to "slow" diffusion, also could not be fitted with a single distribution, but is centered at approximately -4, which corresponds to a diffusion coefficient of $1.8 \times 10^{-2} \mu m^2/sec$.

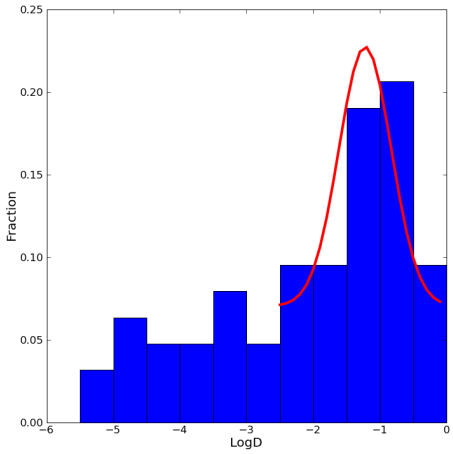

Figure 11.8: *A histogram of the of trajectories vs. LogD, The natural logarithm of the diffusion coefficient, for S2R+ cells. The Gaussian fit serves only as a guide for the peak of the histogram.)*

Chapter 11

NIH 3T3 cells

The 3T3 cell line was originally derived from mouse embryos [220]. These flat and adherent fibroblasts are widely used in cell culture experiments. We chose this cell line as a candidate for internalization experiments due to its robustness and ease of use. The 3T3 cells were treated just like the HeLa and S2R+, with pinocytic influx (see **Figure 11.9**). The QDs diffusing inside the cells were tracked, and their trajectories were analyzed. The resulting diffusion coefficients were used to draw a histogram of LogD (the natural logarithm of the diffusion coefficient).

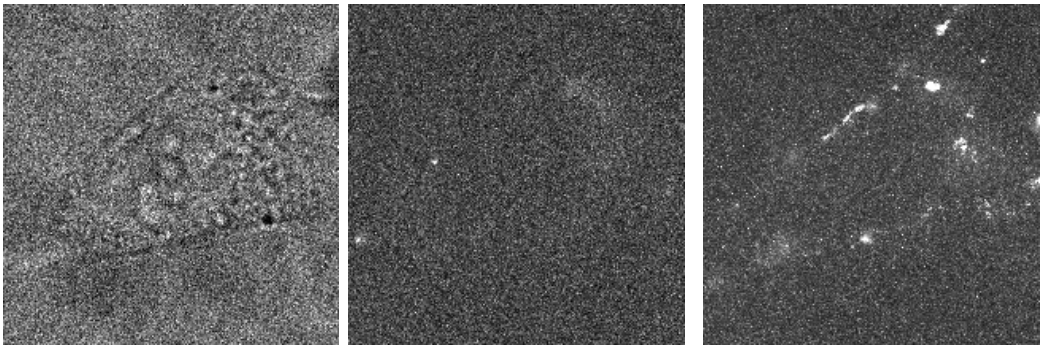

(a) *A transmission-light image of a 3T3 cell.*

(b) *A single frame from a movie taken in the QD channel, following internalization.*

(c) *A maximum intensity projection of a movie taken in the QD channel, following internalization.*

Figure 11.9: *Quantum dot internalization into 3T3 cells, using pinocytic influx.*

Trajectory analysis As in the previous cases, we calculated diffusion coefficients from the resulting trajectories and compiled them into a histogram. In the case of 3T3, the histogram showed a broad peak around LogD=-3.21 ± 0.17, which corresponds to 0.04 $\mu m^2/sec$ with standard errors -0.06, and + 0.08 $\mu m^2/sec$. In this case, it was hard to detect sub-populations within the distribution. However, the distribution and the range of diffusion coefficients strongly resemble those of HeLa cells.

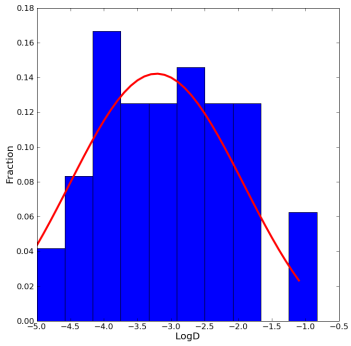

Figure 11.10: *A histogram of the fraction of trajectories vs. LogD (The natural logarithm of the diffusion coefficient) for 3T3 cells. The Gaussian fit serves only as a guide for the peak of the histogram. The data consists of 58 trajectories.*

11.2.3 Introduction of QDs into neuroblasts

We then tested the efficiency of pinocytic influx to introduce QDs into neuroblasts. The efficiency of the influx method for internalization of QDs into neuroblasts varied from cell to cell, from few, to dozens of QDs per cell but in general, was lower than the efficiency for the HeLa, 3T3 or S2R+. We have also found, that due to the thickness of neuroblasts, it was hard to record long QD trajectories, as the QDs frequently go in and out of focus. While HeLa, 3T3 and even S2R+ are adherent and considered "flat", neuroblasts are quasi-spherical.

The effect of pinocytic influx on cell division As the focus of this work is asymmetric cell division, it was important to test whether the shock, associated with this internalization method, could stop or affect cell division. We found that even though the fraction of cells that underwent full division was somewhat diminished (about 50% compared to the untreated sample), some neuroblasts still managed to divide, and the cells showed no morphological abnormalities that could indicate for low viability or death, following the osmotic shock treatment. The fraction of mitotic cells, at prophase or later (showing a PON4-GFP crescent), did not decrease significantly. Although this work deals with asymmetric cell division, this test is more important as a proof of cell viability, since at this stage we do not need to follow protein localization throughout the division, but only around prophase, in which the protein is polarized.

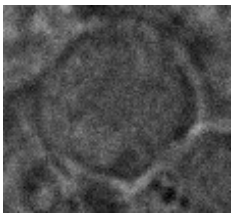

(a) *A transmission light image of a dividing neuroblast.*

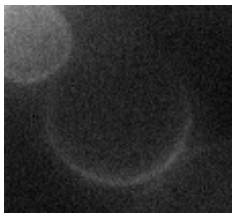

(b) *The GFP channel image of a dividing PON-GFP neuroblast, showing a PON-GFP crescent.*

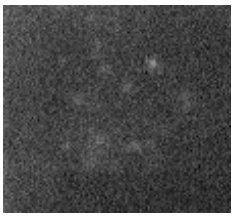

(c) *A single frame from a movie taken in the QD channel, in the same cell.*

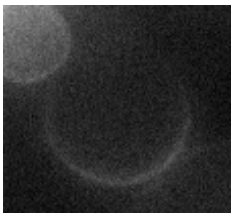

(d) *A maximum-intensity projection of the movie taken in the QD channel, superimposed on the image from the GFP channel.*

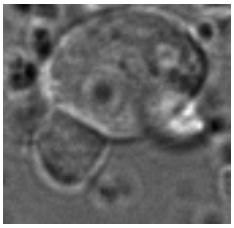

(e) *A transmission light image of an interphase neuroblast.*

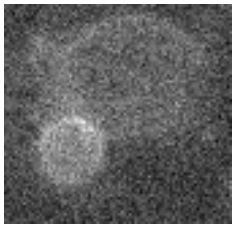

(f) *The GFP channel image of an interphase PON-GFP neuroblast. PON-GFP is not polarized, and can be seen in a small neighboring cell (probably a GMC).*

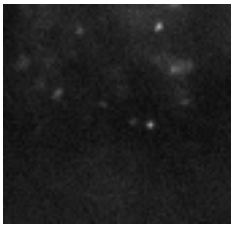

(g) *A single frame from the movie, taken in the QD channel for the same cell.*

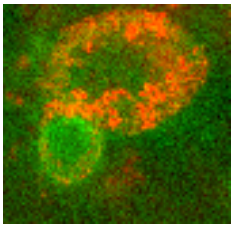

(h) *A maximum-intensity projection of the movie in the QD channel on the image taken in the GFP channel. The QDs are excluded from the cell nucleus.*

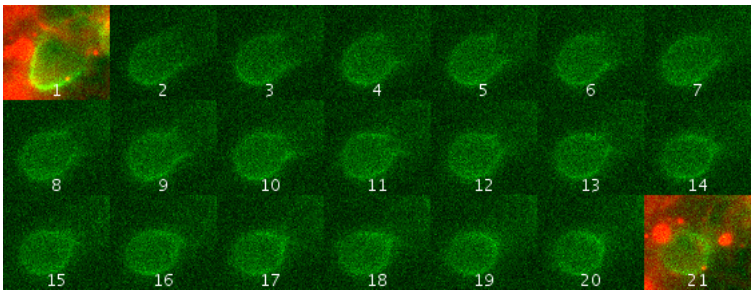

(i) *A neuroblast cell division after pinocytic influx treatment (the first and last images were taken in the QD channel, and all the rest are in the GFP channel.*

Figure 11.11: *Internalization of QDs into neuroblasts by means of pinocytic influx. The difference between mitotic and interphase cells can be seen: in the mitotic cell (where the PON-GFP crescent is apparent), the QDs diffuse almost freely inside the cytoplasm, whereas in an interphase cell, they are excluded from the nucleus.* ***Figure 11.11(i)*** *shows a neuroblast division after pinocytic influx treatment.*

11.2.4 A comparison between Micro-injection and the Influx methods

HeLa cells were used to compare between the two methods. Non-labeled QDs were internalized and tracked, and the characteristic diffusion coefficients were compared. The main difference between the two methods can be seen, when observing the LogD histograms of both methods. Even though the central peaks in both distributions are relatively close (as we found in the last subsections), the fraction of "slow" QDs in the case of microinjection is higher.

Cell line	Characteristic diffusion coefficient
HeLa	0.047 $\mu m^2/sec$
3T3	0.04 $\mu m^2/sec$
S2	**0.3** $\mu m^2/sec$

Table 11.1: *The characteristic diffusion coefficients found for the different cell lines.*

	HeLa	3T3	S2R+
HeLa	-	**0.36**	$1.2 * 10^{-12}$
3T3	-	-	$1.6 * 10^{-7}$
S2R+	-	-	-

Table 11.2: *A summary of the two-sample Kolmogorov-Smirnov test for the distributions of diffusion coefficients. We compared the distributions of diffusion coefficients for the three cell lines, in order to determine whether the difference in diffusion coefficients is significant.*

A comparison of different cell lines

We have compared the distributions of diffusion coefficients between three cell lines: HeLa S2R+, and 3T3. We found that the characteristic diffusion coefficients in HeLa and 3T3 (both mammalian cells) were relatively close, whereas that of the S2R+ cells (an insect cell line), was much higher. The results are summarized in **Table 11.2**. We have also compared the distributions of diffusion coefficients using a Kolmogorov-Smirnov test in order to verify the significance of this difference. We found that the difference between the distributions of diffusion coefficients of HeLa and 3T3 cells is not significant (a P-value of $0.36 > 0.05$), whereas the difference between the distributions for each of these cell lines and the S2R+ cell line are significant (P-values$< 1 * 10^{-6}$). We therefore conclude that QD diffusion coefficients can vary dramatically between cell lines. In order to compare the diffusion between the different cell lines, we chose only diffusion coefficients above a certain limit, since very low diffusion coefficients are less likely to arise from pure diffusion. This way, we remove the static, trapped or confined QDs, and concentrate on the mobile QDs, which can be better modeled by Brownian motion, which are the majority of the data, with diffusion coefficients above $0.02 \mu m^2/sec$.

11.2.5 The variation of diffusion coefficients inside the cytoplasm of living cells

An additional information that was extracted from the trajectory data was the spatial variation of diffusion coefficient inside the cytoplasm. The centerpoint of every trajectory was calculated, and thus, a "map" of diffusion coefficients was compiled. From looking at the data, we found that the low diffusion coefficients are located closer to the nucleus, and the higher diffusion coefficients are more in the cell periphery (see **Figure 11.12**). In the current experimental conditions, this could not be generalized or well quantified, due to cell-cell differences in morphology. However, if a large number of QDs were internalized, the data from a single cell could already be statistically significant and provide some some information about the properties of the cytoplam (such a study is beyond the scope of this project).

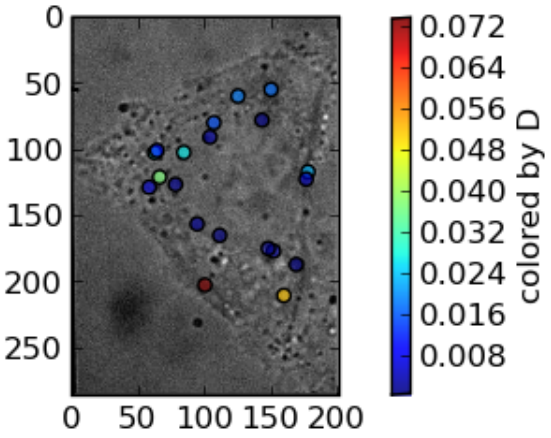

Figure 11.12: *An example for the variation of diffusion coefficient on the location within the cell cytoplasm: low diffusion coefficients are concentrated around the nucleus.*

11.2.6 The significance of QD surface chemistry

In order to improve our understanding of the effect of QD surface chemistry, we have tested the behavior of QDs with a different surface chemistry, peptide coating, [93] inside living cells. Owing to their unique surface chemistry, these QDs are significantly smaller than commercial QDs. The peptide coating also allows a flexible design of surface chemistry by combining natural and artificial amino-acids and various chemical moieties. We have tested QDs with amine terminated peptides, and cysteine terminated peptides. These QDs were internalized into S2R+ cells, and then observed under the microscope. With both types of peptide-coated QDs, the results have shown a very clear difference between the peptide QDs and the commercial ones (655 NH_2-PEG QDs): in contrast to the commercial QDs, the peptide-coated QDs appeared to be concentrated in large aggregates inside the cell, which were practically immobile. We therefore conclude that the surface chemistry of the QDs can have a major effect on intracellular diffusion. In this case, we believe that the peptide-coated QDs are not as passivated as the commercial NH_2-PEG, and in the intracellular environment, which has a very high protein concentration, the QDs can bind non-specifically to cellular proteins and remain "stuck".

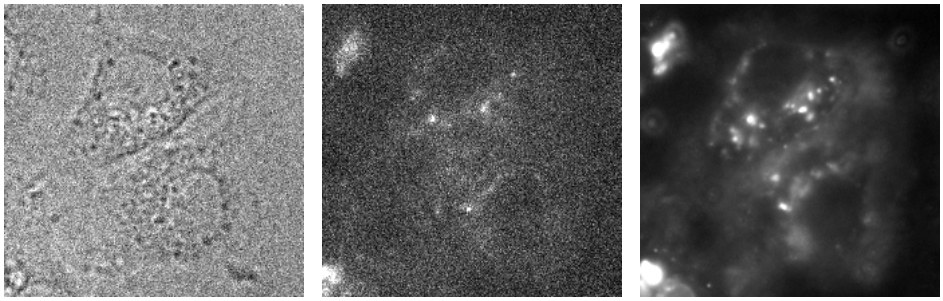

(a) *A transmission light image, showing two S2R+ cells, after the internalization of cysteine-terminated peptide QDs.*

(b) *A single image at the QD channel, showing immobile QDs (605nm).*

(c) *A projection of the movie in the QD channel, showing the QD aggregates.*

Figure 11.13: *An example for the behavior of peptide coated QDs inside cells, following pinocytic influx.*

Chapter 12

Protein preparation and biotinylation

With the internalization methods established, we continued to the production of the proteins needed for the experiments: the ACD proteins PON, Pins and Miranda, the anti-GFP single-chain variable fragment, as well as other proteins needed for tests and protein modification (GFP, nucleoplasmin, and BirA)

12.1 PON constructs

12.1.1 Baculovirus constructs

We found out that all the expressed PON constructs had a very low solubility and could not be retrieved with a sufficient yield. The fusion with GFPuv, which is a highly soluble protein, was not enough to solubilize PON. In order to confirm that, we performed a fractionation of SF9 cells infected with HisTag-GFP-PON4-AviTag virus, into cell membranes, nuclei and cytoplasm. PON-GFP was found almost exclusively in the non-soluble fractions of cell membranes and nuclei. Therefore, we have decided not to use this construct for the time being.

12.1.2 Bacterial construct

We have also tried an alternative approach, by producing MBP-GFP-PON4-AviTag-biotin, which may have an improved solubility, and also allows *in-vivo* biotinylation by co-transforming the bacteria with pCDF BirA and adding biotin to the medium. The protein was purified using an amylose resin. The purified fractions showed very low yield, due to low solubility (the protein itself is >100kD, which also makes it more difficult to express in bacteria), and degradation. In this case too, the work with this protein was discontinued.

12.2 PINS construct

12.2.1 Baculovirus construct

Purification

By using the purification procedure described in the **Methods** part, we obtained relatively pure HisTag-Pins-AviTag, from the baculovirus-infected SF9 cells. The PAGE analysis is shown in **Figure 12.1**.

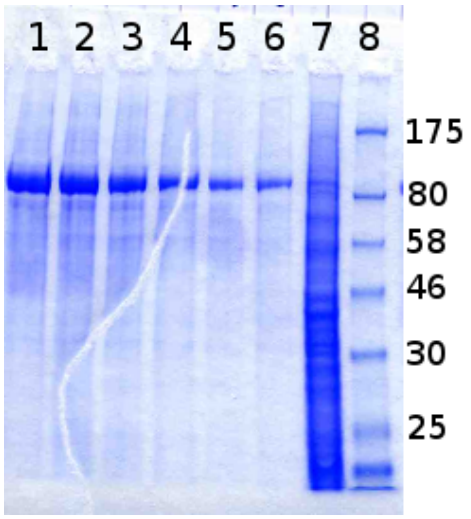

Figure 12.1: *The result of an affinity purification of full-length HisTag-Pins-AviTag from baculovirus-infected SF9 cells:* ***Lanes 1-6****, fractions of the purified protein;* ***Lane 7****, the non-soluble fraction;* ***Lane 8****, the molecular weight marker (NEB) with the weights indicated in kD.*

Biotinylation

In-vitro **biotinylation** The baculovirus constructs for Pins contained an AviTag sequence, which is recognized by the *E. coli* enzyme BirA (biotin ligase). In order to be able to couple these proteins to QDs, they had to be biotinylated. The purified protein was biotinylated *in-vitro* as described in the **Methods** part, and tested using a polyacrylamide gel-shift assay. The PAGE analysis of the gel-shift assay is shown in Fig. 12.2. Two important results were obtained: first, Pins, biotinylated *in vitro*, is nearly 100% biotinylated (in the lane where streptavidin was added, no band corresponding to free Pins was detected.). Second, by using the opposite ends, two-tag design (N-terminal HisTag, C-terminal Avitag-biotin) only the full length protein is biotinylated: the $\sim$ 30kD degradation product, which still has the HisTag, was eluted together with the full length Pins, but does not shift on the gel, since it lacks the C-terminal AviTag and therefore cannot be biotinylated.

Mass spectrometry Pins was run on a PAGE that was sampled and sent to mass spectrometry analysis. The results confirmed the peptide sequence.

12.2.2 Bacterial expression

Cloning and design

We have seen that Pins produced in SF9 cells is soluble, but the yield was not satisfactory. Therefore, we decided to express it in bacteria (at the same time, a work was published, showing that bacterially expressed Pins is active [173].), using the pET32b vector for increased solubility (Novagen). The resulting construct was co-transformed into *E. coli* BL21 Rosetta bacteria together with pCDF Duet BirA for improved biotinylation in vivo. The advantages in this case are: expression is fast (a couple of hours vs. three days for baculovirus) and biotinylation occurs *in-vivo*, which saves time and material. Due to the addition of S-TAG and TRX-tag, which exist in pET32, the bacterial construct is expected to be somewhat bigger than the baculovirus construct ($\sim$ 95kD vs. $\sim$ 80kD)

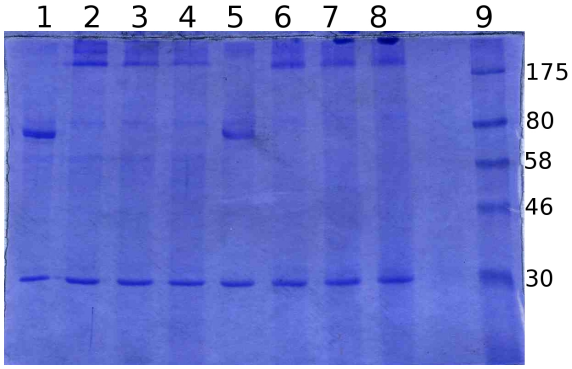

Figure 12.2: *A gel-shift assay test for Pins biotinylation. HisTag-Pins-AviTag was expressed in SF9 and purified using its HisTag. The purified protein was biotinylated in-vitro, using the BirA enzyme we produced and purified. Then, it was incubated with streptavidin and loaded on a polyacrylamide gel, to test for retardation. A retardation of the band, is attributed to the additional molecular weight of streptavidin, due to its binding to the biotinylated protein. Lanes 2-4 and 6-8 contain HisTag-Pins-biotin to which streptavidin was added, and lanes 1,5 contain native Pins. Two important points can be seen in this gel: first, Pins binds to streptavidin and second, the in-vitro biotinylation efficiency is high (it is hard to detect any band corresponding to the original molecular weight of Pins, except for lanes 1 and 5, which are the negative control).*

Expression and purification

The plasmid was co-transformed with pCDF Duet BirA into BL21-Rosetta bacteria and expressed as described in the methods part. Cells were lysed and the protein was purified using NiNTA resin. The resulting fractions were analyzed by PAGE.

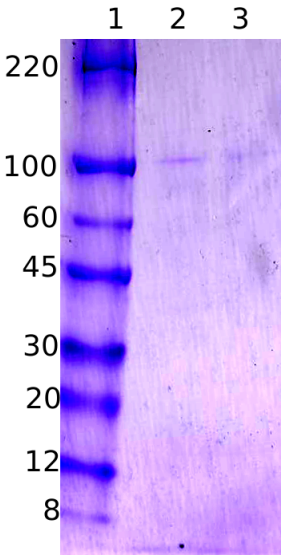

Figure 12.3: *A PAGE, showing the result of a bacterial Pins purification. Lane 1 is the molecular weight marker (SIGMA) with molecular weights indicated in kD, lanes 2,3 are purified fractions. In this figure, the concentration is not very high, but the sample is pure.*

In-vivo biotinylation

In-vivo biotinylation was tested, using a PAGE retardation assay. The results showed that biotinylation was very efficient, and specific. Owing to the opposite-ends, two-tag design, after a purification using the N-terminal HisTag, the only protein fragment that contained the AviTag (biotinylation-recognition sequence) was the full length Pins. Therefore, even in a semi-crude sample, only the full length protein was found to be biotinylated (see **Figure 12.4**). This demonstrates another advantage of the two-tag design: it is, in itself, a purification method. Therefore it does not require additional purification steps (only the full-length protein will be biotinylated and eventually bind to the QD).

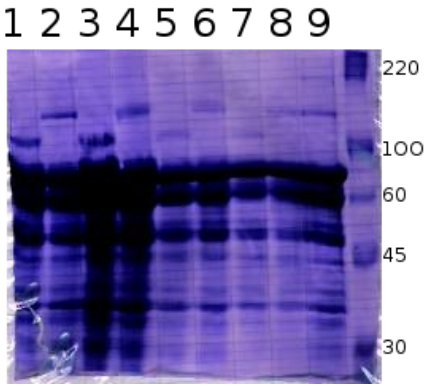

Figure 12.4: *A streptavidin gel-shift assay test for biotinylated Pins, produced in bacteria, using a relatively crude sample. This image serves to demonstrate the potential of the opposite-ends, two-tag system: even though the sample contains degradation products, only the band corresponding to full-length Pins (HisTag-Pins-AviTag-biotin), at* $\sim 95kD$*, is shifted, due to the binding to streptavidin. This is of course due to the fact that the protein was purified using an N-terminal HisTag, but the biotinylated AviTag is at the C-terminus. Different fractions were incubated with streptavidin and loaded on a PAGE. Lanes 1,3,5,7 were loaded with Pins that was pre-incubated with active streptavidin. Lanes 2,4,6,8 were loaded with Pins that was pre-incubated with passivated streptavidin (the streptavidin was pre-incubated with biotin, in order to saturate all binding sites).*

12.3 Miranda construct

Purification

The protein was purified using the standard purification conditions mentioned above. The gel shows that Miranda was well purified (a clean band can be detected at $\sim 100kD$, which is the predicted size for Miranda) as shown in **Figure 12.5(a)**.

In-vivo biotinylation

As mentioned before, in the **Methods** part, Miranda was cloned into a dual expression baculovirus vector (based of pFastBacDual from Invitrogen). During the expression (upon infection of SF9 cells by a virus containing our Miranda construct), biotin was added, in order to allow the coexpressed BirA enzyme to biotinylate the AviTag fused to Miranda. In order to test the biotinylation, we performed a PAGE migration assay with streptavidin. The results, shown in **Figure 12.5(b)**, show that nearly all the purified protein was biotinylated. The band at around 55kD is the streptavidin that was added in excess.

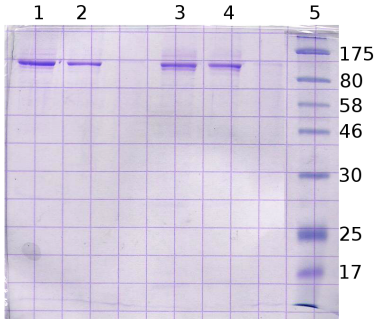

(a) *A PAGE, showing the quality of the purification of HisTag-Miranda-AviTag. Lanes 1-4 were loaded with different fractions of the purified protein. Lane 5 is the molecular weight marker (NEB) with molecular weights indicated in kD. As expected from the molecular weight of Miranda, the band appears at* $\sim 100kD$.

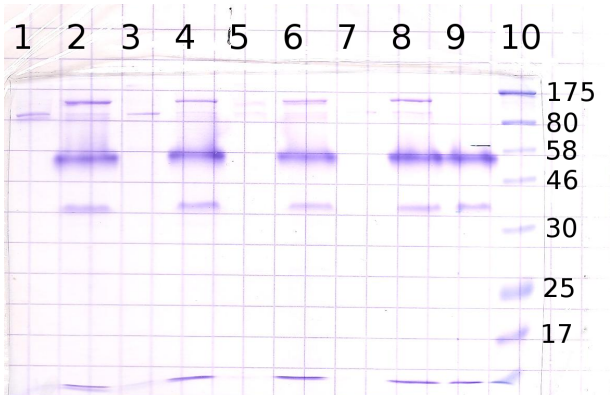

(b) *A PAGE shift assay, for the biotinylation of HisTag-Miranda-AviTag expressed in a dual bacoluvirus/SF9 system with BirA. Lanes 1-8 are 4 fractions, each fraction with and without streptavidin added. Lane 9 contains streptavidin only. Lane 10 is the molecular weight marker (NEB) with molecular weights indicated in kD. The biotinylation can be seen here from the shifts between lanes 1 and 2, 3 and 4 (other lanes are already too weak), which correspond to the retardation due to streptavidin that was bound to the biotinylated Miranda.*

Figure 12.5: *Purification and biotinylation of the dual Miranda construct.*

Validating by Mass spectrometry Miranda was run on a PAGE, the band was sampled and sent to mass spectrometry analysis that confirmed the peptide sequence.

12.4 Anti-GFP single chain variable fragment (ScFv)

Using our optimized protocol for periplasmic extraction, combined with a standard NiNTA protocol, we obtained relatively pure anti-GFP ScFv.

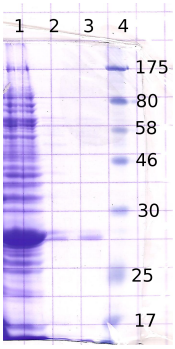

Figure 12.6: *A PAGE analysis of anti-GFP ScFv purification. Lane 1 is a crude sample, Lane 2 and 3 are fractions from a NiNTA purification.*

12.5 Proteins for control and modification

12.5.1 Biotinylated GFPuv

Both HT-GFP-AT and HT-AT-GFP have shown strong expression. However, we chose to use HT-GFP-AT since it may cause less steric hindrance for the simultaneous binding to the biotin and the HisTag and also, as mentioned before, since two tags at opposite ends of the sequence ensure that only the full length protein will be able to bind QD-SAV. The GFP constructs purified on an agarose-NiNTA column and the PAGE analysis (see **Figure 12.7**) showed a very minor degradation and negligible dimerization (high molecular weight band).

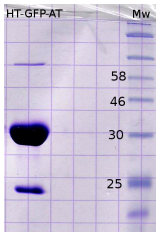

Figure 12.7: *A PAGE analysis of a HT-GFPuv-AT-biotin purification. The large band around 30kD corresponds to the HisTag-GFPuv-AviTag. The degradation (low molecular weight band around 25kD), and dimerization (high molecular weight band around 65kD) are negligible.*

In-vivo Biotinylation

We produced monobiotinylated GFPuv, by using *E. coli* over-expressing HisTag-GFPuv-AviTag and BirA (both are independent constructs that were co-transformed into the bacteria), with a biotin-supplemented medium. The biotinylation was tested using a gel-shift assay (see **Figure 12.8**).

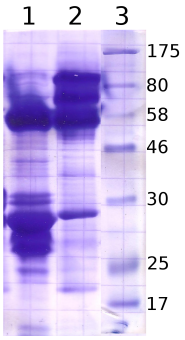

Figure 12.8: *A PAGE shift assay, using a crude GFP sample. Lane 1 contains non-biotinylated HisTag-GFPuv-AviTag (which was expressed without BirA coexpression and without the addition of biotin to the medium, and therefore cannot be biotinylated), incubated with streptavidin. Lane 2 contains biotinylated HisTag-GFPuv-AviTag (coexpressed with BirA, with the addition of biotin to the medium and therefore biotinylated in-vivo) incubated with streptavidin. Lane 3 contains the molecular weight marker (NEB), with molecular weights indicated in kD. The two additional high molecular weight bands in lane 2 are correspond to streptavidin with one GFP bound to it (a little bit under 80kD), and streptavidin with two GFP molecules bound to it (the band above 80kD). The efficiency is not 100% though, as we can see from residual GFP in lane 2, around 30kD (even though this could be a C-terminal degradation product, which does not contain the AviTag and as a result, cannot be biotinylated.). The bands around 55kD correspond to excess, free streptavidin.*

12.5.2 BirA

The Enzyme BirA (Biotin ligase) was purified as a GST fusion protein from pGEX2T vector (Amersham), using a glutathione resin and thrombin elution. The eluate was passed through a benzamidine column (Amersham) in order to remove the thrombin, before running an ion exchange purification. The quality of the material is shown in **Figure 12.9**. This enzyme was subsequently used for *in-vitro* biotinylation, throughout the project.

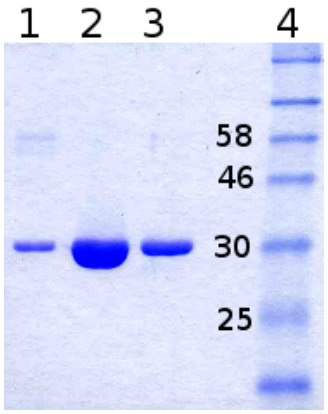

Figure 12.9: *A coomassie gel for purified BirA: Lanes 1-3 are different fractions, Lane 4 is the molecular weight marker (molecular weights are indicated in kD.) The expected size of BirA is about 30kD.*

12.5.3 Nucleoplasmin

Nucleoplasmin was purified on NiNTA resin using the standard procedure mentioned in the **Methods** part. Even though its molecular weight is 22kD, we detected a band 30kD, which is consistent with previous studies of nucleoplasmin [221] in particular, and acidic nuclear proteins in general [222] that reported such anomalous PAGE migration.

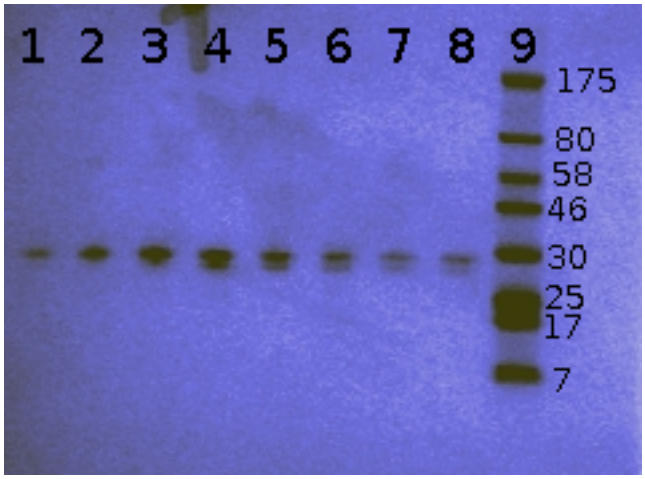

Figure 12.10: *A PAGE loaded with purified fractions of nucleoplasmin (lanes 1-8). Lane 9 is the molecular weight marker (NEB) with molecular weights indicated in kD. Even though nucleoplasmin is 22kD, it migrates slower, due to its exceptional acidity [222, 221].*

Chapter 13

QD-protein complexes: coupling and characterization

The coupling of proteins to QDs is a key step in single QD tracking experiments. Before we internalize the QD-protein complexes and track them inside the cell, we must know that the proteins are tightly bound to the QDs, that there are no free QDs, and, ideally, that the complexes are monovalent (*i.e.* one protein is bound to one QD and vice versa). As mentioned in the **Methods** part, we have chosen the biotin-streptavidin system for the coupling of ACD proteins to QDs. This is done by engineered proteins constructs, that are biotinylated *in-vivo* at a single site, and commercial, streptavidin-coated QDs (Invitrogen). The coupling reaction, however, is very simple and only requires an incubation of the biotinylated protein and the streptavidin-coated QDs (QD-SAV) in a buffer solution. As discussed in the **Methods** part, the effect of the proteins on the migration of the QDs can be either acceleration (in the case of QD-SAV, coupling to GFP and Pins increases the mobility of the complex, see **Figures 13.3,13.1**) or retardation (for QD-SAV and Miranda, and in most cases for proteins bound to highly mobile QDs such as EO6D QDs, see **Figures 13.2, 15.6**), depending on the trade-off between charge and size.

This chapter also describes the results for a novel solid-support coupling method and a characterization method based on electrotransfer, both of which are brought as a proof-of-principle and were only applied to the protein HisTag-GFP-AviTag-biotin, the protein we used for all tests.

13.1 Coupling of proteins and QDs using the biotin-streptavidin pair

In order to probe the activity of Pins and Miranda in the cell cytoplasm, we first biotinylated them and then coupled them to streptavidin coated QDs (QD-SAV). The verification and characterization of the binding was done using agarose gel electrophoresis (see **Methods**).

13.1.1 Pins coupling to QD-SAV

We incubated a range of ratios of HisTag-Pins-AviTag-biotin/QD-SAV and loaded the result on an agarose gel, in order to test the quality of the coupling. Similarly to GFP (see **Figure 13.3**), Pins increases the mobility of the QDs. Another important result that arises from this gel, is that the binding of biotinylated Pins to the QD-SAV is indeed specific (*i.e.* through the biotin). This can be seen by comparing the migration in lanes 1 and 8, where no Pins was added, to the migration in lane 7 in which excess Pins was added, but the QD-SAV were passivated with excess biotin beforehand (the migration in these lanes looks the same and therefore means that the Pins/QD ratio in lane 8 is the same as in lanes 1 and 7, *i.e.* 0/1). These results were used

at a later stage, in the preparation of QD-pins complexes (QD-SAV::Pins) for internalization: the coupling was performed with a ratio of 1/8, ensuring that there are no free QDs (in this ratio, no QDs can be detected with a migration corresponding to free QDs see **Figure 13.1**).

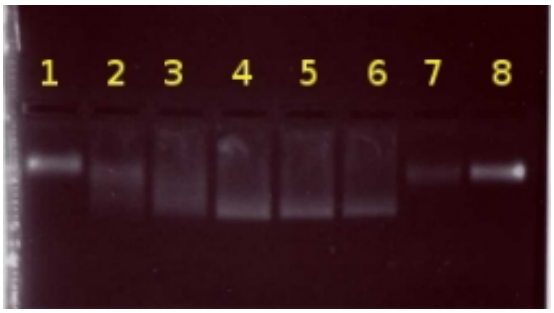

Figure 13.1: *A gel showing increasing ratios of biotinylated Pins/QD. The ratios in lanes 1-6 are 0/1, 2/1, 4/1, 6/1, 8/1, 16/1 (Pins/QD). Lane 7 was loaded with a coupling reaction with a nominal ratio of 16/1, but QD-SAV were pre-incubated with excess biotin. Lane 8 is a duplicate of lane 1. This gel shows the* ***specificity of the binding between Pins and QD-SAV****: when using QDs that are passivated with biotin, even with the highest concentration of biotinylated Pins, we could not detect any difference in migration due to binding (compare lanes 6,7 and 8).*

13.1.2 Miranda

We incubated a range of HisTag-Miranda-AviTag-biotin/QD-SAV ratios and loaded the result on an agarose gel. Unlike GFP and Pins, Miranda decreases the mobility of the QDs. The effect of Miranda on the QDs is strong retardation (see **Figure 13.2**). From this result we derived the ratio of HisTag-Miranda-AviTag-biotin to QD-SAV that will be used in the ACD experiments, 8/1 (lane 5 in **Figure 13.2**)

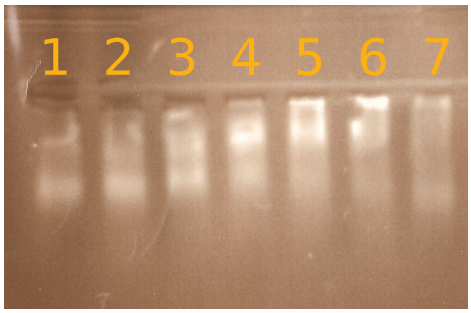

Figure 13.2: *An agarose gel showing a range of molar Miranda/QD-SAV ratios. The ratios in lanes 1-6 are 0/1, 1/1, 2/1, 4/1, 8/1, 16/1. Lane 7 was loaded with a coupling reaction with a ratio of 16/1, but QD-SAV were pre-incubated with excess biotin. The results show binding of Miranda to the QDs (manifested by the retardation effect), but unlike the case of Pins, cannot rule out that some of the binding is non-specific (i.e. not mediated by the biotin).*

13.1.3 GFP

A range of ratios of HisTag-GFPuv-AviTag-biotin was incubated with QD-SAV. The results were loaded on a an agarose gel. The results show that the binding of biotinylated GFP to QDs is specific.

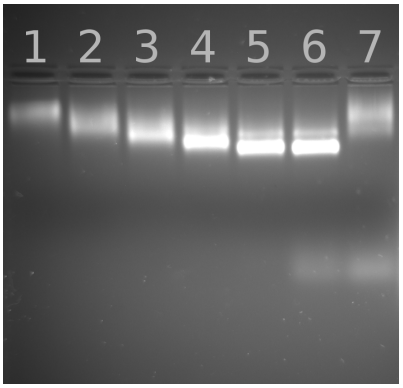

Figure 13.3: *An agarose gel, showing the mobilities of QD-SAV::GFP complexes with different stoichiometries. Lanes 1-6 were loaded with biotin-GFP::QD-SAV complexes that were prepared using the following nominal molar ratios: 0/1,1/1,2/1,4/1,8/1,16/1. Lane 7 is a control, was prepared using a ratio of 16/1 (16 GFP molecules per QD), but using biotin-saturated QD-SAV.*

13.2 Electro-transfer characterization of QDs

We have developed a method for the characterization of QD-protein complexes, using electro-transfer. As explained in the **Methods** part, the main advantage of this method is that it should allow an independent measurement of the QDs and the proteins associated to them. Moreover, it measures only the proteins bound to the QDs and not the free, unconjugated excess proteins, in the mixture. In short, the QD complexes are resolved on a gel, and then transferred onto a nitrocellulose membrane, using an electric field. Then, the QDs and the proteins are quantified, respectively, using fluorescence and chemiluminescence (protein quantification using chemiluminescence is a well established method [223]).

As can be seen from the results, QDs can be efficiently transferred onto a nitrocellulose membrane (see **Figure 13.4**), and later to be reacted with primary and secondary antibodies (see **Figure 13.5**). The main advantage of this method, lies in its potential ability to quantify protein/QD ratios. The main problem in doing so is that proteins are usually quantified by absorbance/fluorescence. Since the specific absorbance of QDs is very high (at least 2 orders of magnitude) compared to proteins, an estimation of the sample stoichiometry can be very hard. Moreover, in some cases the non-conjugated QDs already contain proteins (for example when conjugating a biotinylated protein to a streptavidin QD), in an unknown and variable stoichiometry, that add a source of noise to the measurement. This method works around these problem, by quantifying the QDs using fluorescence, and the protein using specific chemiluminescence, which is not affected by QDs (there is no excitation). The chemiluminescence assay uses antibodies that are specific against some domain within the protein and therefore is not affected by other proteins. Using the ratio between the chemiluminescent signal of the protein and the fluorescent signal of the QD, one can obtain information about the average stoichiometry of the sample. Furthermore, when the sample can be resolved into discrete bands on a gel, the stoichiometry of each band can be analyzed separately.

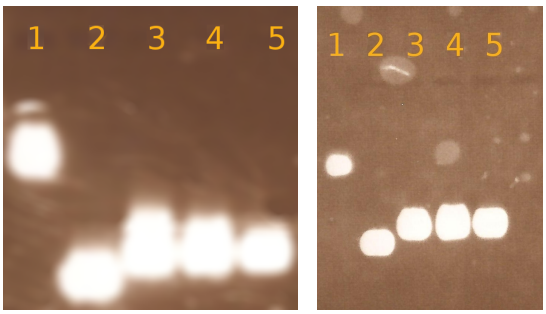

(a) *An agarose gel, loaded with different types of QDs.* (b) *The nitrocellulose membrane, after an electrotransfer from the gel.*

Figure 13.4: *An example for the capabilities of electrotransfer, applied to peptide-coated QDs. The lanes in the gel contain: 1, the protein HisTag-GFPuv-biotin; 2, methoxy-terminated peptide-coated QDs; 3, cysteine-terminated peptide-coated QDs; 4, lysine-terminated peptide-coated QDs; 5, lysine/cysteine-terminated (1/1), peptide-coated QDs.*

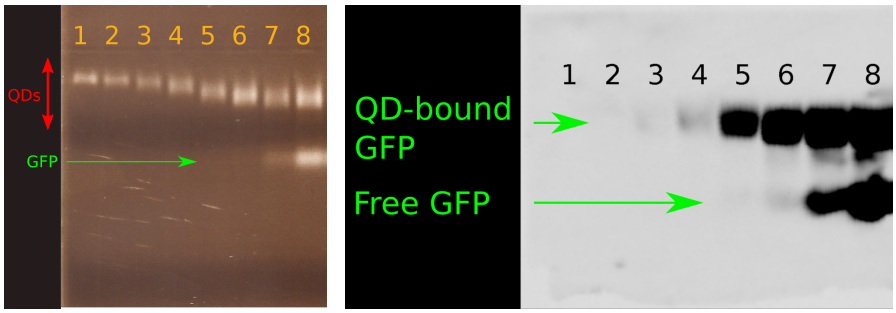

(a) *The agarose gel. By using UV excitation both QDs and free GFP can be seen.* (b) *The nitrocellulose membrane, after blotting with anti-His. The blotting with anti-his antibody, and then by a secondary antibody labeled with HRP, reveals only the HisTag-GFP-biotin, with no background from the QDs, since no excitation light is used. The chemiluminescence is generated by the reaction of HRP (horseradish peroxidase), with a chemical substrate and requires no excitation. Notice how the free and bound proteins are separated. Even though GFP has a strong signal, here we used chemiluminescence, which is not affected by the QDs, and can be applied to any protein with a specific tag that can be targeted by an antibody.*

Figure 13.5: *The results of electro-transfer and then blotting of GFP-QD-SAV complexes prepared in a range of molar ratios. The molar GFP/QD-SAV ratios in lanes 1-9 are: 0/1,0.5/1,1/1,2/1,4/1,8/1,16/1,32/1,50/1. Lane 10 is a control for specificity - using a ratio of 50/1 with biotin-passivated QD-SAV.*

13.3 Coupling on a solid support

This method was originally developed in order to couple QDs to proteins without generating free QDs (the problems arising from free QDs are discussed in the **Introduction**), with the potential of separating complexes of different protein/QD ratios, using gradient elution (such a method was reported for gold particles, during this project [224]). However, in this section we present an argument that this method may also be used to control the valence of QD-protein complexes using spatial constraints, as an alternative to the existing method, based on gel separation [10]. We tested the solid-support coupling method (described in detail in the **Methods** part) for HisTag-GFPuv-AviTag-biotin. In brief, NiNTA-agarose beads were incubated with HisTag-GFPuv-Avitag-biotin in order to bind it through its HisTag. Then, unbound, excess HisTag-GFPuv-AviTag-biotin was washed away, and QDs were added for incubation, in order for them to bind the biotin groups of the HisTag-GFPuv-AviTag-biotin molecules that are bound to the resin through their HisTag. Then, unbound QDs were washed away and free streptavidin sites were passivated using biotin. Finally, the complexes were eluted using imidazole, which competes with the HisTag (see **Figure 8.5**). This was, only QDs that bind the full length HisTag-GFPuv-Avitag-biotin are retained, and finally eluted by the imidazole (HisTag-GFPuv-Avitag-biotin serves as a "bridge" between the QD-SAV and the resin). As can be seen at a first glance (see **Figure 13.6**), the method succeeds in separating QDs bound to GFP from free QDs (this can be seen from the difference in migration: due to the negative charge of GFP, GFP-bound QDs migrate faster than free QDs (see **Figure 13.3**). Furthermore, the agarose gel analysis also gives an indication that the spatial constraints limit the GFP/QD ratio, judging from differences in migration (see **Figure 13.7**). The gel in **Figure 13.7** shows that QD-SAV::GFP that were prepared in solution, in saturating conditions (see **Figure 13.3**), migrated faster than QD-SAV::GFP that were prepared on solid support with the same ratio. This means that the steric constraints imposed by the solid support method reduce the number of GFP molecules bound to the QD-SAV to below the saturation, which is already detected in a preparation at nominal ratio of 16/1 (see **Figure 13.3**), even in conditions of very high excess (50/1).

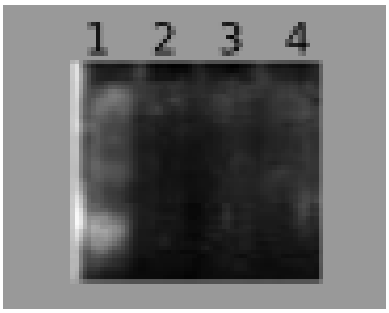

(a) *A first test for the solid support purification method. An agarose gel of the imidazole eluate in the following conditions (lane order): 1, using the standard protocol, with HisTag-GFP-biotin and later QD-SAV; 2, the same conditions, but no GFP (only QD-SAV added, to test non-specific binding); 3, using the standard protocol, with HisTag-GFP-biotin but with biotin-passivated QD-SAV; 4, using commercial 655 NH_2-PEG QDs, which are not supposed to bind neither GFP nor the resin. Here we would expect that only the active QD-SAV that were not passivated will be retained on the resin and then eluted. As we expected, the active QDs appear in lane 1 in this gel, and do not appear in the flow-through.*

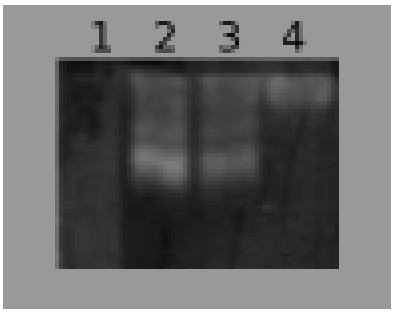

(b) *The flow-through (non-retained material that did not bind to the resin, and was washed away), analyzed using an agarose gel for the same conditions as above (lane order): 1, using the standard protocol, with HisTag-GFP-biotin and later QD-SAV; 2, using the normal conditions without GFP ; 3, using the standard protocol, with HisTag-GFP-biotin but with biotin-passivated QD-SAV; 4, using commercial 655 NH_2-PEG QDs (with low mobility). What we would expect in this case is that in experiments with no GFP, which serves as a "bridge" between the QD and the resin, experiments in which the QD-SAV were passivated (and therefore unable to bind the biotinylated GFP), or when using inert QDs (such as the 655 NH_2-PEG QDs), the QDs will not be retained on the resin and appear in the flow-through and not in the eluate. The results fit the expectations: the QDs appear in lanes 2,3,4 in this gel (the flow-through), and not in the eluate.*

Figure 13.6: *A first test for the solid-support coupling method: the first step is to show that within our limits of detection, no "free" QDs are retained on the NiNTA agarose beads. The results show that using the reactive QD-SAV, almost all the QDs appear in the eluate, whereas using passivated QDs (passivated QD-SAV or NH_2-PEG-QDs, which have no streptavidin) all the QDs appear in the flow-through. We therefore conclude that the specific binding of QDs to the resin is mediated by the biotin group of the HisTag-GFP-biotin. It is also possible that some QDs bind non-specifically to the resin but cannot be eluted by imidazole. Such QDs do not concern us except for the loss of material. In addition, there is a large difference in migration between the eluted QDs and the flow-through QDs (the ones that did not bind to the resin), due to the attached GFP which accelerates QD-SAV.*

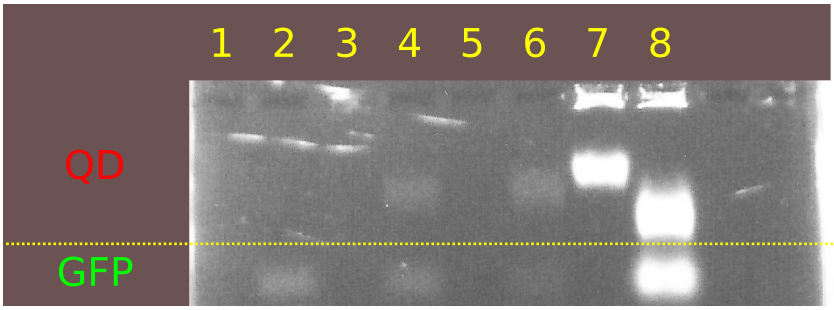

(a) *The first part of the gel: lanes 1-6 are arranged in couples of flow-through (whatever was not bound to the resin) and eluate for different conditions. Lanes 1,2 are for 1pmole QD-SAV+biotin (passivated), 50pmole HisTag-GFP-biotin; Lanes 3,4,5,6 are for 0.5pmole QD-SAV, 25pmole HisTag-GFP-biotin. Lane 7 contains 1pmole of QDs incubated with 300mM imidazole (as a control for quenching). Lane 8 contains QD-SAV mixed with HisTag-GFP-biotin in a ratio of 50/1, in solution.*

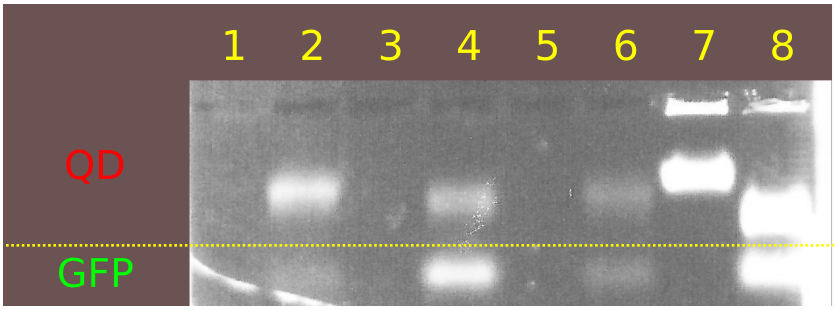

(b) *The second part of the gel: lanes 1-6 are arranged in couples of flow-through (whatever was not bound to the resin) and eluate for different conditions. Lanes 1,2 are for 1pmole QD-SAV, 50pmole HisTag-GFP-biotin; Lanes 3,4 are for 1pmole QD-SAV, 500pmole HisTag-GFP-biotin; Lanes 5,6 are for 0.5pmole QD-SAV,25 pmole HisTag-GFP-biotin. Lane 7 contains 1pmole QD incubated with 300mM imidazole (as a control for fluorescence quenching). Lane 8 contains QD-SAV mixed with HisTag-GFP-biotin in a ratio of 50/1. By comparing the pairs 1,2;3,4;5,6 we can see that QD-SAV are retained and then eluted, bound to GFP (together with some free GFP). The aggregates seen in wells 7 and 8, which probably come from the QD sample, are also absent in the eluted fractions.*

Figure 13.7: *Another example of the solid-support purification method. In short, HisTag-GFP-biotin was loaded on NiNTA resin, which binds HisTag. The resin was then washed from free GFP and loaded with QD-SAV (in order to bind to the GFP biotin group). The resin was then rinsed, to remove "free" QD-SAV, and then eluted with 300mM imidazole. The eluate was then loaded on an agarose gel for analysis. Interestingly, these gels support our argument that this method controls the valence of the complexes: when comparing lanes 6 and 8, both prepared with the same protein/QD nominal ratio, we can see a reproducible difference in migration. The QDs in lane 8, prepared in a solution with 50/1 ratio of GFP/QD, migrate faster than the QDs in lane 7, which were prepared on a resin using the same ratio. This implies that the QDs prepared in solution are bound to more GFP than the ones made on the resin. Furthermore, we have found, in gel assays, that the QD-SAV::GFP complexes already saturate at a ratio of 16/1, while here, the results show that QD-SAV::GFP complexes prepared on the solid resin, are not saturated even at a nominal ratio of 50/1 (they still migrate slower than the QD-SAV::GFP prepared in solution in saturating conditions (a protein/QD molar ratio of 50/1, way above the saturating conditions that were found for QD-SAV::GFP, 16/1, shown in* ***Figure 13.3****), and therefore, in average, have a less GFP molecules bound on a QD) meaning that the solid-support probably works efficiently to control stoichiometry.*

Potential application for stoichiometry control Even with the high excess of GFP to QD (50/1) used in our tests, the solid-support coupling of GFP to streptavidin QDs seems to result in a lower stoichiometry than coupling in solution at the same conditions (time, temperature and stoichiometric ratio). This can be seen by comparing the migration of of lanes 4 and 6 to lane 8, in **Figure 13.7(a)** and by comparing the migration of of lanes 2,4, and 6 to lane 8, in **Figure 13.7(b)**. The QD-GFP complexes prepared in solution migrate faster than the ones prepared on the resin (we have shown that in the case of GFP and commercial QD-SAV, the higher the GFP/QD stoichiometry, the faster the migration, see **Figure 13.3**.).

Quantitative argument If we knew the average surface density of biotinylated GFP, than the probability that a QD that is already bound to one protein would reach one or more proteins could be calculated using 2D/radial Poisson distribution. The Poisson distribution is usually written as:

$$Pr(N = n) = \frac{e^{-\lambda}\lambda^n}{n!} \tag{13.1}$$

In the context of the solid-support coupling, this is a probability mass function, describing the probability for having n neighboring protein molecules, within a given area, given a density parameter λ. Since in this case we are interested in having a monovalent probe, which is bound to one protein only, we "place" the origin on a given protein bound to the surface, and calculate the probability for n=0, *i.e.* for finding 0 neighboring proteins (a situation called "0 encounters", "0 hits" or "0 events") within a radius $r = R_{lim}$ from the origin, which is the diameter of the QD+two protein molecules (see **Figure 13.9**). The Poisson probability mass function for zero events is:

$$Pr(N = 0) = e^{-\lambda} \tag{13.2}$$

For a radial 2D case:

$$Pr(N = 0) = e^{-\rho\pi r^2} \tag{13.3}$$

Where ρ is the Poisson density parameter, and r spans the area for which we count the number of events (or "hits"). When applied to QD-protein surface coupling, ρ is the surface density of the proteins and r, as mentioned above, is the radius of the region that is spanned by a QD bound to a protein at the origin, and has a second protein bound to its surface (see **Figure 13.9**). The probability for more than 0 events, *i.e.* that the QD would encounter another protein except the one originally bound to it, is simply:

$$Pr(N > 0) = 1 - e^{-\rho\pi r^2} \tag{13.4}$$

The dependence of the function on r is also important, in order to understand the significance of QD size effect on this method. Therefore we differentiate equation 13.4 with respect to r, to get:

$$P(r)dr = 2\pi\rho r e^{-\rho\pi r^2} dr \tag{13.5}$$

This is a probability density function that describes the probability for having the first encounter (or "event") at a distance between r and $r + dr$, for a QD already bound to a protein at the origin. The maximum of this function can give us the most probable r for the first encounter with another protein:

$$r_{mp} = \sqrt{\frac{1}{2\pi\rho}} \tag{13.6}$$

which can be used to characterize the system.

In order to calculate the theoretical fraction of polyvalent QDs (under the assumptions that will be mentioned below), we substitute the expected diameter of a QD+two protein molecules

(see **Figure 13.8**) in equation 13.4 (or integrate equation 13.7 from 0 to the expected diameter of a QD+two protein molecules).

$$Pr(r) = \int_0^{QD+2XProt} 2\pi\rho r e^{-\rho\pi r^2}\, dr \tag{13.7}$$

A calculation using the experimental conditions From the manufacturer's data (SIGMA), the specific surface area of 6% agarose beads matrix is $5m^2/ml$. Therefore, if we load $50pmole$ of protein on $25ul$ of resin, and assume that all of it is bound and biotinylated (two very conservative assumptions), then the average surface density of biotinylated GFP is $\rho = 2.4 * 10^{14}\ GFPmolecules/m^2 = 2.4 * 10^{-4}\ GFPmolecules/nm^2$. Considering that the diameter of a GFP molecule is ∼4nm and that of a QD-SAV is ∼23nm, a QD can bind to two HisTag-GFP-biotin at the same time only if the distance between their attachment sites on the resin is smaller or equal to a "limit distance" (or radius) $R_{lim} = 23nm + 2 * 4nm = 31nm$, where the first term is the diameter of the QD-SAV followed by twice the diameter of GFP. Therefore, in order to know the fraction of polyvalent QDs in the sample, we use equation 13.4 with $r = R_{lim} = 31nm$. The predicted fraction of monovalent QD-SAV::GFP for the conditions described above is 48%. In addition, we can also calculate the most probable radius for first encounter:

$$r_{mp} = \sqrt{\frac{1}{2\pi\rho}} = 25.8nm \tag{13.8}$$

This number can be serve as a rough estimate, whether the given density is low enough to obtain a considerable fraction of monovalent QDs, knowing the size of the QD-protein complex. These calculations is based on several conservative assumptions: First, we assumes that all the GFP molecules that were added bound to the resin, and were biotinylated. Second, we assume that if two GFP molecules are separated by a distance smaller than R_{lim} and a QD-SAV binds to one of them, it will always bind the other one. Third, we also assume that the contact surfaces between beads are negligible (and therefore the binding of one QD-SAV to two GFPs on two different beads is also negligible).

The currently used method (and as far as we know, the only one) for stoichiometry control is based on gel separation. The QD-protein complexes are prepared, loaded on a gel and separated based on electrophoretic mobility. Then, the band corresponding to 1/1 (monovalent) is extracted from the gel. In a recent report, Howarth *et al.* [10] conjugated QDs to monovalent streptavidin and used this method, to purify the streptavidin-QD complexes with only one monovalent streptavidin on the surface, in order to make the QDs truly monovalent. This later allowed them to bind one biotinylated protein of interest per QD. This method, however, is somewhat limited. First, one is forced to use engineered, monovalent variant of streptavidin [102], which requires a complicated purification protocol, once the clone is obtained (under license from A. Ting). Our solid-support method does not require monovalent streptavidin, since even in the high surface density used in our experiment, if we substitute $r = 5nm$ (the diameter of streptavidin) instead of the size of a QD, the probability of binding more than one protein per streptavidin is very low (less than 2%). Our method can also be used with crude, partially degraded protein samples (thanks to the two-tag design).

We have demonstrated that this method can be used to obtain monovalent QDs using a simple calculation.

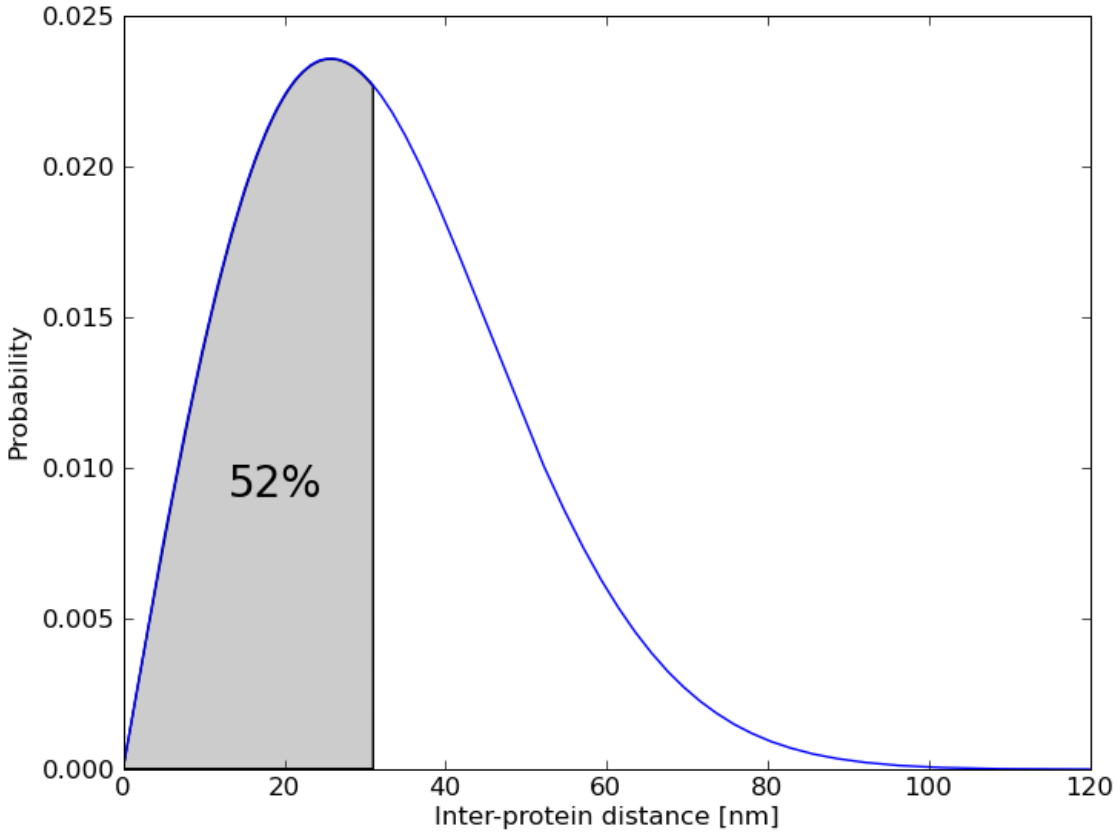

Figure 13.8: *A graph, showing the probability function for a first encounter between* r *and* $r+dr$*, with* $\rho = 2.4 * 10^{-4} nm^{-2}$*. This probability is simply calculated from equation 13.4, but here, as a demonstration, we plot equation 13.7 and integrate it (getting the same result). Equation 13.7 is integrated from 0 to 31nm, the diameter of a commercial, 655nm streptavidin-coated QD (QD-SAV) + twice the diameter of GFP, which yields a probability of 52% for non-monovalent QDs, or 48% for monovalent QDs.*

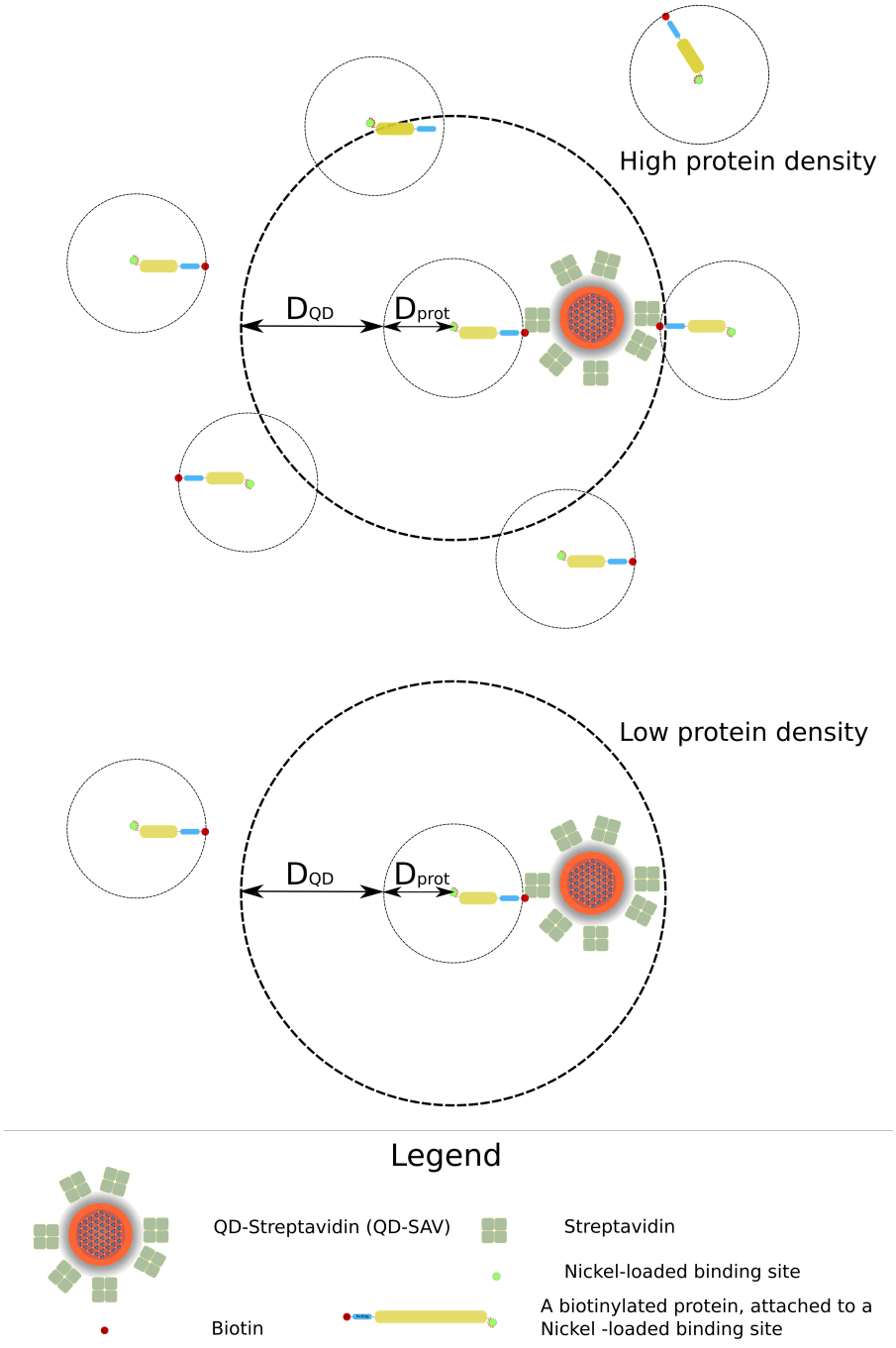

Figure 13.9: *A scheme showing how the valence of QDs can be controlled by the surface density of the biotinylated proteins bound to the resin (NiNTA resin in this case). At a high density, the proteins are closer to each other and therefore a QD-SAV is more likely, once bound to one protein, to reach its close neighbor. At a low surface density of proteins, a QD-SAV, bound to a given protein is less likely to bind another protein, since the proteins are further apart.*

Chapter 14

Intracellular targeting and tracking

With the purified proteins at hand and with the QD coupling and internalization protocols established, we moved on to intracellular targeting. This chapter starts with the various tests performed, in order to establish the targeting methods, and proceeds to the applications of targeting in asymmetrically dividing neuroblasts.

14.1 Preliminary tests

In order to validate the targeting methods, we performed a few preliminary tests. As a first targeting test, before we moved to QDs, we chose to use a small protein that specifically targets the cell nucleus.

14.1.1 Localization of dye-labeled nucleoplasmin in the nuclei of cells.

In order to see whether a protein retains its targeting functionality during the pinocytic influx procedure, we internalized a protein that targets a specific domain in the cell, and observed its intracellular localization pattern. The protein chosen was nucleoplasmin-HisTag (NP) [203, 202, 204]. This protein is a chromatin remodeling factor that enters the nucleus using its nuclear localization sequence (NLS), and then binds tightly to nucleosomes. It was expressed, purified and then incubated with Tris-NTA-Cy3 [225] (a functionalized dye with high affinity to HisTag). Subsequently, the excess, unbound dye was removed using a spin-column (Harvard apparatus), and the labeled protein was internalized using pinocytic influx. After letting the cells recuperate from the shock, they were mounted on the microscope and observed, using a Cy3 filter set. The cells have shown a strong fluorescent spot, coincident with the cell nucleus (see **Figure 14.1**).

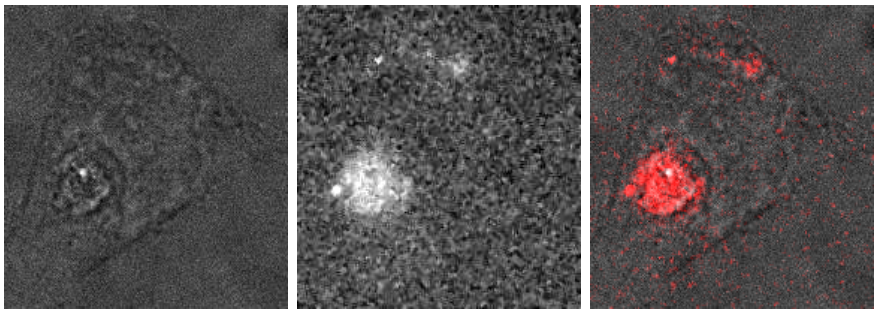

(a) *A transmission light image of a call.*

(b) *A fluorescent image (Cy3) of the cell, after the internalization of Cy3-NP using pinocytic influx.*

(c) *A superposition of the two channels.*

Figure 14.1: *The localization of nucleoplasmin-HisTag (NP) in the nucleus of 3T3 cells. NP was labeled with Cy3 and introduced into the cytoplasm of cells, using pinocytic influx. As can be seen in the figures, NP targeted the nucleus, using its nuclear localization sequence (NLS). This serves to show that the conditions inside the pinosomes do not necessarily impair the protein's ability to bind to its target, once it is again free in the cytoplasm.*

14.1.2 Localization Anti-GFP QDs in Fly brain cells expressing GFP/YFP labeled centrosomes

When trying to target intracellular proteins that are not statically localized in defined domains (*i.e.* have some diffuse, continuous localization pattern), using a small number of probes, it is harder to tell whether or not we have succeeded in targeting the protein. If we can assume that the ensemble localization pattern can be seen as an empirical probability density distribution, then when we have a few particles, we need to sample this distribution for very a long time, in order to have a localization pattern for the particles that agrees with it. Since this is the case for some asymmetrically localized proteins like PON, we needed to validate our targeting method on a defined target, before proceeding to the actual experiment. In order to do so, we chose to target the centrosomes, which are point-like intracellular structures. More specifically, we chose to use the protein Asterless [226, 227] (Asl), which is highly concentrated at the pericentriolar region (an amorphous mass of protein surrounding the centrioles). Asterless is a constitutive pancentriolar protein, involved in the organization of microtubule asters [228]. Therefore, we used a fly clone expressing Asl-YFP, driven by a ubiquitin promoter (and therefore expressed in all almost cell types). We collected third-instar larvae, dissected them as described in the methods section, and prepared glass cover-slips with the dissociated larval brains. Then, we used pinocytic influx to internalize anti-GFP QDs, pre-coupled as described in the methods section.

Results In 40% of the cells (14/35), we found a clear colocalization (pixel-on-pixel) between the QDs and the YFP signal. In 20% of the cells, we found that the QDs were localized (static or slowly diffusing) in the close vicinity (2-3 pixels) of the Asl-YFP signal. In the last 40%, the QDs appeared to freely diffuse inside the cell. The results show that at least some of the QDs can target the protein Asterless. The fact that not all QDs localized in the centrosomes can be attributed to the fact that pericentriolar proteins are relatively less accessible [229]. An example is shown in **Figure 14.2**.

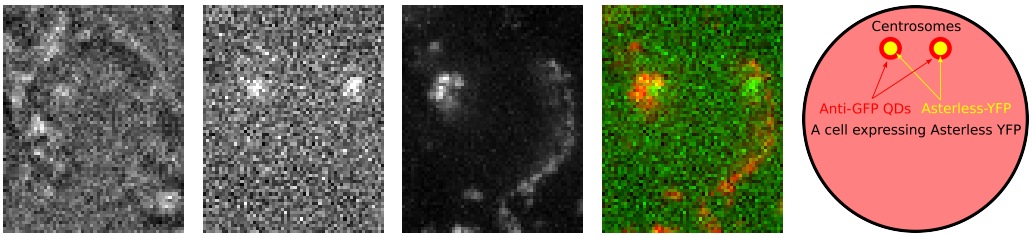

(a) *A transmission-light image of a fly brain cell.*

(b) *An image of the same cell at the YFP channel. The two centrosomes can be seen as two fluorescent spots.*

(c) *A maximum intensity projection of a movie in the QD channel, taken for this cell at a frame rate of 50ms.*

(d) *An overlay of the YFP image and the QD maximum projection, shows localization of QDs on one centrosome, and one QD that is diffusing inside the cell.*

(e) *The expected pattern of localization for QD::AntiGFPIgG inside cells expressing Asterless-YFP.*

Figure 14.2: *Targeting the pancentriolar protein Asterless fused to YFP, using anti-GFP QDs. For clarity, YFP is shown in green in multicolor images.*

14.2 Targeting PON-GFP with anti-GFP QDs (QD::AntiGFPIgG)

As explained in the **Introduction**, PON is adaptor protein implicated asymmetric cell division. At the onset of prophase, PON becomes polarized and concentrates mostly at the neuroblast's basal cortex (see **Figure 2.7,14.3(a)**). In PON-GFP expressing neuroblasts PON can be seen as a fluorescent crescent in the GFP channel. After having found that PON is a very unstable protein and therefore not suitable for coupling to QDs *in-vitro*[1], we decided to use and endogenous targeting strategy instead, and target the endogenously expressed PON-GFP, using QDs functionalized with an anti-GFP antibody (QD::AntiGFPIgG), which are described in the **Methods** part. The next step was to target endogenously expressed PON4-GFP in *Drosophila* neuroblasts. Third-instar larvae from PON4-GFP-expressing *Drosophila melanogaster*, which we obtained using the genetic manipulations described in the **Methods** part, were collected and dissected, in order to collect brains. The brains were dissociated and cultured on glass cover-slips as described in the **Methods** part. Then, the functionalized QDs were internalized into the cells using the pinocytic influx method (also described in the **Methods** part). Cells were left to recuperate for ∼30' and then mounted on the microscope to be observed. As in all ACD experiments, the neuroblasts were identified using their fluorescent PON-GFP crescent, since the expression of PON-GFP is driven by the Insc driver, which is specific for neuroblasts. Using the appropriate filter sets for GFP and 655nm QDs in conjunction with a UV lamp and a CCD camera, movies were collected at frame rates of 15-50ms. The movies were then processed with the MTT algorithm [208] (see **Methods**), in order to detect QD spots. Then, the positions of QDs were transformed into a polar coordinate system and normalized, in order to pool all the results together and analyze them on the same coordinate system. As a control, we have performed a similar experiment, using quantum dots coupled to an inert antibody (anti-mouse secondary antibody).

[1]It is still possible though, that using our solid-support coupling method, coupling QDs to PON will still be possible, as this method is suitable for partially degraded samples (see **Methods**).

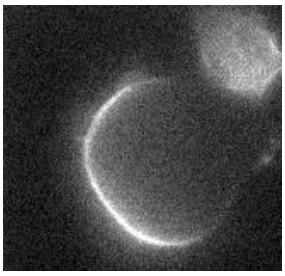

(a) *A dividing neuroblast expressing PON-GFP, after the internalization of anti-GFP conjugated QDs: GFP channel.*

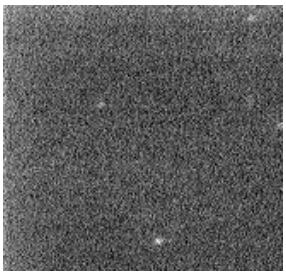

(b) *A dividing neuroblast expressing PON-GFP, after internalization of anti-GFP conjugated QDs: GFP channel.*

(c) *A dividing neuroblast expressing PON-GFP, after internalization of anti-GFP conjugated QDs: a maximum intensity projection of a movie taken in the QD channel*

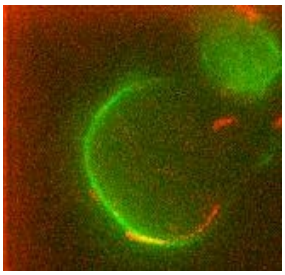

(d) *A superposition of the image taken in the GFP channel and the maximum-intensity projection of the movie in the QD channel.*

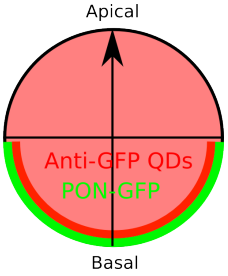

(e) *The expected localization pattern for anti-GFP QDs in dividing neuroblasts expressing PON-GFP (PON-GFP is indicated in green and QDs are indicated in red).*

Figure 14.3: *An example for a colocalization of anti-GFP QDs and PON-GFP.*

Analysis An observation of the movies by eye revealed a clear localization of the functionalized QDs in the basal part of the cell ($90\% basal, N_{cells} = 30$), whereas the control experiments, which used quantum dots coupled to an inert antibody QD::InertAntibody), have not shown any specific localization ($50\% basal, N_{cells} = 26$). The colocalization of QDs and GFP was further analyzed by plotting angular histograms of the GFP signal and detected QDs, for the actual experiment (using QD::AntiGFPIgG) and the control experiment (using inert QDs with

an anti-mouse secondary antibody - QD::InertAntibody).

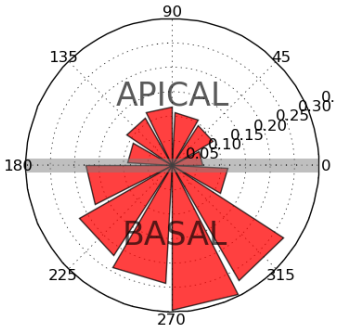

(a) *An angular histogram of detected targeted QDs.*

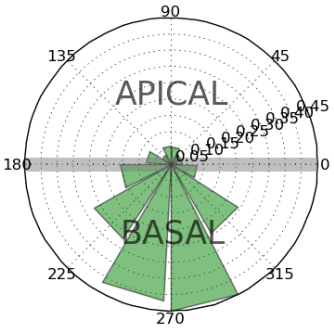

(b) *A reference angular histogram of the GFP signal for targeted QDs (serves as a directional marker).*

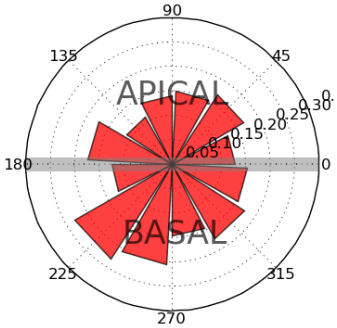

(c) *Angular histogram of detected QDs in control experiments.*

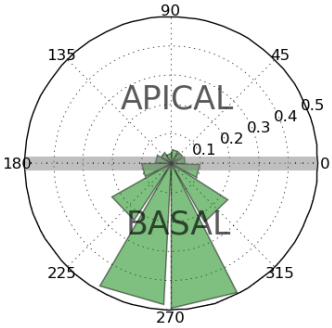

(d) *Reference angular histogram of the GFP signal for the control experiments (serves as a directional marker).*

Barycenter analysis The main limitation of the histogram representation is, that it can become biased towards movies of cells with many QDs, since it counts the total number of detected QDs. Therefore, in order to get a more balanced representation, we calculated the barycenters of all the spots detected in the QD channel, for each given cell and plotted them using a common polar coordinate system (thus giving each cell an equal weight, whereas in the latter method, movies with more detected QDs have a more significant weight).

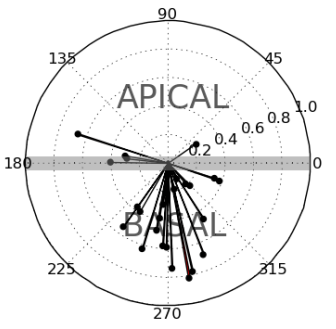

(e) *Barycenters of the Anti-GFP conjugated QDs,* ***targeting the protein PON-GFP****.*

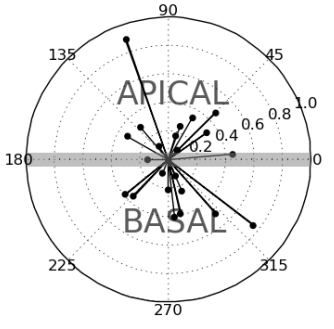

(f) *Control-Barycenters of QDs conjugated to secondary antibodies (with no known specificity in Drosophila neuroblasts).*

Colocalization scores An additional method of analysis was our colocalization "scoring" method (see **Methods**). We applied the algorithm described in the **Methods** part, on the data from the experiments with the activated QDs (QD::AntiGFPIgG), as well as for the control (QD::InertAntibody using an inactive secondary antibody). For every cell, the algorithm assigned a colocalization score, based on the localization bias of the QDs towards the PON-GFP signal. The results are represented in boxplots (this representation was chosen, as it does not imply anything on the distribution of the data.). We then used the Kolmogorov-Smirnov test, for the distributions of scores, comparing QD::AntiGFPIgG and QD::InertAntibody, to verify the statistical significance of these results. The test gave a P-value of 0.029, which we consider as significant (less than 0.05).

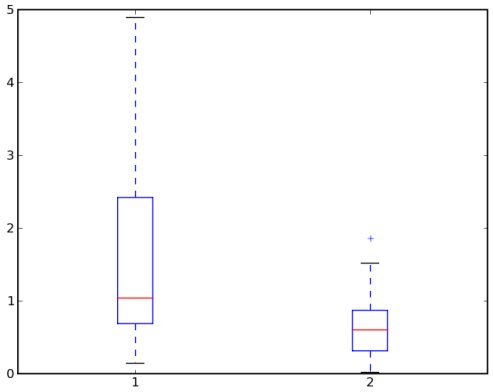

Figure 14.4: *Box plots of the localization scores: 1, for QD::AntiGFPIgG; 2, for QD::InertAntibody (control experiment).*

14.3 Localization of Miranda in mitotic neuroblast cells

On the timeline of cell division, Miranda polarization occurs after PON polarization. While the former forms a crescent as early as prophase, the latter forms a basal crescent only at metaphase. In this experiment, purified, monobiotinylated Miranda protein was incubated with QD-SAV, according to the ratio determined on an agarose gel (1/8, see **Figure 13.2**). After the incubation, free biotin binding sites on the QDs were saturated with excess biotin. Then, the QD-SAV::Miranda complexes were internalized using the pinocytic influx method, into plated, dissociated brain cells from PON-GFP flies, prepared beforehand. After recovery in an incubator, the sample was mounted on the microscope and observed using the appropriate filter sets.

The recorded movies, taken at a frame rate of 15-50ms, were first processed by the MTT software [208], in order to produce trajectories of different lengths. The trajectory data were then fed into our colocalization software, in order to analyze the efficiency of the targeting.

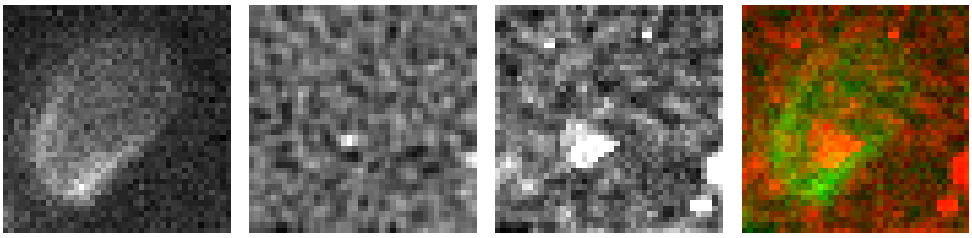

(a) *A dividing neuroblast expressing PON-GFP, after internalization of Miranda-conjugated QDs: GFP channel.*

(b) *A single image, in the QD channel.*

(c) *A dividing neuroblast expressing PON-GFP, after internalization of QD-SAV::Miranda: a maximum intensity projection of a movie taken in the QD channel*

(d) *A superposition of the image taken in the GFP channel and the maximum-intensity projection of the movie in the QD channel.*

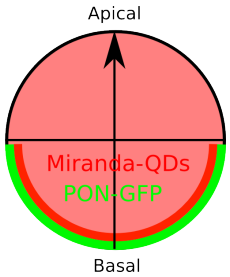

(e) *The expected localization of QD-SAV::Miranda in dividing neuroblasts expressing PON-GFP.*

Figure 14.5: *An example for a colocalization of QD-SAV::Miranda and PON-GFP.*

Analysis Like in the case of PON, we plotted angular histograms for the QD and GFP signal.

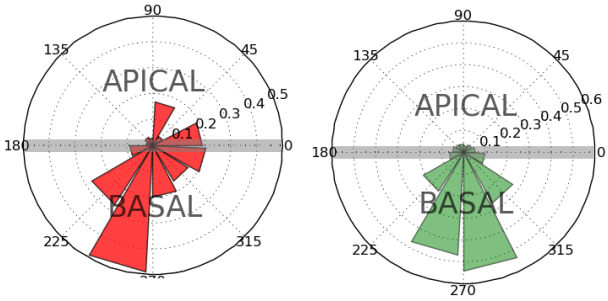

(a) *An angular histogram of detected targeted QDs (QD-SAV::Miranda).*

(b) *A reference angular histogram of the GFP signal for targeted QDs.*

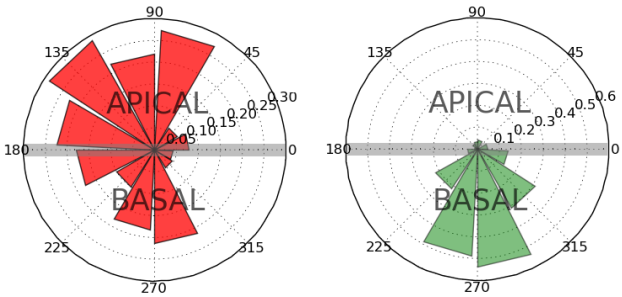

(c) *An angular histogram of detected QDs in control experiments (QD-SAV::biotin).*

(d) *A reference angular histogram of the GFP signal for the control experiments.*

Chapter 14

Barycenter analysis Similarly to what was done for PON, we have calculated the barycenter of all detected QDs for each cell, normalized all points into a single, polar coordinate system and plotted the results. As can be seen in the following comparison between the QD-SAV::Miranda and the passivated QDs, (QD-SAV in which all the streptavidin has been passivated with biotin, QD-SAV::biotin) the QDs are indeed localized in the basal part of the cell, as is expected from the Miranda protein. An analysis of the barycenter localization for QDs showed 85% basal localization for the QD-SAV::Miranda (22/26) vs. 57% for the control (for which we should expect something around 50%). This deviation should probably be explained by the later polarization of Miranda.

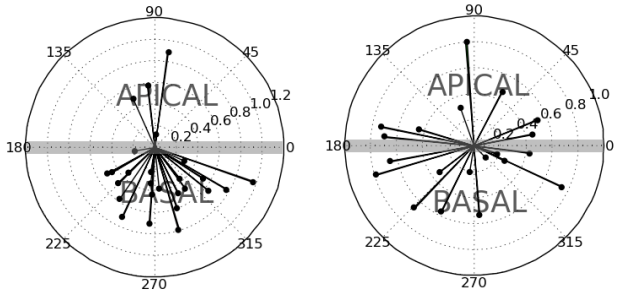

(e) *Barycenters of QD-SAV::Miranda.*

(f) *Barycenters of the inert QDs (QD-SAV::biotin) in control experiments.*

Colocalization scores We have also analyzed the localization of QD-SAV::Miranda using our scoring method. By looking at the box-plots, it is clear that Miranda-QDs do localize in the basal part of the cell. The results were validated using a Kolmogorov-Smirnov test for the distribution of scores that yielded a significant P-value of 0.036

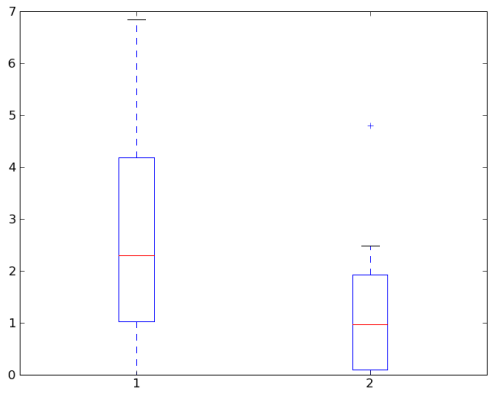

Figure 14.6: *Box plots of the localization scores: left, QD-SAV::Miranda; right, control experiments (QD-SAV::biotin).*

14.4 Localization of Pins in neuroblast cells

The protein Pins (partner of Inscuteable), is known to be localized in the apical cortex, and to be implicated in spindle alignment. However, the mechanism by which Pins localizes is still under debate. Especially, the mode of movement of Pins inside the cell when it is not localized, is not known. Following the coupling of QD-SAV and biotinylated Pins, the complexes were internalized into neuroblasts, and observed. The movies, taken at frame rates of 15-50ms, were analyzed by detecting QD signal and calculating the colocalization (or exclusion, in this case, since Pins is excluded from the area where GFP-PON is) using our colocalization software.

14.4.1 Localization of Pins in dividing neuroblast cells

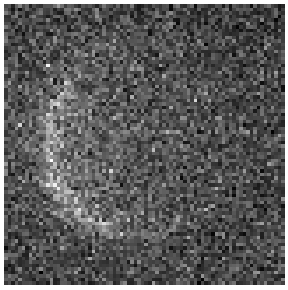

(a) *A dividing neuroblast expressing PON-GFP, after internalization of streptavidin QDs coupled to biotin-Pins (QD-SAV::Pins): GFP channel.*

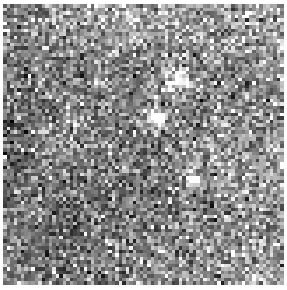

(b) *A single image of QD-SAV::Pins inside the dividing neuroblast.*

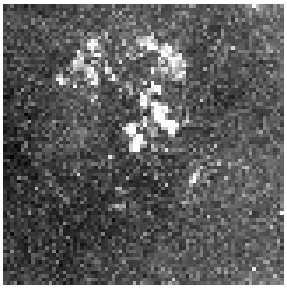

(c) *A dividing neuroblast expressing PON-GFP, after internalization of QD-SAV::Pins: a maximum intensity projection of a movie taken in the QD channel.*

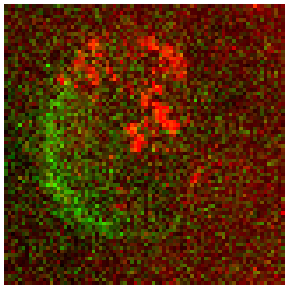

(d) *A superposition of the image taken in the GFP channel and the maximum-intensity projection of the movie in the QD channel.*

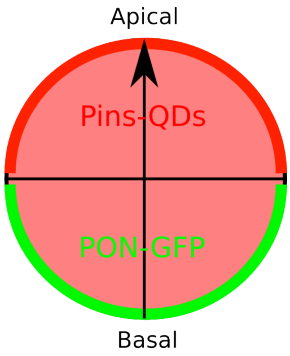

(e) *The expected distribution for QD-SAV::Pins in dividing neuroblasts.*

Figure 14.7: *An example for Pins localization in PON-GFP neuroblasts. Pins seems to be localized in the apical part of the cell (PON serves as a marker for the basal part).*

Analysis An observation of QD-SAV::Pins inside dividing neuroblasts, reveals a rather limited spatial distribution, concentrated at the apical part of the cell.

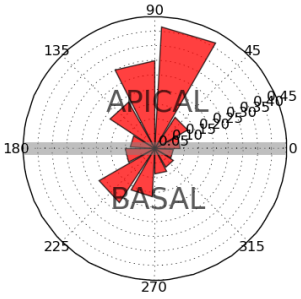

(a) *An angular histogram of QD-SAV::Pins.*

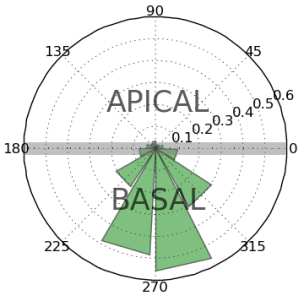

(b) *A reference angular histogram of the GFP signal for the targeting experiments with QD-SAV::Pins (GFP serves as a directional marker).*

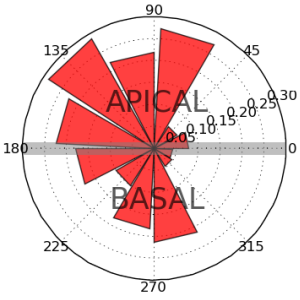

(c) *An angular histogram of detected passivated QDs (QD-SAV::biotin) in control experiments.*

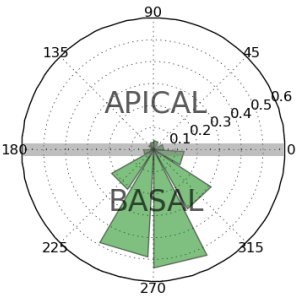

(d) *A reference angular histogram of the GFP signal for the control experiments (GFP serves as a directional marker).*

Chapter 14

Barycenter analysis In the case of QD-SAV::Pins, the barycenter analysis shows that in most cells, the QD-SAV::Pins were localized in the apical part of the cell. The effect can be seen even more clearly when comparing the QD-SAV::Pins with the QD-SAV::Miranda. We found that in 80% of the cells (20/25), the barycenter of the detected QD spots was in the apical "hemisphere", vs. 46% (11/24) in the control dataset, using QD-SAV::biotin (where we would expect around 50%).

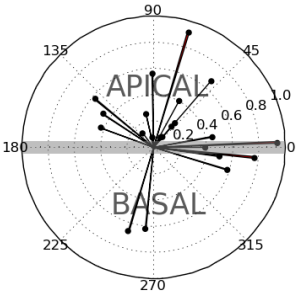

(e) *Barycenters of **QD-SAV::Pins**.*

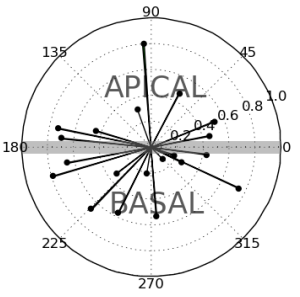

(f) *Barycenters of the **inert QDs** (QD-SAV::biotin) in control experiments.*

Colocalization scores Here, as expected, the analysis shows an opposite trend to that of Miranda or PON. In the experiments performed with QD-SAV::Pins, we can see that the scores are **lower** then in the experiments conducted with passivated QDs (QD-SAV::biotin). This is because the apically localized QD-SAV::Pins shows less overlap with the PON-GFP signal than the QD-SAV::biotin. The significance of the results was verified using a 2-sample Kolmogorov Smirnov test that yielded a P-value of 0.032. In this calculation the number of cells with QD-SAV-Pins is 25, and for the control the number of cells is 24 (the control dataset, using passivated QD-SAV, is the same one which was used as a control for Miranda).

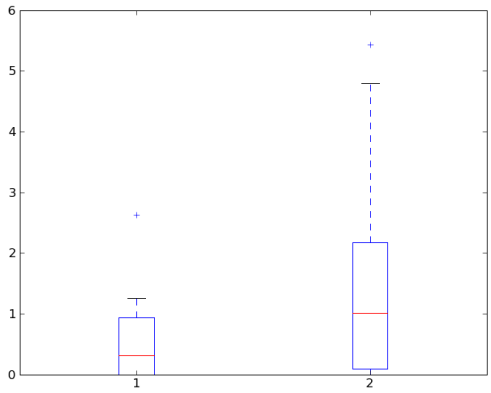

Figure 14.8: *Box plots of the localization scores: left-target QDs, right-control experiments.*

14.4.2 Polarized vs. unpolarized cells

Even though this project concentrates on dividing neuroblasts, observations made on non-polarized cells into which QD-SAV::Pins were internalized reveal a striking difference in the behavior, compared to polarized neuroblasts. In these cells, the QDs were practically immobile, whereas in polarized neuroblasts they were mobile, although limited to the apical domain.

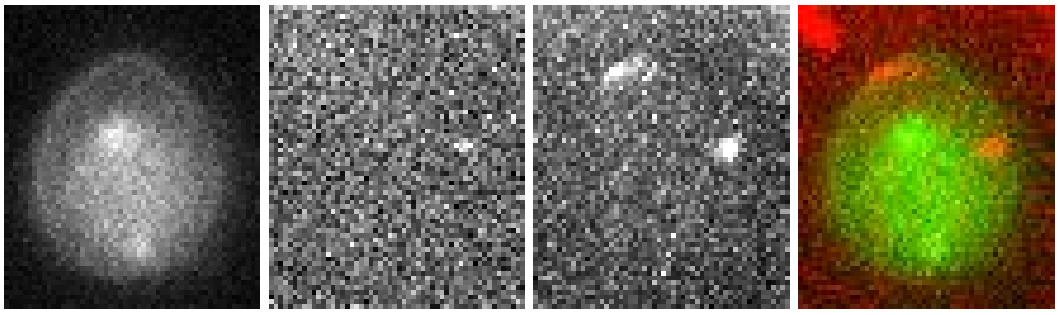

(a) *An interphase PON-GFP neuroblast, following an internalization of QD-SAV::Pins, GFP channel.*

(b) *A single image at the QD channel, of the PON-GFP neuroblast, after the internalization of QD-SAV::Pins using the pinocytic influx method.*

(c) *The interphase PON-GFP neuroblast, following an internalization of QD-SAV::Pins, a maximum projection of the QD channel.*

(d) *A maximum-intensity projection of the QD channel (in red), superimposed on the GFP image of an interphase neuroblast cell, expressing PON-GFP. This image shows the typical localization pattern for such cells: QDs are confined in small areas, practically immobile.*

Chapter 15

ScFv functionalized QDs

15.1 Introduction

As mentioned in the **Introduction**, SQDT imposes strict requirements on the quality of QD probes: They are required to be specific to their target, tightly binding and ideally, monovalent. The first requirement can be met by various targeting molecules such as IgGs or streptavidin, provided that the QD itself does not form significant non-specific interactions with the biological medium. These two examples usually also have high affinity to tier target. The second requirement, monovalence, is one of the major challenges in single particle tracking. Even though sometimes seems like a minor detail is one of the major challenges in SQDT. The most prominent (and probably the only) example for monovalent probes is the work done by Howarth *et al.* [10].

The specificity and high affinity of antibodies hold a lot of potential for such experiments. However, immunoglobulins are at least divalent (*e.g.* IgGs, see **Figure 15.4(b)**), and therefore may crosslink two molecules of interest, which may yield uninterpretable results (see **Introduction**). For this reason, we are using ScFvs (Single chain variable fragments), which are monovalent antibody fragments, that consist of a fusion between the variable part of the heavy and light (VL and VH) chains via a flexible peptide linker (see **Figure 15.1(g)**). They are relatively small (<30kD) and can be produced in various expression systems much more easily than IgGs. These properties make them good candidates for therapeutics (*e.g.* ScFv-based systems to target tumors having short retention time and high accessibility). While in the pharmaceutical research monovalence is usually not important (in fact, in some cases multi-ScFv constructs were used, sometimes even combining different functionalities), for single molecule tracking it is crucial.

Howarth *et al.* [10] reported using an engineered ScFv, to which a single cysteine was added in order to allow chemical biotinylation and subsequently binding to monovalent streptavidin QDs that were purified from an agarose gel. In this work, we use a simpler scheme to prepare monovalent ScFv QDs that can target a very common protein tag, GFP. GFP and its variants, such as YFP and CFP, are widely used in fluorescence imaging, as fusion tags for endogenously expressed proteins. Many such applications have been reported, in which GFP did not interfere with the function of the protein to which it was fused. Therefore, by using such a probe, one can take advantage of the wide variety of existing cellular systems (either transfected or stable cell lines) that already have a GFP fusion tag, in order to address biological questions, at the single molecule level. Another component of this targeting system are EO6D-QDs. These are quantum dots coated with a synthetic peptide, which contains three cysteine amino acids, a PEG chain and an aspartic acid ligand [230]. These quantum dots bind to HisTag with a nanomolar affinity. Another advantage of the EO6D-QDs, is that their coating, small peptides, makes them significantly smaller than commercial QDs (∼10nm vs ∼25nm).

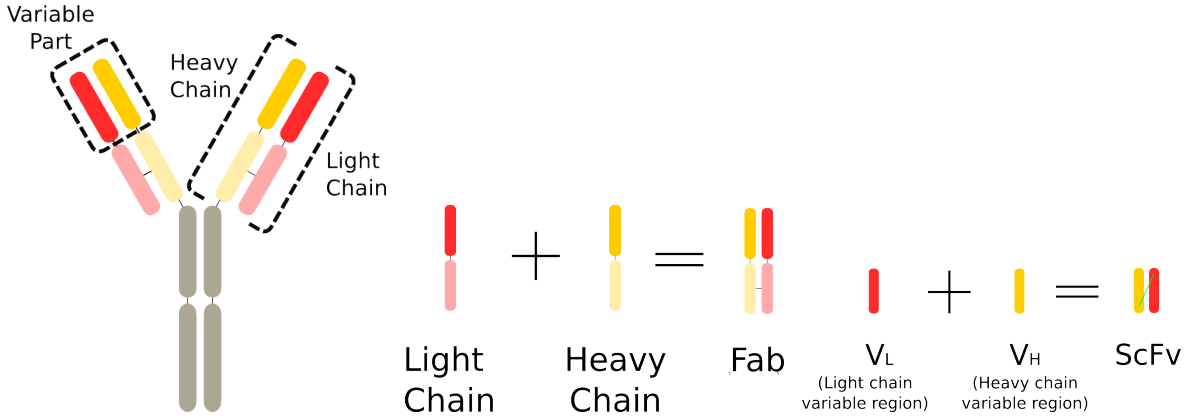

(e) *A full IgG* (f) *An Fab fragment* (g) *A single-chain variable fragment (ScFv).*

Figure 15.1: *A scheme of different IgG fragments.*

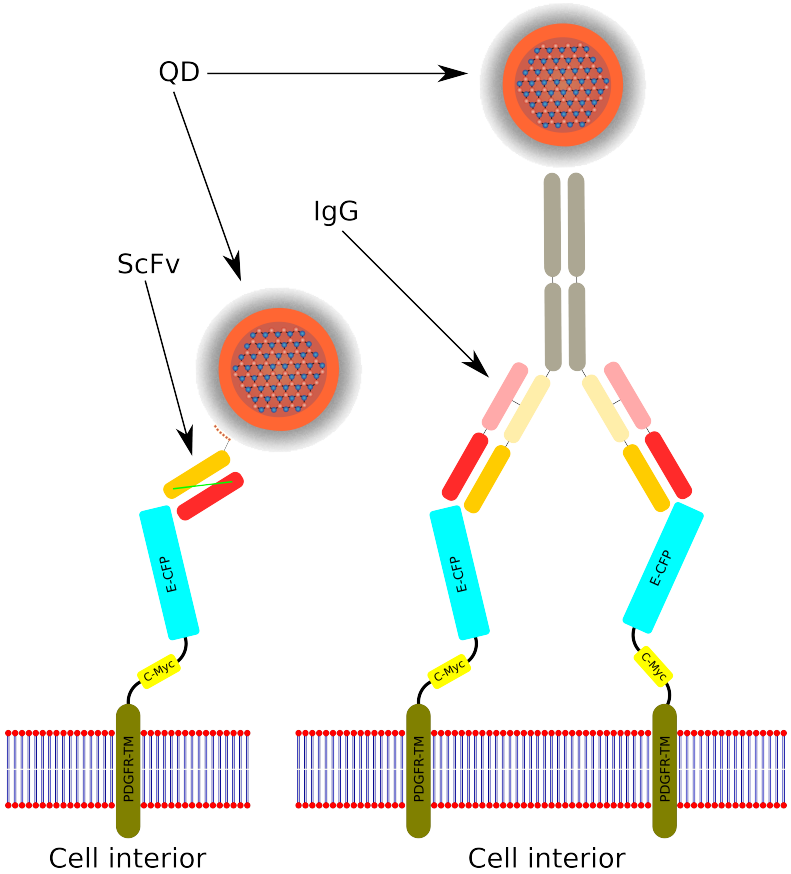

Figure 15.2: *A comparison between a QD with a single ScFv and a QD with a single IgG (divalent antibody). Even in an ideal case, where a QD is attached to only one IgG, it can still bind two targets, wheres the ScFv can only bind one. In the case of membrane receptors (like PCMX), crosslinking two membrane receptors my may also have physiological implications (such as for receptor dimerization). The membrane protein in this schematic represents the construct we used for targeting, which is based on the pDisplay plasmid and has the transmembrane domain of the PDGF receptor, fused to a myc tag and enhanced CFP (E-CFP), which is a variant of GFP, and therefore can be targeted by the anti-GFP ScFv.*

Types of ScFv-conjugated QDs used in this project We have used three types of QDs in this project: 655nm NH_2-PEG-QD::polyScFv, EO6D-QD::polyScFv, EO6D-QD::monoScFv. The first uses a non-specific coupling of the ScFv to the QD using a the homobifunctional crosslinker BS_3 (Pierce), the second uses the affinity of QDs coated with the peptide EO6D to HisTag, in order to bind multiple ScFvs, whereas the last also uses this phenomenon, but in a controlled manner, using the conditions derived from the results of the agarose gels (see **Figure 15.6**) to obtain monovalent QDs. In the following sections we will compare the diffusion of these QDs, when attached to PCMX.

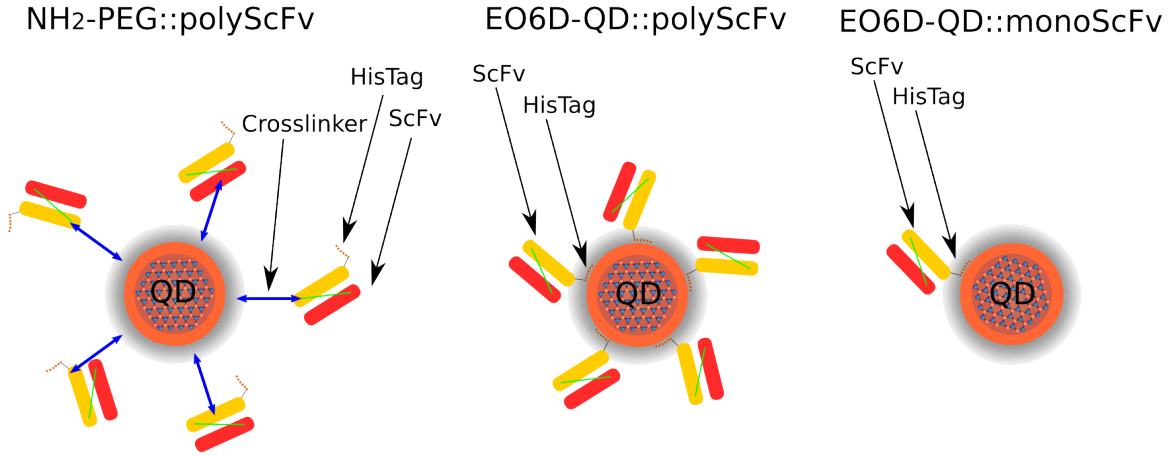

Figure 15.3: *A scheme showing the various types of ScFv QDs used in this project. On the left, 655nm NH_2-PEG-QD::polyScFv (a NH_2-PEG-QD labeled with many ScFvs, using a crosslinker). In the middle, EO6D-QD::polyScFv (EO6D with many HisTag-ScFv bound to it). On the left EO6D-QD::monoScFv (EO6D with one HisTag-ScFv bound to it).*

15.2 Preliminary *in-vitro* tests

After having successfully purified the anti-GFP ScFv, we performed a simple "binary" test to determine whether the ScFv binds to GFP. This was done *in vitro*, using two eppendorf tubes. In one tube, we immobilized ScFv on a NiNTA resin (the ScFv has a HisTag), while the other only contained the resin. Then, the resin was rinsed, and crude MBP-GFP-PON (described in the **Methods** part) was added (see **Figure 15.4(b)**). After rinsing off unbound MBP-GFP-PON, we observed both tubes under UV excitation. As can be seen in **Figure 15.4(a)**, the resin that was functionalized with ScFv was found to be fluorescent (*i.e.* it bound the MBP-GFP-PON), whereas the resin that was not pre-loaded with ScFv showed no fluorescence.

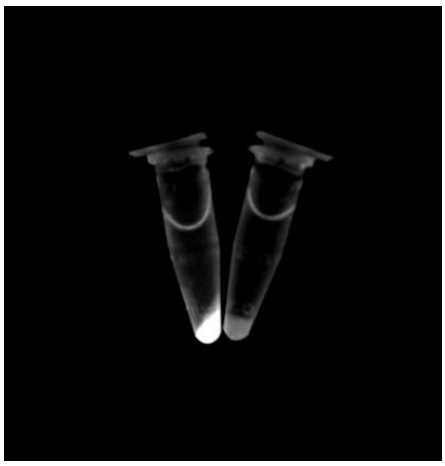

(a) *A first, "binary", in-vitro binding test, for the purified anti-GFP ScFv. The tube on the left contains NiNTA resin that was pre-loaded with ScFv, prior to incubation with MBP-GFP-PON, whereas the one on the right was not pre-loaded with the anti-GFP ScFv. After incubation with MBP-GFP-PON and an extensive wash, both tubes were observed under UV excitation. Clearly, only the resin that was loaded with anti-GFP ScFv is fluorescent and therefore, binds to GFP. This test gives a first, simple indication that the ScFv are functional.*

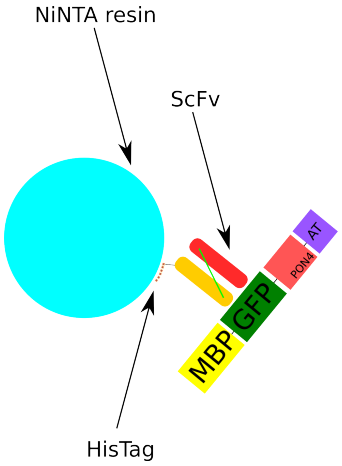

(b) *A scheme of the in-vitro binding test.*

Figure 15.4: *A first, "binary" in vitro test, to show that the ScFvs bind GFP.*

15.3 Quantification and binding kinetics

The binding kinetics of the anti-GFP ScFv were measured on a Rif/TIRFS system [22], described in the **Methods** part (see **Figure 15.5**). The resulting thermodynamic dissociation constant was $K_d = \frac{[ScFv][GFP]}{[ScFv \bullet GFP]} = 480 \pm 90nM$, and the dissociation rate constant was $k_d = 2.4 * 10^{-3} sec^{-1}$. With such a rate constant, if we neglect re-binding, the number of bound QDs goes down by a factor of $\frac{1}{e}$ every 7'. In the field of single molecule imaging, this is considered as a low affinity. IgG antibodies usually have much higher affinities: In some cases, it has been shown that only the divalence of an antibody can increase its affinity towards its target by up to three and even four orders of magnitude [231, 232]. Even so, the affinity of optimized ScFvs can be much higher than what we found: Wittrup *et al.* [233] have developed, by directed evolution, an ScFv with a 48fM affinity to its target. Even though the affinity is relatively low,

this targeting method can still be used for some biological applications where the timescale in on the order of 10'.

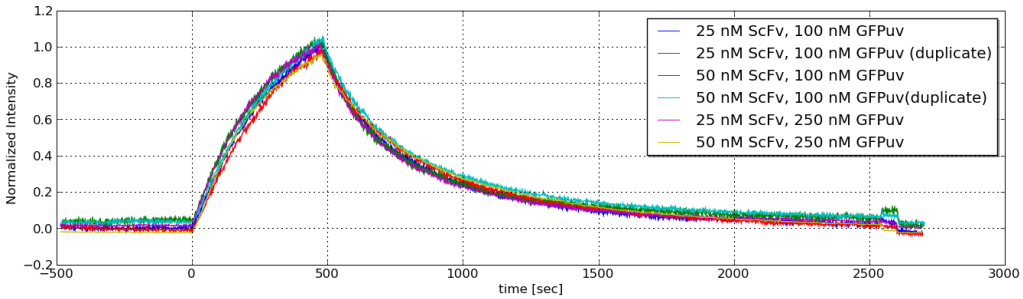

Figure 15.5: *Binding measurements for anti-GFP ScFv on a TIRFS system (the method is explained in detail in the* ***Methods*** *section.).*

15.4 Agarose gel electrophoresis

In order to characterize the binding of QD-EO6D to the anti-GFP ScFv, we prepared QD-EO6D::ScFv complexes with different nominal stoichiometric ratios, and analyzed them on an agarose gel. The results show a good separation between complexes of QD-EO6D::ScFv with different ScFv/QD ratios. These results were used to determine the optimal coupling conditions for the tracking experiments. In order to have monovalent probes, we used the conditions in lane no. 2, *i.e.* conditions in which almost all the QDs have either 0 or 1 ScFv bound to them. This way, the free QDs will not bind to the cells, and will be washed away and only the ScFv-bearing QDs, which will be monovalent, will bind to the target protein.

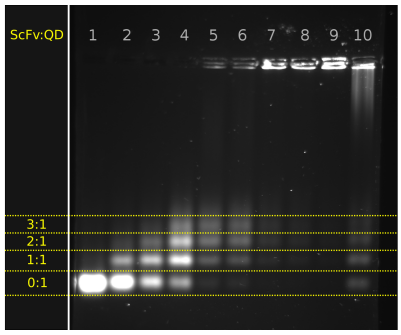

Figure 15.6: *An agarose gel showing the high resolution that can be obtained by combining EO6D-coated QDs and anti-GFP ScFvs. The lanes were loaded with linearly increasing ratios of ScFv/QD. Starting from 0 (lane 1),1.3/1,2.6/1,3.9/1...., until 10.2/1 (lane 9). Lane 10 has an ScFv/QD ratio of 10.2 supplemented with 400mM Imidazole. On the left, the ScFv/QD ratio is indicated in yellow. It can be seen that the imidazole removes some of the ScFv from the QDs, but not all.*

15.5 Experiments on live cells and tracking of single GFPs

After having shown that the ScFv can bind GFP *in-vitro*, we now needed to show that indeed, it can be used to target GFP variants *in-vivo*. As a first test, we incubated the cells transfected with PDGFR-CFP-MYC extracellular domain (PCMX) with dye labeled anti GFP ScFv: the

HisTag single chain fragment was incubated with a Tris-NTA Cy3 dye, which binds tightly to HisTag [234], and then incubated with the cells. Images were taken and analyzed for colocalization (see figure 15.8). The images show significant and specific colocalization between the labeled ScFv and the PCMX when looking by eye (see **Sub-Figures 15.12(d)- 15.7(a)**). A more quantitative analysis was performed using cytofluorograms (a scatter-plot of the two channel intensities for every given pixel) and intensity correlation plots (correlating the product of the deviations for the mean in both channels with the intensity in a given channel), which are discussed in the **Methods** part. These showed a good colocalization for the dye labeled ScFvs, and no significant colocalization for the negative control (Tris-NTA Cy3 with no ScFv).

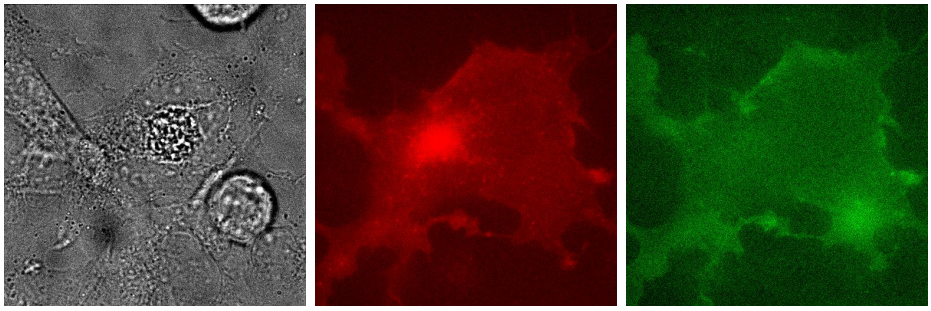

(a) *A transmission light image(indicative of the specificity of the ScFv to CFP expressing cells).*

(b) *An image in the CFP channel.*

(c) *An image in the Cy3 channel.*

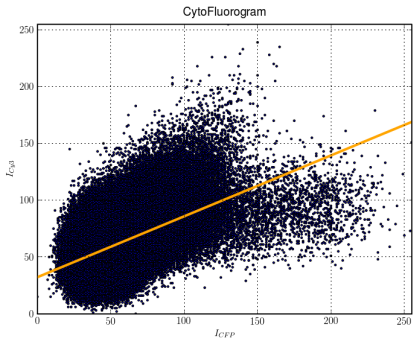

(d) *A cytofluorogram for a colocalization test*

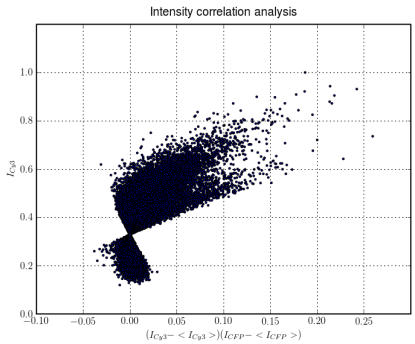

(e) *An intensity correlation analysis for a colocalization test.*

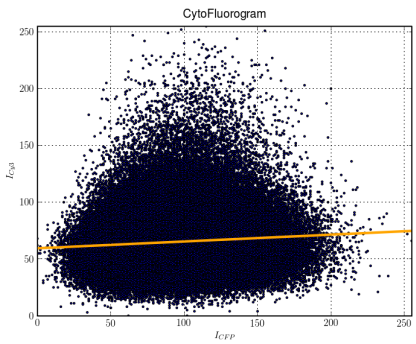

(f) *A cytofluorogram for a control.*

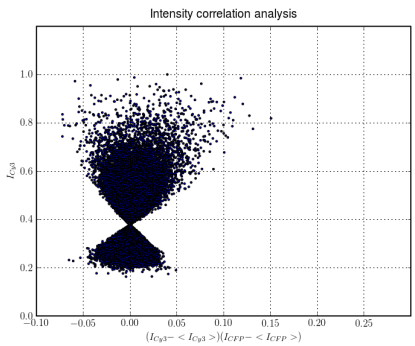

(g) *An intensity correlation analysis for a control*

Figure 15.7: *A colocalization test for the dye labeled anti-GFP ScFv and a CFP labeled receptor. This test shows that a dye-labeled ScFv can bind to the CFP labeled receptor.*

15.6 Polyvalent ScFv QD

15.6.1 655nm NH_2-PEG-QD::polyScFv

colocalization

As a first test for ScFv-QDs with live cells, we prepared polyvalent ScFv QDs using non-specific, chemical conjugation. We used the homobifunctional crosslinker BS_3 (Pierce) to chemically conjugate anti-GFP ScFvs to commercial NH_2-PEG-QD (Invitrogen). The reaction was performed using a high nominal ratio of 20 ScFv/QD. These QDs were incubated for 5' with HeLa cells transfected with a plasmid encoding for PCMX (see figure 15.2). We then rinsed off unbound QDs and observed the cells. The binding of the 655nm NH_2-PEG-QD::Poly-ScFv QDs was found to be specific to transfected cells.

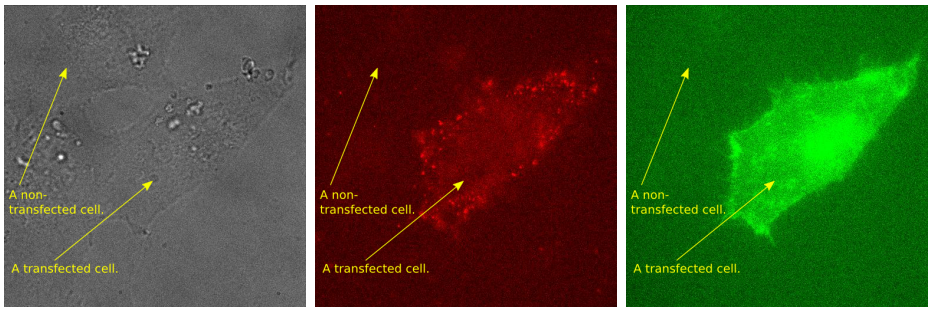

(a) *A transmission light image of the cells, revealing the non-transfected cells, which were not targeted by the QDs.*

(b) *An image taken at the QD channel (655nm), showing the bound QDs.*

(c) *An image taken at the CFP channel showing that indeed, the cell to which the QDs are bound is transfected and expressing PCMX.*

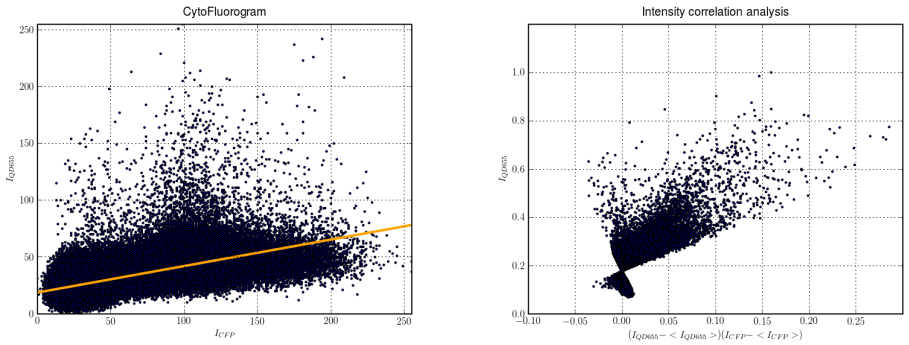

(d) *Cytofluorogram describing the colocalization of NH_2-PEG-QD::polyScFv (QD channel) and PCMX (CFP channel).*

(e) *Intensity correlation analysis (ICA) describing the colocalization of NH_2-PEG-QD::polyScFv (QD channel) and PCMX (CFP channel).*

Figure 15.8: *The colocalization of NH_2-PEG-QD::Poly-ScFv and PCMX.*

Single QD tracking

In the next step, the movement of NH_2-PEG-QD::Poly-ScFv QDs, attached to PCMX in HeLa cells, was tracked and analyzed using MSD analysis.

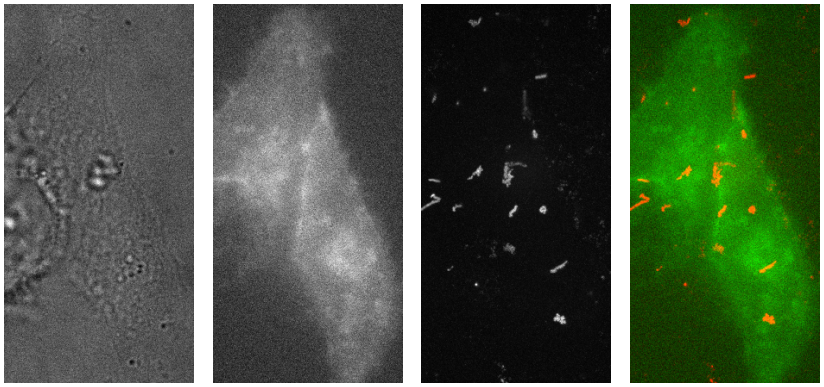

(a) *A transmission light image of a HeLa cell.*

(b) *An image of the CFP channel, showing the expressed CFP-labeled receptor.*

(c) *A maximum-intensity projection of the movie in the QD channel. Note the different shapes of trajectories: some more confined, others span large areas.*

(d) *A superposition of the CFP channel (green) and QD channel (red).*

Trajectory analysis The resulting trajectories (n=168) were analyzed by calculating the MSD and fitting it with a model for Brownian motion. The diffusion coefficients were compiled into a histogram on a logarithmic scale. As can be seen in **Figure 15.6.1** the results a monomodal distribution on the natural-logarithmic scale. This is in agreement with previous experimental and theoretical works [235, 236] that have shown that in cases of pure Brownian motion, the diffusion coefficients should be distributed according to a log-normal law. Therefore, in order to describe the distribution with a small number of parameters, we fitted the distribution of LogD (the natural logarithm of the diffusion coefficient) with a Gaussian. The result was a mean of -2.78± 0.07 corresponding to a characteristic diffusion coefficient of $6.2 \times 10^{-2} \mu m^2/sec$ with standard errors $+0.5 \times 10^{-2} \mu m^2/sec$ and $-0.4 \times 10^{-2} \mu m^2/sec$ (the log-normal distribution is right-skewed).

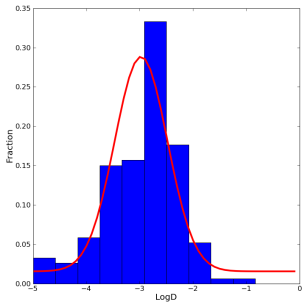

Figure 15.9: *The distribution of the natural logarithm of the diffusion coefficients (LogD) for polyvalent-ScFv QDs (NH_2-PEG-QD::Poly-ScFv) bound to PCMX.*

15.6.2 EO6D-QD::polyScFv

We prepared polyvalent EO6D-QD::ScFv by incubating EO6D-QD with excess ScFv, at a nominal ratio of 1:20 (QD:ScFv) for one hour at room temperature. According to the results of the agarose gel electrophoresis, these QDs should have at least four ScFv molecules per QD (see **Figure 15.6**). The QDs were then incubated with the cells for 5'. Subsequently, the cells were washed, and mounted on a microscope for observation and tracking.

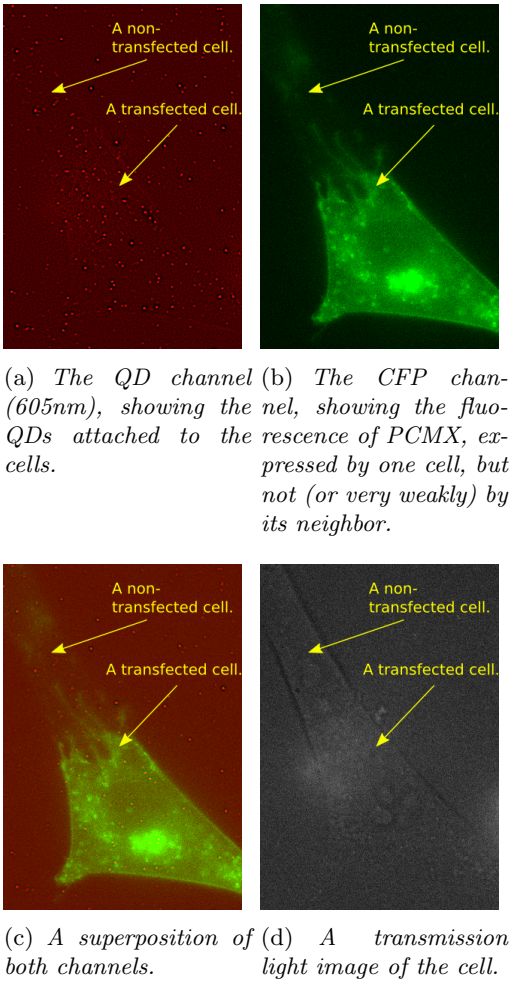

(a) *The QD channel (605nm), showing the QDs attached to the cells.*

(b) *The CFP channel, showing the fluorescence of PCMX, expressed by one cell, but not (or very weakly) by its neighbor.*

(c) *A superposition of both channels.*

(d) *A transmission light image of the cell.*

Figure 15.10: *The binding of EO6D-QD::polyScFv to PCMX on cell membranes. The preference of the EO6D-QD::polyScFv to the PCMX producing cell over its neighbor (upper left) can be seen here. Some QDs can be seen to stick to the glass due to non-specific interactions of the EO6D-QD.*

Trajectory analysis

Similarly to the analysis of the trajectories of the NH_2-PEG-QD::Poly-ScFv, we calculated the diffusion coefficients using MSD analysis, and obtained a histogram of LogD (the natural logarithm of the diffusion coefficient). By fitting LogD with a Gaussian model, we obtained a mean of -2.96± 0.11 corresponding to a characteristic diffusion coefficient of $5.18 \times 10^{-2} \mu m^2/sec$ with standard errors $-0.54 \times 10^{-2} \mu m^2/sec$ and $+0.60 \times 10^{-2} \mu m^2/sec$.

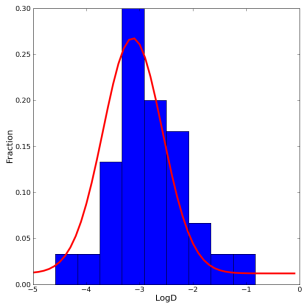

Figure 15.11: *The distribution of diffusion coefficients for polyvalent-ScFv QDs bound to PCMX.*

15.7 Monovalent ScFv QDs

15.7.1 Single-QD tracking

QDs were prepared with the nominal ratio corresponding to monovalent QDs. We then incubated them with cells transfected with PCMX and tracked individual QDs.

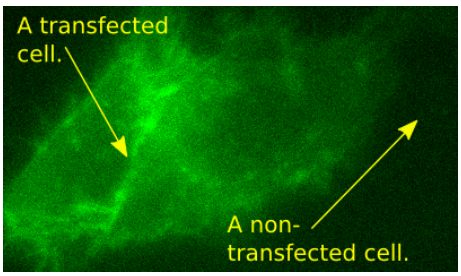

(a) *The CFP channel.*

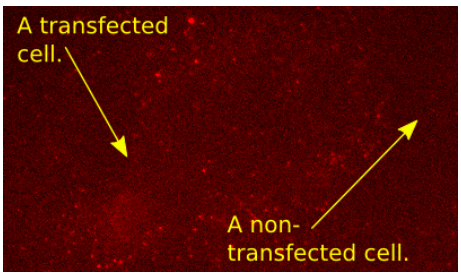

(b) *The QD channel.*

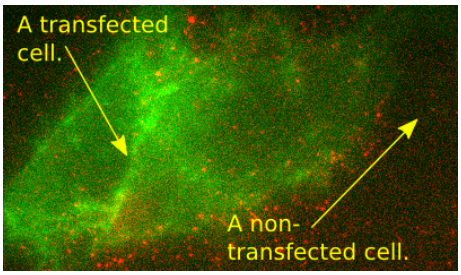

(c) *A superposition of both channels. For clarity, the green channel is a bit more transparent, in order to be able to see the overlap between the channels.*

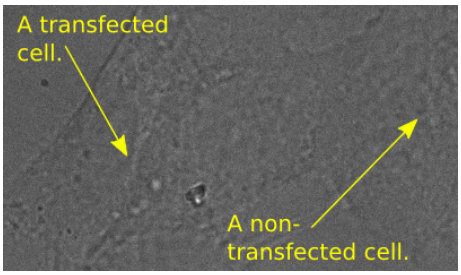

(d) *A transmission light image of the cell.*

Trajectory analysis

The MSD was fitted with a Brownian model and histograms were compiled, as in the previous types of QD::ScFv. By fitting LogD with a Gaussian model, we obtained a mean of -2.95± 0.16 corresponding to a characteristic diffusion coefficient of $5.23 \times 10^{-2} \mu m^2/sec$ with standard errors $+0.91 \times 10^{-2} \mu m^2/sec$ and $-0.77 \times 10^{-2} \mu m^2/sec$.

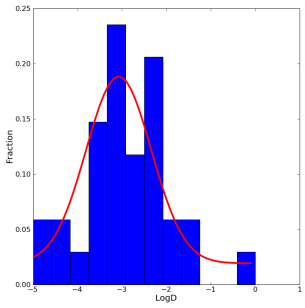

Figure 15.12: *The distribution of diffusion coefficients for monovalent-ScFv QDs bound to PCMX.*

15.7.2 A comparison of diffusion coefficients between monovalent and polyvalent ScFv QDs

We compared the diffusion of monovalent and polyvalent ScFv QDs. A Kolmogorov-Smirnov test was used to determine whether the distributions of diffusion coefficients are significantly different. The value of the Kolmogorov Smirnov statistic was 0.191 with a P-value of 0.535. The results show that the distributions are not significantly different ($p>0.05$). These results are consistent with a previous study with QD::IgG complexes that were used for tracking extracellular membrane receptors and did not find a significant difference between monovalent and polyvalent QDs [191].

Even though we do not know how a polyvalent probe should behave, we would still expect polyvalent and monovalent probes to behave differently, even in cases limited to pure diffusion, like this one. One possible explanation for this behavior could be very low activity (on the order of 0.05) of the ScFv, which effectively scales down the ScFv/QD ratio in the case of excess ScFv, to around 1 and the monovalent QDs to around 0.05 (This way, 95% of the nominally monovalent QDs will be washed away, but the rest should behave as truly monovalent QDs). From the strong signal we observed in the TIRFS kinetics measurements, we tend to rule out the possibility that the ScFv itself has a very low activity. However, it is still possible that the ScFv bound to EO6D-QDs has a lower activity. this could be due to non-specific binding of ScFv to the EO6D-QD, which may prevent ScFv binding to GFP (the *in-vitro* binding tests for the ScFv, including the TIRFS measurements were performed using an ScFv that was immobilized through its HisTag to a surface, similarly to the case of QD bound ScFv. However, we do not know what happens when the ScFv is bound using a different domain.), in most cases, from binding its target (*e.g.* if the ScFv is bound in a way that masks its binding domain). Another possibility is that due to steric constraints, such as the angles or distances between ScFvs on the QD surface, make the binding of a second target less probable (an accessibility problem).

Part IV

Discussion and perspectives

The goal of this project was to develop an integrated approach towards a single molecule study of asymmetric cell division (ACD). We went from cDNA fragments for proteins, which are implicated in ACD, to observing internalized complexes of these proteins with QDs. In order to achieve this, we had to cope with technical challenges from different fields and disciplines: from molecular cloning, protein expression and purification, through fly culture and genetics (in order to generate the PON-GFP flies), cell culture (from HeLa cells to dissection and culture of fly brains), QD surface chemistry and internalization into cells, single molecule tracking and finally, data analysis. In every step of the way, we verified and tested our system: starting from the internalization of QDs we then proceeded to cloning and protein purification. At this stage, all the constructs were verified using digestion, PCR and finally sequencing, and the produced protein constructs were verified using PAGE and by blotting of the C and N terminal domains, as well as by testing the biotinylation (some constructs were even tested with mass-spec.). Then, the biotinylation, and binding to QD-SAV were tested using PAGE and agarose gels. In the next step, intracellular targeting, we tested the internalization and targeting of specific sites within living cells. Only then, when we were confident that all the elements of the system are functioning, we proceeded to the targeting inside neuroblasts. The challenges encountered will be discussed in this part, along with future perspectives and directions for the project.

Chapter 16

Discussion

16.1 Intracellular targeting

In this important part of the work, we have shown the feasibility of using QDs for intracellular targeting in primary neuroblasts.

As far as we know, this has been the first report of intracellular QD targeting in primary tissue. Internalization into primary cells is usually more challenging for two main reasons: first, the specific requirements concerning cell culture, which usually make primary cells more vulnerable and harder to manipulate. Second, in many cases, dissociated tissue contains residual connective material and intracellular matrix, which isolate the cells from their environment and make internalization much harder.

In this project, we have demonstrated the two approaches for intracellular tracking assays: the endogenous and exogenous approaches. The endogenous coupling approach, was used to target the protein Asterless-YFP in *Drosophila* brain cells and PON-GFP in *Drosophila* neuroblasts, using QD::AntiGFPIgG (QDs coupled to an anti-GFP antibody). In these two cases, the colocalization was clear and the results have shown that the QD::AntiGFPIgG was active, and free to explore the cytoplasm.

The exogenous coupling approach was demonstrated using the ACD proteins Pins and Miranda. These protein constructs were designed with opposite-ends two tags, which enable a stable binding of the non-degraded full size protein to QD-SAV. This binding was verified using agarose gel electrophoresis. An analysis of the localization of these proteins in dividing neuroblasts revealed localization patterns that are in agreement of the existing immunofluorescence results from the literature.

As we mentioned before, the experimental conditions did not allow us to record trajectories that are long enough for significant diffusion measurements (about 50 points). Even though we have not been able to obtain sufficiently long trajectories to allow the calculation of diffusion parameters, some analysis should be possible by observing the spatial distribution of step sizes and short-range diffusion coefficients. Such analysis is currently underway.

Except for intracellular tracking and the analysis of protein dynamics, this method for colocalization analysis of QDs inside cells, can be applied to study various mutations and conditions in live cells, similarly to what is done today with fluorescent proteins. The method used today in the study of polarization in *Drosophila melanogaster* and *Caenorhabditis elegans* uses genetic engineering and crosses, in order to obtain mutant strains, in which the localization of a protein of interest is reported by a fluorescent protein fused to it. The alternative of using QDs coupled to the protein of interest to study localization in different scenarios can be advantageous: it requires much less genetic work (mutations can be introduced when cloning the protein *in-vitro* before coupling it to the QD), it is much more sensitive (for some proteins the expression is very weak and does not give a significant signal) and it allows to study lethal mutations without any manipulations of the organism (these can be introduced into the protein that is coupled to the

QD).

16.2 The development of monovalent ScFv-based probes

We have demonstrated the use of a monovalent QD probe based on a single-chain variable fragment (ScFv) against GFP and HisTag-reactive QDs. The applications for such a probe are potentially very wide: due to the popularity of GFP and its variants (most, if not all, of which can be targeted by this ScFv), many cellular systems exist, in which some GFP derivative is fused to an extracellular membrane protein. We have found that the ScFv used in this project has a rather low affinity towards its target (480 nM) and a relatively short "on-time" (the kinetic dissociation constant is $k_d = 2.4 * 10^{-3} sec^{-1}$). However, for extracellular tracking assays, this could sometimes be enough: with the given dissociation constant, every 7' we are left, on average, with $1/e$ of the QDs we had before. This can be partially compensated by loading a large number of QDs onto the cells. However, the low affinity limits the use of such probe to extracellular membrane tracking. This is because in membrane tracking detached probes can be washed away, whereas in intracellular tracking they remain inside the cell and cannot be distinguished from the bound ones and given the low affinity of this ScFv it is highly likely to detach from its target even during a very short experiment. Higher affinities can extend the applicability of this method for intracellular targeting and *in-vitro* labeling (*e.g.* the ScFv labeled QD is incubated *in-vitro* with the protein of interest and then internalized and observed inside the cell, similarly to what we have done to target PON-GFP with QD::AntiGFPIgG). Even though ScFvs usually have affinities that are lower than those of antibodies, several groups have succeeded in optimizing ScFvs using different display and selection techniques, obtaining affinities up to the femtomolar range [233].

The combination of HisTag binding QDs and a selection of HisTag labeled ScFvs (such as the one used in this project) is an example for a modular,"toolbox-like", approach for single molecule targeting and tracking, using a monovalent probe. Another very prominent monovalent probe is the recently published monovalent streptavidin [102]. Even though this probe boasts a very high affinity, its production is more time consuming and laborious than that of ScFvs. High affinity ScFvs are also superior to monovalent streptavidin in the case of endogenous labeling (targeting an endogenously expressed protein inside the cell) due to the presence of free biotin, and other biotinylated proteins, inside the cell. Therefore, it cannot be applied to intracellular tracking unless it undergoes another coupling step in which it binds to a biotinylated protein of interest.

An interesting application for our labeling approach could be in ultra-sensitive scanning of single-chain display libraries against membrane proteins. Many of the vectors already in use for the construction of such libraries contain HisTag, and therefore, there are already many available libraries of HisTag ScFvs. The simple and fast coupling procedure (an incubation of the HisTag labeled ScFv and the EO6D QDs) allows a quick test for candidate ScFvs, directly on live cells. High throughput scanning methods for live cells already exist for applications such as RNAi screens [237]. Therefore, a combination of our ScFv-labeling labeling strategy with such systems may have advantages over the currently used scanning and selection methods. Such a method could never replace the conventional, affinity based selection methods, as they can work with $\sim 10^{12}$ clones at the same time and a high throughput cell scanning methods can hardly surpass $\sim 10^5$ [237]. But, when optimizing smaller libraries of ScFv candidates, at a more advanced phase, such scanning method can provide more information, which can only be obtained from live cell imaging, such as specificity and possible physiological effects such as endocytosis. This should also be possible using conventional fluorescent probes (similar to what we have done with the Tris-NTA -dye, which is reactive against HisTag), but here, QDs present several advantages: first, due to the high signal-to-noise ratio of QDs, a much more sensitive scan can be performed: smaller differences in binding could be detected, as well as the binding

to proteins that exist in very small numbers. In addition, the QDs can also be tracked, which may provide more information (but will of course consume more time and computer memory).

16.3 QD size and Bio-compatibility - Is smaller necessarily better?

From the comparison of peptide-coated QDs and the commercial amino-PEG QDs, it seems that the QD surface chemistry can significantly affect the efficiency of the internalization method. This has been demonstrated by incubating non-specific peptide-coated QDs with proteins and running the result on an agarose gel. As we see it, it is crucial that the QDs be well passivated. In the pursuit of making QDs smaller and smaller, the passivation of the QD surface may be compromised. This is of utmost importance in intracellular targeting experiments ("endogenous" labeling).

In such assays, even if the QD "finds" and binds its target, we have no way to know whether it is also bound to other proteins. This should be much more pronounced in crowded environments, such as intranuclear tracking: in addition to the high charge density, the nuclear environment has a very high concentration of proteins that may compete with the target protein. Testing the passivation of a QD is not an easy task, since it is hard to detect an interaction with unknown proteins. Nevertheless, qualitative tests can be performed, for example, by comparing the migration of different QDs following incubation with cell lysate. It should be mentioned, of course, that in most cases if the QDs qualitatively behave in the same way as a reference ensemble of fluorescent proteins, it is usually satisfactory. On the other hand, a small size may be important in some contexts. For example, polarization is generated, in some cases, by a process that changes the diffusion coefficient [177]. By conjugating a protein to a large particle, this difference in diffusion coefficient can be suppressed, due to the contribution of the large particle. Small size is also important for the resolution of different protein::QD stoichiometries on a gel. For proteins that have a retardation effect, the higher the mobility of the free QDs, the stronger will be their effect on the QD mobility in the gel [10]. In such cases, we would prefer smaller QDs, which are usually more mobile.

16.4 QD internalization methods and intracellular diffusion

16.4.1 Internalization: microinjection vs. pinocytic influx

We have compared the two prominent QD internalization methods: microinjection and pinocytic influx. In this study, we found that pinocytic influx can be applied to a wider range of cell types, whereas in some cases, such as for neuroblasts, the cells were very hard to inject. Another advantage of the pinocytic influx is that a single osmotic shock internalizes QDs into many cells in parallel whereas microinjection works "serially", cell-by cell. A comparison of the distribution of diffusion coefficients shows that in the case of microinjection there are more QDs showing "slow" diffusion: for microinjection, 45% of QDs have a diffusion coefficient lower than $1.8 \times 10^{-2} \mu m^2/sec$ whereas for pinocytic influx, only 25%. This is also the reason why, when looking at the histogram of LogD for microinjection (see **Figure 11.10**), it is easier to resolve the peak corresponding to "fast" diffusion around LogD=-3. In the case of *Drosophila Melanogaster* neuroblasts, standard microinjection was not able to internalize QDs without killing the cell. By using pinocytic influx, however, we managed to internalize QDs into these cells, even though the yield was lower than for HeLa or NIH3T3 cell lines.

16.4.2 Intracellular diffusion

We have identified some of the key factors that influence the QD diffusion inside the cell, in the case of simple diffusion (we did not address issues like anomalous diffusion, confinement and trapping). We found that the diffusion coefficients can vary from cell line to cell line, and even inside the cell. However, we have not found any significant difference between mobile QDs internalized by microinjection and mobile QDs internalized by the pinocytic influx (the difference was mainly in the immobile fraction of the QDs, with very low diffusion coefficients, which we do not analyze.).

Diffusion coefficients

We have shown that for QDs diffusing inside HeLa cells, the free, "fast", diffusing QDs can be usually be resolved from the confined, "slow" diffusing QDs. The characteristic diffusion coefficients, such as $4.7 \times 10^{-2} \mu m^2/sec$ for QDs in HeLa cells, can be used as a reference number for intracellular tracking experiments. This can serve as an indication for the time it should take a QD to explore the whole cell, under the assumption that the diffusion could be regarded as a pure, 2D, Brownian process.

Differences between cell types

We have shown that the diffusion coefficients of non-conjugated QDs can be significantly different between cell types (in the case S2, HeLa and 3T3). This raises an interesting question: If the diffusion is so different, is it also reflected in diffusion-limited cellular processes? Is it possible that intracellular diffusion inside two cells with very similar generation time (and therefore probably similar rates of metabolism), should have such dramatically different rates of intracellular diffusion?

Chapter 16

16.5 Coupling and characterization methods

16.5.1 Conjugation

We have found that streptavidin-biotin conjugation, based on site-specific *in-vivo* biotinylation, is a robust and efficient method for the conjugation of proteins to QDs. The high efficiency of *in-vivo* biotinylation, together with the two-tag system, provide a simple way to conjugate full length proteins, while minimizing the conjugation of degradation products, which may be inactive.

16.5.2 Electrotransfer of QDs

Throughout this project, several purification and characterization methods have been employed for QD-protein complexes. Electrophoresis methods (polyacrylamide gels, agarose gels and capillary electrophoresis), and size exclusion chromatography. We have shown the applicability of vertical electro-transfer for the characterization of QD-protein complexes. It allows one to correlate between migration, and the concentration of a given protein on the surface of the QD. Using the right calibration, this method should be able to provide a direct measurement of the average number of protein molecules per QD, by combining fluorescence and chemiluminescence signals. When the resolution of the agarose gel is high enough to produce discrete bands, this method can be applied to each band and give an information regarding the entire distribution of protein/QD ratio.

16.5.3 Coupling on a solid support

Another method that was developed during this project is the solid-support-based coupling of QDs (see description in **Methods** and **Results**): the primary aim of this method is to remove "free QDs", which do not have the protein of interest bound to them, from the sample and increase the chances that the proteins attached to the QD are not degraded, by combining the two-tag system that could now allow to couple QDs to proteins prone to degradation, such as PON. In addition, we have presented a simple mathematical argument, why this method could also be used to generate monovalent QDs (see **Results**).

We found that owing to the large surface area of the agarose-NiNTA resin, we can obtain a sample with a high fraction of monovalent QD-protein complexes (almost 50%) with no "free QDs", even at high protein concentrations. We therefore see no reason why this method should not be used to obtain samples with a very high monovalent fraction (we estimate that by reducing the surface density by 5, we can obtain a sample of about 95% monovalent QDs and no free QDs). This is also a reason why this method should be performed on resin instead of small chips for example, since the latter have a much lower specific area.

The desired protein surface density to produce monovalent QDs can either be calculated (see the calculation in **Results**), or determined experimentally. The latter can be done by decreasing the protein concentration more and more, keeping the QD concentration the same, until a "critical" concentration is reached, under which the concentration of QDs that can be retained on the resin (by binding to the biotin of resin-immobilized proteins) starts to drop sharply (see **Figure 16.1**). This happens when the number of binding sites for QDs and the number of QDs become comparable. This surface density of proteins can be used as a starting point for producing monovalent QDs.

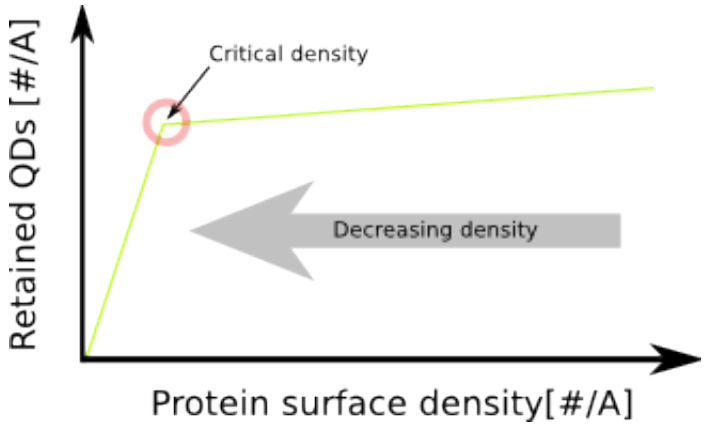

Figure 16.1: *A scheme describing the method to experimentally find a protein surface density that can produce monovalent QDs.*

The alternative method to obtain monovalent QDs was described by Howarth *et al.* [10]. In order to obtain truly monovalent QDs, they conjugated non-commercial QDs to monovalent streptavidin, and separated the resulting mixture on a gel. Then, the band corresponding to 1streptavidin/QD was extracted, and the recovered QDs were coupled to a biotinylated protein. This method has a few drawbacks: first, it requires the use of monovalent streptavidin, which is not easy to produce once the DNA construct is obtained (under license) from A. Ting. Second, this method relies on a gel separation that can only be achieved with certain QD-protein combinations (the gel resolution may not be very high, for example, if we choose to use the monovalent streptavidin, together with a low mobility QD such as the commercial NH_2-PEG-QD). Third, the procedure is cumbersome, and may be hard to upscale and fourth, the effect of the agarose gel on the QDs is not known. In contrast, our solid-support coupling

method should work with any QD (assuming it does not suffer from non-specific binding to the resin) and with normal, tetravalent streptavidin, since, due to the small size of streptavidin, the probability that it would bind two proteins while it is bound to the surface is negligible in the experimental protein surface density. (after the binding of QDs to the surface immobilized proteins, unwanted binding after the elution is avoided by blocking the available streptavidin sites using excess biotin.). In fact, even with a high protein density as the one we used, the chance for a polyvalent streptavidin is estimated at <2%.

The only problem that remains with the coupling on a solid support is how to prove that the valence is indeed 1. The average ratio of protein per QD could be determined using the electrotransfer/western blot method described above, combining absorbance/fluorescence quantification for QDs and specific chemiluminescence for the proteins. What is important in the electrotransfer/western method for QDs is that it separates the free proteins in the solution from the ones that are bound to the QDs. In more specific cases, one can use biochemical activity (for enzymes) or fluorescence[1]. Usually, the average ratio of protein/QD is not enough, since we do not know what are the proportions of the QDs with 0,1,2.... proteins in the sample (we believe this should follow a Poisson-law, but this has not been proven yet.). But in this case, since are using the solid-support coupling method, we know that **we do not have any QDs with 0 proteins in the sample**, (In a control experiment with passivated QD-SAV, we did not detect any "free QDs" that were retained throughout the experiment and eluted at the end) so if average will be close to 1 protein per QD, we will be able to have an estimate for the minimal fraction of monovalent QDs. For example, if we find that the average ratio of protein molecules per QD is 1.1, and we know that there are no free QDs (QDs with 0 proteins per QD):

$$1.1\frac{proteins}{QD} = \frac{n_{1/1} * 1\frac{protein}{QD} + n_{2/1} * 2\frac{proteins}{QD} + n_{3/1} * 3\frac{proteins}{QD} + n_{4/1} * 4\frac{proteins}{QD} + ...}{n_{1/1} + n_{2/1} + n_{3/1} + n_{4/1} + ...} \tag{16.1}$$

Where $n_{x/1}$ is the number of QD-protein complexes with a ratio of x proteins per QD (or valence x). But if we use a conservative estimate that all the polyvalent QDs are divalent (*i.e.* minimal fraction of monovalent QDs for a given total number of proteins and QDs which was measured), then:

$$1.1\frac{proteins}{QD} = \frac{n_{1/1} * 1\frac{protein}{QD} + n_{2/1} * 2\frac{proteins}{QD}}{n_{1/1} + n_{2/1}} \Rightarrow n_{1/1} = 9 * n_{2/1} \Rightarrow \tag{16.2}$$

⇒**The minimal fraction of $n_{1/1}$(monovalent) is 90%**

16.6 Limitations of the system

16.6.1 Tracking in thick samples

Intracellular tracking experiments require that the depth of the cell be taken into consideration. Compared to extracellular tracking of membrane receptors, where the movement of the probe along the optical axis is relatively restrained, the movement along this axis of QDs in the cytoplasm, can span 10-20 μm. Works that have been performed in the field of intracellular tracking, were limited to relatively flat cell lines such as HeLa [59] and COS-7 [242], and treated the movement of QDs as quasi-2D. However, in many biological scenarios (such as asymmetric cell division in neuroblasts), the sample has a significant thickness. In such cases, tracked QDs

[1] maybe the most promising method is a highly sensitive FRET-based assay [238, 239] based on the detection of S-tag [240, 241], which boasts a femtomolar sensitivity. This system can be applied to constructs cloned into our modified pET32a vector (we have added the AviTag), which contains an S-tag, such as the bacterially produced Pins.

leave the focal plane for long periods of time and therefore make tracking very difficult. In order to cope with this difficulty, a partial solution could be to use stronger laser excitation, which would allow much shorter exposures and therefore faster acquisition. This way, a sufficient amount of data could be acquired at a time period that is comparable to the residence time of a QD within the focal plane. This method has two main limitations, though: first is of course the short observation time, which limits the time period of observation for a given QD. This could be a significant limitation in processes that extend over longer times. The second limitation is, that in some cases, the movement along the optical axis may have a biological significance, and by ignoring it, some biological information will be lost.

The second option is the employment of novel 3D tracking methods. There are currently two main approaches for for coping with 3D tracking that have been applied to QDs: one is based on optical astigmatism and the other, on bifocal imaging. In the former [243], a cylindrical lens, is introduced into the optical emission path. As a result, a single QD will no longer appear as a circular fluorescent spot, but rather as an ellipse. The distance from the focal plane can be derived from the ellipticity (a measure for the deviation from a perfect sphere) of the spot, and the angle of its primary axis with a reference axis. In the latter [24, 244], the images are acquired simultaneously in two different focal planes. Then, by comparing the two resulting fluorescent spots generated for a given particle, throughout the movie, its location along the optical axis can be estimated.

Still, these methods have been shown as a proof-of-principle, in systems that are relatively simple. Moreover, the range over which these techniques can measure the location along the optical axis is limited to a couple of microns, whereas the size of a cell is within the range of 10-20 μm. Due to lack of time, these methods were not implemented in this project.

16.6.2 Internalization

Even though in principle, a few QDs per neuroblast cell should be enough for a tracking movie, increasing the number of internalized QDs could be beneficial, considering the problem mentioned above. Having many QDs within the cell can partially compensate for the QD disappearance by increasing the probability that some QDs will stay enough time in the focal plane. However, after testing many methods, from lipids, through cell penetrating peptides, sonoporation and more, the influx method still remains the best solution.

Chapter 17

Future prospects in the study of neuroblast ACD

17.1 The study of neuroblast asymmetric cell division using QDs

As mentioned before, we have found that the study of neuroblast asymmetric cell division using single QD tracking is limited by the finite thickness of neuroblasts. However, even in the current conditions, some additional information may be obtained beyond pure colocalization. We intend to analyze the spatial variation of QD mobility, for the cases of PON targeting or for QD-SAV::Miranda and QD-SAV::Pins, using the existing data. By pooling together all the short trajectories (2-10 points), and analyzing the spatial distribution of step sizes we may be able to compare the step size histograms for the basal and apical parts of the cell. Under some assumptions, we may be able to observe, and possibly calculate the differences in diffusion coefficients between the apical and basal parts of the cell. This analysis is currently underway.

17.2 Applications for protein constructs

A great amount of work was invested in the cloning and purification of several proteins implicated in ACD. Except for being used in the continuation of project, once the 3D problem is resolved, they can be used in cellular assays in other organisms, replacing their homologs and thus saving the time needed for cloning and expression. These protein constructs can also be used in biophysical and biochemical *in-vitro* studies, such as the study of Siegrist *et al.* about the binding dynamics of Pins [173]. In the case of PON, which we found unstable and unusable, it is possible that more elaborate purification techniques my provide better results. In cell fractionation experiments, we have found that in SF9 cells, large quantities of PON remained associated with the plasma and nuclear membranes (data not shown). Therefore, by employing purification strategies that are used for membrane proteins, the result may be improved.

17.3 Emerging techniques

During this project, a new field of fluorescent imaging has emerged. The field of superresolution imaging has emerged, including techniques such as PALM [245, 246], STORM [247] and derivatives thereof, all based on photoactivation and multicolor photoswitching of individual fluorophores, to break the diffraction limit. This is usually done by repeatedly exciting the sample in a way that activates a small subset of the fluorescent proteins and produces a very sparse array of fluorescent spots, which can be localized with superresolution accuracy, by fitting their point-spread function. These methods were first applied to fixed samples, but were

later extended to live cells and recently to single protein tracking [248]. We believe, that these techniques can address some of the problems encountered by SQDT in neuroblasts. First of all, even though we have shown that the pinocytic influx internalization method can be used to internalize QDs into neuroblasts, the number of QDs that are internalized is usually very small (2-5 QDs/cell). Using an approach based on photoactivable proteins, such proteins can be fused to the protein of interest, using genetic engineering to generate what is called a transgenic fly (a well established technique), in which a copy of the protein of interest (for example PON, Pins or Miranda) fused to a photoactivable/switchable-FP will be overexpressed. It has been shown, at least for some photoactivable proteins, that such a fusion is not disruptive to the host cell [249]. The number of fluorophores, in such case, can be very high (a protein can be overexpressed in many thousands of copies in a given cell). By repeatedly activating and observing the fluorescent proteins in the sample, many cycles of tracking can be performed. The large number of fluorescent proteins would be very advantageous: a single cell can yield a significant data set composed of trajectories from many single fluorescent proteins, and cell to cell differences could be detected. This could also partially compensate for the 3D problem, by activating and observing a large number of fluorescent proteins that would increase the number of long trajectories that do not go out of focus, even if the probability to observe them is very low. If needed, these techniques could probably be combined with the 3D tracking techniques mentioned above. Another advantage is the time factor: once the transgenic fly is ready (this could take about three months), the experiments will be much faster. This method saves all the time spent on protein expression and purification, coupling to QDs, controlling the valence (the new, monomeric fusion proteins are inherently monovalent) and of course internalization. The cells will also probably show a higher viability, not having to go through the osmotic shock, which is relatively harsh, will not require a recuperation time, and will possibly be more likely to divide. It must be taken into consideration that though the photostability of these proteins is still far below that of QDs, this is currently not the limiting factor in such tracking experiments, due to the 3D problem.

Therefore, such a method should be considered in the study of asymmetric cell division. A possible experiment could be planned as follows: a transgenic fly is produced by standard methods, containing a photoactivable fluorescent protein fused to the protein of interest, under the control of a strong, specific driver (*e.g.* a combination of Inscuteable-GAL4 and a UAS). Third instar larvae will be collected and dissected, using the same protocol as in the QD tracking experiments. Neuroblasts will be observed, except that here, no internalization is needed. During the time course of division, fluorescent proteins will be repeatedly photoactivated and observed. Such an experiment can yield much more trajectories, out of which some should be long enough for analysis. The resulting data will be much more statistically significant, and may even allow for cell-cell comparison. The cells should be in better shape (not having to undergo the shock involved in internalization) and therefore more cells will be in division.

Part V

Appendices

Appendix A

Cloning steps for baculovirus constructs

A.1 PON

A.2 Pins

A.3 Miranda

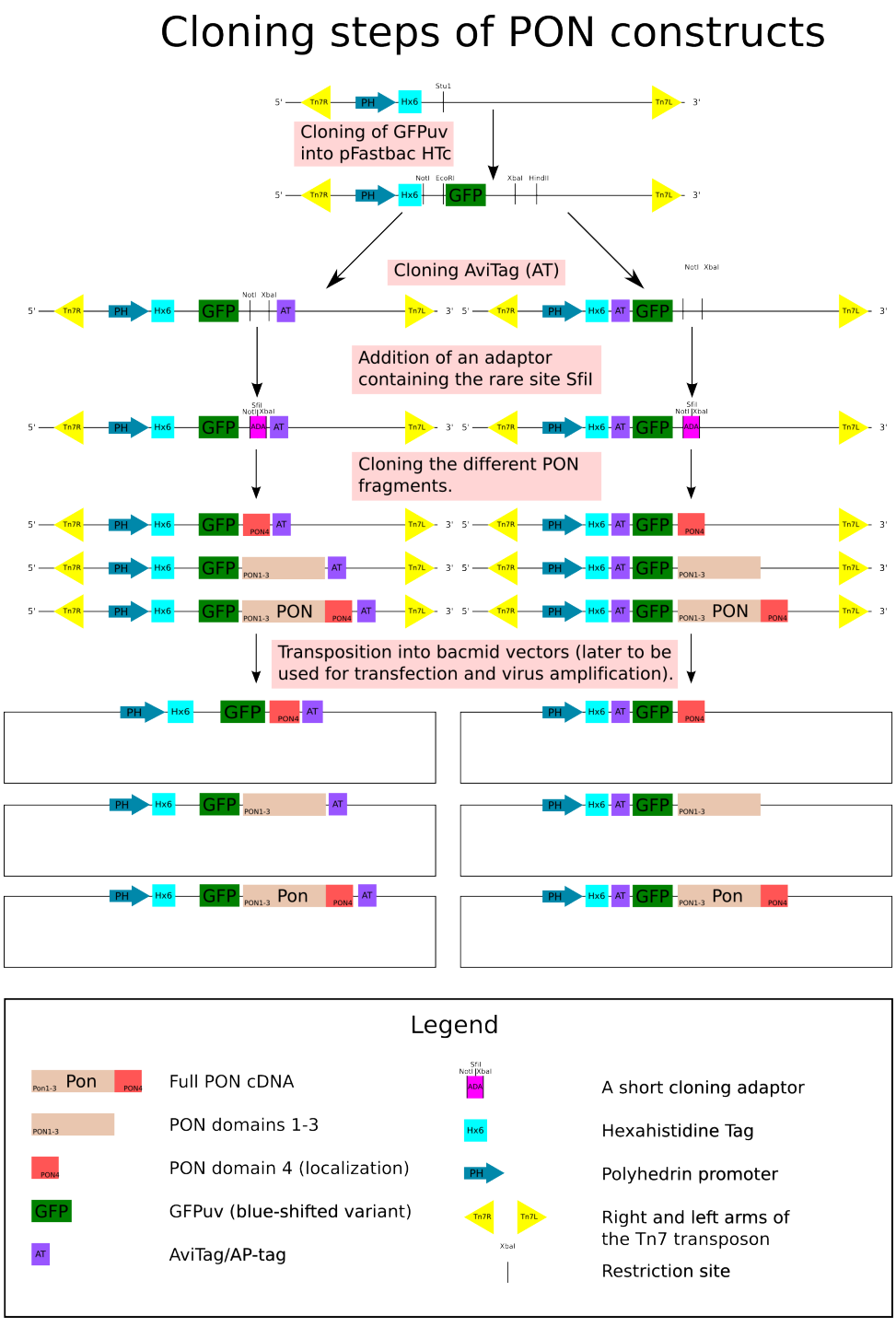

Appendix A

Figure A.1: *Summary of the cloning steps for PON: 1, Cloning GFP into the StuI site of pFastBac HTc; 2, Cloning the AviTag (marked "AT") at the C/N termini; 3, Cloning the adaptor (containing the SfiI site); 4 Cloning the different PON cDNA variants; 5, Recombination into the bacmid, using the Tn7 transposon arms.*

Cloning steps of Pins Baculovirus construct

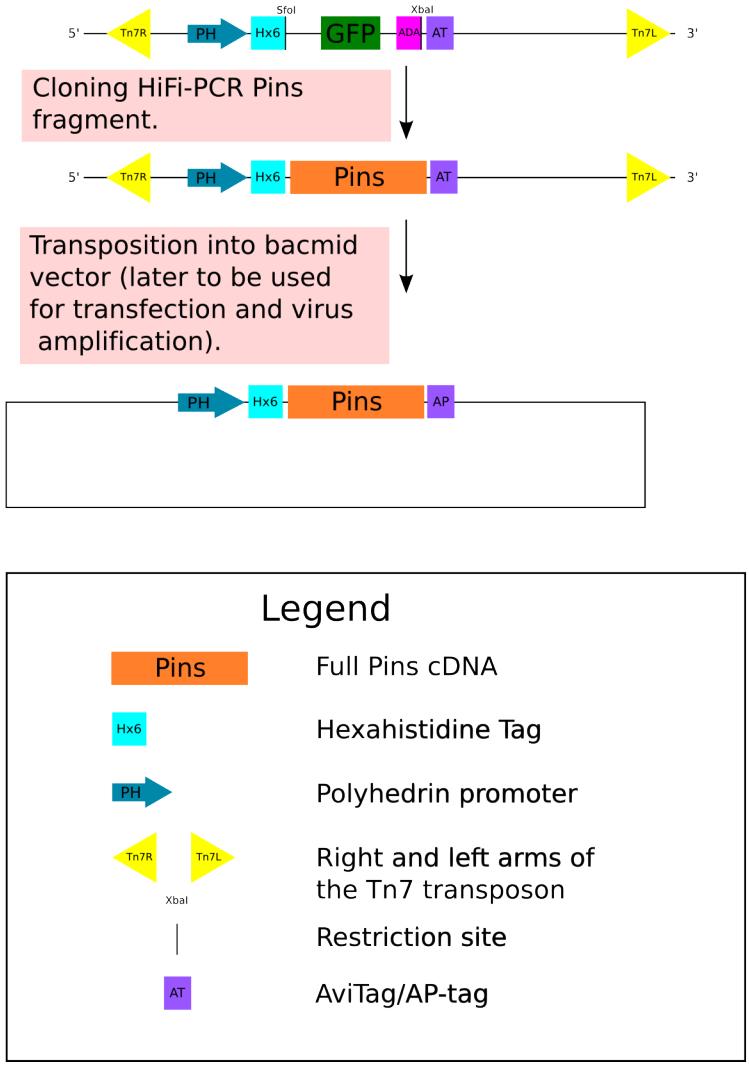

Figure A.2: *A scheme, summarizing the cloning steps of the Pins baculovirus construct.*

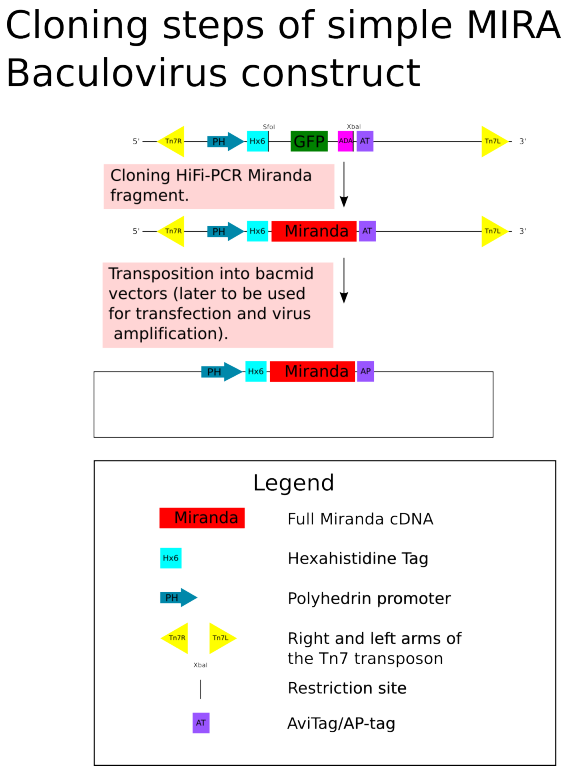

(a) *A scheme summarizing the cloning of the simple Miranda construct.*

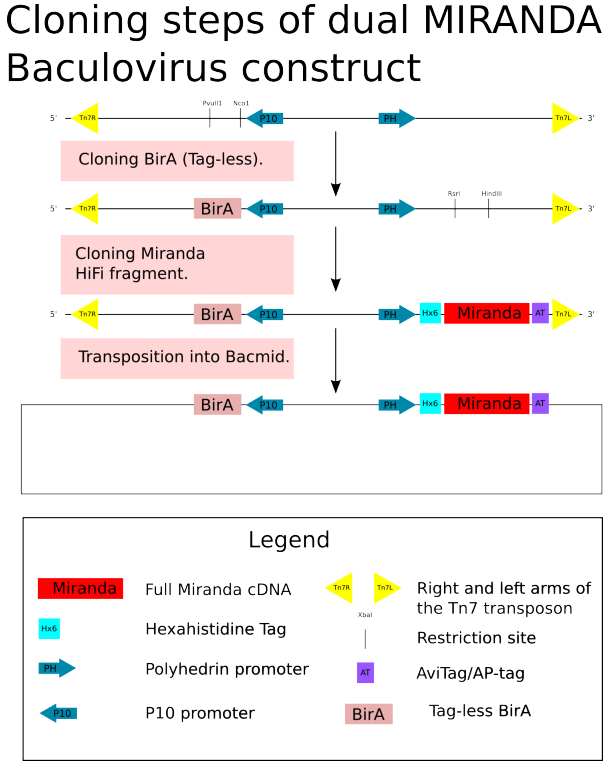

(b) *A scheme summarizing the cloning of the dual Miranda construct.*

Figure A.3: *A summary of the cloning steps for the simple Miranda pFastBac construct.*

Appendix A

Appendix B

Special media and buffers for fly work

FEED medium for neuroblast culture For ∼22ml of medium, mix:

1. 20ml Schneider medium (Invitrogen)
2. 2.5ml fetal calf serum
3. 1.25ml fly extract
4. 0.25ml glucose 0.1gr/ml
5. 0.125ml insulin at 1mg/ml

and pass through a $0.22\mu m$ filter.

Dissection buffer For 100ml of dissection buffer:

- 800mg NaCl
- 20mg KCl
- 5mg NaH_2PO_4
- 100mg $NaHCO_3$
- 100mg glucose
- 100ml H_2O

Appendix B

Appendix C

Primers

C.1 AviTag and adaptor

- AviTag1: the sense strand of the C-terminal AviTag insert: 5'-CTAGAGGTGGCGGTCTGAACGACATCTTCGAGGCTCAGAAAATCGAATGGCACGAAT-AAA-3'.

- AviTag2: the antisense strand of the C-terminal AviTag insert: 5'-AGCTTTTATTCGTGCCATTCGATTTTCTGAGCCTCGAAGATGTCGTTCAGACCGCCAC-CT-3'.

- AviCR: a PCR primer (reverse) for the C-terminal AviTag (used for verification and sequencing) 5'-CGTGCCATTCGATTTTCTG-3'.

- AviTag1: the sense strand s of the N-terminal AviTag insert: 5'-GCCGGTGGCGGTCTGAACGACATCTTCGAGGCTCAGAAAATCGAATGGCACGAAATC-GATGTG-3'.

- AviTag2: the antisense strand of the N-terminal AviTag insert: 5'-AATTCACATCGTTTCGTGCCATTCGATTTTCTGAGCCTCGAAGATGTCGTTCAGACCG-CCACCGGC-3'.

- AviNF: a PCR primer (forward) for the N-terminal AviTag (used for verification and sequencing) 5'-GCGGTCTGAACGACATCTT-3'.

- ADANOTSFI1: the sense strand of the SfiI adaptor for pFastBac HTc 5'-GGCCGCGTTTAAACGGCCGTGGGGGCCTT-3'.

- ADANOTSFI2: the antisense strand of the SfiI adaptor for pFastBac HTc 5'-CTAGAAGGCCCCCACGGCCGTTTAAACGC-3'.

Pins

- PinspFBNt: a primer for the N terminus (5') of full length Pins, for cloning into pFastBac. The sequence is: 5'-TCCTCGCTCTCTGCGTCCGC-3'.

- PinspFBCtXbaI: a primer for the C terminus (3') of the full length Pins, for cloning into pFastBac, into the XbaI site, after digestion. The sequence is: 5'-GCTCTAGACTTTCCAGCTCCGCCGGC-3'.

- Pins601: a sequencing primer, in the middle of the Pins gene. The sequence is 5'-TACCAGGAGAATCTGAAGCT-3'

PON

- PONFLpFBNt: a primer for the N-terminus of the full PON gene, or the PON123 fragment (the PON gene, with the first three domains, which is localization-defective and can be used as a negative control), used for cloning into the pFastBac NotI site. The sequence is: 5'-GCGGCCGCGCTGGAGACGAAGAGCATAGCT-3'

- PON4pFBNt: a primer for the N-terminus of the PON4 domain (the fourth domain, which is required for asymmetric localization), used for cloning into the pFastBac NotI site. The sequence is: 5'-GCGGCCGCGTTCAAGGCACCCGCGCGCTTC-3'

- PONFLpFBCtSfiIstop: a primer for the C-terminus of the full PON gene, or the PON4 fragment, used for cloning into the pFastBac SfiI site. This primer is used for the N-terminal AviTag construct, and therefore contains a stop codon. The sequence is: 5'-GCCTATGCAACCGCCAAGTAGGGCACC-3'

- PONFLpFBCtSfiIfus: a primer for the C-terminus of the full PON gene, or the PON4 fragment, used for cloning into the pFastBac SfiI site. This primer is used for the C-terminal AviTag construct and allows fusion with the downstream AviTag. The sequence is: 5'-GCCTATGCAACCGCCAAGTGGGGCACC-3'

- PONF123FBCtSfiIstop: a primer for the C-terminus of the PON123 fragment, used for cloning into the pFastBac SfiI site. This primer is used for the N-terminal AviTag construct, and therefore contains a stop codon. The sequence is: 5'-AGGCCCCCACGGCCAGTCTAGATCATCGGGCTC-3'

- PONF123FBCtSfiIfus: a primer for the C-terminus of the full PON gene, or the PON4 fragment, used for cloning into the pFastBac NotI site. This primer is used for the N-terminal AviTag construct, and therefore contains a stop codon. The sequence is: 5'-AGGCCCCCACGGCCAGTCATCATCGGGCTC-3'

- PON600: a sequencing primer in the middle of the full PON gene. The sequence is 5'-CTGCAATCCCTCGGGTGTGG-3'

Miranda

- MIRApFBNt: a primer for the N terminus (5') of the full length Miranda, used for cloning into pFastBac. The sequence is 5'-TCTTTCTCCAAGGCCAAGTT-3'.

- MirapFBCtXbaI: a primer for the C terminus (3') of the full length Miranda, used for cloning into pFastBac, into the XbaI site. The sequence is 5'-GCTCTAGAGATGTTGCGCGCCTTGAGCA-3'.

- MiraEcoRI: a sequencing primer in the middle of the Miranda gene (at the EcoRI site).

Numb

- NUMBCtPFBXba1: a primer for the N terminus (5') of the full length Numb, used for cloning into pFastBac. The sequence is 5'-GCTCTAGAGAGCTGCACCTGGAATGACT-3'.

- NUMBNtPFB: a primer for the C-terminus (5') of the full length Numb, used for cloning into pFastBac. The sequence is 5'-GGAAACTCCTCGTCACACAC-3'.

- NUMB435: a sequencing primer, in the middle on the Numb gene. The sequence is 5'-GAAGGTCAGCTTCTGTGCAC-3'.

Miranda

- MIRApFBNt: a primer for the N terminus (5') of the full length Miranda, used for cloning into pFastBac. The sequence is 5'-TCTTTCTCCAAGGCCAAGTT-3'.
- MirapFBCtXbaI: a primer for the C terminus (3') of the full length Miranda, used for cloning into pFastBac, into the XbaI site. The sequence is 5'-GCTCTAGAGATGTTGCGCGCCTTGAGCA-3'.
- MiraEcoRI: a sequencing primer in the middle of the Miranda gene (at the EcoRI site).

Numb

- NUMBCtPFBXba1: a primer for the N terminus (5') of the full length Numb, used for cloning into pFastBac. The sequence is 5'-GCTCTAGAGAGCTGCACCTGGAATGACT-3'.
- NUMBNtPFB: a primer for the C-terminus (5') of the full length Numb, used for cloning into pFastBac. The sequence is 5'-GGAAACTCCTCGTCACACAC-3'.
- NUMB435: a sequencing primer, in the middle on the Numb gene. The sequence is 5'-GAAGGTCAGCTTCTGTGCAC-3'.

Appendix C

Appendix D

Constructs

During this project, we have produced several DNA constructs that could be used in future studies. All DNA constructs have been verified by sequencing. All baculovirus constructs exist as plasmids, bacmids and active viruses, ready for infection.

D.1 Proteins related to asymmetric cell division

D.1.1 Pins

Baculovirus/SF9

This is a pFastBac HTc construct, with HisTag-Pins-AviTag (see **Figure D.1**, top).

E. coli We a TRXTag-HisTag-STag-Pins-AviTag, based on the pET32a backbone(Novagen) (see **Figure D.1**, bottom). This construct is co-transformed into *E. coli* bacteria together with pCDF-Duet-BirA (Tag-less), for highly efficient *in-vivo* biotinylation. BL21-Rosetta bacteria, co-transformed with both plasmids, were stored at -80^o. The TRX tag enhances solubility, the S-tag can be used for purification and highly sensitive quantification [238, 239], the HisTag is also used for purification, and the AviTag is used for specific biotinylation, by BirA [238, 239], *in-vivo* or *in-vitro*. Bacterially expressed Pins has been found active to be active [173].

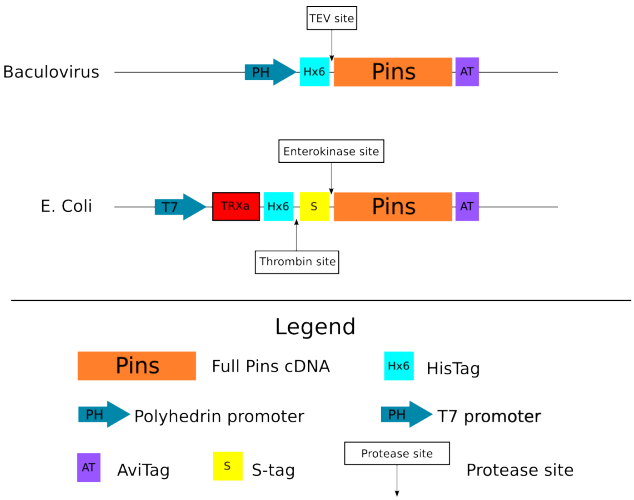

Figure D.1: *Pins constructs*

D.1.2 Miranda

For Miranda we have cloned two constructs for Baculovirus/SF9: one using the pFastBac HTc backbone, and one using the pFastBac Dual backbone, for dual expression with BirA, which specifically biotinylates Miranda while it is still inside the SF9 cells. In both cases, the Miranda fragment is the same: HisTag-Miranda-AviTag (see **Figure D.2**).

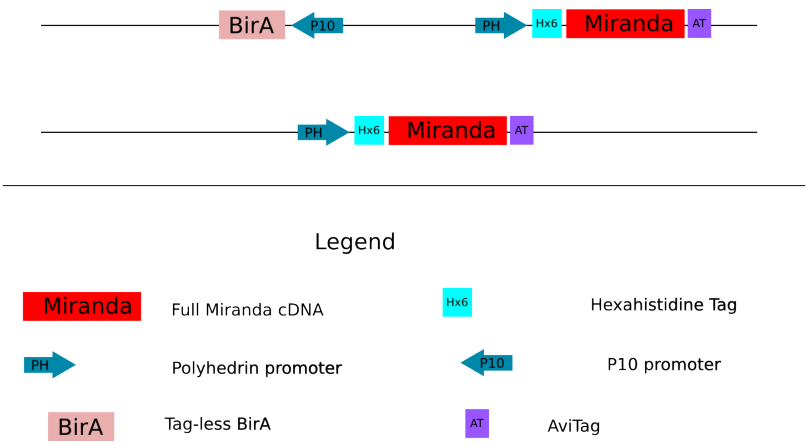

Figure D.2: *A scheme of the Miranda baculovirus constructs: top, dual construct; bottom, simple construct.*

Appendix D

D.1.3 PON

Baculovirus/SF9

HisTag-AviTag-GFP-PON4 and HisTag-GFP-PON4-AviTag These are two versions of a baculovirus construct, containing the fourth domain of the PON gene (sufficient for localization), one with both HisTag and AviTag at the N-terminus, and one with an N-terminal HisTag and a C-terminal AviTag (see D.3). The latter was used in the project, while the former was cloned and sequenced, but not used.

HisTag-GFP-PON123-AviTag This is a baculovirus construct, containing the first three domains of the PON gene (without the localization domain), with an N-terminal HisTag and a C-terminal AviTag (see D.3).

HisTag-GFP-PONFL-AviTag This is a baculovirus construct, containing the full PON gene, with an N-terminal HisTag and a C-terminal AviTag (see D.3).

E. coli

MBP-GFP-PON4-AviTag This construct is used for expression and *in-vivo* biotinylation of a fusion protein, composed of MBP (for purification, either using elution with maltose, or protease cleavage), GFPuv, and the fourth domain of PON (see **Figure D.3**). The plasmid should be co-transformed with the pCDF plasmid encoding for a Tag-less BirA. BL21-Rosetta bacteria, co-transformed with both plasmids, were stored at -80^o.

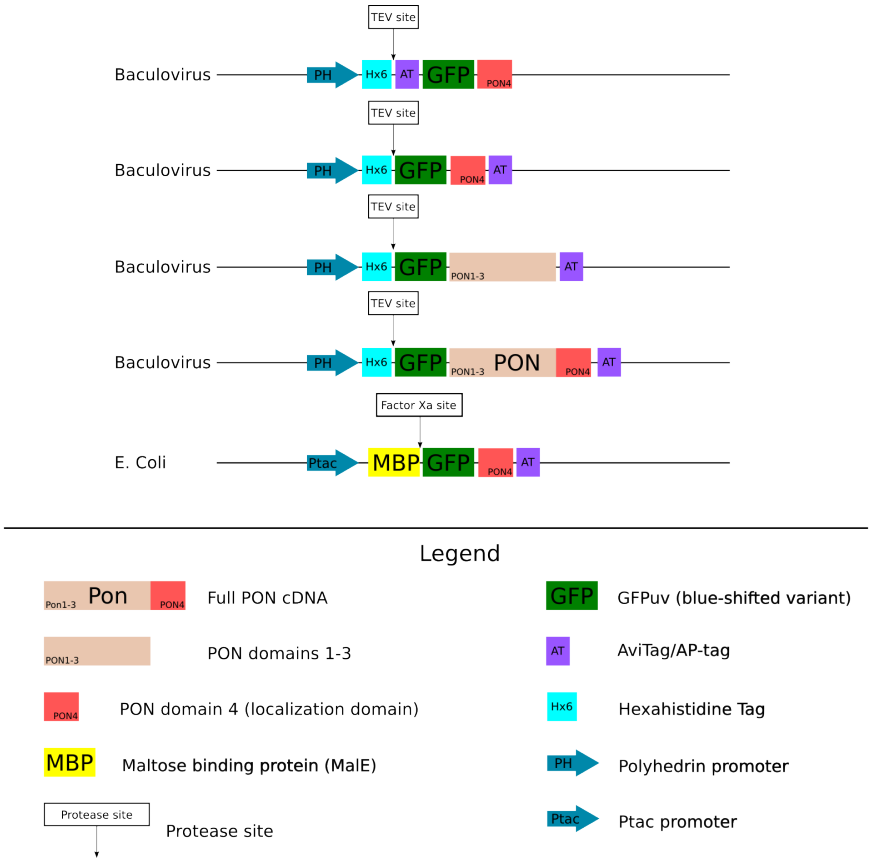

Figure D.3: *The PON constructs*

D.1.4 Numb

Numb was cloned and expressed, but finally not used, due to lack of time.

Baculovirus/SF9: Dual Expression with BirA

We have cloned a dual expression construct, based on the pFastBac Dual backbone, for HisTag-Numb-AviTag (see **Figure D.4**), together with BirA for expression and simultaneous biotinylation in SF9 cells.

E. coli We have cloned a TRXTag-HisTag-STag-Numb-AviTag construct, based on the pET32a backbone(Novagen) (see **Figure D.4**). This construct is co-transformed into *E. coli* bacteria together with pCDF-Duet-BirA (Tag-less), for highly efficient *in-vivo* biotinylation. BL21-Rosetta bacteria, co-transformed with both plasmids, were stored at -80^o.

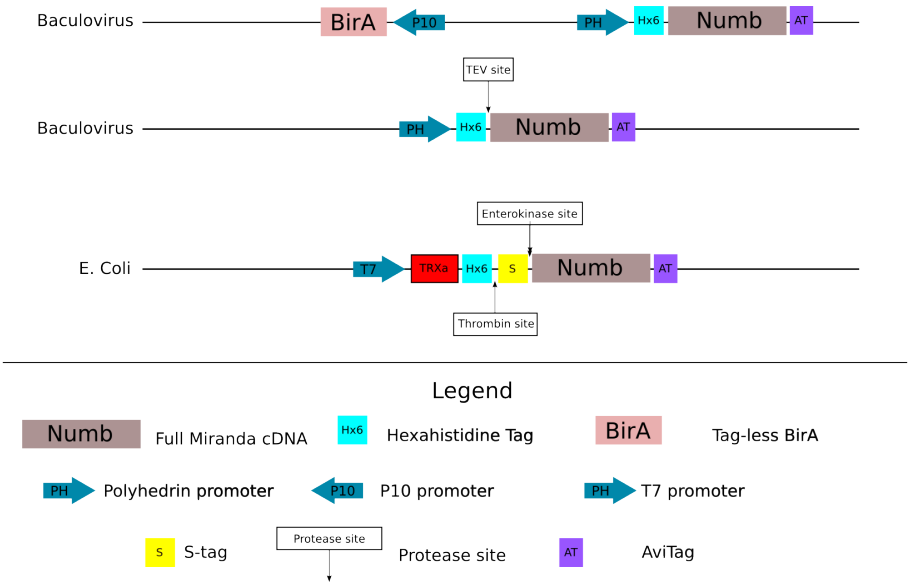

Figure D.4: *Numb constructs for E. coli and baculovirus*

Appendix D

D.2 monobiotinylated GFP

We have cloned and produced this protein, which turned out to be useful for many applications (coupling tests for QD-SAV, kinetic measurements for anti-GFP ScFv, solid-support coupling and more). This construct contains GFPuv (a slightly blue-shifted variant of GFP) with an N-terminal HisTag (removable using a TEV protease) and a C-terminal AviTag (**see Figure D.5**). By co-transfecting *E. coli* with this construct and pCDF-BirA (Tag-less), which biotinylates the protein *in-vivo*, we produced high quantities of monobiotinylated HisTag-GFPuv-AviTag. BL21 Rosetta bacteria, co-transfected with both plasmids were stored at -80°C.

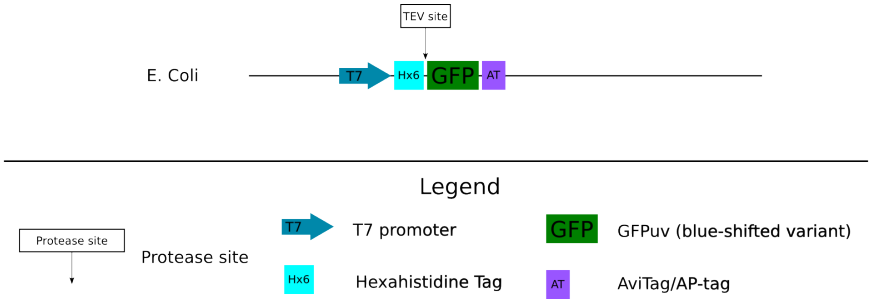

Figure D.5: *The monobiotinylated GFP constructs*

D.3 Single-chain variable fragments (ScFv)

We have cloned two single chain constructs: anti-GFP (cDNA obtained from F. Perez) and anti-myc (cDNA obtained from S. Dübel). Both constructs were cloned into the periplasmic expression vector pET26b (Novagen). These constructs contain an N-terminal PelB leader sequence, which directs the expressed protein into the bacterial periplasm, followed by a signal peptidase site, which is recognized and cleaved by the bacteria as soon as the protein reaches the periplasmic space. In addition, the constructs contain a C-terminal HisTag for purification (see **Figure D.6**).

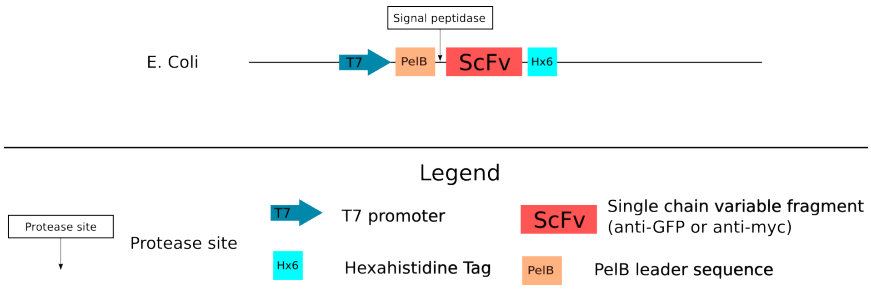

Figure D.6: *Pins constructs*

Appendix D

Part VI

Bibliography

Bibliography

[1] Scott R Wheeler, Stephanie B Stagg, and Stephen T Crews. Multiple notch signaling events control drosophila cns midline neurogenesis, gliogenesis and neuronal identity. *Development*, 135(18):3071–3079, Sep 2008.

[2] Carlos Bustamante. In singulo biochemistry: when less is more. *Annu Rev Biochem*, 77:45–50, 2008.

[3] Ben N G Giepmans, Stephen R Adams, Mark H Ellisman, and Roger Y Tsien. The fluorescent toolbox for assessing protein location and function. *Science*, 312(5771):217–224, Apr 2006.

[4] Nathan C Shaner, Paul A Steinbach, and Roger Y Tsien. A guide to choosing fluorescent proteins. *Nat Methods*, 2(12):905–909, Dec 2005.

[5] M. Sameiro T Gonalves. Fluorescent labeling of biomolecules with organic probes. *Chem Rev*, 109(1):190–212, Jan 2009.

[6] A. Caspi, R. Granek, and M. Elbaum. Enhanced diffusion in active intracellular transport. *Phys Rev Lett*, 85(26 Pt 1):5655–5658, Dec 2000.

[7] Benoit Dubertret, Paris Skourides, David J Norris, Vincent Noireaux, Ali H Brivanlou, and Albert Libchaber. In vivo imaging of quantum dots encapsulated in phospholipid micelles. *Science*, 298(5599):1759–1762, Nov 2002.

[8] R. Merkel, P. Nassoy, A. Leung, K. Ritchie, and E. Evans. Energy landscapes of receptor-ligand bonds explored with dynamic force spectroscopy. *Nature*, 397(6714):50–53, Jan 1999.

[9] Greg T. Hermanson. *Bioconjugate Techniques, 2nd Edition*. Academic Press, Inc., 2008.

[10] Mark Howarth, Wenhao Liu, Sujiet Puthenveetil, Yi Zheng, Lisa F Marshall, Michael M Schmidt, K. Dane Wittrup, Moungi G Bawendi, and Alice Y Ting. Monovalent, reduced-size quantum dots for imaging receptors on living cells. *Nat Methods*, 5(5):397–399, May 2008.

[11] Michael Hust, Thomas Jostock, Christian Menzel, Bernd Voedisch, Anja Mohr, Mariam Brenneis, Martina I Kirsch, Doris Meier, and Stefan Dbel. Single chain fab (scfab) fragment. *BMC Biotechnol*, 7:14, 2007.

[12] Susanne M Rafelski and Wallace F Marshall. Building the cell: design principles of cellular architecture. *Nat Rev Mol Cell Biol*, 9(8):593–602, Aug 2008.

[13] Michael T Laub, Lucy Shapiro, and Harley H McAdams. Systems biology of caulobacter. *Annu Rev Genet*, 41:429–441, 2007.

[14] Y. Yamashita. Asymmetric stem cell division and pathology: insights from drosophila stem cell systems. *J Pathol*, 217(2):181–185, Jan 2009.

[15] Guy Theraulaz, Jacques Gautrais, Scott Camazine, and Jean-Louis Deneubourg. The formation of spatial patterns in social insects: from simple behaviours to complex structures. *Philos Transact A Math Phys Eng Sci*, 361(1807):1263–1282, Jun 2003.

[16] B. Lu, M. Rothenberg, L. Y. Jan, and Y. N. Jan. Partner of numb colocalizes with numb during mitosis and directs numb asymmetric localization in drosophila neural and muscle progenitors. *Cell*, 95(2):225–235, Oct 1998.

[17] H. Ikeshima-Kataoka, J. B. Skeath, Y. Nabeshima, C. Q. Doe, and F. Matsuzaki. Miranda directs prospero to a daughter cell during drosophila asymmetric divisions. *Nature*, 390(6660):625–629, Dec 1997.

[18] M. Schaefer, A. Shevchenko, A. Shevchenko, and J. A. Knoblich. A protein complex containing inscuteable and the galpha-binding protein pins orients asymmetric cell divisions in drosophila. *Curr Biol*, 10(7):353–362, Apr 2000.

[19] James B Delehanty, Hedi Mattoussi, and Igor L Medintz. Delivering quantum dots into cells: strategies, progress and remaining issues. *Anal Bioanal Chem*, 393(4):1091–1105, Feb 2009.

[20] E. G. Diacumakos. Methods for micromanipulation of human somatic cells in culture. *Methods Cell Biol*, 7:287–311, 1973.

[21] C. Y. Okada and M. Rechsteiner. Introduction of macromolecules into cultured mammalian cells by osmotic lysis of pinocytic vesicles. *Cell*, 29(1):33–41, May 1982.

[22] Martynas Gavutis, Suman Lata, and Jacob Piehler. Probing 2-dimensional protein-protein interactions on model membranes. *Nat Protoc*, 1(4):2091–2103, 2006.

[23] Johanna Andrae, Radiosa Gallini, and Christer Betsholtz. Role of platelet-derived growth factors in physiology and medicine. *Genes Dev*, 22(10):1276–1312, May 2008.

[24] Sripad Ram, Prashant Prabhat, Jerry Chao, E. Sally Ward, and Raimund J Ober. High accuracy 3d quantum dot tracking with multifocal plane microscopy for the study of fast intracellular dynamics in live cells. *Biophys J*, 95(12):6025–6043, Dec 2008.

[25] E. Crivellato and D. Ribatti. Aristotle: the first student of angiogenesis. *Leukemia*, 20(7):1209–1210, Jul 2006.

[26] Robert Hooke. *Micrographia: or, Some physiological descriptions of minute bodies made by magnifying glasses*. J. Martyn and J. Allestry,London, 1665.

[27] Patricia Fara. A microscopic reality tale. *Nature*, 459(7247):642–644, Jun 2009.

[28] Charles Singer. Notes on the early history of microscopy. *Proc R Soc Med*, 7:247279., 1914.

[29] Schleiden MJ. Beitrge zur phytogenesis. *Arch Anat Physiol Wiss Med (J Mller)*, page pp 137176, 1838.

[30] Theodor Schwann. *Mikroscopische Untersuchungen ber die bereinstimmung in der Struktur und dem Wachstum des Thiere und Pflanzen. W Engelmann: Leipzig No 176.* W Engelmann: Leipzig No 176, 1839.

[31] Indra K Vasil. A history of plant biotechnology: from the cell theory of schleiden and schwann to biotech crops. *Plant Cell Rep*, 27(9):1423–1440, Sep 2008.

[32] [No authors listed]. Albert von klliker (1817-1905) wrzburger histologist. *JAMA*, 206(9):2111–2., 1968 Nov 25;206(9):2111-2.

[33] C. Golgi. On the structure of the nerve cells of the spinal ganglia. 1898. *J Microsc*, 155(Pt 1):9–14, Jul 1989.

[34] M. G. Farquhar and G. E. Palade. The golgi apparatus: 100 years of progress and controversy. *Trends Cell Biol*, 8(1):2–10, Jan 1998.

[35] M. A. Shampo and R. A. Kyle. Ernst ruska–inventor of the electron microscope. *Mayo Clin Proc*, 72(2):148, Feb 1997.

[36] G. Griffiths, J. M. Lucocq, and T. M. Mayhew. Electron microscopy applications for quantitative cellular microbiology. *Cell Microbiol*, 3(10):659–668, Oct 2001.

[37] Fullam EF Porter KR, Claude A. A study of tissue culture cells by electron microscopy : methods and preliminary observations. *The Journal of Experimental Medicine*, 81:233–246, 233-246.

[38] Keith R Porter and Alex B Novikoff. The 1974 nobel prize for physiology or medicine. *Science*, 186(4163):516–520, Nov 1974.

[39] R. D. Allen, G. B. David, and G. Nomarski. The zeiss-nomarski differential interference equipment for transmitted-light microscopy. *Z Wiss Mikrosk*, 69(4):193–221, Nov 1969.

[40] Joseph R. Lakowitz. *Principles of Fluorescence Spectroscopy*. Springer, 2009.

[41] Pawley JB, editor. *Handbook of Biological Confocal Microscopy*. Springer, 2006.

[42] Michiel Mueller. *Introduction to Confocal Fluorescence Microscopy, Second Edition (SPIE Tutorial Texts in Optical Engineering Vol. TT69)*. SPIE, 2008.

[43] E. Wang, C. M. Babbey, and K. W. Dunn. Performance comparison between the high-speed yokogawa spinning disc confocal system and single-point scanning confocal systems. *J Microsc*, 218(Pt 2):148–159, May 2005.

[44] Daniel Axelrod. Total internal reflection fluorescence microscopy in cell biology. *Methods Enzymol*, 361:1–33, 2003.

[45] D. E. Koppel, D. Axelrod, J. Schlessinger, E. L. Elson, and W. W. Webb. Dynamics of fluorescence marker concentration as a probe of mobility. *Biophys J*, 16(11):1315–1329, Nov 1976.

[46] Van Oijen A Hinterdorfer P, editor. *Handbook of Single Molecule Biophysics*, chapter Fluorescence Correlation Spectroscopy in Living Cells, page HanHandbook of Single Molecule Biophysicsdbook of Single Molecule Biophysics. Springer Press, XXIV, 2009.

[47] Yun Chen, B. Christoffer Lagerholm, Bing Yang, and Ken Jacobson. Methods to measure the lateral diffusion of membrane lipids and proteins. *Methods*, 39(2):147–153, Jun 2006.

[48] T. E. Kreis, B. Geiger, and J. Schlessinger. Mobility of microinjected rhodamine actin within living chicken gizzard cells determined by fluorescence photobleaching recovery. *Cell*, 29(3):835–845, Jul 1982.

[49] R. Y. Tsien. The green fluorescent protein. *Annu Rev Biochem*, 67:509–544, 1998.

[50] Robert F Service. Nobel prize in chemistry. three scientists bask in prize's fluorescent glow. *Science*, 322(5900):361, Oct 2008.

[51] J. Lippincott-Schwartz. The secretory membrane system studied in real-time. robert feulgen prize lecture, 2001. *Histochem Cell Biol*, 116(2):97–107, Aug 2001.

[52] Chirlmin Joo, Hamza Balci, Yuji Ishitsuka, Chittanon Buranachai, and Taekjip Ha. Advances in single-molecule fluorescence methods for molecular biology. *Annu Rev Biochem*, 77:51–76, 2008.

[53] Elizabeth Rhoades, Eugene Gussakovsky, and Gilad Haran. Watching proteins fold one molecule at a time. *Proc Natl Acad Sci U S A*, 100(6):3197–3202, Mar 2003.

[54] J. Gelles, B. J. Schnapp, and M. P. Sheetz. Tracking kinesin-driven movements with nanometre-scale precision. *Nature*, 331(6155):450–453, Feb 1988.

[55] A. D. Mehta, M. Rief, J. A. Spudich, D. A. Smith, and R. M. Simmons. Single-molecule biomechanics with optical methods. *Science*, 283(5408):1689–1695, Mar 1999.

[56] Charlie Gosse and Vincent Croquette. Magnetic tweezers: micromanipulation and force measurement at the molecular level. *Biophys J*, 82(6):3314–3329, Jun 2002.

[57] Akihiro Kusumi, Hiroshi Ike, Chieko Nakada, Kotono Murase, and Takahiro Fujiwara. Single-molecule tracking of membrane molecules: plasma membrane compartmentalization and dynamic assembly of raft-philic signaling molecules. *Semin Immunol*, 17(1):3–21, Feb 2005.

[58] Cdric Bouzigues, Mathieu Morel, Antoine Triller, and Maxime Dahan. Asymmetric redistribution of gaba receptors during gaba gradient sensing by nerve growth cones analyzed by single quantum dot imaging. *Proc Natl Acad Sci U S A*, 104(27):11251–11256, Jul 2007.

[59] Sebastien Courty, Camilla Luccardini, Yohanns Bellaiche, Giovanni Cappello, and Maxime Dahan. Tracking individual kinesin motors in living cells using single quantum-dot imaging. *Nano Lett*, 6(7):1491–1495, Jul 2006.

[60] Paolo Pierobon, Sarra Achouri, Sbastien Courty, Alexander R Dunn, James A Spudich, Maxime Dahan, and Giovanni Cappello. Velocity, processivity, and individual steps of single myosin v molecules in live cells. *Biophys J*, 96(10):4268–4275, May 2009.

[61] D. Dunitz, Jack. *X-ray Analysis and the Structure of Organic Molecules.* Verlag Helvetica Chimica Acta, Basel, 1995.

[62] Everett A Lipman, Benjamin Schuler, Olgica Bakajin, and William A Eaton. Single-molecule measurement of protein folding kinetics. *Science*, 301(5637):1233–1235, Aug 2003.

[63] Sergio G Peisajovich and Dan S Tawfik. Protein engineers turned evolutionists. *Nat Methods*, 4(12):991–994, Dec 2007.

[64] Bianxiao Cui, Chengbiao Wu, Liang Chen, Alfredo Ramirez, Elaine L Bearer, Wei-Ping Li, William C Mobley, and Steven Chu. One at a time, live tracking of ngf axonal transport using quantum dots. *Proc Natl Acad Sci U S A*, 104(34):13666–13671, Aug 2007.

[65] Germain Trugnan, Philippe Fontanges, Danile Delautier, and Tounsia Ait-Slimane. [frap, flip, fret, bret, flim, prim...new techniques for a colourful life]. *Med Sci (Paris)*, 20(11):1027–1034, Nov 2004.

[66] W. J A Koopmans, R. Buning, T. Schmidt, and J. van Noort. spfret using alternating excitation and fcs reveals progressive dna unwrapping in nucleosomes. *Biophys J*, 97(1):195–204, Jul 2009.

[67] Jennifer Lippincott-Schwartz, Nihal Altan-Bonnet, and George H Patterson. Photobleaching and photoactivation: following protein dynamics in living cells. *Nat Cell Biol*, Suppl:S7–14, Sep 2003.

[68] Britta Seefeldt, Robert Kasper, Thorsten Seidel, Philip Tinnefeld, Karl-Josef Dietz, Mike Heilemann, and Markus Sauer. Fluorescent proteins for single-molecule fluorescence applications. *J Biophotonics*, 1(1):74–82, Mar 2008.

[69] Shinsuke Aramaki and Kohei Hatta. Visualizing neurons one-by-one in vivo: optical dissection and reconstruction of neural networks with reversible fluorescent proteins. *Dev Dyn*, 235(8):2192–2199, Aug 2006.

[70] Mike Schenkel, Alison M Sinclair, Daniel Johnstone, J. Derek Bewley, and Jaideep Mathur. Visualizing the actin cytoskeleton in living plant cells using a photo-convertible meos::fabd-mtn fluorescent fusion protein. *Plant Methods*, 4:21, 2008.

[71] A. B. Houtsmuller and W. Vermeulen. Macromolecular dynamics in living cell nuclei revealed by fluorescence redistribution after photobleaching. *Histochem Cell Biol*, 115(1):13–21, Jan 2001.

[72] Danile Hernandez-Verdun. Nucleolus: from structure to dynamics. *Histochem Cell Biol*, 125(1-2):127–137, Jan 2006.

[73] Ute Resch-Genger, Markus Grabolle, Sara Cavaliere-Jaricot, Roland Nitschke, and Thomas Nann. Quantum dots versus organic dyes as fluorescent labels. *Nat Methods*, 5(9):763–775, Sep 2008.

[74] R. P. Haugland. *Handbook of Fluorescent Probes and Research Products.* Molecular Probes: Eugene, OR, 2002.

[75] L. A. Ernst, R. K. Gupta, R. B. Mujumdar, and A. S. Waggoner. Cyanine dye labeling reagents for sulfhydryl groups. *Cytometry*, 10(1):3–10, Jan 1989.

[76] X. Michalet, F. F. Pinaud, L. A. Bentolila, J. M. Tsay, S. Doose, J. J. Li, G. Sundaresan, A. M. Wu, S. S. Gambhir, and S. Weiss. Quantum dots for live cells, in vivo imaging, and diagnostics. *Science*, 307(5709):538–544, Jan 2005.

[77] A. Paul Alivisatos, Weiwei Gu, and Carolyn Larabell. Quantum dots as cellular probes. *Annu Rev Biomed Eng*, 7:55–76, 2005.

[78] Stphane Berciaud, Laurent Cognet, and Brahim Lounis. Luminescence decay and the absorption cross section of individual single-walled carbon nanotubes. *Phys Rev Lett*, 101(7):077402, Aug 2008.

[79] David Lasne, Gerhard A Blab, Stphane Berciaud, Martin Heine, Laurent Groc, Daniel Choquet, Laurent Cognet, and Brahim Lounis. Single nanoparticle photothermal tracking (snapt) of 5-nm gold beads in live cells. *Biophys J*, 91(12):4598–4604, Dec 2006.

[80] L. Cognet, C. Tardin, D. Boyer, D. Choquet, P. Tamarat, and B. Lounis. Single metallic nanoparticle imaging for protein detection in cells. *Proc Natl Acad Sci U S A*, 100(20):11350–11355, Sep 2003.

[81] M. Bruchez, M. Moronne, P. Gin, S. Weiss, and A. P. Alivisatos. Semiconductor nanocrystals as fluorescent biological labels. *Science*, 281(5385):2013–2016, Sep 1998.

[82] Shanmin Gao, Jun Lu, Nan Chen, Yan Zhao, and Yi Xie. Aqueous synthesis of iii-v semiconductor gap and inp exhibiting pronounced quantum confinement. *Chem Commun (Camb)*, (24):3064–3065, Dec 2002.

[83] John P Zimmer, Sang-Wook Kim, Shunsuke Ohnishi, Eichii Tanaka, John V Frangioni, and Moungi G Bawendi. Size series of small indium arsenide-zinc selenide core-shell nanocrystals and their application to in vivo imaging. *J Am Chem Soc*, 128(8):2526–2527, Mar 2006.

[84] Steven F Lee and Mark A Osborne. Brightening, blinking, bluing and bleaching in the life of a quantum dot: friend or foe? *Chemphyschem*, 10(13):2174–2191, Sep 2009.

[85] Paul Abbyad, William Childs, Xinghua Shi, and Steven G Boxer. Dynamic stokes shift in green fluorescent protein variants. *Proc Natl Acad Sci U S A*, 104(51):20189–20194, Dec 2007.

[86] Gopal Iyer, Fabien Pinaud, James Tsay, Jack J Li, Laurent A Bentolila, Xavier Michalet, and Shimon Weiss. Peptide coated quantum dots for biological applications. *IEEE Trans Nanobioscience*, 5(4):231–238, Dec 2006.

[87] Aaron R Clapp, Ellen R Goldman, and Hedi Mattoussi. Capping of cdse-zns quantum dots with dhla and subsequent conjugation with proteins. *Nat Protoc*, 1(3):1258–1266, 2006.

[88] Victor Roullier, Samuel Clarke, Changjiang You, Fabien Pinaud, G. Graldine Gouzer, Dirk Schaible, Valrie Marchi-Artzner, Jacob Piehler, and Maxime Dahan. High-affinity labeling and tracking of individual histidine-tagged proteins in live cells using ni2+ tris-nitrilotriacetic acid quantum dot conjugates. *Nano Lett*, 9(3):1228–1234, Mar 2009.

[89] Emma E Lees, Tich-Lam Nguyen, Andrew H A Clayton, Benjamin W Muir, and Paul Mulvaney. The preparation of colloidally stable, water-soluble, biocompatible, semiconductor nanocrystals with a small hydrodynamic diameter. *ACS Nano*, 3(7):2049, Jul 2009.

[90] Michael J Murcia, Daniel E Minner, Gina-Mirela Mustata, Kenneth Ritchie, and Christoph A Naumann. Design of quantum dot-conjugated lipids for long-term, high-speed tracking experiments on cell surfaces. *J Am Chem Soc*, 130(45):15054–15062, Nov 2008.

[91] Wenhao Liu, Mark Howarth, Andrew B Greytak, Yi Zheng, Daniel G Nocera, Alice Y Ting, and Moungi G Bawendi. Compact biocompatible quantum dots functionalized for cellular imaging. *J Am Chem Soc*, 130(4):1274–1284, Jan 2008.

[92] Kimihiro Susumu, H. Tetsuo Uyeda, Igor L Medintz, Thomas Pons, James B Delehanty, and Hedi Mattoussi. Enhancing the stability and biological functionalities of quantum dots via compact multifunctional ligands. *J Am Chem Soc*, 129(45):13987–13996, Nov 2007.

[93] Fabien Pinaud, David King, Hsiao-Ping Moore, and Shimon Weiss. Bioactivation and cell targeting of semiconductor cdse/zns nanocrystals with phytochelatin-related peptides. *J Am Chem Soc*, 126(19):6115–6123, May 2004.

[94] Gopal Iyer, Fabien Pinaud, James Tsay, and Shimon Weiss. Solubilization of quantum dots with a recombinant peptide from escherichia coli. *Small*, 3(5):793–798, May 2007.

[95] S. Salman Ashraf, R. Edward Benson, E. Sturgis Payne, Cale M Halbleib, and Hanne Grn. A novel multi-affinity tag system to produce high levels of soluble and biotinylated proteins in escherichia coli. *Protein Expr Purif*, 33(2):238–245, Feb 2004.

[96] Fabien Pinaud, Xavier Michalet, Gopal Iyer, Emmanuel Margeat, Hsiao-Ping Moore, and Shimon Weiss. Dynamic partitioning of a glycosyl-phosphatidylinositol-anchored protein in glycosphingolipid-rich microdomains imaged by single-quantum dot tracking. *Traffic*, Mar 2009.

[97] Marie-Virginie Ehrensperger, Cyril Hanus, Christian Vannier, Antoine Triller, and Maxime Dahan. Multiple association states between glycine receptors and gephyrin identified by spt analysis. *Biophys J*, 92(10):3706–3718, May 2007.

[98] Peter M Haggie, Jung Kyung Kim, Gergely L Lukacs, and A. S. Verkman. Tracking of quantum dot-labeled cftr shows near immobilization by c-terminal pdz interactions. *Mol Biol Cell*, 17(12):4937–4945, Dec 2006.

[99] Betty Y S Kim, Wen Jiang, John Oreopoulos, Christopher M Yip, James T Rutka, and Warren C W Chan. Biodegradable quantum dot nanocomposites enable live cell labeling and imaging of cytoplasmic targets. *Nano Lett*, 8(11):3887–3892, Nov 2008.

[100] Roberto Bonasio, Christopher V Carman, Enoch Kim, Peter T Sage, Kerry R Love, Thorsten R Mempel, Timothy A Springer, and Ulrich H von Andrian. Specific and covalent labeling of a membrane protein with organic fluorochromes and quantum dots. *Proc Natl Acad Sci U S A*, 104(37):14753–14758, Sep 2007.

[101] Murat Sunbul, Michelle Yen, Yekui Zou, and Jun Yin. Enzyme catalyzed site-specific protein labeling and cell imaging with quantum dots. *Chem Commun (Camb)*, (45):5927–5929, Dec 2008.

[102] Mark Howarth, Daniel J-F Chinnapen, Kimberly Gerrow, Pieter C Dorrestein, Melanie R Grandy, Neil L Kelleher, Alaa El-Husseini, and Alice Y Ting. A monovalent streptavidin with a single femtomolar biotin binding site. *Nat Methods*, 3(4):267–273, Apr 2006.

[103] James B Delehanty, Hedi Mattoussi, and Igor L Medintz. Delivering quantum dots into cells: strategies, progress and remaining issues. *Anal Bioanal Chem*, 393(4):1091–1105, Feb 2009.

[104] Igor Nabiev, Siobhan Mitchell, Anthony Davies, Yvonne Williams, Dermot Kelleher, Richard Moore, Yurii K Gun'ko, Stephen Byrne, Yury P Rakovich, John F Donegan, Alyona Sukhanova, Jennifer Conroy, David Cottell, Nikolai Gaponik, Andrey Rogach, and Yuri Volkov. Nonfunctionalized nanocrystals can exploit a cell's active transport machinery delivering them to specific nuclear and cytoplasmic compartments. *Nano Lett*, 7(11):3452–3461, Nov 2007.

[105] Xiaolin Nan, Peter A Sims, Peng Chen, and X. Sunney Xie. Observation of individual microtubule motor steps in living cells with endocytosed quantum dots. *J Phys Chem B*, 109(51):24220–24224, Dec 2005.

[106] James B Delehanty, Igor L Medintz, Thomas Pons, Florence M Brunel, Philip E Dawson, and Hedi Mattoussi. Self-assembled quantum dot-peptide bioconjugates for selective intracellular delivery. *Bioconjug Chem*, 17(4):920–927, 2006.

[107] W. C. Chan and S. Nie. Quantum dot bioconjugates for ultrasensitive nonisotopic detection. *Science*, 281(5385):2016–2018, Sep 1998.

[108] J. A. Kloepfer, R. E. Mielke, M. S. Wong, K. H. Nealson, G. Stucky, and J. L. Nadeau. Quantum dots as strain- and metabolism-specific microbiological labels. *Appl Environ Microbiol*, 69(7):4205–4213, Jul 2003.

[109] Ken-Tye Yong, Jun Qian, Indrajit Roy, Hoon Hi Lee, Earl J Bergey, Kenneth M Tramposch, Sailing He, Mark T Swihart, Anirban Maitra, and Paras N Prasad. Quantum rod bioconjugates as targeted probes for confocal and two-photon fluorescence imaging of cancer cells. *Nano Lett*, 7(3):761–765, Mar 2007.

[110] Mara M Echarte, Luciana Bruno, Donna J Arndt-Jovin, Thomas M Jovin, and La I Pietrasanta. Quantitative single particle tracking of ngf-receptor complexes: transport is bidirectional but biased by longer retrograde run lengths. *FEBS Lett*, 581(16):2905–2913, Jun 2007.

[111] Subhasish K Chakraborty, James A J Fitzpatrick, Julie A Phillippi, Susan Andreko, Alan S Waggoner, Marcel P Bruchez, and Byron Ballou. Cholera toxin b conjugated quantum dots for live cell labeling. *Nano Lett*, 7(9):2618–2626, Sep 2007.

[112] Jun Qian, Ken-Tye Yong, Indrajit Roy, Tymish Y Ohulchanskyy, Earl J Bergey, Hoon Hi Lee, Kenneth M Tramposch, Sailing He, Anirban Maitra, and Paras N Prasad. Imaging pancreatic cancer using surface-functionalized quantum dots. *J Phys Chem B*, 111(25):6969–6972, Jun 2007.

[113] Ken-Tye Yong, Hong Ding, Indrajit Roy, Wing-Cheung Law, Earl J Bergey, Anirban Maitra, and Paras N Prasad. Imaging pancreatic cancer using bioconjugated inp quantum dots. *ACS Nano*, 3(3):502–510, Mar 2009.

[114] Hongwei Duan and Shuming Nie. Cell-penetrating quantum dots based on multivalent and endosome-disrupting surface coatings. *J Am Chem Soc*, 129(11):3333–3338, Mar 2007.

[115] Lifeng Qi and Xiaohu Gao. Quantum dot-amphipol nanocomplex for intracellular delivery and real-time imaging of sirna. *ACS Nano*, 2(7):1403–1410, Jul 2008.

[116] Amy E Jablonski, William H Humphries, and Christine K Payne. Pyrenebutyrate-mediated delivery of quantum dots across the plasma membrane of living cells. *J Phys Chem B*, 113(2):405–408, Jan 2009.

[117] Kyungsuk Yum, Sungsoo Na, Yang Xiang, Ning Wang, and Min-Feng Yu. Mechanochemical delivery and dynamic tracking of fluorescent quantum dots in the cytoplasm and nucleus of living cells. *Nano Lett*, 2009.

[118] Yo Ishihama and Takashi Funatsu. Single molecule tracking of quantum dot-labeled mrnas in a cell nucleus. *Biochem Biophys Res Commun*, 381(1):33–38, Mar 2009.

[119] Xing Chen, Andras Kis, A. Zettl, and Carolyn R Bertozzi. A cell nanoinjector based on carbon nanotubes. *Proc Natl Acad Sci U S A*, 104(20):8218–8222, May 2007.

[120] Sangjin Park, Youn-Su Kim, Won Bae Kim, and Sangyong Jon. Carbon nanosyringe array as a platform for intracellular delivery. *Nano Lett*, 9(4):1325–1329, Apr 2009.

[121] Fanqing Chen and Daniele Gerion. Fluorescent cdse/zns nanocrystal-peptide conjugates for long-term, nontoxic imaging and nuclear targeting in living cells. *Nano Letters*, 4(10):1827–1832, 2004.

[122] Jonathan R Slotkin, Lina Chakrabarti, Hai Ning Dai, Rosalind S E Carney, Tsutomu Hirata, Barbara S Bregman, G. Ian Gallicano, Joshua G Corbin, and Tarik F Haydar. In vivo quantum dot labeling of mammalian stem and progenitor cells. *Dev Dyn*, 236(12):3393–3401, Dec 2007.

[123] S. N. Bhatia A. M. Derfus, W. C. W. Chan. Intracellular delivery of quantum dots for live cell labeling and organelle tracking. *Advanced Materials*, 12:961–966, 2004.

[124] Giovanni Cappello, Paolo Pierobon, Clmentine Symonds, Lorenzo Busoni, J. Christof M Gebhardt, Matthias Rief, and Jacques Prost. Myosin v stepping mechanism. *Proc Natl Acad Sci U S A*, 104(39):15328–15333, Sep 2007.

[125] Christina Tekle, Bo van Deurs, Kirsten Sandvig, and Tore-Geir Iversen. Cellular trafficking of quantum dot-ligand bioconjugates and their induction of changes in normal routing of unconjugated ligands. *Nano Lett*, 8(7):1858–1865, Jul 2008.

[126] Paul R Pryor and J. Paul Luzio. Delivery of endocytosed membrane proteins to the lysosome. *Biochim Biophys Acta*, 1793(4):615–624, Apr 2009.

[127] H. Qian, M. P. Sheetz, and E. L. Elson. Single particle tracking. analysis of diffusion and flow in two-dimensional systems. *Biophys J*, 60(4):910–921, Oct 1991.

[128] John Avery. *Information Theory and Evolution*. World Scientific, 2000.

[129] John J Tyson, Reka Albert, Albert Goldbeter, Peter Ruoff, and Jill Sible. Biological switches and clocks. *J R Soc Interface*, 5 Suppl 1:S1–S8, Aug 2008.

[130] Sophie Dumont and Timothy J Mitchison. Compression regulates mitotic spindle length by a mechanochemical switch at the poles. *Curr Biol*, 19(13):1086–1095, Jul 2009.

[131] Concepcin Gmez-Moutn and Santos Maes. Establishment and maintenance of cell polarity during leukocyte chemotaxis. *Cell Adh Migr*, 1(2):69–76, Apr 2007.

[132] Pascale G Charest and Richard A Firtel. Feedback signaling controls leading-edge formation during chemotaxis. *Curr Opin Genet Dev*, 16(4):339–347, Aug 2006.

[133] David Pruyne, Aster Legesse-Miller, Lina Gao, Yuqing Dong, and Anthony Bretscher. Mechanisms of polarized growth and organelle segregation in yeast. *Annu Rev Cell Dev Biol*, 20:559–591, 2004.

[134] Rex A Cole and John E Fowler. Polarized growth: maintaining focus on the tip. *Curr Opin Plant Biol*, 9(6):579–588, Dec 2006.

[135] B. L. Tang. Protein trafficking mechanisms associated with neurite outgrowth and polarized sorting in neurons. *J Neurochem*, 79(5):923–930, Dec 2001.

[136] Pierre Gnczy. Mechanisms of asymmetric cell division: flies and worms pave the way. *Nat Rev Mol Cell Biol*, 9(5):355–366, May 2008.

[137] Deborah J Andrew and Andrew J Ewald. Morphogenesis of epithelial tubes: Insights into tube formation, elongation, and elaboration. *Dev Biol*, Sep 2009.

[138] Marion Segalen and Yohanns Bellache. Cell division orientation and planar cell polarity pathways. *Semin Cell Dev Biol*, Apr 2009.

[139] H. R. Horvitz and I. Herskowitz. Mechanisms of asymmetric cell division: two bs or not two bs, that is the question. *Cell*, 68(2):237–255, Jan 1992.

[140] Aakanksha Singhvi and Gian Garriga. Asymmetric divisions, aggresomes and apoptosis. *Trends Cell Biol*, 19(1):1–7, Jan 2009.

[141] Kornelia Polyak and William C Hahn. Roots and stems: stem cells in cancer. *Nat Med*, 12(3):296–300, Mar 2006.

[142] Juergen A Knoblich. Mechanisms of asymmetric stem cell division. *Cell*, 132(4):583–597, Feb 2008.

[143] L. Shapiro. Differentiation in the caulobacter cell cycle. *Annu Rev Microbiol*, 30:377–407, 1976.

[144] Zhanna Shcheprova, Sandro Baldi, Stephanie Buvelot Frei, Gaston Gonnet, and Yves Barral. A mechanism for asymmetric segregation of age during yeast budding. *Nature*, 454(7205):728–734, Aug 2008.

[145] F. Chang and D. G. Drubin. Cell division: why daughters cannot be like their mothers. *Curr Biol*, 6(6):651–654, Jun 1996.

[146] R. M. Long, R. H. Singer, X. Meng, I. Gonzalez, K. Nasmyth, and R. P. Jansen. Mating type switching in yeast controlled by asymmetric localization of ash1 mrna. *Science*, 277(5324):383–387, Jul 1997.

[147] Bob Goldstein and Ian G Macara. The par proteins: fundamental players in animal cell polarization. *Dev Cell*, 13(5):609–622, Nov 2007.

[148] Jrg Betschinger and Jrgen A Knoblich. Dare to be different: asymmetric cell division in drosophila, c. elegans and vertebrates. *Curr Biol*, 14(16):R674–R685, Aug 2004.

[149] M. Gho, Y. Bellache, and F. Schweisguth. Revisiting the drosophila microchaete lineage: a novel intrinsically asymmetric cell division generates a glial cell. *Development*, 126(16):3573–3584, Aug 1999.

[150] G. V. Reddy and V. Rodrigues. A glial cell arises from an additional division within the mechanosensory lineage during development of the microchaete on the drosophila notum. *Development*, 126(20):4617–4622, Oct 1999.

[151] Y. Bellache, M. Gho, J. A. Kaltschmidt, A. H. Brand, and F. Schweisguth. Frizzled regulates localization of cell-fate determinants and mitotic spindle rotation during asymmetric cell division. *Nat Cell Biol*, 3(1):50–57, Jan 2001.

[152] John T Chang, Vikram R Palanivel, Ichiko Kinjyo, Felix Schambach, Andrew M Intlekofer, Arnob Banerjee, Sarah A Longworth, Kristine E Vinup, Paul Mrass, Jane Oliaro, Nigel Killeen, Jordan S Orange, Sarah M Russell, Wolfgang Weninger, and Steven L Reiner. Asymmetric t lymphocyte division in the initiation of adaptive immune responses. *Science*, 315(5819):1687–1691, Mar 2007.

[153] J. Januschke and C. Gonzalez. Drosophila asymmetric division, polarity and cancer. *Oncogene*, 27(55):6994–7002, Nov 2008.

[154] V. Hartenstein. *Atlas of Drosophila development*. Cold Spring Harbor Laboratory Press, Cold Spring Harbor, NY., 1993.

[155] Mark E Fortini. Notch signaling: the core pathway and its posttranslational regulation. *Dev Cell*, 16(5):633–647, May 2009.

[156] Karsten H Siller, Clemens Cabernard, and Chris Q Doe. The numa-related mud protein binds pins and regulates spindle orientation in drosophila neuroblasts. *Nat Cell Biol*, 8(6):594–600, Jun 2006.

[157] C. Y. Peng, L. Manning, R. Albertson, and C. Q. Doe. The tumour-suppressor genes lgl and dlg regulate basal protein targeting in drosophila neuroblasts. *Nature*, 408(6812):596–600, Nov 2000.

[158] Y. Cai, W. Chia, and X. Yang. A family of snail-related zinc finger proteins regulates two distinct and parallel mechanisms that mediate drosophila neuroblast asymmetric divisions. *EMBO J*, 20(7):1704–1714, Apr 2001.

[159] Claudia S Barros, Chris B Phelps, and Andrea H Brand. Drosophila nonmuscle myosin ii promotes the asymmetric segregation of cell fate determinants by cortical exclusion rather than active transport. *Dev Cell*, 5(6):829–840, Dec 2003.

[160] Veronika Erben, Markus Waldhuber, Diana Langer, Ingrid Fetka, Ralf Peter Jansen, and Claudia Petritsch. Asymmetric localization of the adaptor protein miranda in neuroblasts is achieved by diffusion and sequential interaction of myosin ii and vi. *J Cell Sci*, 121(Pt 9):1403–1414, May 2008.

[161] Scott X Atwood and Kenneth E Prehoda. apkc phosphorylates miranda to polarize fate determinants during neuroblast asymmetric cell division. *Curr Biol*, Apr 2009.

[162] Robert Hoffmann and Alfonso Valencia. A gene network for navigating the literature. *Nat Genet*, 36(7):664, Jul 2004.

[163] Johanna Langevin, Roland Le Borgne, Franois Rosenfeld, Michel Gho, Franois Schweisguth, and Yohanns Bellache. Lethal giant larvae controls the localization of notch-signaling regulators numb, neuralized, and sanpodo in drosophila sensory-organ precursor cells. *Curr Biol*, 15(10):955–962, May 2005.

[164] Hongyan Wang, Yingshi Ouyang, W. Gregory Somers, William Chia, and Bingwei Lu. Polo inhibits progenitor self-renewal and regulates numb asymmetry by phosphorylating pon. *Nature*, 449(7158):96–100, Sep 2007.

[165] B. Lu, L. Ackerman, L. Y. Jan, and Y. N. Jan. Modes of protein movement that lead to the asymmetric localization of partner of numb during drosophila neuroblast division. *Mol Cell*, 4(6):883–891, Dec 1999.

[166] Cayetano Gonzalez. Spindle orientation, asymmetric division and tumour suppression in drosophila stem cells. *Nat Rev Genet*, 8(6):462–472, Jun 2007.

[167] Cheng-Yu Lee, Ryan O Andersen, Clemens Cabernard, Laurina Manning, Khoa D Tran, Marcus J Lanskey, Arash Bashirullah, and Chris Q Doe. Drosophila aurora-a kinase inhibits neuroblast self-renewal by regulating apkc/numb cortical polarity and spindle orientation. *Genes Dev*, 20(24):3464–3474, Dec 2006.

[168] Elena Rebollo, Paula Sampaio, Jens Januschke, Salud Llamazares, Hanne Varmark, and Cayetano Gonzlez. Functionally unequal centrosomes drive spindle orientation in asymmetrically dividing drosophila neural stem cells. *Dev Cell*, 12(3):467–474, Mar 2007.

[169] Emmanuel Caussinus and Cayetano Gonzalez. Induction of tumor growth by altered stem-cell asymmetric division in drosophila melanogaster. *Nat Genet*, 37(10):1125–1129, Oct 2005.

[170] Karsten H Siller and Chris Q Doe. Spindle orientation during asymmetric cell division. *Nat Cell Biol*, 11(4):365–374, Apr 2009.

[171] Rick W Nipper, Karsten H Siller, Nicholas R Smith, Chris Q Doe, and Kenneth E Prehoda. Galphai generates multiple pins activation states to link cortical polarity and spindle orientation in drosophila neuroblasts. *Proc Natl Acad Sci U S A*, 104(36):14306–14311, Sep 2007.

[172] Y. Bellache, A. Radovic, D. F. Woods, C. D. Hough, M. L. Parmentier, C. J. O'Kane, P. J. Bryant, and F. Schweisguth. The partner of inscuteable/discs-large complex is required to establish planar polarity during asymmetric cell division in drosophila. *Cell*, 106(3):355–366, Aug 2001.

[173] Sarah E Siegrist and Chris Q Doe. Microtubule-induced pins/galphai cortical polarity in drosophila neuroblasts. *Cell*, 123(7):1323–1335, Dec 2005.

[174] Roland Wedlich-Soldner, Steve Altschuler, Lani Wu, and Rong Li. Spontaneous cell polarization through actomyosin-based delivery of the cdc42 gtpase. *Science*, 299(5610):1231–1235, Feb 2003.

[175] Roland Wedlich-Soldner and Rong Li. Spontaneous cell polarization: undermining determinism. *Nat Cell Biol*, 5(4):267–270, Apr 2003.

[176] Alexandra V. Pokhilko Andrew B. Goryachev. Dynamics of cdc42 network embodies a turing-type mechanism of yeast cell polarity. *FEBS letters*, 582:1437–1443, 2008.

[177] A. M. Turing. The chemical basis of morphogenesis. *Philosophical Transactions of the royal society of London, Series B, Biological sciences*, 237:37–72, 1952.

[178] Roland Wedlich-Soldner, Stephanie C Wai, Thomas Schmidt, and Rong Li. Robust cell polarity is a dynamic state established by coupling transport and gtpase signaling. *J Cell Biol*, 166(6):889–900, Sep 2004.

[179] Nai-Jia Linda Liu, Rachel J Dutton, and Kit Pogliano. Evidence that the spoiiie dna translocase participates in membrane fusion during cytokinesis and engulfment. *Mol Microbiol*, 59(4):1097–1113, Feb 2006.

[180] Brian R Daniels, Edward M Perkins, Terrence M Dobrowsky, Sean X Sun, and Denis Wirtz. Asymmetric enrichment of pie-1 in the caenorhabditis elegans zygote mediated by binary counterdiffusion. *J Cell Biol*, 184(4):473–479, Feb 2009.

[181] James N Weiss, Zhilin Qu, and Alan Garfinkel. Understanding biological complexity: lessons from the past. *FASEB J*, 17(1):1–6, Jan 2003.

[182] Michael Socolich. *Drosophila genetics*. 2003.

[183] Susan Tweedie, Michael Ashburner, Kathleen Falls, Paul Leyland, Peter McQuilton, Steven Marygold, Gillian Millburn, David Osumi-Sutherland, Andrew Schroeder, Ruth Seal, Haiyan Zhang, and FlyBase Consortium. Flybase: enhancing drosophila gene ontology annotations. *Nucleic Acids Res*, 37(Database issue):D555–D559, Jan 2009.

[184] Joseph B Duffy. Gal4 system in drosophila: a fly geneticist's swiss army knife. *Genesis*, 34(1-2):1–15, 2002.

[185] Zimm G.G. Lindsley D.L. *The Genome of Drosophila melanogaster*. 1992.

[186] David O Morgan. *The Cell Cycle: Principles of Control*. New Science Press, 2002.

[187] S. Duffy, K. L. Tsao, and D. S. Waugh. Site-specific, enzymatic biotinylation of recombinant proteins in spodoptera frugiperda cells using biotin acceptor peptides. *Anal Biochem*, 262(2):122–128, Sep 1998.

[188] A. Len-Del-Rio, D. Leclerc, B. Akerman, N. Wakamatsu, and R. A. Gravel. Isolation of a cdna encoding human holocarboxylase synthetase by functional complementation of a biotin auxotroph of escherichia coli. *Proc Natl Acad Sci U S A*, 92(10):4626–4630, May 1995.

[189] P. Saviranta, T. Haavisto, P. Rappu, M. Karp, and T. Lvgren. In vitro enzymatic biotinylation of recombinant fab fragments through a peptide acceptor tail. *Bioconjug Chem*, 9(6):725–735, 1998.

[190] Suman Lata, Annett Reichel, Roland Brock, Robert Tamp, and Jacob Piehler. High-affinity adaptors for switchable recognition of histidine-tagged proteins. *J Am Chem Soc*, 127(29):10205–10215, Jul 2005.

[191] Laurent Groc, Mathieu Lafourcade, Martin Heine, Marianne Renner, Victor Racine, Jean-Baptiste Sibarita, Brahim Lounis, Daniel Choquet, and Laurent Cognet. Surface trafficking of neurotransmitter receptor: comparison between single-molecule/quantum dot strategies. *J Neurosci*, 27(46):12433–12437, Nov 2007.

[192] David W. Russell Joseph Sambrook. *Molecular cloning : a laboratory manual*. Cold Spring Harbor, N.Y. : Cold Spring Harbor Laboratory., 2001.

[193] Kingston RE Ausubel FM, Brent R, editor. *Short Protocols in Molecular Biology, Vol I,II*. Wiley, 2002.

[194] AG Ogston. The spaces in a uniform random suspension of fibres. *Transactions of the Faraday Society*, 54:1754 – 1757, 1958.

[195] J. F. Mercier and G. W. Slater. An exactly solvable ogston model of gel electrophoresis iv: sieving through periodic three-dimensional gels. *Electrophoresis*, 19(10):1560–1565, Jul 1998.

[196] J. F. Mercier, F. Tessier, and G. W. Slater. An exactly solvable ogston model of gel electrophoresis: Viii. nonconducting gel fibers, curved field lines, and the nernst-einstein relation. *Electrophoresis*, 22(13):2631–2638, Aug 2001.

[197] G. W. Slater and H. L. Guo. An exactly solvable ogston model of gel electrophoresis. ii. sieving through periodic gels. *Electrophoresis*, 17(9):1407–1415, Sep 1996.

[198] G. W. Slater and H. L. Guo. An exactly solvable ogston model of gel electrophoresis: I. the role of the symmetry and randomness of the gel structure. *Electrophoresis*, 17(6):977–988, Jun 1996.

[199] J. Labrie, J. F. Mercier, and G. W. Slater. An exactly solvable ogston model of gel electrophoresis. v. attractive gel-analyte interactions and their effects on the ferguson plot. *Electrophoresis*, 21(5):823–833, Mar 2000.

[200] W. N. Burnette. "western blotting": electrophoretic transfer of proteins from sodium dodecyl sulfate–polyacrylamide gels to unmodified nitrocellulose and radiographic detection with antibody and radioiodinated protein a. *Anal Biochem*, 112(2):195–203, Apr 1981.

[201] I. Laffafian and M. B. Hallett. Gentle microinjection for myeloid cells using slam. *Blood*, 95(10):3270–3271, May 2000.

[202] Adelina Prado, Isbaal Ramos, Lindsay J Frehlick, Arturo Muga, and Juan Ausi. Nucleoplasmin: a nuclear chaperone. *Biochem Cell Biol*, 82(4):437–445, Aug 2004.

[203] Carme Arnan, Nria Saperas, Clia Prieto, Manel Chiva, and Juan Ausi. Interaction of nucleoplasmin with core histones. *J Biol Chem*, 278(33):31319–31324, Aug 2003.

[204] Jeffery M Betthauser, Martha Pfister-Genskow, Hongzhi Xu, Paul J Golueke, Jenine C Lacson, Richard W Koppang, Cena Myers, Bing Liu, Ina Hoeschele, Kenneth J Eilertsen, and Gregory H Leno. Nucleoplasmin facilitates reprogramming and in vivo development of bovine nuclear transfer embryos. *Mol Reprod Dev*, 73(8):977–986, Aug 2006.

[205] S. Chatterjee and U. Stochaj. Diffusion of proteins across the nuclear envelope of hela cells. *Biotechniques*, 24(4):668–674, Apr 1998.

[206] Pearu Peterson Eric Jones, Travis Oliphant and others. *SciPy: Open Source Scientific Tools for Python*. 2001.

[207] J.D. Hunter. Matplotlib: A 2d graphics environment. *Computing in Science & Engineering*, 9:90–95, 2007.

[208] Arnauld Serg, Nicolas Bertaux, Herv Rigneault, and Didier Marguet. Dynamic multiple-target tracing to probe spatiotemporal cartography of cell membranes. *Nat Methods*, 5(8):687–694, Aug 2008.

[209] Daniel Sage, Franck R Neumann, Florence Hediger, Susan M Gasser, and Michael Unser. Automatic tracking of individual fluorescence particles: application to the study of chromosome dynamics. *IEEE Trans Image Process*, 14(9):1372–1383, Sep 2005.

[210] Russell E Thompson, Daniel R Larson, and Watt W Webb. Precise nanometer localization analysis for individual fluorescent probes. *Biophys J*, 82(5):2775–2783, May 2002.

[211] M. F. Sanner. Python: a programming language for software integration and development. *J Mol Graph Model*, 17(1):57–61, Feb 1999.

[212] M. J. Saxton. Single-particle tracking: models of directed transport. *Biophys J*, 67(5):2110–2119, Nov 1994.

[213] Sbastien Courty, Cdric Bouzigues, Camilla Luccardini, Marie-Virginie Ehrensperger, Stphane Bonneau, and Maxime Dahan. Tracking individual proteins in living cells using single quantum dot imaging. *Methods Enzymol*, 414:211–228, 2006.

[214] Michael J Saxton. A biological interpretation of transient anomalous subdiffusion. i. qualitative model. *Biophys J*, 92(4):1178–1191, Feb 2007.

[215] Matthias Weiss, Markus Elsner, Fredrik Kartberg, and Tommy Nilsson. Anomalous subdiffusion is a measure for cytoplasmic crowding in living cells. *Biophys J*, 87(5):3518–3524, Nov 2004.

[216] A. Kusumi, Y. Sako, and M. Yamamoto. Confined lateral diffusion of membrane receptors as studied by single particle tracking (nanovid microscopy). effects of calcium-induced differentiation in cultured epithelial cells. *Biophys J*, 65(5):2021–2040, Nov 1993.

[217] S. Bolte and F. P. Cordelires. A guided tour into subcellular colocalization analysis in light microscopy. *J Microsc*, 224(Pt 3):213–232, Dec 2006.

[218] K. Kinosita, H. Itoh, S. Ishiwata, K. Hirano, T. Nishizaka, and T. Hayakawa. Dual-view microscopy with a single camera: real-time imaging of molecular orientations and calcium. *J Cell Biol*, 115(1):67–73, Oct 1991.

[219] S. Yanagawa, J. S. Lee, and A. Ishimoto. Identification and characterization of a novel line of drosophila schneider s2 cells that respond to wingless signaling. *J Biol Chem*, 273(48):32353–32359, Nov 1998.

[220] G. J. TODARO and H. GREEN. Quantitative studies of the growth of mouse embryo cells in culture and their development into established lines. *J Cell Biol*, 17:299–313, May 1963.

[221] C. Dingwall, S. M. Dilworth, S. J. Black, S. E. Kearsey, L. S. Cox, and R. A. Laskey. Nucleoplasmin cdna sequence reveals polyglutamic acid tracts and a cluster of sequences homologous to putative nuclear localization signals. *EMBO J*, 6(1):69–74, Jan 1987.

[222] J. A. Kleinschmidt, C. Dingwall, G. Maier, and W. W. Franke. Molecular characterization of a karyophilic, histone-binding protein: cdna cloning, amino acid sequence and expression of nuclear protein n1/n2 of xenopus laevis. *EMBO J*, 5(13):3547–3552, Dec 1986.

[223] Walker JM, editor. *The Protein Protocols Handbook, Second Edition*, chapter Quantification of Proteins on Western Blots Using ECL. Humana Press, 2002.

[224] Raphal Lvy, Zhenxin Wang, Laurence Duchesne, R. Christopher Doty, Andrew I Cooper, Mathias Brust, and David G Fernig. A generic approach to monofunctionalized protein-like gold nanoparticles based on immobilized metal ion affinity chromatography. *Chembiochem*, 7(4):592–594, Apr 2006.

[225] Jennifer Julia Strunk, Ingo Gregor, Yvonne Becker, Peter Lamken, Suman Lata, Annett Reichel, Jrg Enderlein, and Jacob Piehler. Probing protein conformations by in situ non-covalent fluorescence labeling. *Bioconjug Chem*, 20(1):41–46, Jan 2009.

[226] M. G. Giansanti, M. Gatti, and S. Bonaccorsi. The role of centrosomes and astral microtubules during asymmetric division of drosophila neuroblasts. *Development*, 128(7):1137–1145, Apr 2001.

[227] S. Bonaccorsi, M. G. Giansanti, and M. Gatti. Spindle self-organization and cytokinesis during male meiosis in asterless mutants of drosophila melanogaster. *J Cell Biol*, 142(3):751–761, Aug 1998.

[228] Hanne Varmark, Salud Llamazares, Elena Rebollo, Bodo Lange, Jose Reina, Heinz Schwarz, and Cayetano Gonzalez. Asterless is a centriolar protein required for centrosome function and embryo development in drosophila. *Curr Biol*, 17(20):1735–1745, Oct 2007.

[229] S. D. Fuller, B. E. Gowen, S. Reinsch, A. Sawyer, B. Buendia, R. Wepf, and E. Karsenti. The core of the mammalian centriole contains gamma-tubulin. *Curr Biol*, 5(12):1384–1393, Dec 1995.

[230] Aurelien Dif, Fouzia Boulmedais, Mathieu Pinot, Victor Roullier, Michele Baudy-Floc'h, Frederic M Coquelle, Samuel Clarke, Pierre Neveu, Francoise Vignaux, Roland Le Borgne, Maxime Dahan, Zoher Gueroui, and Valerie Marchi-Artzner. Small and stable peptidic pegylated quantum dots to target polyhistidine-tagged proteins with controlled stoichiometry. *J Am Chem Soc*, Sep 2009.

[231] Steward MW. *Antibodies: Thier structure and function.* Chapman and Hall, 1984.

[232] E. N. Kaufman and R. K. Jain. Effect of bivalent interaction upon apparent antibody affinity: experimental confirmation of theory using fluorescence photobleaching and implications for antibody binding assays. *Cancer Res*, 52(15):4157–4167, Aug 1992.

[233] E. T. Boder, K. S. Midelfort, and K. D. Wittrup. Directed evolution of antibody fragments with monovalent femtomolar antigen-binding affinity. *Proc Natl Acad Sci U S A*, 97(20):10701–10705, Sep 2000.

[234] Suman Lata, Martynas Gavutis, Robert Tamp, and Jacob Piehler. Specific and stable fluorescence labeling of histidine-tagged proteins for dissecting multi-protein complex formation. *J Am Chem Soc*, 128(7):2365–2372, Feb 2006.

[235] M. J. Saxton. Single-particle tracking: the distribution of diffusion coefficients. *Biophys J*, 72(4):1744–1753, Apr 1997.

[236] W. F. Wade, J. H. Freed, and M. Edidin. Translational diffusion of class ii major histocompatibility complex molecules is constrained by their cytoplasmic domains. *J Cell Biol*, 109(6 Pt 2):3325–3331, Dec 1989.

[237] Beate Neumann, Michael Held, Urban Liebel, Holger Erfle, Phill Rogers, Rainer Pepperkok, and Jan Ellenberg. High-throughput rnai screening by time-lapse imaging of live human cells. *Nat Methods*, 3(5):385–390, May 2006.

[238] B. R. Kelemen, T. A. Klink, M. A. Behlke, S. R. Eubanks, P. A. Leland, and R. T. Raines. Hypersensitive substrate for ribonucleases. *Nucleic Acids Res*, 27(18):3696–3701, Sep 1999.

[239] Gael Carney, Shu Wei, and William B Rizzo. Sjgren-larsson syndrome: seven novel mutations in the fatty aldehyde dehydrogenase gene aldh3a2. *Hum Mutat*, 24(2):186, Aug 2004.

[240] I. C. Ho, M. R. Hodge, J. W. Rooney, and L. H. Glimcher. The proto-oncogene c-maf is responsible for tissue-specific expression of interleukin-4. *Cell*, 85(7):973–983, Jun 1996.

[241] R. T. Raines, M. McCormick, T. R. Van Oosbree, and R. C. Mierendorf. The s.tag fusion system for protein purification. *Methods Enzymol*, 326:362–376, 2000.

[242] Shane R Nelson, M. Yusuf Ali, Kathleen M Trybus, and David M Warshaw. Random walk of processive, quantum dot-labeled myosin va molecules within the actin cortex of cos-7 cells. *Biophys J*, 97(2):509–518, Jul 2009.

[243] Laurent Holtzer, Tobias Meckel, and Thomas Schmidt. Nanometric three-dimensional tracking of individual quantum dots in cells. *Applied Physics Letters*, 90(5):053902, 2007.

[244] Tomonobu M Watanabe, Takashi Sato, Kohsuke Gonda, and Hideo Higuchi. Three-dimensional nanometry of vesicle transport in living cells using dual-focus imaging optics. *Biochem Biophys Res Commun*, 359(1):1–7, Jul 2007.

[245] Eric Betzig, George H Patterson, Rachid Sougrat, O. Wolf Lindwasser, Scott Olenych, Juan S Bonifacino, Michael W Davidson, Jennifer Lippincott-Schwartz, and Harald F Hess. Imaging intracellular fluorescent proteins at nanometer resolution. *Science*, 313(5793):1642–1645, Sep 2006.

[246] Marko Kaksonen and David G Drubin. Palm reading: Seeing the future of cell biology at higher resolution. *Dev Cell*, 11(4):438–439, Oct 2006.

[247] Mark Bates, Bo Huang, Graham T Dempsey, and Xiaowei Zhuang. Multicolor super-resolution imaging with photo-switchable fluorescent probes. *Science*, 317(5845):1749–1753, Sep 2007.

[248] Suliana Manley, Jennifer M Gillette, George H Patterson, Hari Shroff, Harald F Hess, Eric Betzig, and Jennifer Lippincott-Schwartz. High-density mapping of single-molecule trajectories with photoactivated localization microscopy. *Nat Methods*, 5(2):155–157, Feb 2008.

[249] Sean A McKinney, Christopher S Murphy, Kristin L Hazelwood, Michael W Davidson, and Loren L Looger. A bright and photostable photoconvertible fluorescent protein. *Nat Methods*, 6(2):131–133, Feb 2009.